

Development of a new 3D beam finite element with deformable section

Sasa Gao

► To cite this version:

Sasa Gao. Development of a new 3D beam finite element with deformable section. Mechanics of the structures [physics.class-ph]. Université de Lyon, 2017. English. NNT: 2017LYSEI026 . tel-02090796

HAL Id: tel-02090796

<https://tel.archives-ouvertes.fr/tel-02090796>

Submitted on 5 Apr 2019

HAL is a multi-disciplinary open access archive for the deposit and dissemination of scientific research documents, whether they are published or not. The documents may come from teaching and research institutions in France or abroad, or from public or private research centers.

L'archive ouverte pluridisciplinaire **HAL**, est destinée au dépôt et à la diffusion de documents scientifiques de niveau recherche, publiés ou non, émanant des établissements d'enseignement et de recherche français ou étrangers, des laboratoires publics ou privés.



N° d'ordre NNT: 2017LYSEI026

THÈSE de DOCTORAT DE L'UNIVERSITÉ DE LYON
préparée au sein de
l'Institut National des Sciences Appliquées de Lyon

École Doctorale 162
Mécanique, Énergétique, Génie civil, Acoustique

Spécialité/ discipline de doctorat
MÉCANIQUE – GÉNIE MÉCANIQUE – GÉNIE CIVIL

Soutenue publiquement le 05 Avril, 2017, par:

Sasa Gao

Development of a new 3D beam finite element with deformable section
(Développement d'un nouveau 3D poutre élément finis avec section déformable)

Devant le jury composé de:

Damien SOULAT	Professeur (ENSAIT)	Rapporteur
Philippe LE GROGNEC	Professeur (ENSTA Bretagne)	Rapporteur
Emmanuelle VIDAL-SALLE	Professeur (INSA de Lyon)	Directrice de thèse
Christophe BINETRUY	Professeur (École Centrale de Nantes)	Examinateur
Nahiène HAMILA	Maître de Conférences (INSA de Lyon)	Examinateur

LaMCoS - UMR CNRS 5514 - INSA de Lyon
20, avenue Albert Einstein, 69621 Villeurbanne Cedex (FRANCE)

Département FEDORA – INSA Lyon - Ecoles Doctorales – Quinquennal 2016-2020

SIGLE	ECOLE DOCTORALE	NOM ET COORDONNEES DU RESPONSABLE
CHIMIE	CHIMIE DE LYON http://www.edchimie-lyon.fr Sec : Renée EL MELHEM Bat Blaise Pascal 3 ^e etage secretariat@edchimie-lyon.fr Insa : R. GOURDON	M. Stéphane DANIELE Institut de Recherches sur la Catalyse et l'Environnement de Lyon IRCELYON-UMR 5256 Équipe CDFA 2 avenue Albert Einstein 69626 Villeurbanne cedex directeur@edchimie-lyon.fr
E.E.A.	ELECTRONIQUE, ELECTROTECHNIQUE, AUTOMATIQUE http://edea.ec-lyon.fr Sec : M.C. HAVGOUDOUKIAN Ecole-Doctorale.eea@ec-lyon.fr	M. Gérard SCORLETTI Ecole Centrale de Lyon 36 avenue Guy de Collongue 69134 ECULLY Tél : 04.72.18 60.97 Fax : 04 78 43 37 17 Gerard.scorletti@ec-lyon.fr
E2M2	EVOLUTION, ECOSYSTEME, MICROBIOLOGIE, MODELISATION http://e2m2.universite-lyon.fr Sec : Sylvie ROBERJOT Bât Atrium - UCB Lyon 1 04.72.44.83.62 Insa : H. CHARLES secretariat.e2m2@univ-lyon1.fr	M. Fabrice CORDEY CNRS UMR 5276 Lab. de géologie de Lyon Université Claude Bernard Lyon 1 Bât Géode 2 rue Raphaël Dubois 69622 VILLEURBANNE Cédex Tél : 06.07.53.89.13 cordey@univ-lyon1.fr
EDISS	INTERDISCIPLINAIRE SCIENCES-SANTE http://www.ediss-lyon.fr Sec : Sylvie ROBERJOT Bât Atrium - UCB Lyon 1 04.72.44.83.62 Insa : M. LAGARDE secretariat.ediss@univ-lyon1.fr	Mme Emmanuelle CANET-SOULAS INSERM U1060, CarMeN lab, Univ. Lyon 1 Bâtiment IMBL 11 avenue Jean Capelle INSA de Lyon 696621 Villeurbanne Tél : 04.72.68.49.09 Fax : 04 72 68 49 16 Emmanuelle.canet@univ-lyon1.fr
INFOMATHS	INFORMATIQUE ET MATHÉMATIQUES http://infomaths.univ-lyon1.fr Sec : Renée EL MELHEM Bat Blaise Pascal 3 ^e etage infomaths@univ-lyon1.fr	Mme Sylvie CALABRETTA LIRIS – INSA de Lyon Bat Blaise Pascal 7 avenue Jean Capelle 69622 VILLEURBANNE Cedex Tél : 04.72. 43. 80. 46 Fax 04 72 43 16 87 Sylvie.calabretto@insa-lyon.fr
Matériaux	MATERIAUX DE LYON http://ed34.universite-lyon.fr Sec : M. LABOUNE PM : 71.70 –Fax : 87.12 Bat. Direction Ed.materiaux@insa-lyon.fr	M. Jean-Yves BUFFIERE INSA de Lyon MATEIS Bâtiment Saint Exupéry 7 avenue Jean Capelle 69621 VILLEURBANNE Cedex Tél : 04.72.43 71.70 Fax 04 72 43 85 28 jean-yves.buffiere@insa-lyon.fr
MEGA	MECANIQUE, ENERGETIQUE, GENIE CIVIL, ACOUSTIQUE http://mega.universite-lyon.fr Sec : M. LABOUNE PM : 71.70 –Fax : 87.12 Bat. Direction mega@insa-lyon.fr	M. Philippe BOISSE INSA de Lyon Laboratoire LAMCOS Bâtiment Jacquard 25 bis avenue Jean Capelle 69621 VILLEURBANNE Cedex Tél : 04.72.43.71.70 Fax : 04 72 43 72 37 Philippe.boisse@insa-lyon.fr
ScSo	ScSo* http://recherche.univ-lyon2.fr/scso/ Sec : Viviane POLSINELLI Brigitte DUBOIS Insa : J.Y. TOUSSAINT Tél : 04 78 69 72 76 viviane.polsinelli@univ-lyon2.fr	M. Christian MONTES Université Lyon 2 86 rue Pasteur 69365 LYON Cedex 07 Christian.montes@univ-lyon2.fr

*ScSo : Histoire, Géographie, Aménagement, Urbanisme, Archéologie, Science politique, Sociologie, Anthropologie

Acknowledgment

I wish to thank a number of persons for their help and support during my PhD thesis.

First and foremost, I would like to express my appreciation to Professor Emmanuelle Vidal-Salle for her supervision and guidance through the whole work. Her consistent concern, creative advice and countless encouragement have helped me a lot, which make me complete my PhD thesis on time. Her enthusiasm and meticulousness on scientific research impress me deeply, which give me a super model to follow in the future research work.

I also want to thank gorgeously Dr. Francis Sabourin for his generous help and advices. And our work is rightly inspired by his previous work on enhanced shell element.

I'm also grateful to Dr. Nahiene Hamila, Dr. Julien Colmars, Dr. Naim Naouar, Dr. Eduardo Guzman and Professor Philippe Boisse for their assistance and advice on my PhD work.

Appreciation should be also going to my colleagues and friends: Ismael Azelef, Dawei Wang, Hu Xiong, Jie Wang and so on, for their support and help. I have been so happy with them.

I also want to acknowledge the financial support provided by China Scholarship Council (CSC) in my PhD study in France. I'm indebted to my research laboratory, LaMCoS, INSA-Lyon, for its technical support.

Finally, I'm very grateful to my loving parents for their concern and support throughout my life, especially their selfless love and care for Siyu Liang during the period when I'm busy with my thesis. I'm also grateful to my girl Siyu Liang who gives me unlimited joy at the end of my thesis. Appreciation should be also addressed to my brother Hongzhi Gao who always gives me great support and encouragement during my life.

Last but not the least, I heartily appreciate my husband, Biao Liang, for his countless encouragement and help during the whole period of my PhD studies and the joyful days we spent in Lyon (France).

Abstract

The present work aims to present a new tool for modelling textile materials using the yarn as constitutive element. Since fiber tows length is much higher than their transverse dimensions, beam elements seem to be the most convenient structural finite element tool. Unfortunately, classical beam theories assume that the cross section acts as a rigid which can't describe the transverse compression and shape change of the yarn. This thesis is devoted to propose a new 3D beam element with deformable section while breaking from classical beam hypothesis.

The new beam element is an evolution of a two nodes Timoshenko beam element with an extra node located at mid-length. That extra node allows the introduction of three extra strain components: ε_{yy} , ε_{zz} and $2\varepsilon_{yz}$ so that full 3D stress/strain constitutive relations can be used directly. The proposed element has been introduced in a Matlab finite element code and a series of linear/small strain cases have been realized and the results are systematically compared with the corresponding values from ABAQUS/Standard 3D simulations. Such results show, if needed, that the 8 extra degrees of freedom are sufficient to introduce the coupling between ε_{yy} and ε_{zz} . After that, the second step is to introduce the orthotropic behavior and carry out validation for large displacements/small strains based on Updated Lagrangian Formulation. A series of numerical analyses are carried out which shows that the enhanced 3D element provides an excellent numerical performance. Indeed, the final goal is to use the new 3D beam elements to model yarns in a textile composite preform. For this purpose, the third step is introducing contact behavior and carrying out validation for new 3D beam to beam contact with rectangular cross section. The contact formulation is derived on the basis of Penalty Formulation and Updated Lagrangian formulation using physical shape functions with shear effect included. An effective contact search algorithm, which is necessary to determine an active set for the contact contribution treatment, is elaborated. And a consistent linearization of contact contribution is derived and expressed in suitable matrix form, which is easy to use in FEM approximation. Finally, some numerical examples are presented which are only qualitative analysis of contact and checking the correctness and the effectiveness of the proposed 3D beam element.

KEYWORDS: Enhanced 3D beam element; Rectangular cross-section; Section deformation; Full 3D constitutive law; Large displacements/small strains; Updated Lagrangian Formulation; Frictionless contact; Hermite smoothing

Résumé

Le présent travail a le but de présenter un nouvel outil pour modéliser matériaux textiles qui considère le fil comme élément constitutif. Étant donné que la longueur des fibres est plus élevée que leurs dimensions transversales, les poutre éléments finis semblent être l'outil le plus avantageux. Malheureusement, les théories de poutres classiques supposent que la section transversale agit comme une rigide qui ne peut pas décrire la compression transversale et le changement de forme du fil. Cette thèse est consacrée à proposer un nouvel élément de 3D poutre à section déformable en rompant avec l'hypothèse de poutre classique.

Le nouvel élément de poutre est une évolution d'un élément de Timoshenko poutre avec un noeud supplémentaire situé à mi-longueur. Ce noeud supplémentaire permet l'introduction de trois composantes supplémentaires de contrainte: ϵ_{yy} , ϵ_{zz} and $2\epsilon_{yz}$ afin que la loi constitutionnelle 3D complète puisse être utilisée directement. L'élément proposé a été introduit dans un code d'éléments finis dans Matlab et une série d'exemples de linéaires / petites contraintes ont été réalisées et les résultats sont systématiquement comparés avec les valeurs correspondantes des simulations ABAQUS / Standard 3D. Ces résultats montrent, si nécessaire, que les 8 degrés de liberté supplémentaires sont suffisants pour introduire le couplage entre ϵ_{yy} et ϵ_{zz} . Ensuite, la deuxième étape consiste à introduire le comportement orthotrope et à effectuer la validation de déplacements larges / petites contraintes basés sur la formulation Lagrangienne mise à jour. Une série d'analyses numériques est réalisée qui montre que l'élément 3D amélioré fournit une excellente performance numérique. En effet, l'objectif final est d'utiliser les nouveaux éléments de poutre 3D pour modéliser des fils dans une préforme composite textile. A cet effet, la troisième étape consiste à introduire un comportement de contact et à effectuer la validation pour un nouveau contact entre 3D poutres à section rectangulaire. La formulation de contact est dérivée sur la base de formulation de pénalité et de formulation Lagrangian mise à jour utilisant des fonctions de forme physique avec l'effet de cisaillement inclus. Un algorithme de recherche de contact efficace, qui est nécessaire pour déterminer un ensemble actif pour le traitement de contribution de contact, est élaboré. Et une linéarisation constante de la contribution de contact est dérivée et exprimée sous forme de matrice appropriée, qui est facile à utiliser dans l'approximation FEM. Enfin, on présente quelques exemples numériques qui ne sont que des analyses qualitatives du contact et de la vérification de l'exactitude et de l'efficacité de l'élément de 3D poutre proposé.

MOTS CLÉS : Élément de 3D poutre amélioré; Section rectangulaire; Déformation de la section; Loi constitutionnelle 3D complète; Déplacements larges / petites contraintes; Mise à jour de la formulation Lagrangienne; Contact sans frottement; Lissage Hermite

Contents

Contents	i
List of Figures	v
List of Tables	ix
1 Introduction	1
1.1 Introduction to composite materials	2
1.1.1 Definition of composite materials	2
1.1.2 Classification	2
1.1.3 Types of textile architecture	5
1.1.4 Advantages and applications	6
1.2 Scales of analysis for composites	9
1.2.1 Microscopic scale	9
1.2.2 Mesoscopic scale	11
1.2.3 Macroscopic scale	13
1.2.4 Research scale of the thesis	16
1.2.5 Deformation mechanisms at mesoscopic scale	16
1.3 Motivation and objectives	21
2 Development of the new 3D beam element	23
2.1 Introduction	23
2.2 Review of the related work	24
2.2.1 Evolution of beam models	24
2.2.2 Introduction to the beam element	25
2.3 The assumption and the inspiration of the new 3D beam element	30
2.3.1 Assumption	30
2.3.2 The review of the related work on shell enrichment elements	31
2.4 Modelling of the new 2D beam element with thickness change	33
2.4.1 Geometry and kinematics	34
2.4.2 Gradient matrix	35
2.4.3 Stiffness matrix and integration strategy	36
2.5 Extension to 3D beam element with deformable section	37

2.5.1	Geometry and kinematics	38
2.5.2	Shape functions and gradient matrix	39
2.5.3	Stiffness matrix and integration strategy	41
2.6	Numerical validation for linear small strain conditions	43
2.6.1	Tension	44
2.6.2	Pure bending	44
2.6.3	Shear + bending	50
2.6.4	Transverse compression	53
2.6.5	Torsion	54
2.7	The advantages of the new 3D beam compared with solid element	54
2.8	Conclusions and developments	55
3	Analysis of large displacements/small strains behavior	57
3.1	Introduction and review of literature	57
3.2	Incremental T.L. and U.L. continuum mechanics formulations	59
3.2.1	Total Lagrangian (T.L.) formulation	60
3.2.2	Updated Lagrangian (U.L.) formulation	61
3.3	Calculation formulation chosen	62
3.3.1	U.L. and T.L. formulations of general 3D beam element	62
3.3.2	The calculation method chosen	64
3.4	Properties of isotropic and orthotropic materials	65
3.5	Formulation for large rotations/small strains behavior	66
3.5.1	Small rotation theory	66
3.5.2	Motion decomposition of rotation vector	66
3.5.3	Updated Lagrangian formulation for rotation vector of 2D beam element	68
3.5.4	Incremental displacement field of classical 2D beam	69
3.5.5	Incremental displacement field of classical 3D beam	69
3.5.6	Incremental displacement field for enhanced 2D beam elements	71
3.6	Extend to enhanced 3D beam elements with large rotation/ small strain behavior	74
3.7	Numerical studies	79
3.7.1	Large displacement/rotation analysis of a cantilever with isotropic material	80
3.7.2	Large displacement/rotation analysis of a cantilever with orthotropic material	84
3.8	Conclusions and future developments	90
4	Enhanced 3D beam to beam contact	93
4.1	Introduction and review of the related work	93
4.2	Frictionless Contact between Solids	94
4.3	Finite element method in contact analysis	96
4.4	Weak formulation and kinematic variables of contact contribution	98

4.5	Contact search	101
4.6	Finite element formulation of contact contribution	104
4.7	Smooth contact between enhanced 3D beam contact	108
4.7.1	3D curve smoothing using Hermite polynomial	108
4.7.2	Finite element discretization of smooth contact	110
4.8	Numerical examples	111
4.8.1	Example 1: point to point contact	112
4.8.2	Example 2: edge to edge contact	115
4.8.3	Example 3: surface to surface contact	117
4.9	Conclusions and future developments	119
Conclusions and perspectives		121
Appendices		123
A Strain-displacement transformation matrix B		125
B Calculations of matrix D and E		129
B.1	Calculation of matrix D	129
B.2	Calculation of matrix E	130
C Matrices G and H in Smoothing Procedures		131
Bibliography		133

Contents

List of Figures

1.1	Examples of composite materials with different forms of constituents and distributions of the reinforcements: (a) Random fiber (short fiber) reinforced composites. (b) Continuous fiber reinforced composites. (c) Particulate composites. (d) Flake composites. (e) Filler composites.	3
1.2	Classification of composites based on reinforcement [ALT 13].	4
1.3	Classification of composites based on matrix materials [ALT 13].	5
1.4	Classification of composites based on matrix materials [SHE 07].	6
1.5	Applications of composites.	8
1.6	Three modelling scales of textile composites.	9
1.7	Modelling considering each fiber as a 3D beam [DUR 05].	10
1.8	Relaxation processes of 3-D woven fabrics. (a) Initial fabric geometry. (b) Relaxed micro-geometry [MIA 08].	11
1.9	Mesoscopic model of a glass balanced plain weave [GAT 10]. (a) 47214 DoF. (b) 216 DoF.	12
1.10	Geometrical model and mesh for the G986 RUC [NGU 13].	12
1.11	Validation of no sliding assumption between yarns in the forming [BOI 93].	13
1.12	A representative cell of the meso-mechanical model for NCF [CRE 06]. .	14
1.13	Discretization of plain weave fabric [BAL 08].	15
1.14	Schematic of semi-discrete elements and their forming simulations.(a) Shell element [HAM 08]. (b) Solid element [DEL 09].	15
1.15	Non-linear tensile curve for an initially twisted fiber bundle [BOI 12]. .	18
1.16	Yarn's tensile behavior test device proposed by Florimond [FLO 13]. (a) Configuration of test device. (b) Yarn's tensile test result.	18
1.17	Two modes of yarn's shearing: (a) Transverse shearing. (b) Longitudinal shearing [FLO 13].	20
1.18	Fibers distribution in a yarn: (a) Unloaded. (b) Subjected to biaxial tension [BAD 09].	20
2.1	Evolution of beam models. (a) Bernoulli-Euler beam. (b) Timoshenko beam. (c) Proposed 3D beam.	24
2.2	Two-nodes beam element.	26
2.3	Euler-Bernoulli beam.	26
2.4	Timoshenko beam.	28

2.5	Enriched shell elements: (a). Enriched three-node shell element. (b). Enriched four-node shell element.	31
2.6	Additional of two degrees of freedom on Timoshenko beam element.	34
2.7	Five through-thickness integration points [ABA 13]. (a). 2D circular cross section. (b). 2D rectangular cross section.	37
2.8	Additional of a central node based 3D Timoshenko beam.	39
2.9	Presentation of the additional node with 8 degrees of freedom.	40
2.10	Integration points [ABA 13]. (a). Circular cross section.(b). Rectangular cross section.	43
2.11	Mesh model. (a).In Matlab. (b). In Abaqus.	43
2.12	Results comparison of ABAQUS and Matlab under tension. (a). Distribution of displacement U_x . (b). Distribution of displacement errors U_xError	45
2.13	A cantilever beam subjected to a constant moment	46
2.14	Results comparison of ABAQUS and Matlab under pure bending. (a). Displacement U_y of the centroidal axis. (b). Distribution of displacement errors U_yError	47
2.15	Results comparison of ABAQUS and Matlab under pure bending. (a). Displacement distribution of cross section. (b). Displacement errors of cross section.	48
2.16	Results comparison of ABAQUS and Matlab under tension. (a). Displacement U_y of the centroidal axis. (b). Error of U_yError for the centroidal axis.	49
2.17	A cantilever beam subjected to a concentrated force.	50
2.18	Results comparison of ABAQUS and Matlab. (a). Displacement U_y of the centroidal axis. (b). Distribution of displacement errors U_yError	51
2.19	Results comparison of ABAQUS and Matlab. (a). Relative displacement of cross section. (b). Displacement errors of cross section.	52
2.20	Isovalues of U_y on deformed configuration of cross section at $x=5.5$ mm given by ABAQUS and MATLAB	53
2.21	Cantilever under transverse compression.	54
2.22	Cantilever under torsion.	55
2.23	Rotation angle comparisons with ABAQUS and MATLAB. (a). Rotation angle α_x . (b). Error of rotation angle α_x	56
3.1	Motion of body in Cartesian coordinate frame [BAT 75].	59
3.2	Motion of the 3D beam element and its local coordinate axes shown in global coordinate frame [BAT 76].	63
3.3	Description of small rotation theory.	67
3.4	Motion decomposition of rotational vector.	67
3.5	Motion decomposition of rotational vector.	68
3.6	Presentation of the 3D Timoshenko beam element in initial configuration.	70
3.7	Presentation of the enhanced 2D beam element with large rotation in initial configuration.	71

3.8	Presentation of the enhanced 3D beam element with large rotation at initial configuration.	75
3.9	Definition of Euler's angles.	79
3.10	Displacements of the centroidal axis in x and y direction.	81
3.11	Rotations angles of the centroidal axis around z axis.	81
3.12	Comparisons of the displacement distribution of cross section. (a). Distribution of v_c^+ and v_c^- . (b). Distribution of v_a^+	82
3.13	Comparisons of the displacement distribution of cross section. (a). Distribution of w_c^+ and w_c^- . (b). Distribution of w_a^+ and w_d^+	83
3.14	Displacements of the centroidal axis in x and y direction.	84
3.15	Comparisons of the displacement distribution of cross section. (a). Distribution of v_c^+ and v_c^- . (b). Distribution of v_a^+ and v_b^+	85
3.16	Comparisons of the displacement distribution of cross section. (a). Distribution of w_c^+ and w_c^- . (b). Distribution of w_a^+ and w_d^+	86
3.17	Displacements of the centroidal axis in x and y direction.	87
3.18	Rotations angles of the centroidal axis around z axis.	87
3.19	Comparisons of the displacement distribution of cross section. (a). Distribution of v_c^+ and v_c^- . (b). Distribution of v_a^+ and v_b^+	88
3.20	Comparisons of the displacement distribution of cross section. (a). Distribution of w_c^+ and w_c^- . (b). Distribution of w_a^+ and w_d^+	89
3.21	Displacements of the centroidal axis in x and y direction.	90
3.22	Comparisons of the displacement distribution of cross section. (a). Distribution of v_c^+ and v_c^- . (b). Distribution of v_a^+ and v_b^+	91
3.23	Comparisons of the displacement distribution of cross section. (a). Distribution of w_c^+ and w_c^- . (b). Distribution of w_a^+ and w_d^+	92
4.1	Deformation of two bodies and penetration function:(a) separate bodies. (b) penetration [LIT 10].	95
4.2	Contact finite elements: (a) node-to-node. (b) node-to-segment. (c) node-to-surface. (d) beam-to-beam [LIT 10].	97
4.3	The closest points on two curves.	98
4.4	Contact between edges of beams with rectangular cross-sections. (a) One pair. (b) Two pairs. (c) Four pairs. (d) More than four pairs [LIT 02b]. . .	102
4.5	Search of the closest edges [LIT 10].	102
4.6	Contact criterion for beams with rectangular cross sections. (a) Separation. (b) Penetration. [LIT 02b, LIT 10]	103
4.7	Illustration of the beam finite element with rectangular cross section. . . .	105
4.8	Construction of inscribed curve segment.	108
4.9	Illustration of unit cell with rectangular cross-section.	111
4.10	Initial configuration of contact between one pair of points. (a). 3D view. (b). Plane XY. (c). Plane XZ. (d). Plane YZ.	112
4.11	Displacements of the centroidal axis in three directions. (a) Beam m . (b) Beam s	113

4.12	Displacement distribution comparisons of cross section of beam m . (a). Distribution of v_c^+ and v_c^- . (b). Distribution of v_a^+ and v_b^+ . (c). Distribution of w_c^+ and w_c^- . (d). Distribution of w_a^+ and w_d^+	113
4.13	Displacement distribution comparisons of cross section of beam s . (a). Distribution of v_c^+ and v_c^- . (b). Distribution of v_a^+ and v_b^+ . (c). Distribution of w_c^+ and w_c^- . (d). Distribution of w_a^+ and w_d^+	114
4.14	Initial configuration of contact between edge to edge. (a). 3D view. (b). Plane XY. (c). Plane XZ. (d). Plane YZ.	115
4.15	Displacements of the centroidal axis in three directions. (a) Beam m . (b) Beam s	116
4.16	Displacement distribution comparisons of cross section of beam m . (a). Distribution of v_c^+ and v_c^- . (b). Distribution of v_a^+ and v_b^+ . (c). Distribution of w_c^+ and w_c^- . (d). Distribution of w_a^+ and w_d^+	116
4.17	Displacement distribution comparisons of cross section of beam s . (a). Distribution of v_c^+ and v_c^- . (b). Distribution of v_a^+ and v_b^+ . (c). Distribution of w_c^+ and w_c^- . (d). Distribution of w_a^+ and w_d^+	117
4.18	Initial configuration of contact between surface to surface. (a). 3D view. (b). Plane XY. (c). Plane XZ. (d). Plane YZ.	118
4.19	Displacements of the centroidal axis in three directions. (a) Beam m . (b) Beam s	118
4.20	Displacement distribution comparisons of cross section of beam m . (a). Distribution of v_c^+ and v_c^- . (b). Distribution of v_a^+ and v_b^+ . (c). Distribution of w_c^+ and w_c^- . (d). Distribution of w_a^+ and w_d^+	119
4.21	Displacement distribution comparisons of cross section of beam s . (a). Distribution of v_c^+ and v_c^- . (b). Distribution of v_a^+ and v_b^+ . (c). Distribution of w_c^+ and w_c^- . (d). Distribution of w_a^+ and w_d^+	120

List of Tables

2.1	Cross section deformation comparison of ABAQUS and Matlab under tension	44
2.2	Cross section deformation comparison of results from ABAQUS and Matlab under transverse compaction	54

List of Tables

Chapter 1

Introduction

Textile reinforcements are widely used in composite industry. In order to save time (and money), it is of primary importance to reduce the time between product idea and its delivery. To achieve this goal, it is necessary to have a good comprehension of the fabric behavior. Composite materials are certainly the materials for which the interaction between design and process is the most important because each composite structural component is made of a unique material if one considers the reinforcement distribution (in terms of fiber orientation, fiber density …). Consequently, designing a composite structural part requires the knowledge of mechanical behavior of the dry reinforcement (which can be woven, knitted, braided …).

The need of efficient modelling textile materials at meso-scale increased considerably in the last decade. Several approaches have been proposed which present different kinds of drawbacks, the most important being their high computation time. My thesis aims to present a new tool for modelling textile materials using the yarn as constitutive element. Because fiber tows length is much higher than their transverse dimensions, beam elements seem to be the most convenient structural finite element tool. Unfortunately, classical beam theories assume that the cross section acts as a rigid which can't describe the transverse compression and shape change of the yarn. Therefore, we present a new 3D beam element with the aim to achieve the results with section changes while breaking from classical beam hypothesis.

The main features of newly proposed 3D beam element are: each element has two end nodes which are treated by combining Saint-Venant and Timoshenko hypothesis; the transverse strains of both thickness and width direction are introduced based on the additional central node. The transverse strain distributions are linear, and the formulations of displacement are completely quadratic by adding the terms coupling the deformation in both transverse directions; fully 3D constitutive stress/strain relations can be used directly.

The whole work is composed of three steps, the first step is the proposition of the new 3D beam and validation for linear small strain conditions, and the following steps are: carrying out validation for large displacements/ small strains; introducing contact behavior and carrying out validation for new 3D beam to beam contact.

1.1 Introduction to composite materials

1.1.1 Definition of composite materials

A composite material can be defined as a combination of two or more materials, which when combined give properties superior to the properties of the individual components [CAM 03]. Thus, a composite material is heterogeneous at a microscopic scale but statistically homogeneous at macroscopic scale. The materials which form the composite are also called as constituents or constituent materials. The constituent materials of a composite have significantly different properties. Further, it should be noted that the properties of the composite formed may not be obtained from these constituents. However, a combination of two or more materials with significant properties will not be enough to be called as a composite material. In general, the following conditions must be fulfilled to be called a composite material:

- (1) The combination of materials should result in significant property changes. One can see significant changes when one of the constituent material is in platelet or fibrous form.
- (2) The content of the constituents is generally more than 10% (by volume).
- (3) In general, a given property of one constituent is much greater (5 times) than the corresponding property of the other constituent.

The main advantages of composite materials are their high strength and stiffness, combined with low density, when compared with bulk materials, allowing for a weight reduction in the finished part. The reinforcing phase provides the strength and stiffness. In most cases, the reinforcement is harder, stronger, and stiffer than the matrix [CAM 10]. There are two categories of constituent materials: reinforcement and matrix. The reinforcement is used to strengthen the matrix in terms of strength and stiffness. The reinforcement can be cut, aligned, placed in different ways to tailor the properties of the resulting composite. The matrix performs several critical functions, including maintaining the reinforcement in the proper orientation, spacing and protecting it from chemical aggression and the environment attack, it also bonds the reinforcement so that it can transmit loads from the matrix to the reinforcement through shear loading at the interface [CAM 03]. The properties of the composites depend on the properties of the constituents, their relative proportion, geometry, distribution, and orientation of the reinforcements. The main factors are the properties and the relative amount of constituents. Hence, it is possible to get the desired properties in the final composite by selecting the right combination of materials in their proper proportion.

1.1.2 Classification

Composites can be broadly classified into natural and synthetic composites. Natural composites exist from both animals and plants. Although the constituents are present in fine

scale in the natural composites, it is very difficult to tailor the properties of natural composites. It is different for synthetic composites because they are artificial composites. There is sufficient flexibility of selecting a suitable reinforcement and a matrix from the wide variety of reinforcements and matrices to get composites with the desired properties. Figure 1.1 shows several typical examples of composite materials.

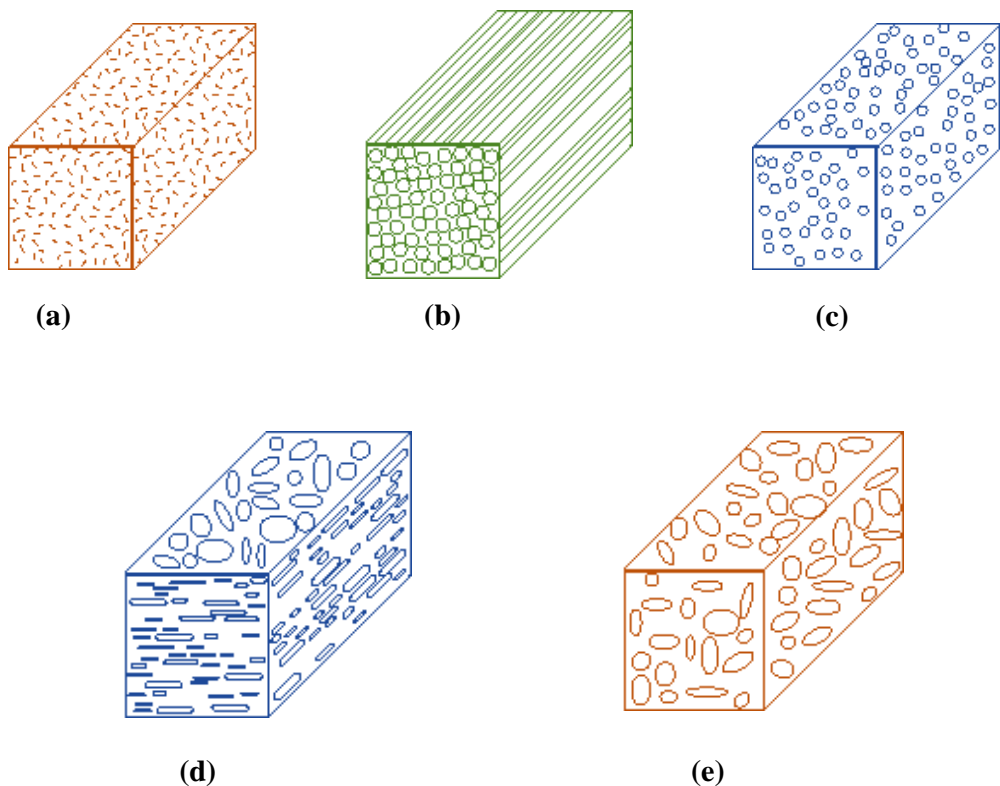


Figure 1.1 – Examples of composite materials with different forms of constituents and distributions of the reinforcements: (a) Random fiber (short fiber) reinforced composites. (b) Continuous fiber reinforced composites. (c) Particulate composites. (d) Flake composites. (e) Filler composites.

Based on the reinforcement, the composites can be classified as fiber-reinforced composites (FRCs), particulate composites, flake and filler composites, shown in Figure 1.2.

Fiber is an individual filament of the material. A filament with length to diameter ratio above 1000 is called a fiber. The fibrous form of the reinforcement is widely used. The fibers can be in the following two forms:

Continuous fibers: the fibers used in a composite are very long and unbroken or cut to form a continuous fiber composite. Thus, a composite formed using continuous fibers is called as fibrous composite. The fibrous composite is the most widely used form of composite for structural applications.

Short/chopped fibers: the fibers are chopped into small pieces when used for fabricating a composite. A composite with short fibers as reinforcements is called as short

1. Introduction

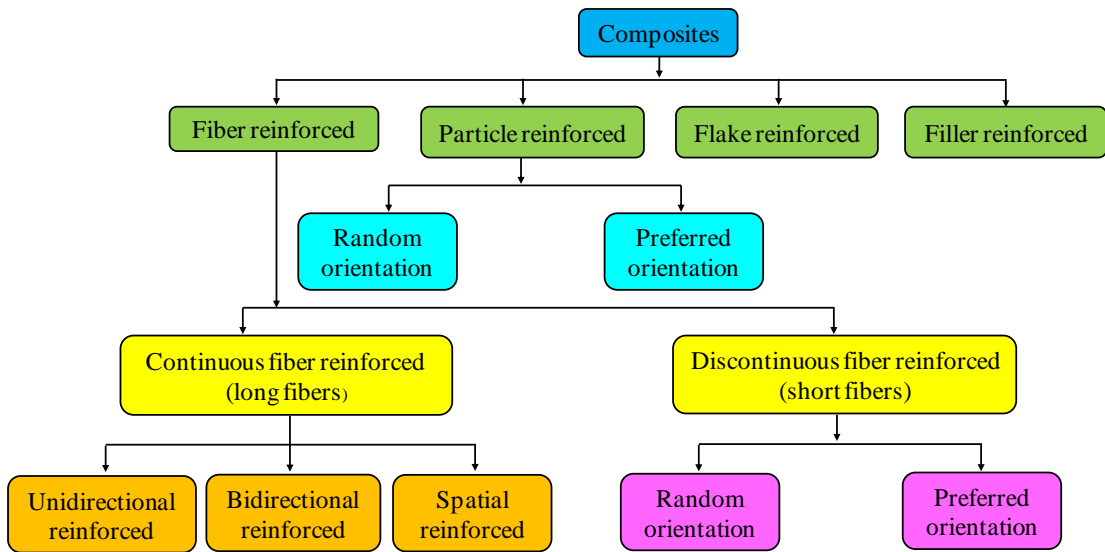


Figure 1.2 – Classification of composites based on reinforcement [ALT 13].

fiber composite.

In the fiber reinforced composites, the fiber is the major load carrying constituent. Continuous fibers are arranged usually in uni- or bi-directional. In case of mat materials, the fibers are randomly arranged. The arrangement and the orientation of continuous or short fibers determines the mechanical properties of composites and the behavior ranges from a general anisotropy to a quasi-isotropy.

Particulates: the reinforcement is in the form of particles which are of the order of a few microns in diameter. The particles are generally added to increase the modulus and decrease the ductility of the matrix materials. In this case, the load is shared by both particles and matrix materials. However, the load shared by the particles is much larger than the matrix material. For example, carbon black (as a particulate reinforcement) is added in rubber (as matrix material) in an automobile application. The composite with reinforcement in particle form is called a particulate composite. Particulate reinforcements have different shapes. They may be spherical, platelet or of any regular or irregular geometry. Their arrangement may be random or regular with preferred orientations.

Flake is a small, flat, thin piece or layer (or a chip) that is broken from a larger piece. Since these are two dimensional in geometry, they impart almost equal strength in all directions of their planes. Thus, these are very effective reinforcement components. The flakes can be packed more densely when they are laid parallel, even denser than unidirectional fibers and spheres.

In filler composites, composites are filled by a secondary material along with the main reinforcement. The percentage of filler material is quite less than the main reinforcement. Particle fillers are the most commonly used filler materials to improve the properties of matrix materials.

As previously mentioned, in a composite, typically, there are two constituents. One

of the constituent acts as a reinforcement and the other acts as a matrix. Sometimes, the constituents are also referred as phases. Matrices can be polymers, metals or ceramics. Based on the matrix material, the composites are classified into polymer matrix composites (PMCs), metal matrix composites (MMCs), and ceramic matrix composites (CMCs). The classification of composites based on matrix material is shown in Figure 1.3. The three types of composites differ in the manufacturing method adopted, mechanical behaviors, and functional characteristics.

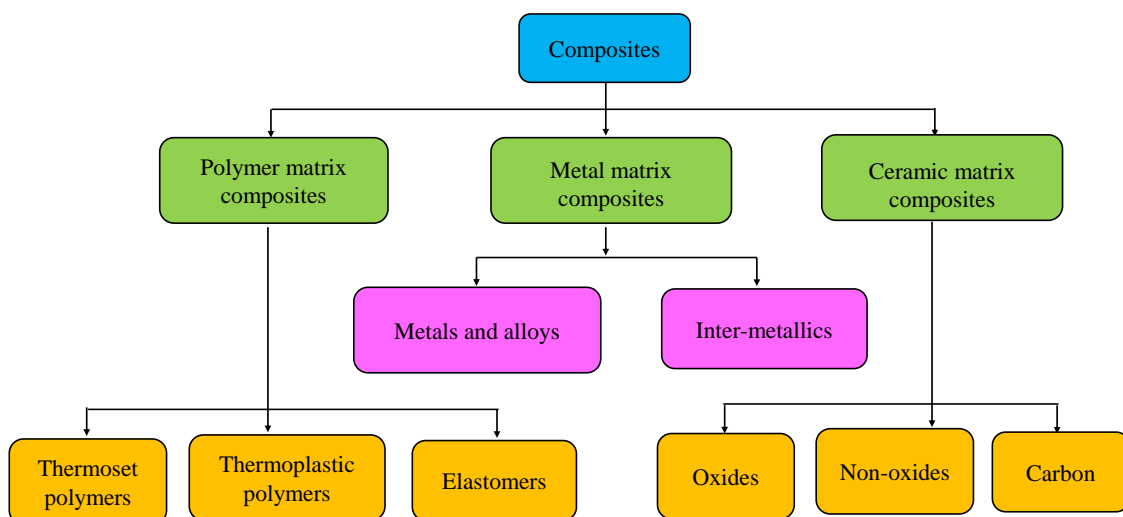


Figure 1.3 – Classification of composites based on matrix materials [ALT 13].

1.1.3 Types of textile architecture

In case of structural applications, continuous fibers are used. Textile reinforced composites are a subclass of composites where the reinforcement is a textile material comprised of a network of natural or artificial fibers, typically arranged as tows or yarns. The main categories of textile architecture relevant to composite materials are woven, braided, weft-knitted and non-crimp (Figure 1.4).

Woven fabrics consist of usually two orthogonal series of yarns, referred to as warp and weft yarns, interlaced to form a self-supporting textile structure. There are a number of possible interlacing patterns, the simplest of which is the plain weave where each warp yarn interlaces with each weft yarn. More complex interlacing patterns can be categorized as twill, satin, crowfoot, rib, basket, herringbone, crepe, etc. Multilayer woven fabrics, also known as interlock weaves, are composed of several layers of warp and weft yarns woven together. The number of possible interlacing patterns is virtually infinite, however they are broadly categorized as orthogonal, through-thickness and angle interlock (also known as layer-to-layer).

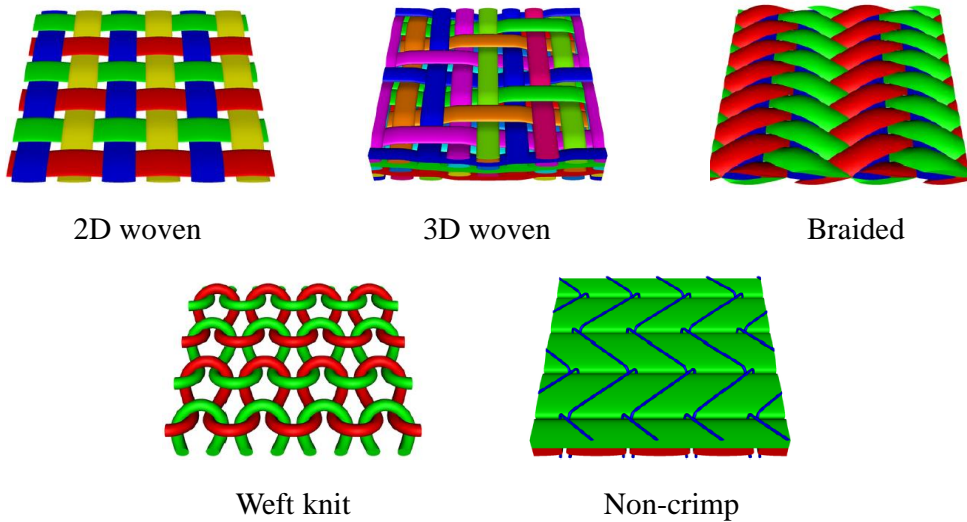


Figure 1.4 – Classification of composites based on matrix materials [SHE 07].

1.1.4 Advantages and applications

The advantages of composites are many, including lighter weight, the ability to tailor the layup for optimum strength and stiffness, improved fatigue life, corrosion resistance, and with good design practice, reduced assembly costs due to fewer detail parts and fasteners [CAM 10].

The list of advantages of composite is quite long. One can find more on advantages of composite in reference books and open literature. The following lists some advantages of composites:

Specific stiffness and strength:

The composite materials have high specific stiffness and strengths. Thus, these materials offer better properties with less weight compared with conventional materials. Due to this, one gets improved performance at reduced energy consumption.

Tailorable design:

A large set of design parameters are available to choose, making the design procedure more versatile. The available design parameters are:

- (1) Choice of materials (fiber/matrix), volume fraction of fiber and matrix, fabrication method, layer orientation, number of layer/laminae in a given direction, thickness of individual layers, type of layers (fabric/unidirectional) and stacking sequence.
- (2) A component can be designed to have desired properties in specific directions.

Fatigue life:

The composites can withstand more number of fatigue cycles than that of aluminum. The critical structural components in aircraft require high fatigue life. The use of composites in fabrication of such structural components is thus justified.

Dimensional stability:

Due to temperature, strain can change shape, size, increase friction, wear and thermal stresses. The dimensional stability is very important in application like space antenna. For composites, with proper design it is possible to achieve almost zero coefficient of thermal expansion.

Corrosion resistance:

Polymer and ceramic matrix materials used to fabricate composites have high resistance to corrosion from moisture, chemicals.

Cost effective fabrication:

The components fabricated from composite are cost effective with automated methods like filament winding, pultrusion and tape laying. There is a lesser wastage of the raw materials as the product is fabricated to the final product size unlike in metals.

Conductivity:

The conductivity of the composites can be achieved to make it an insulator or a highly conducting material. For example, glass/polyesters are non-conducting materials. These materials can be used in space ladders, booms etc. where one needs higher dimensional stability, whereas copper matrix material gives a high thermal conductivity.

Composite materials have a long history of usage. Their precise beginnings are unknown, but all recorded history contains references to some form of composite material. Recently, the use of composite materials is more and more extensive and expanding. Applications include aerospace, transportation, construction, marine goods, sporting goods, and more recently infrastructure, with construction and transportation being the largest (Figure 1.5).

The primary reason for that composite materials are chosen for components is because of weight saving for its relative stiffness and strength. Therefore, the component weight can be drastically reduced by using composites. For example, carbon-fiber reinforced composite can be five times stronger than 1020 grade steel while having only one fifth of the weight. Aluminum (6061 grade) is much nearer in weight to carbon-fiber composite, though still somewhat heavier, but the composite can have twice the modulus and up to seven times the strength.

The first modern composite material was fiberglass. It is still widely used today for boat hulls, sport equipment, building panels and many car bodies. The matrix is a polymer and the reinforcement is glass that has been made into fine threads and often woven into a sort of cloth. Individually, the glass is very strong but brittle and it will break if bent sharply. The polymer matrix holds the glass fibers together and also protects them from damage by sharing out the forces acting on them.

Some advanced composites are now made using carbon fibers instead of glass. These materials are lighter and stronger than fiberglass but more expensive to produce. They are used in aircraft structures and expensive sport equipment such as golf clubs.

Carbon nanotubes have also been used successfully to make new composites. These are even lighter and stronger than composites made with ordinary carbon fibers but they are still extremely expensive. They do, however, offer possibilities for making lighter cars

1. Introduction



Aerospace



Heavy Truck



Complex Construction



Wind Turbine



Automotive



Marine

Figure 1.5 – Applications of composites.

and aircraft (which will use less fuel than the heavier vehicles we have now).

The new Airbus A380, the world's largest passenger airliner, makes use of modern composites in its design. More than 20% of the A380 is made of composite materials, mainly polymer reinforced with carbon fibers. The design is the first large-scale use of glass-fiber-reinforced aluminum, a new composite that is 25% stronger than conventional airframe aluminum but 20% lighter.

Development and applications of composite materials and structural elements composed of composite materials have been very rapid in the last decades. The motivations for this development are the significant progress in material science and technology of the composite constituents. The requirements for high performance materials is not only in aircraft and aerospace structures, but also in the development of very powerful experimental equipment and numerical methods and the availability of efficient computers.

There is unabated thirst for new materials with improved desired properties. All the desired properties are difficult to find in a single material. For example, a material which needs high fatigue life may not be cost effective. The list of the desired properties, depending upon the requirement of the application, is given: strength, stiffness, toughness, high corrosion resistance, high wear resistance, high chemical resistance, high environmental degradation resistance, reduced weight, high fatigue life, thermal insulation or conductivity, electrical insulation or conductivity, acoustic insulation, radar transparency, energy

dissipation, reduced cost, attractiveness, recyclability, etc. The list of desired properties is not exhaustive. It should be noted that the most important characteristics of composite materials is that their properties are tailorble, that is, one can design the required properties. By choosing an appropriate combination of matrix and reinforcement material, a new material can be made that exactly meets the requirements of a particular application.

1.2 Scales of analysis for composites

In the following a composite material is constituted by a matrix and a fiber reinforcement. The matrix is a polyester or epoxy resin with fillers. The most advanced composites are polymer matrix composites, which have become more and more important in a variety of engineering fields. The rapid growth in the use of composite materials in structures requires the development of structure mechanics for modelling the mechanical behavior and the analysis of structural elements made of composite material.

As mentioned previously, since composite materials consist of two or more constituents, the modelling, analysis and design of structures composed of composites are different from conventional materials such as steel. In reality, a textile fabric is an assembly of yarns, each yarn is an assembly of fibers, and each fiber is a flexible one-dimensional physical entity. Consequently, the mechanics of woven materials can be addressed at three different scales: the macroscopic scale relevant to pieces of fabric, the mesoscopic scale related to yarns, and the microscopic scale concerning fibers inside yarns. Figure 1.6 shows us the three modelling scales of textile composites.

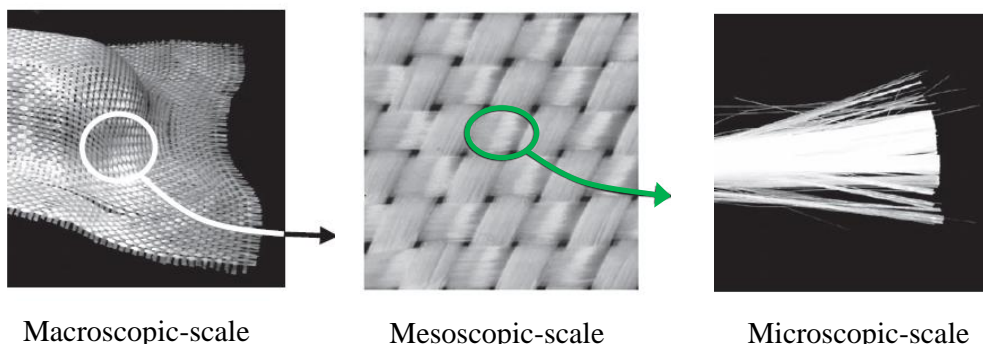


Figure 1.6 – Three modelling scales of textile composites.

1.2.1 Microscopic scale

The textile materials are made of a very large number of continuous fibers, the diameter of which is some μm (e.g. 7 μm for a carbon fiber). The level of the fiber is called microscopic scale (Figure 1.6). This is the lowest level of observation, wherein fiber and matrix phases are modeled separately and the average properties of a single reinforced layer are determined from individual constituent properties by a suitable homogenization

1. Introduction

technique. In this way, the approaches focuses on the microscopic scale can avoid these assumptions about the behavior of intermediate components, and predict mechanisms taking place at the scale of the fibers. By describing the mechanical state of all individual fibers involved in the sample, such kind of approach is also useful for the prediction of damage, in particular due to fiber breakage.

Some mechanical analyses have been performed in which each fiber is considered as a 3D beam interacting with its numerous neighbors (Figure 1.7) [DUR 05, DUR 08, DUR 09, DUR 10]. This approach considers small samples of woven fabrics as collections of individual fibers undergoing large deformations, and needs to model not only the behavior of all individual fibers, but also contact-friction interactions developed between them. The very large number of fibers within a yarn and consequently within a reinforcement reduces the conclusions that can be obtained from such an analysis.

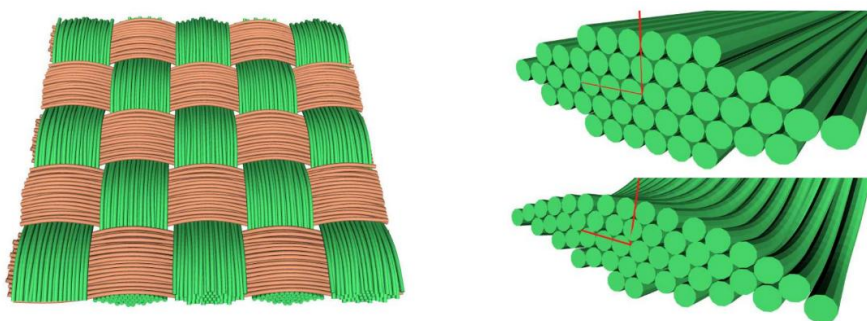


Figure 1.7 – Modelling considering each fiber as a 3D beam [DUR 05].

Similar approaches at microscopic scale can be found in the literature. For example, at the scale of fibers, for the computation of the initial configuration of braided structures or 3D interlock woven fabric, digital elements have been used by Miao [MIA 08] (Figure 1.8). Since these digital elements have neither bending nor torsional stiffness, fibers must be tightened to find a solution. Finckh [FIN 04] proposed to simulate the weaving process and to apply dynamic loading cases using an explicit solver. Other approaches tackle the problem at the scale of yarns, representing yarns by beams or 3D models and studying interactions between them can be seen in [BOI 05, LOM 07, BRI 04].

At the most fundamental level, composites are mixtures of fibers (or particles), matrix and an interface material which connects fibers (or particles) to the matrix material. Micromechanics helps us to understand interactions between different constituents of composite on a microscopic scale. Such a field of study helps us understand:

- Failure mechanisms in fibers (tensile, buckling, splitting, etc).
- Failure mechanism in matrix (tensile, compressive, shear).
- Interface failure mechanisms.
- Fracture toughness, fatigue life, and strength.

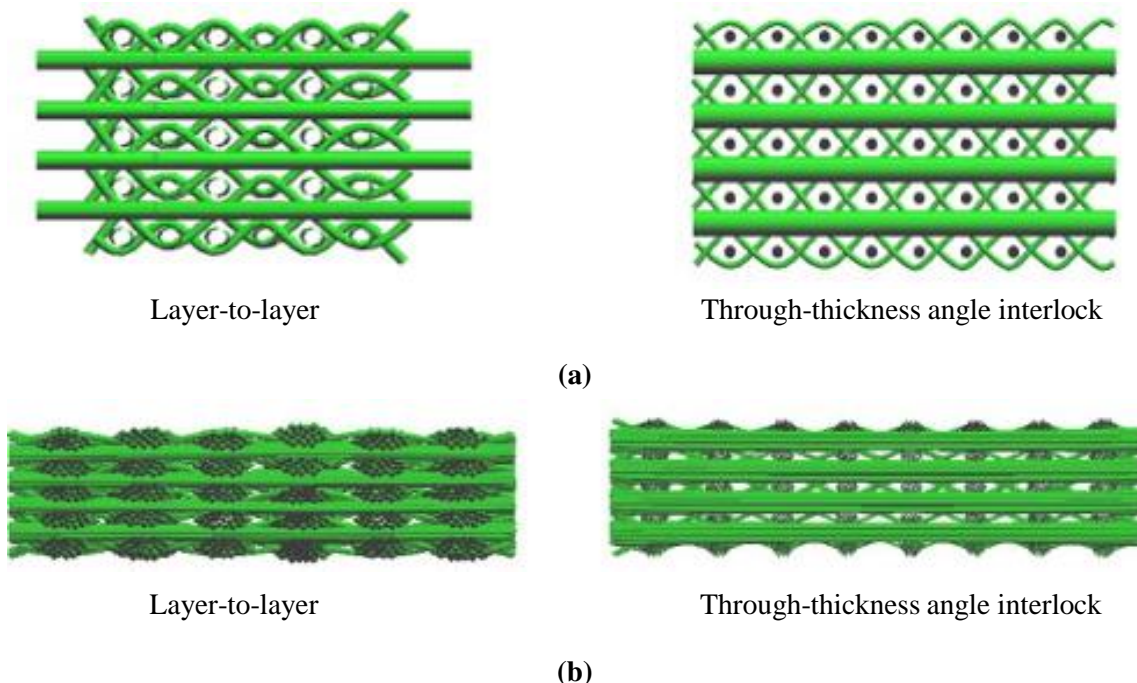


Figure 1.8 – Relaxation processes of 3-D woven fabrics. (a) Initial fabric geometry. (b) Relaxed micro-geometry [MIA 08].

- Basis of macro-level elastic properties.

However, micromechanics is an unsuitable tool to understand behavior of large structures, due to computational limitations. When dealing with woven fabrics at the scale of fibers, the difficulties lie in the detection and modelling of numerous contact-friction interactions taking place within the collection of fibers. Within the framework of large deformations, nonlinear problems require optimized algorithms to be solved efficiently, especially when high numbers of degrees of freedom and contacts are considered.

1.2.2 Mesoscopic scale

At mesoscopic level, a textile composite can be seen as an assembly of yarns or tows, coupled with matrix. In a woven fabric, the fibers are grouped in yarns (3000-48,000 fibers per yarn in a standard composite reinforcement). By developing models for yarns or tows, considered as continuous media, it is possible to build intermediate approaches to study the behavior of fabrics at mesoscopic scale, considering the fabric as an assembly of interlacing tows. The working scale corresponds to the yarn dimension, typically one to several millimeters.

Some approaches are available in the references concerning the modelling of fabrics at mesoscopic scale, considering the yarns as beams that bend according to the beam theory [COR 09, CHE 99, VAS 10]. Using beam elements seems a good idea because of

1. Introduction

the geometry of yarn, unfortunately, classical beam theories assume that the cross section acts as a rigid which can't describe the transverse deformation of the yarn (i.e. transverse compression and shape change), which is essential to the yarn behavior.

In [GAT 10], each yarn is modelled by a set of shell elements (Figure 1.9). The model's initial geometry accounts for the weaving of the reinforcement and contacts between yarns are considered.

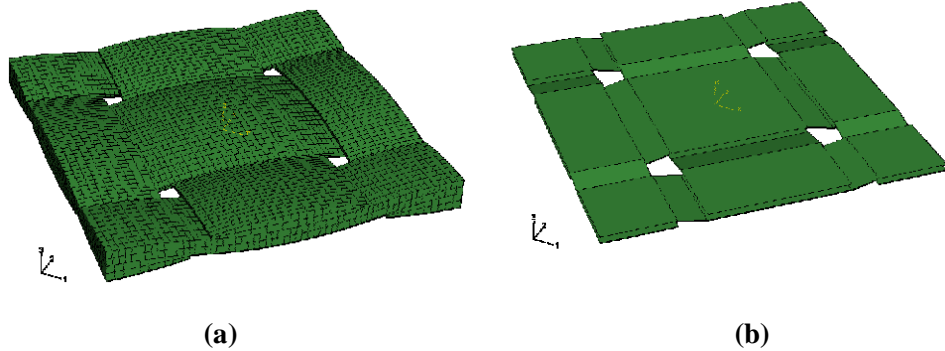


Figure 1.9 – Mesoscopic model of a glass balanced plain weave [GAT 10]. (a) 47214 DoF. (b) 216 DoF.

Nguyen [NGU 13] has proposed an approach to analyze the compressive behavior of a textile composite reinforcement at mesoscopic scale. Each yarn is modelled by a 3D solid in contact and friction with the other yarns (Figure 1.10).

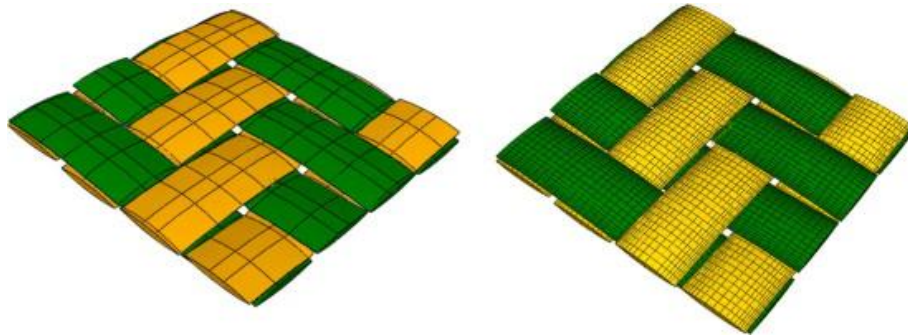


Figure 1.10 – Geometrical model and mesh for the G986 RUC [NGU 13].

The mesoscopic compression simulations have two main objectives. Firstly, they can be used as virtual compressive tests to determine the compressive behavior of a composite textile reinforcement (made of several layers with different directions, possibly with shear). In addition to the compaction curve, they give the internal geometry of the yarns after compaction. This is important for a good determination of the mechanical properties of the composite and to analyze damage via meso-macro approaches [WHI 95, VIO 09, PRO 11]. Secondly, they can be used to calculate the permeability tensor of the deformed reinforcement [WHI 95, VIO 09, PRO 11] while varying some parameters and thus to avoid permeability measurements that are complex.

1.2.3 Macroscopic scale

The macroscopic level refers to the whole component level, with dimensions on the order of ten centimeters to several meters. At this level, a woven fabric can be seen as a continuous material with a specific behavior, the composite material is treated as a homogenous material. For the actual fibers, their orientation and packing arrangement, the lamination, and the binding matrix are all indistinguishable. The stiffness and strength of the material can be characterized by making a number of tests, from which macroscopic properties are determined. This analysis is known as macro-mechanics. Once these property data are known, macro-mechanics analysis will supply answers as to the load-carrying capacity and stiffness of a structure consisting of this material.

Such an approach of study is suitable well for individual composite layers. It helps us to predict failure and performance of individual laminae, in terms of properties of the composite. However, such an approach does not refer to local failure mechanisms because homogenized models are derived to represent the fabric as a shell. Only the averaged properties of a lamina are considered and the microstructure of the lamina is ignored. Many approaches are available in the literatures concerning the modellings and simulations of fabrics at macroscopic scale: continuous approaches, discrete approaches, demi-discrete approaches.

The continuous approach considers the fibrous reinforcement or prepreg as a continuum [KIN 05, ROG 89, PEN 05, LIA 14, TEN 07, KHA 10, AIM 09]. As seen in the preceding sections, the reinforcement is not continuous at lower scales, but a continuous material can be assumed to be superimposed on the fibrous material. This needs the assumption that there is no significant sliding between fibers and yarns during the deformation. Several experiments have already confirmed this assumption. For instance, Boisse et al [BOI 93] have done a forming experiment for woven fabric on a hemispherical punch (Figure 1.11). A set of lines following the warp and weft yarn directions were drawn on the fabric before forming. These lines became curved after forming but remained continuous, which implies that, due to the weaving, there was no large sliding between warp and weft yarns. The advantage of the continuous approach is that it can be implemented in commercial FE codes.

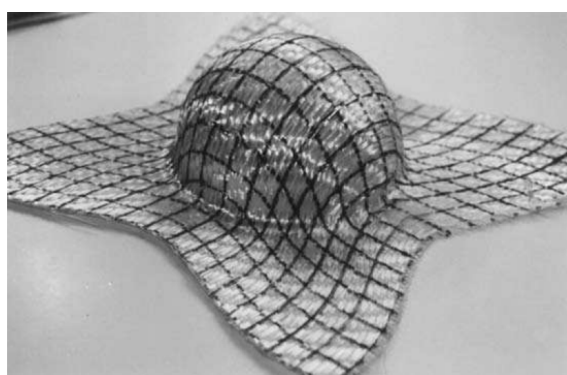


Figure 1.11 – Validation of no sliding assumption between yarns in the forming [BOI 93].

1. Introduction

The discrete approach considers and models the components of fibrous reinforcement at lower scale. Analysis is carried out at unit cell level in which each yarn and fabric is modeled. Nevertheless, because of very large number of yarns or fibers, the computational effort is significant so that these approaches are limited to small domain analysis. In the discrete approach, the discrete models of fabrics are based on modelling yarns by elements such as beam or solid elements. A meso-mechanical modelling of the biaxial NCF composed of two separate ply layers has been proposed by Creech and Pickett [CRE 06]. 3D solid elements were used to discretize the yarns and interconnecting bar elements were used to approximate the stitching (Figure 1.12). Contact and frictional sliding between yarns and stitches were treated using an appropriate contact algorithm and additional stitch-to-yarn connection elements.

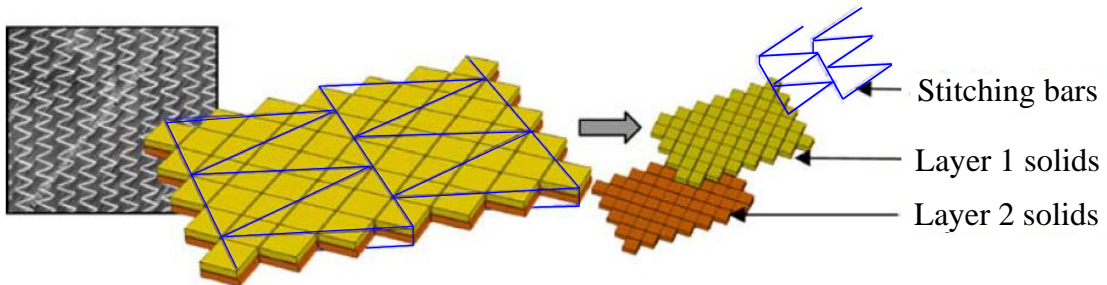


Figure 1.12 – A representative cell of the meso-mechanical model for NCF [CRE 06].

In order to represent fabrics and fabric reinforced membranes with the Discrete Element Method (DEM), Ballhause et al [BAL 08] have discretized the microstructure into concentrated mass points and interactions between these points, which have to represent the relevant microstructure mechanisms. The process of the model generation is shown in Figure 1.13. The fabric's unit cell is discretized and a great number of model unit cells are then assembled in order to form a macroscopic patch of material. This geometrical representation is a common simplification applied by many researchers, e.g. Kawabata et al [KAW 73a, KAW 73b], who analytically derived equations for the plain weave material behavior based on the geometry of a unit cell. Although piecewise linear yarns are only a coarse approximation of the curved yarn path, Kawabata et al. were able to obtain good agreement with experimental results.

The semi-discrete approach is a compromise between the continuous and discrete approaches. Specific finite elements are constructed, which are made of a discrete number of yarns or woven representative unit cells. Hamila and Boisse [HAM 08, HAM 09] proposed a semi-discrete triangular shell finite element which was composed of unit cells. These unit cells were subjected to tension, in plane shearing and bending. The displacement of any point in the representative unit cell came from element interpolation. A semi-discrete solid element made of yarn segments for simulating 3D interlock was proposed by De Luycker [DEL 09]. The yarns were only accounting for the tension energy of fabric, other parts of energy were considered in the solid element. The forming simulation results with the two types of elements are shown in Figure 1.14.

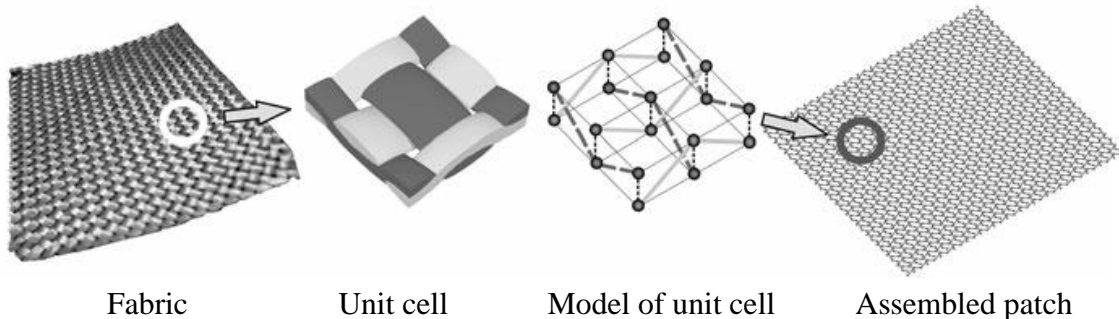


Figure 1.13 – Discretization of plain weave fabric [BAL 08].

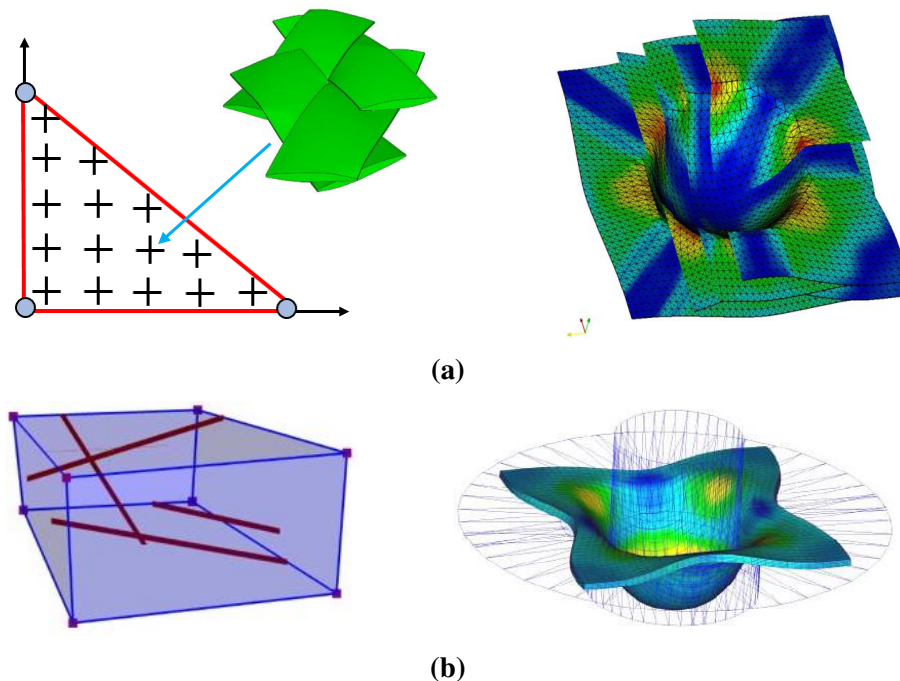


Figure 1.14 – Schematic of semi-discrete elements and their forming simulations.(a) Shell element [HAM 08]. (b) Solid element [DEL 09].

These macroscopic simulations consider the deformation of a whole preform (in particular to simulate draping processes), then the internal woven structure of the fabric is not described. In my thesis, the work will focus at mesoscopic scale.

1.2.4 Research scale of the thesis

As introduced previously, when the reinforcement is observed at the macroscopic level, the fabric is considered as an anisotropic continuous material exhibiting mechanical properties inherited from its meso-and microstructures. The fabric is modelled using membranes, or shells if bending is taken into account [SPE 07, DON 01, KIN 05, SHA 07]. The modelling must take into account the behavior specificities of the fabric [CAR 01], especially the necessary property updating due to large strains (especially large in-plane shear) [PEN 05, YU 02, YU 05, XUE 05]. The main drawback of that approach is the fact that it does not include crimp and interlacement effects, which are important features of fabric reinforcement behavior. One way to identify macroscopic properties of fabrics is to use homogenization of results coming from lower-scale observations. The best approach would consist in realizing simulations at a scale from which the material is really continuous, i.e. the scale of the fiber. Some authors [DUR 05, DUR 09, MIA 08, ZHO 04] adopted this approach with applications to metallic braids [DUR 05, ZHO 04, WAN 01] and knitted fabrics [DUH 06]. All of those simulations use a reduced number of fibers in each yarn for computational time reasons. The consistency of those approaches is then questionable when the number of fibers is greater than 5000.

An intermediate way is to build a model representative of the yarn behavior and able to capture its main specificities in terms of forces and geometry. This constitutes a good compromise between realism and complexity. At this scale, the fibrous reinforcement is modeled by an interlacement of yarns assumed to be homogeneous that have to be accurately represented. Our research mainly focuses at mesoscopic scale, considering the fabric as an assembly of interlacing yarns. Consequently, the interaction between yarns and the geometry of yarns are needed to be explicitly defined and described. Next, we will introduce the deformation mechanisms at mesoscopic scale.

1.2.5 Deformation mechanisms at mesoscopic scale

As mentioned previously, a mesoscopic modelling of woven reinforcements considers the material at the yarn level. This means that the meso-structure of the fabric is explicitly modelled. Consequently, the mechanical behavior of the yarn material needs to be studied. As the microstructure of the fiber bundle, i.e. the fiber arrangement, is not explicitly modelled, the constitutive behavior of the yarn material must exhibit specificities linked to the fact that the material is not really continuous in the same manner as fabric material. Depending on the application it is built for, the yarn arrangement is not always the same. Some yarns are built with parallel fibers while others are twisted. In order to guarantee a high tensile stiffness for high-performance composites, the twist angle is generally weak. Anyway, high-resolution X-ray tomography imaging shows that the yarn material

is strongly oriented [BAD 09]. The consequence, from a mechanical point of view, is the strong tensile stiffness in relation to the other rigidities of the material, as mentioned for fabric materials. The possible relative movement between fibers inside the bundle makes the bending stiffness of a yarn particularly weaker than the classical beam bending stiffness, even though the slenderness of the yarn is similar to that of a beam. In the same manner, the transverse behavior of the yarn strongly depends on the actual fiber volume fraction: the denser the tow, the stiffer it is.

At mesoscopic scale, the main interesting aspects are yarn's deformation behaviors, which include: tensile, bending, shear, and transverse compaction. These behaviors not only depend on single yarn, but also on the interactions between them.

1.2.5.1 Yarn's tensile deformation

A yarn is made up of thousands of fibers joined together. When subjected to longitudinal tension, the fibers are reorganized in order to better resist the tensile load. Consequently, depending on the micro-structure of the yarn (namely the twist angle and fiber density), the tensile response would present various initial non-linearities [RAO 00]. The tensile loading induces an untwisting movement. When this straightening movement is achieved, the tensile behavior of the yarn becomes linear, which can be seen in Figure 1.15. Consequently, the yarn tensile behavior depends mainly on three parameters: the number of fibers, the nature of the fibers and the twist angle. For the nominal tensile stiffness, only the first two parameters are relevant. Such a stiffness is generally expressed in N (implying newtons per unit strain for a single yarn) and not via a Young's modulus as for classical continuum mechanics analyses. By such a choice, it is not necessary to measure the yarn section, which is a parameter really difficult to obtain. In the case of a yarn made of parallel fibers, if it is possible to realize a tensile test ensuring that the applied load is exactly longitudinal, the relative positions of the fibers would not change. As this is not possible, boundary conditions cause the cross-section of the yarn to change. Moreover, for uncoated fiber bundles, the cohesion between fibers is only ensured by the environment of the tow: if the yarn is extracted from the fabric, it does not maintain its cohesion. Consequently, it is easier to realize tensile tests on fabrics than on single yarns [BUE 01]. In that case, X-ray tomography shows that the density of the fiber bundle increases when subjected to tension because of the boundary conditions [BAD 09].

Since yarn is made of fibers, when a yarn is stretched, not all fibers inside would be stretched simultaneously. The tension test of yarn has been standardized (using the ASTM D4018-81) [TES 87]. The sample is required to be composed of at least 10000 fibers and impregnated with resin to make all fibers in a yarn as straight as possible. Florimond [FLO 13] proposed an alternative tensile test device for yarn made of less than 2000 fibers (Figure 1.16a). Two round metal bars were installed on the top and bottom clamps of a tensile machine respectively. The yarn twined around these metal bars, when it was subjected to tension, it equals two yarns under tension. The testing results indicate it can capture the non-linear tensile phenomenon of yarn (Figure 1.16b).

1. Introduction

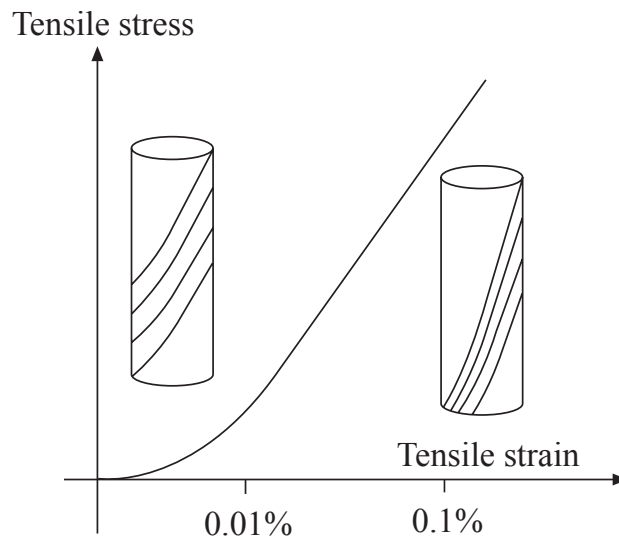


Figure 1.15 – Non-linear tensile curve for an initially twisted fiber bundle [BOI 12].

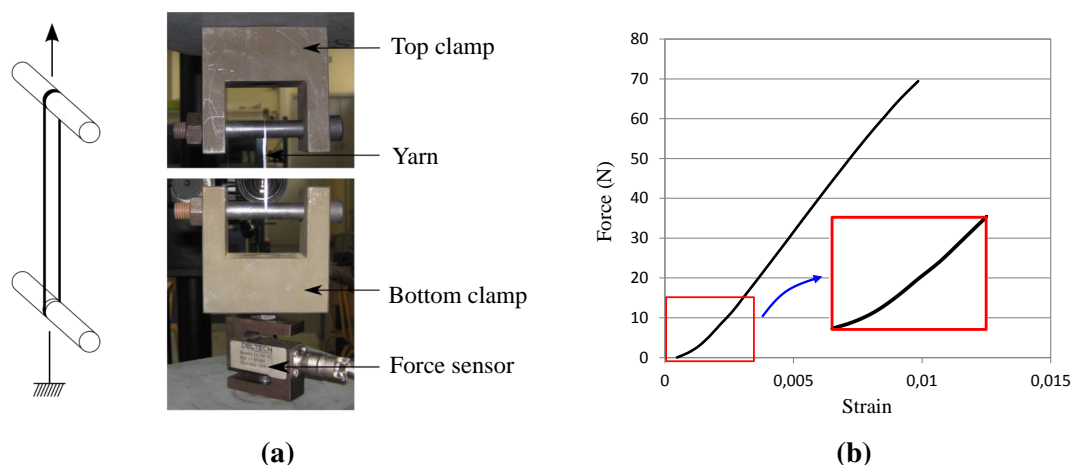


Figure 1.16 – Yarn's tensile behavior test device proposed by Florimond [FLO 13]. (a) Configuration of test device. (b) Yarn's tensile test result.

1.2.5.2 Yarn's bending deformation

Since yarn is made up of thousands of fibers, those fibers can move in relation to their neighbors and this makes the yarn very soft in response to certain types of loading. In particular, even though a yarn has the geometry of a beam, its bending stiffness is smaller because of the relative motion that can occur between the fibers constituting the tow [LAH 04, DEB 10, LIA 14]. Consequently, it is very easy to bend a yarn as it is quite like bending each fiber. Nevertheless, it has been shown that it is necessary to take the lower bending stiffness into account in a mesoscopic analysis of a yarn [GAT 10]. Although the bending stiffness of each fiber plays a major role in yarn bending behavior, there are few studies about yarn's bending behavior, partly because the bending stiffness is very small, it's neglected. Another important reason is its complexities. When a yarn is bent, there could exist relative sliding between fibers. This makes yarn's bending stiffness not directly related to its in-plane tensile modulus as the classical continuum materials. Yarn's bending stiffness not only depends on the fibers, but also their inter-friction force. Some mechanical models have been proposed to calculate yarn's bending stiffness from fibers [GRO 66, POP 66, GRO 80]. However, these models are based on many assumptions which can only be applied to some simple cases. On the experimental aspect, Cornelissen et al [COR 09] conducted a cantilever bending test to identify yarn's bending stiffness as the slope of moment-curvature curve. It's the most direct way to characterize yarn's bending stiffness.

1.2.5.3 Yarn's shearing deformation

There are two modes of shearing for yarn: transverse shearing and longitudinal shearing (Figure 1.17). Yarn's transverse shearing is defined as the shape change of transverse cross-section of yarn, in which fibers are redistributed. The main resistance of yarn's transverse shearing comes from fibers' inter-friction force, which is strongly influenced by yarn's compression. This is also true for longitudinal shearing of yarn, in which friction provides the main rigidity. The coupling between the shearing and compaction makes it very difficult to directly characterize yarn's shearing by experiment. An inverse method is usually used to identify yarn's shearing behavior [FLO 13].

1.2.5.4 Yarn's transverse compaction

Yarn's transverse compaction is defined as the area variation of yarn's transverse cross section when compressed. The rigidity in yarn's transverse cross-section is much smaller than rigidity in the longitudinal direction, which makes compression one of the main deformation modes. Yarn's compression directly affects fiber's volume fraction and distribution, which would ultimately influence the permeability of resin. When a yarn is compressed, the space between fibers would reduce. Initially, there is little or no resistance to the compression. As compression continues, more and more fibers would come into contact, resulting in a great increase in compression rigidity. The whole process can be seen in Figure 1.18, where the yarn is subjected to the compression introduced by the

1. Introduction

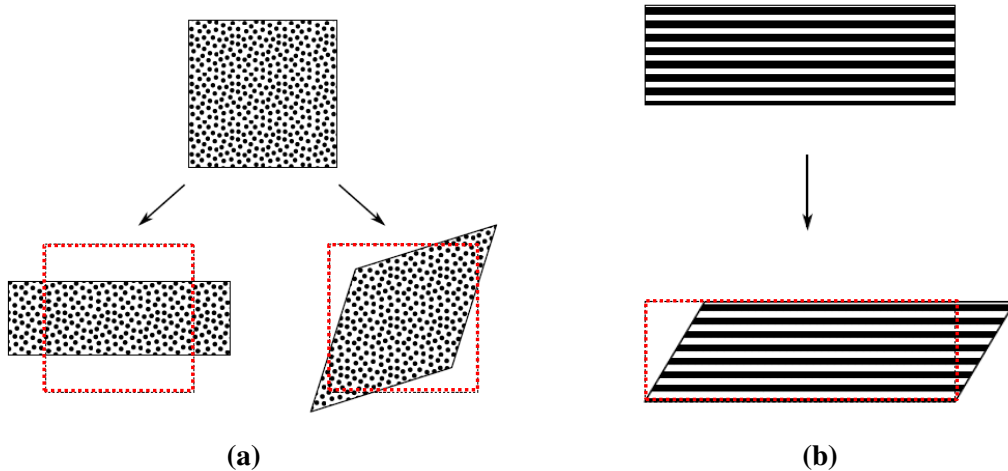


Figure 1.17 – Two modes of yarn's shearing: (a) Transverse shearing. (b) Longitudinal shearing [FLO 13].

biaxial loading. The experimental characterization of single yarn's transverse compaction is very difficult to implement, primarily due to its small dimension. It's often conducting the compaction test at the macroscopic scale and using an inverse method to identify single yarn's transverse compaction behavior [GAS 00].

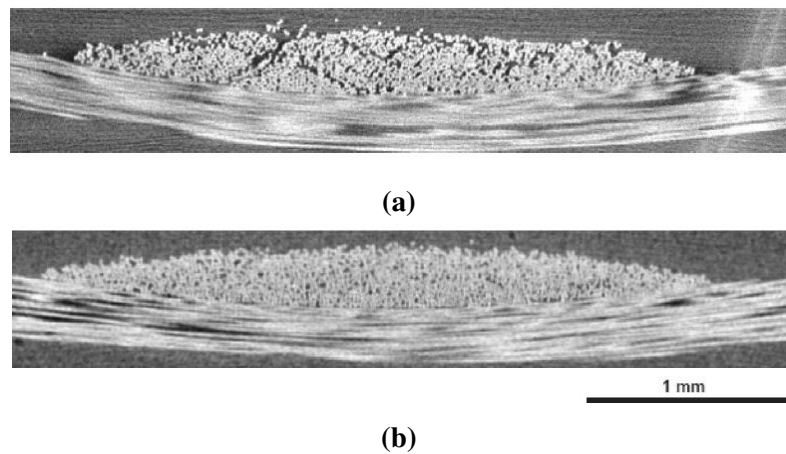


Figure 1.18 – Fibers distribution in a yarn: (a) Unloaded. (b) Subjected to biaxial tension [BAD 09].

Transverse compaction of single- and multi-layer [SAU 98, NGU 13] fabrics is strongly non-linear. That non-linearity is mainly due to the non-linearity of the yarn compaction itself. The compaction phenomenon is the fact that fibers get closer inside the bundle. Consequently, when the voids become smaller than the fiber diameter, it becomes more difficult to continue the compaction movement. The high stiffness of carbon or glass fibers makes it difficult to deform the fibers themselves. Generally, it is admitted

that the transverse compressive stiffness of the fiber bundle is dependent on longitudinal tension. Direct experimental evidence is rare but this can be illustrated by biaxial tensile tests [BUE 01, GAS 00]. It can be explained by the fact that fiber bundles are not granular materials: they have a third dimension and the organization of the fibers in the longitudinal direction is not perfect. When fibers move against one another, their global twist changes (even if we consider an untwisted yarn) and they can be tightened by those small movements. As the tensile stiffness is very high, small tension can produce a large effect.

1.3 Motivation and objectives

As mentioned previously, the transverse deformation of the yarn (i.e. transverse compression and shape change) is very essential to the yarn behavior, solid elements spend high computation time while classical beam theories can't meet the requirements. Therefore, in order to reduce the computation time and obtain the expectation results at the same time, we present a new tool for modelling textile materials using the yarn as constitutive element. A new 3D beam element with section changes is proposed which can be used to model yarn at the mesoscopic scale while breaking from classical beam assumptions. The whole work can be divided into three steps: proposal of the new 3D beam, carrying out validation for large displacements and small strains, finally construct contact between 3D beam to beam.

In chapter 2, we start from 2D beam element with thickness change by adding a transverse strain component, which is inspired by previous works on the shell elements. Then, the formulation is extended to 3D beam elements, two transverse strain components are added with coupling so that the deformation of cross section can be taken into account. Then, a series of numerical examples are carried out using a FEM code for the new-proposed 3D beam element developed in Matlab, and the results are systematically compared with corresponding values of ABAQUS/Standard 3D simulations, which don't show any significant discrepancies.

The results presented in chapter 2 are only the first step of a more ambitious work. After the new 3D beam element is constructed, the second step is to carry out validation for large displacements/small strains. In essence, the large displacement motion of a general body can be considered as a function of time, in order to simplify the kinematic formulation and obtain a more effective numerical solution, a nonlinear theory of deformation based on the updated Lagrangian method is chosen. The work employs small strain theory on each element like the co-rotational technique, and only the unit vectors of the cross-sections are employed instead of the complicated three-dimensional rotational vectors or angles. A series of sample analyses are carried out, and the results are systematically compared with the corresponding values of ABAQUS/Standard 3D simulations. The results obtained are in good agreement which shows that the enhanced 3D element provides an excellent numerical performance under large displacements/small strains.

Indeed, the final goal is to use those new 3D beam elements to model yarns in a textile composite preform. For that purpose, the third step aims to introduce contact behavior and

1. Introduction

carry out validation for the new 3D beam to beam simulation. In chapter 4, frictionless contact between the new 3D beams with rectangular cross-section is considered. In the analysis, large displacement/small strains are allowed. The contact formulation is derived on the basis of penalty method and updated Lagrangian method using physical shape functions with shear effect included. An effective contact search algorithm, which is necessary to determine an active set for the contact contribution treatment, is elaborated. And a consistent linearization of contact contribution is derived and expressed in suitable matrix form, easy to use in FEM approximation. Finally, several numerical examples are shown using the FEM code developed in Matlab.

Chapter 5 presents the key outcomes of the whole work and major conclusions, and several recommendations for the future work are made.

Chapter 2

Development of the new 3D beam element

In this chapter, we present a new 3D beam element with the aim to achieve the results with section changes while breaking from classical beam hypothesis. Firstly, we start from 2D beam element with thickness change by adding a transverse strain component. Secondly, the formulation is extended to 3D beam elements, two transverse strain components are added with coupling so that full 3D constitutive law can be used. Finally, some numerical examples are presented using the new 3D beam elements which show that the results are exactly the same as those given by 3D element in ABAQUS/Standard.

2.1 Introduction

A large amount of studies have been developed to understand and model the fabric behavior at micro- (fiber) or meso- (yarn) scale. Those works have shown that at the microscopic scale, some mechanical analyses have been performed in which each fiber is considered as a 3D beam interacting with its numerous neighbors [DUR 05, DUR 08, DUR 09, DUR 10, XUE 05]. The very large number of fibers within a yarn results in large computation. For computational reasons, those modellings are generally limited to a small piece of fabric so that the whole composite part is generally modelled at higher scale considering the textile preform as a continuum [KIN 05, ROG 89, PEN 05, LIA 14, TEN 07]. These macroscopic simulations consider the deformation of a whole preform (in particular to simulate draping processes), then the internal woven structure of the fabric is not described. An intermediate way consists in developing models for yarns or tows, considered as continuous media, it is possible to build intermediate approaches to study the behavior of fabrics at mesoscopic scale, considering the fabric as an assembly of interlacing tows (or yarns). Some approaches are available in the references concerning the modelling of fabrics at mesoscopic scale, considering the yarns as beams that bend according to the beam theory [COR 09, CHE 99, VAS 10] or shell elements [GAT 10].

Using structural elements seems a good idea because of the geometry of the yarn,

unfortunately, classical beam theories assume that the cross section acts as a rigid which can't describe the transverse deformation of the yarn. The objective of the present chapter is to propose a new 3D beam element with section changes which can be used to model yarn at the mesoscopic scale and describe its transverse behaviors.

2.2 Review of the related work

2.2.1 Evolution of beam models

The simplest beam theory is the classical theory known as Euler-Bernoulli theory, which assumes that the cross section of the beam is rigid and shear deformations are neglected. After deformation, the cross sections remain straight, unstretched and normal to the longitudinal axis, as shown in Figure 2.1(a).

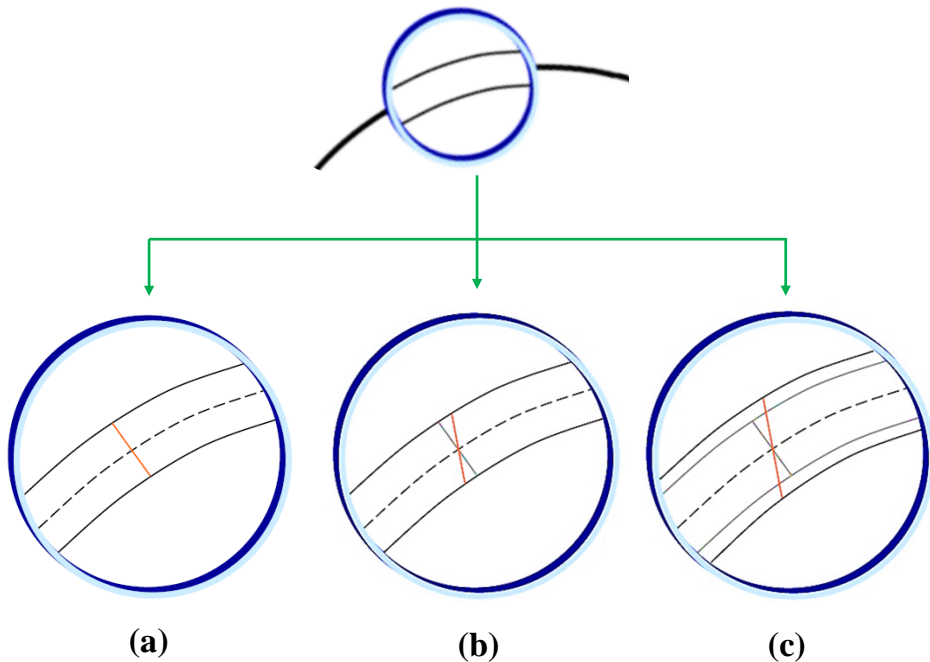


Figure 2.1 – Evolution of beam models. (a) Bernoulli-Euler beam. (b) Timoshenko beam. (c) Proposed 3D beam.

Experiments have demonstrated that Euler-Bernoulli assumption is more accurate for thin beams. For a thick beam, the cross-section is not necessarily perpendicular to the beam axis, and shear force is a more dominant factor in the damage of material. So Bernoulli-Euler beam theory is acceptable only for long slender beams. In the case that a beam is relatively short or thick, shear effects can be significant, and Timoshenko beam theory will be used. The critical difference in Timoshenko theory is the assumption that cross-section of the beam is no more normal to longitudinal axis after deformation (Figure

2.1b). The cross section still remains plane but rotates by an amount, equal to the rotation of the longitudinal axis minus the shear strain.

Theoretically, Timoshenko beam theory is more general, and Euler-Bernoulli theory can be considered as a special case of Timoshenko assumption by enforcing the constraint condition between deflection and cross-section rotation. But when it concerns the deformation of cross section, the situation is different. All of these theories have limitations because they are based on the assumption that the cross section is rigid and don't change. But actually, it changes. The objective of our work is to propose a new approach to solve this problem.

Based on the requirements, we propose a new 3D beam with section changes while breaking from classical beam hypothesis (Figure 2.1c). The new 3D beam is inspired by previous work on shell enrichment. Firstly, we start from 2D beam element with thickness change by adding a transverse strain component. Then, the formulation is extended to 3D beam elements.

2.2.2 Introduction to the beam element

2.2.2.1 Euler-Bernoulli beam element

The Euler-Bernoulli equation for beam bending is:

$$\rho \frac{\partial^2 v}{\partial t^2} + \frac{\partial^2}{\partial x^2} (EI \frac{\partial^2 v}{\partial x^2}) = q(x, t) \quad (2.1)$$

Where $v(x, t)$ is the transverse displacement of the beam, ρ is the mass density per volume, EI is the beam rigidity, $q(x, t)$ is the externally applied pressure loading, t and x indicate the time and spatial coordinate along the beam axis. We apply the Galerkin's method to the beam Equation (2.1) to develop the finite element formulation and the corresponding matrix equations.

The average weighted residual of Equation (2.1) is:

$$I = \int_0^L \left(\rho \frac{\partial^2 v}{\partial t^2} + \frac{\partial^2}{\partial x^2} (EI \frac{\partial^2 v}{\partial x^2}) - q \right) w dx = 0 \quad (2.2)$$

Where L is the length of the beam and w is a test function. The weak formulation of Equation (2.2) is obtained from integrations by parts twice for the second term of the equation. In addition, discretization of the beam into a number of finite elements gives:

$$I = \sum_{i=1}^n \left[\int_{\Omega_e} \rho \frac{\partial^2 v}{\partial t^2} w dx + \int_{\Omega_e} EI \frac{\partial^2 v}{\partial x^2} \frac{\partial^2 w}{\partial x^2} dx - \int_{\Omega_e} q w dx \right] + \left[V w - M \frac{\partial w}{\partial x} \right]_0^L = 0 \quad (2.3)$$

Where $V = EI(\partial^3 v / \partial^3 x)$ is the shear force, $M = EI(\partial^2 v / \partial^2 x)$ is the bending moment. Ω_e is an element domain and n is the number of elements for the beam.

2. Development of the new 3D beam element

We consider shape function for spatial interpolation of the transverse deflection in terms of nodal variables. To this end, we consider an element with two end nodes, as shown in Figure 2.2. The deformation of a beam must have continuous slope as well as continuous deflection at any two neighboring beam elements. To satisfy this continuity requirement, each node has both deflection v_i and slope θ_i as nodal variables. In this case, any two neighboring beam elements have common deflection and slope at the shared nodal point. This satisfies the continuity of both deflection and slope. The Euler-Bernoulli equation is based on the assumption that the plane normal to the neutral axis before deformation remains normal to the neutral axis after deformation (Figure 2.3).

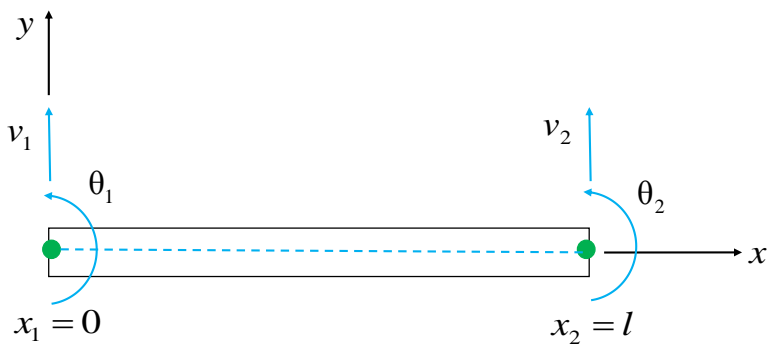


Figure 2.2 – Two-nodes beam element.

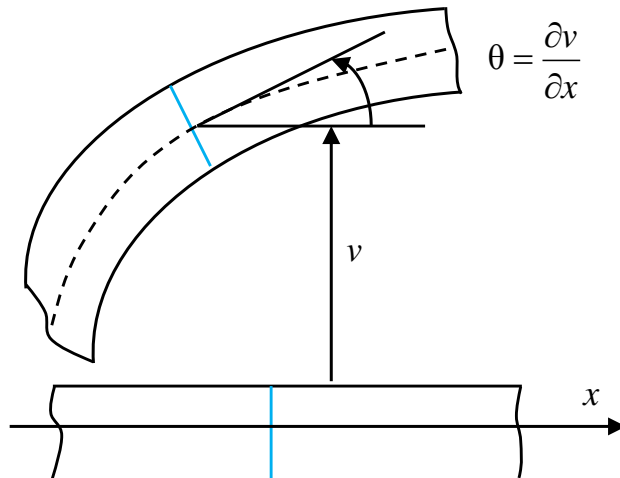


Figure 2.3 – Euler-Bernoulli beam.

This assumption denotes $\theta = \frac{dv}{dx}$ (slope is the first derivative of the deflection in terms of x). Because there are four nodal variables for the beam element, we assume a cubic

polynomial function for $v(x)$:

$$v(x) = c_0 + c_1x + c_2x^2 + c_3x^3 \quad (2.4)$$

From the assumption for the Euler-Bernoulli beam, slope is computed from Equation (2.4):

$$\theta(x) = c_1 + 2c_2x + 3c_3x^2 \quad (2.5)$$

Evaluation of deflection and slope at both nodes yields:

$$\begin{aligned} v(0) &= c_0 \\ \theta(0) &= c_1 = \theta_1 \\ v(l) &= c_0 + c_1l + c_2l^2 + c_3l^3 = v_2 \\ \theta(l) &= c_1 + 2c_2l + 3c_3l^2 = \theta_2 \end{aligned} \quad (2.6)$$

Solving Equation (2.6) for $c_i (i = 0, 1, 2, 3)$ in terms of the nodal variables v_j and $\theta_j (j = 1, 2)$ and substituting the results into Equation (2.4) give:

$$v(x) = H_1(x)v_1 + H_2(x)\theta_1 + H_3(x)v_2 + H_4(x)\theta_2 \quad (2.7)$$

Where:

$$\begin{aligned} H_1(x) &= 1 - \frac{3x^2}{l^2} + \frac{2x^3}{l^3} \\ H_2(x) &= x - \frac{2x^2}{l} + \frac{x^3}{l^2} \\ H_3(x) &= \frac{3x^2}{l^2} - \frac{2x^3}{l^3} \\ H_4(x) &= -\frac{x^2}{l} + \frac{x^3}{l^2} \end{aligned} \quad (2.8)$$

The functions $H_i(x)$ are called Hermitian shape functions. The Hermitian shape functions are C^1 type which means that both v and $\frac{\partial v}{\partial x}$ are continuous between two neighboring elements.

Application of Hermitian shape functions and Galerkin's method to second term of Equation (2.3) results in the stiffness matrix of the beam element, that is:

$$[K^e] = \int_0^l [B]^T EI [B] dx \quad (2.9)$$

Where,

$$[B] = \{ H_1'' \ H_2'' \ H_3'' \ H_4'' \} \quad (2.10)$$

And the corresponding element nodal degrees of freedom is $\{d^e\} = \{ v_1 \ \theta_1 \ v_2 \ \theta_2 \}^T$. In Equation (2.10), double prime denotes the second derivative of the function.

2.2.2.2 Timoshenko beam element

The Timoshenko beam element includes the effect of transverse shear deformation. As a result, the cross section normal to the beam axis before is no more normal to the beam axis after deformation. Figure 2.4 shows the deformation in contrast to that in Figure 2.3. While Galerkin's method was used to derive the finite element matrix equation for the Euler-Bernoulli beam equation, the energy method is used for the present formulation for the Timoshenko beam.

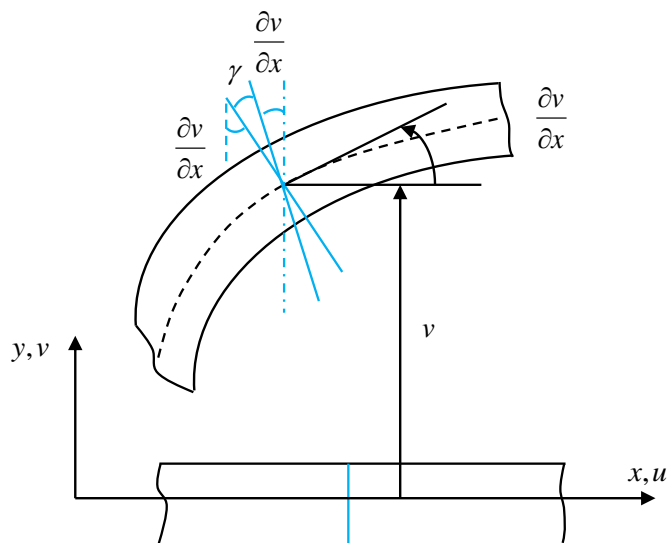


Figure 2.4 – Timoshenko beam.

Let u and v be the axial and transverse displacements of a beam, respectively. Because of transverse shear deformation, the slope of the beam θ is different from $\frac{dv}{dx}$. Instead, the slope equals $\frac{dv}{dx} - \gamma$, where γ is the transverse shear strain. As a result, the displacement field for the Timoshenko beam can be written as:

$$u(x, y) = -y\theta_x \quad (2.11)$$

$$v(x, y) = v \quad (2.12)$$

Where x axis is located along the neutral axis of the beam and the beam is not subjected to an axial load such that the neutral axis doesn't have the strain. According to Equation (2.11) and (2.12), the axial and shear strains are:

$$\epsilon(x, y) = -y \frac{d\theta_x}{dx} \quad (2.13)$$

$$\gamma = -\theta + \frac{dv}{dx} \quad (2.14)$$

As explained in the previous part on the energy method, the element stiffness matrix can be obtained from the strain energy expression for an element. The strain energy for an element of length l is:

$$U = \frac{b}{2} \int_0^l \int_{-h/2}^{h/2} \boldsymbol{\epsilon}^T E \boldsymbol{\epsilon} dy dx + \frac{b\mu}{2} \int_0^l \int_{-h/2}^{h/2} \boldsymbol{\gamma}^T G \boldsymbol{\gamma} dy dx \quad (2.15)$$

In which the first term is the bending strain energy and the second term is shear strain energy. Moreover, b and h are the width and height of the beam respectively, and μ is the correction factor for the shear energy whose value is normally $\frac{5}{6}$ for a rectangular cross section.

Substituting Equation (2.13) and (2.14) into Equation (2.15) and taking the integration with respect to y gives:

$$U = \frac{b}{2} \int_0^l \left(\frac{d\theta}{dx} \right)^T EI \left(\frac{d\theta}{dx} \right) dy dx + \frac{\mu}{2} \int_0^l \left(-\theta + \frac{dv}{dx} \right)^T GA \left(-\theta + \frac{dv}{dx} \right) dy dx \quad (2.16)$$

Where I and A are the moment of inertia and area of the beam cross-section.

In order to derive the element stiffness matrix for Timoshenko beam, the variable v and θ need to be interpolated within each element. As seen in Equation (2.16), v and θ are independent variables. That is, we can interpolate them independently using proper shape functions. This results in satisfaction of inter-element compatibility, continuity of both the transverse displacement and slope between two neighboring elements. As a result, any kind of C^0 shape function can be used for the present beam. Shape functions of C^0 are much easier to construct than the shape functions of C^1 . It's especially very difficult to construct the shape functions of order C^1 for two dimensional and three dimensional analysis such as the classical plate theory. We use simple linear shape functions for both variables, that is:

$$v = [H_1 \ H_2] \begin{Bmatrix} v_1 \\ v_2 \end{Bmatrix} \quad (2.17)$$

$$\theta = [H_1 \ H_2] \begin{Bmatrix} \theta_1 \\ \theta_2 \end{Bmatrix} \quad (2.18)$$

Where H_1 and H_2 are linear shape functions. The linear element looks like that in Figure 2.2, but the shape functions used are totally different from those for the Hermitian beam element. Using Equation (2.17) and (2.18) along with strain energy expression Equation (2.16) yields the following element stiffness matrix for the Timoshenko beam:

$$[K^e] = [K_b^e] + [K_s^e] \quad (2.19)$$

Where:

$$[K_b^e] = \frac{EI}{l} \begin{bmatrix} 0 & 0 & 0 & 0 \\ 0 & 1 & 0 & -1 \\ 0 & 0 & 0 & 0 \\ 0 & -1 & 0 & 1 \end{bmatrix} \quad (2.20)$$

$$[K_s^e] = \frac{\mu G A}{4l} \begin{bmatrix} 4 & 2l & -4 & 2l \\ 2l & l^2 & -2l & l^2 \\ -4 & -2l & 4 & -2l \\ 2l & l^2 & -2l & l^2 \end{bmatrix} \quad (2.21)$$

One thing needs to be noted here is that bending stiffness term Equation (2.20) is obtained using the exact integration of the bending energy while the shear stiffness term, Equation (2.21), is obtained using the reduced integration technique. For the present calculation, the one point Gauss quadrature rule is used. The major reason is if the beam thickness becomes so small compared to its length, the shear energy dominates over the bending energy. As seen in Equation (2.20) and (2.21), the bending stiffness is proportional to hl , where h and l are the thickness and length of a beam element, respectively. Hence, as $\frac{h}{l}$ becomes smaller for very thin beam, the bending term becomes negligible compared to the shear term. This is not correct in the physical sense. As the beam becomes thinner, the bending strain energy is more significant than the shear energy. This phenomenon is called shear locking. In order to avoid the shear locking, the shear strain energy is under-integrated. Because of the under-integration, the present beam stiffness matrix is rank deficient. That is, it contains some fictitious rigid body modes (or zero energy modes).

2.3 The assumption and the inspiration of the new 3D beam element

2.3.1 Assumption

At mesoscopic scale, we consider the fabric as an assembly of interlacing yarns; some approaches of modelling fabrics are available in the references, discretizing the yarns with solid elements or beam elements. Since fiber tows length is much higher than their transverse dimensions, beam elements seem to be the most convenient finite element tool. In order to meet the requirements of describing the transverse deformation of the yarn, a new beam theory is proposed, which starts from the 2D situation. A central node with two degrees of freedom is added to an initially 2 nodes element. The two degrees of freedom introduced correspond to the relative displacements of the top and bottom surfaces of a beam respectively, which are used to describe the deformation of the cross section. After the validation of the new 2D beam element, the formulation is extended into three-dimensional.

The proposed 3D beam element is firstly built with 2 end nodes with 6 degrees of freedom with shear deformation and including Saint-Venant torsional effects. A central node with 8 degrees of freedom is added to describe the transverse deformation. This work is inspired by previous works on enriched shell elements [SAN 11, BAS 12], where an additional node is introduced in the center of three-node and four-node shell elements with two through-thickness translational degrees of freedom which makes it possible to

extend plane stress state into full 3D elasticity. Using the same idea, a 2D beam element with thickness change is built by adding a central node with two degrees of freedom to an initially 2 nodes element.

2.3.2 The review of the related work on shell enrichment elements

Classical shell elements based on the degenerated shell concept or classical shell theories generally include the assumption of a plane stress state and can handle analyses of shells satisfactorily. However, problems may arise when they are used to simulate sheet metal forming because the normal stress in the thickness direction is omitted. In order to solve this problem, several authors [SAN 11, BAS 12] have proposed a new approach with an additional node which is introduced with two through-thickness translational degrees of freedom. The method mainly consists of adding a central node at the center of three-node and four-node shell elements with two degrees of freedom (Figure 2.5): two translations normal to the mid-surface for which one corresponds to the top surface ("upper skin" of the shell) and the other to the bottom surface ("lower skin" of the shell).

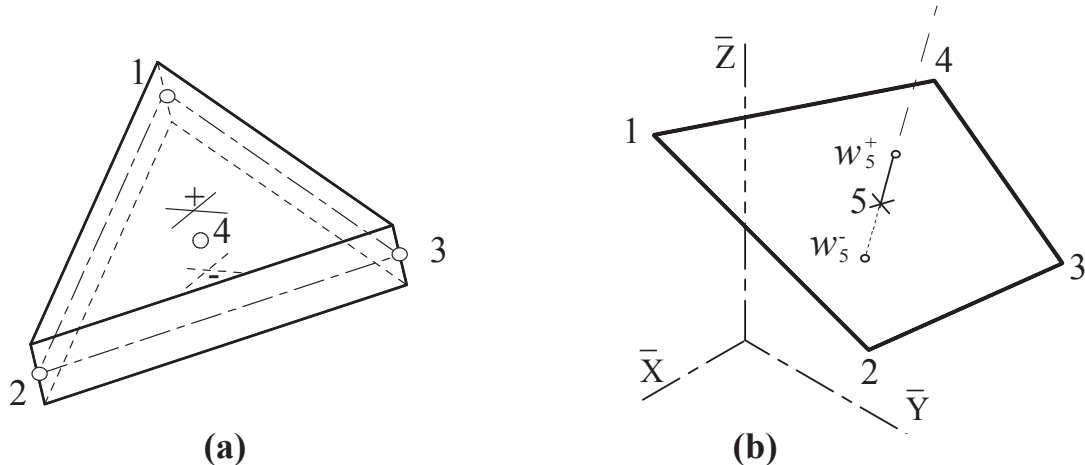


Figure 2.5 – Enriched shell elements: (a). Enriched three-node shell element. (b). Enriched four-node shell element.

We take the enriched four-node shell element for example to show how the extra degrees of freedom act on shell elements in bending cases while breaking from plane stress state hypothesis. The basic element is the 4-node quadrilateral $Q4\gamma24$ proposed by Bathe and Dvorkin.

A supplementary node "5" is located at the center of the element (Figure 2.5b). This central node has two degrees of freedom: two local translations respectively called w_5^+ , w_5^- in the normal direction "z". This feature allows to get a quadratic displacement field "w" according to the location "z" in the thickness direction which gives rise to a strain ϵ_{zz} in addition to the five other components ϵ_{xx} , ϵ_{yy} , $2\epsilon_{xy}$, $2\epsilon_{xz}$, $2\epsilon_{yz}$ ("x", "y" are in-plane coordinates). Because of the fact that this sixth component is linear, a full 3D strain-stress

2. Development of the new 3D beam element

behavior may replace the previous plane stress state hypothesis while giving good results in bending cases.

In the global frame $(\bar{X}, \bar{Y}, \bar{Z})$, the nodal translations and rotations are $\{\mathbf{U}_e\}$ and $\{\Theta_e\}$, so that:

$$\begin{aligned}\{\mathbf{U}_e\}^T &= [U_{\bar{X}1} \ U_{\bar{Y}1} \ U_{\bar{Z}1} \ U_{\bar{X}2} \ U_{\bar{Y}2} \ U_{\bar{Z}2} \ U_{\bar{X}3} \ U_{\bar{Y}3} \ U_{\bar{Z}3} \ U_{\bar{X}4} \ U_{\bar{Y}4} \ U_{\bar{Z}4}] \\ \{\Theta_e\}^T &= [\theta_{\bar{X}1} \ \theta_{\bar{Y}1} \ \theta_{\bar{Z}1} \ \theta_{\bar{X}2} \ \theta_{\bar{Y}2} \ \theta_{\bar{Z}2} \ \theta_{\bar{X}3} \ \theta_{\bar{Y}3} \ \theta_{\bar{Z}3} \ \theta_{\bar{X}4} \ \theta_{\bar{Y}4} \ \theta_{\bar{Z}4}]\end{aligned}\quad (2.22)$$

As written before, the translations associated to the central node in the local frame (x, y, z) , where "z" is the normal direction at the center of the element are gathered in $\{\mathbf{W}_e\}$ so that:

$$\{\mathbf{W}_e\}^T = [w_5^- \ w_5^+] \quad (2.23)$$

The gradient matrices \mathbf{B}^m , \mathbf{B}^b , \mathbf{B}^s related to membrane, bending and shear effects remain those of the element Q4γ24. Thus, with "h" denoting the thickness, the five first strain components are:

$$\begin{Bmatrix} \epsilon_{xx} \\ \epsilon_{yy} \\ \frac{2\epsilon_{xy}}{2\epsilon_{xz}} \\ \frac{2\epsilon_{yz}}{2\epsilon_{xz}} \end{Bmatrix} = \left[\begin{array}{c|c} \mathbf{B}^m & z\mathbf{B}^b \\ \hline g(\zeta)\mathbf{B}_u^s & g(\zeta)\mathbf{B}_\theta^s \end{array} \right] \begin{Bmatrix} \{\mathbf{U}_e\} \\ \{\Theta_e\} \end{Bmatrix}; \begin{cases} z = \zeta h/2; & -\leq \zeta \leq 1 : \text{out-plane} \\ -\leq \xi \leq 1; & -\leq \eta \leq 1 : \text{in-plane} \\ g(\zeta) = \frac{5}{4}(1 - \zeta^2) : \text{Reissner's weight function} \end{cases} \quad (2.24)$$

From now on, the plane stress assumption is regarded as obsolete. Knowing that w_5^- and w_5^+ correspond to the normal displacements of the lower and upper skins facing the node 5, by imposing $w(z = -h/2) = w_5^-$, $w(z = h/2) = w_5^+$ and $w(z = 0) = w_5 = (w_1 + w_2 + w_3 + w_4)/4$, the final quadratic form for $w(z)$ and linear form for ϵ_{zz} become:

$$w(z) = \frac{1}{4}(1 - 4\frac{z^2}{h^2})(w_1 + w_2 + w_3 + w_4) + 2\frac{z^2}{h^2}(w_5^+ + w_5^-) + \frac{z}{h}(w_5^+ - w_5^-) \quad (2.25)$$

$$\epsilon_{zz} = \left(\frac{4z}{h} - 1\right)\frac{w_5^-}{h} - \frac{8z}{h}\frac{w_5}{h} + \left(\frac{4z}{h} + 1\right)\frac{w_5^+}{h}; \quad w_5 = (w_1 + w_2 + w_3 + w_4)/4 \quad (2.26)$$

The sixth component is added to the previous five ones and related to $\{\mathbf{U}_e\}$ and $\{\mathbf{W}_e\}$:

$$\begin{Bmatrix} \epsilon_{xx} \\ \epsilon_{yy} \\ \frac{2\epsilon_{xy}}{2\epsilon_{xz}} \\ \frac{2\epsilon_{yz}}{2\epsilon_{xz}} \\ \epsilon_{zz} \end{Bmatrix} = \left[\begin{array}{c|c|c} \mathbf{B}^m & z\mathbf{B}^b & \\ \hline g(\zeta)\mathbf{B}_u^s & g(\zeta)\mathbf{B}_\theta^s & \\ \hline \zeta\mathbf{B}_u^p & \zeta\mathbf{B}_\theta^p + \bar{\mathbf{B}}_w^p & \end{array} \right] \begin{Bmatrix} \{\mathbf{U}_e\} \\ \{\Theta_e\} \\ \{\mathbf{W}_e\} \end{Bmatrix} = [\mathbf{B}(\xi, \eta, \zeta)]_{6 \times 26} \begin{Bmatrix} \{\mathbf{U}_e\} \\ \{\Theta_e\} \\ \{\mathbf{W}_e\} \end{Bmatrix} \quad (2.27)$$

Where:

$$\begin{aligned}\mathbf{B}_u^p &= -\frac{1}{h} [z_{\bar{X}} \ z_{\bar{Y}} \ z_{\bar{Z}} \ z_{\bar{X}} \ z_{\bar{Y}} \ z_{\bar{Z}} \ z_{\bar{X}} \ z_{\bar{Y}} \ z_{\bar{Z}} \ z_{\bar{X}} \ z_{\bar{Y}} \ z_{\bar{Z}}] \\ \mathbf{B}_w^p &= \frac{2}{h} [1 \ | \ 1] ; \bar{\mathbf{B}}_w^p = \frac{1}{h} [-1 \ | \ 1]\end{aligned}\quad (2.28)$$

Where $z_{\bar{X}}, z_{\bar{Y}}, z_{\bar{Z}}$ are the projections of the normal "z" onto the axes of the global frame ($\bar{X}, \bar{Y}, \bar{Z}$). Inevitably, all those strains are expressed in this local frame and, in the case of an in-plane reduced integration, there is only one local frame to be considered.

According to the order of strain and stress components and in the simplest case of an isotropic elastic case, the 3D constitutive matrix $[D]$ is:

$$\begin{Bmatrix} \sigma_{xx} \\ \sigma_{yy} \\ \sigma_{xy} \\ \sigma_{xz} \\ \sigma_{yz} \\ \sigma_{zz} \end{Bmatrix} = [D] \begin{Bmatrix} \epsilon_{xx} \\ \epsilon_{yy} \\ 2\epsilon_{xy} \\ 2\epsilon_{xz} \\ 2\epsilon_{yz} \\ \epsilon_{zz} \end{Bmatrix} \quad (2.29)$$

$$[D] = [D_{el}] = \begin{bmatrix} \lambda + 2\mu & \lambda & & & & \lambda \\ \lambda & \lambda + 2\mu & & & & \\ & & \mu & & & \\ & & & \mu & & \\ & & & & \mu & \\ \lambda & \lambda & & & & \lambda + 2\mu \end{bmatrix}; \quad \begin{aligned} \lambda &= \frac{\nu E}{(1-2\nu)(1+\nu)} \\ \mu &= \frac{E}{2(1+\nu)} \end{aligned} \quad (2.30)$$

The stiffness matrix $[K_e]$ would be computed thanks to the usual relation:

$$[K_e] = \iiint \mathbf{B}^T [D] \mathbf{B} dV \quad (2.31)$$

This work shows how the extra degrees of freedom act on shell elements in bending cases. Those extra degrees of freedom allow them to actualize the shell thickness and take it into account during deep drawing applications. It is essential to realize that reference [SAN 11] and [BAS 12] should not be only regarded as a presentation of new shell elements but rather as a methodology, which not only can be applied to most classical shell elements but also to other structural elements like beams.

2.4 Modelling of the new 2D beam element with thickness change

Since the normal stresses of classical beam elements are omitted in both thickness and width directions, when they are used to model fabrics at mesoscopic scale, the transverse deformation of the yarn (i.e. its compression and shape change) can't be obtained. The objective of the present work is to propose a new approach to solve this problem. Based on the methodology of shell elements described previously, we build a 2D beam element with thickness change by introducing a central node with two degrees of freedom to an initially 2 nodes element. The two degrees of freedom correspond to the relative displacements of the top and bottom surfaces of a beam respectively which are dedicated to the transverse strain and make it into plane stress state so that calculating the thickness change is possible.

2.4.1 Geometry and kinematics

The geometrical description of the proposed 2D beam element is shown in Figure 2.6. A single extra node (numbered 2) is added in the center of a standard two nodes Timoshenko beam element for which nodes are numbered 1 and 3. This extra node has only two degrees of freedom: two relative translations normal to the centroidal axis through thickness respectively called v_2^+ and v_2^- since they correspond to the normal relative displacements of the top surface ('upper skin' of the beam) and bottom surface ("lower skin" of the beam) facing node 2. These values are defined latter.

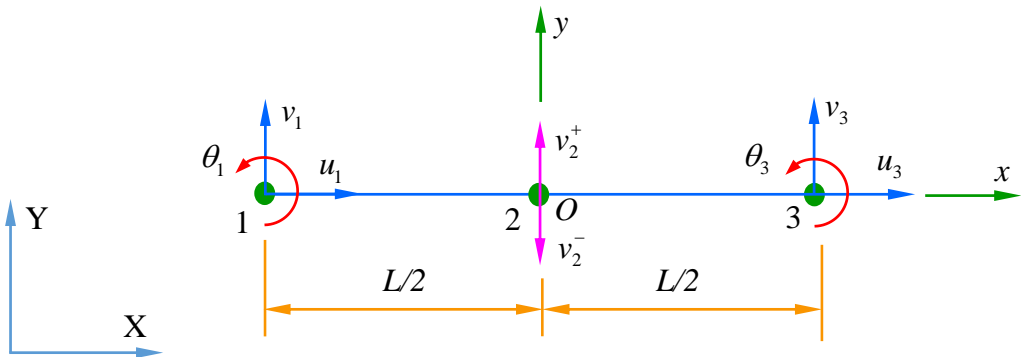


Figure 2.6 – Additional of two degrees of freedom on Timoshenko beam element.

Let u and v be the axial and transverse displacements of a beam respectively, and θ the rotation angle. Working in the local coordinate frame with the original coordinates $O(0,0,0)$, the displacements field for a point P of coordinates (x, y, z) can be obtained (the local coordinate frame x, y, z is only a translation of global frame X, Y, Z). As a result, the displacement field of the enhanced 2D beam element can be written as:

$$\vec{u}_P = \begin{bmatrix} u(x) - \theta(x) \cdot y \\ v(x, y) \end{bmatrix}, x \in [-L/2, L/2] \quad (2.32)$$

For that beam element, length is noted as L ($x_1 = -\frac{L}{2}$, $x_2 = 0$, $x_3 = \frac{L}{2}$), thickness is h . In order to obtain a transverse strain $\epsilon_{yy} = \frac{\partial v}{\partial y}$ which is linear in thickness direction, the function $v(x, y)$ should be quadratic with respect to y , so we assume a quadratic polynomial for $v(x, y)$:

$$v(x, y) = v(x, 0) + b_0 y + c_0 y^2 \quad (2.33)$$

Where b_0, c_0 are coefficients, which can be solved in terms of nodal variables corresponding to node 2; $v(x, 0)$ is transverse displacement of the centroidal axis, the interpolating function will be introduced latter.

Denoting v_2^t and v_2^b the normal displacement of top and bottom surfaces facing node 2 respectively, and by imposing $v(0,0) = (v_1 + v_3)/2$, $v_2^t = v(0,h/2)$, $v_2^b = v(0,-h/2)$, the quadratic form for $v(x,y)$ is:

$$v(x,y) = v(x,0) + \frac{y}{h} (v_2^t - v_2^b) + \frac{2y^2}{h^2} (v_2^t + v_2^b - 2v(0,0)) \quad (2.34)$$

For node 2 ($x_2 = 0$), the function $v(x,y)$ becomes:

$$v(0,y) = \frac{1}{2} (1 - \frac{4y^2}{h^2}) (v_1 + v_3) + \frac{2y^2}{h^2} (v_2^t + v_2^b) + \frac{y}{h} (v_2^t - v_2^b) \quad (2.35)$$

The Equation (2.35) has the same form as the enrichment shell element in reference [SAN 11]. Knowing relative translations normal to the centroidal axis respectively called v_2^+, v_2^- , which are defined as: $v_2^+ = v_2^t - v(0,0)$, $v_2^- = v_2^b - v(0,0)$, the final function for $v(x,y)$ expressed in terms of nodal variables v_2^+ and v_2^- :

$$v(x,y) = v(x,0) + V_1(y)v_2^+ + V_2(y)v_2^- \quad (2.36)$$

Where $V_1(y)$ and $V_2(y)$ are shape functions in thickness direction:

$$\begin{aligned} V_1(y) &= \frac{y}{h} + \frac{2y^2}{h^2} \\ V_2(y) &= -\frac{y}{h} + \frac{2y^2}{h^2} \end{aligned} \quad (2.37)$$

One thing that should be noticed here is that $\sum_{i=1}^2 V_i = \frac{4y^2}{h^2} \neq 1$. The fact that the sum of shape functions V_1 and V_2 is not constant, but quadratic through the thickness, means the partition of unity is not satisfied. This is not a drawback because the transverse displacement is expected to vary quadratically so that ϵ_{xx} and ϵ_{yy} have the same evolution through the thickness.

2.4.2 Gradient matrix

Nodes 1 and 3 have 3 degrees of freedoms u_i , v_i and θ_i as nodal variables. We consider linear shape functions for spatial interpolation of axial and transverse displacements u, v and rotation angle θ , in terms of nodal variables. In order to derive the element stiffness matrix for the 2D beam, the variables u , v and θ need to be interpolated within each element dealt as Timoshenko beam.

$$\begin{aligned} u(x) &= H_1(x)u_1 + H_3(x)u_3 \\ v(x,0) &= H_1(x)v_1 + H_3(x)v_3 \\ \theta(x) &= H_1(x)\theta_1 + H_3(x)\theta_3 \end{aligned} \quad (2.38)$$

Where $H_1(x)$ and $H_3(x)$ are linear shape functions: $H_1(x) = \frac{1}{2}(1 - \xi)$, $H_3(x) = \frac{1}{2}(1 + \xi)$, $\xi = \frac{2x}{L}$. For simplicity, notations, V_1 , V_2 , H_1 and H_3 will be used instead of $V_1(y)$, $V_2(y)$, $H_1(x)$ and $H_3(x)$. V'_1 , V'_2 , H'_1 and H'_3 as the derivative of $V_1(y)$, $V_2(y)$, $H_1(x)$ and $H_3(x)$ in the following derivation.

Due to the strain-displacement relation, we can get the strain expression:

$$\begin{bmatrix} \epsilon_{xx} \\ \epsilon_{yy} \\ \gamma_{xy} \end{bmatrix} = \begin{bmatrix} H'_1 & 0 & -yH'_1 & 0 & 0 & H'_3 & 0 & -yH'_3 \\ 0 & 0 & 0 & V'_1 & V'_2 & 0 & 0 & 0 \\ 0 & H'_1 & -H_1 & 0 & 0 & 0 & H'_3 & -H_3 \end{bmatrix} \begin{Bmatrix} u_1 \\ v_1 \\ \theta_1 \\ v_2^+ \\ v_2^- \\ u_3 \\ v_3 \\ \theta_3 \end{Bmatrix} = [B] \{d^e\} \quad (2.39)$$

Where $[B]$ is the element gradient matrix, and $\{d^e\}$ is the nodal displacement vector.

Compared with Timoshenko beam, the shear strain remains unchanged except that the usual shear factor (whose value is normally 5/6 for a rectangular cross section while 9/10 for a circular cross section) is not used directly. For the rectangular cross section, we use Reissner's weight function instead, and $2\epsilon_{xy}$ becomes:

$$2\epsilon_{xy} = g_y \gamma_{xy}, \quad g_y = \frac{5}{4}(1 - 4\frac{y^2}{h^2}) \quad (2.40)$$

As a result, the element gradient matrix $[B]$ becoming:

$$[B] = \begin{bmatrix} H'_1 & 0 & -yH'_1 & 0 & 0 & H'_3 & 0 & -yH'_3 \\ 0 & 0 & 0 & V'_1 & V'_2 & 0 & 0 & 0 \\ 0 & g_y H'_1 & -g_y H_1 & 0 & 0 & 0 & g_y H'_3 & -g_y H_3 \end{bmatrix} \quad (2.41)$$

2.4.3 Stiffness matrix and integration strategy

Since the transverse strain component ϵ_{yy} is introduced, the plane stress behavior can be used. Take isotropic material for example, the 2D constitutive matrix $[D]$ is:

$$[D] = \frac{E}{1 - \nu^2} \begin{bmatrix} 1 & \nu & 0 \\ \nu & 1 & 0 \\ 0 & 0 & (1 - \nu)/2 \end{bmatrix} \quad (2.42)$$

As a result, the element stiffness matrix can be expressed as:

$$[K^e] = \int_{\Omega_e} [B]^T [D] [B] d\Omega \quad (2.43)$$

in which Ω_e denotes the element domain.

It is well known that the conventional two-node isoparametric Timoshenko beam element suffers from the so-called shear locking [MUK 01, PRA 82, VEI 12], and reduced integration is used to alleviate shear locking. For the proposed 2D beam element, the shear strain energy is under-integrated in order to prevent shear locking. The integral of the element stiffness matrix $[K^e]$ can most conveniently be solved by splitting the expression into two parts: one that arises from the membrane-bending energy called bending stiffness matrix $[K_b^e]$ and one from the shear energy called shear stiffness matrix $[K_s^e]$:

$$[K^e] = [K_b^e] + [K_s^e] \quad (2.44)$$

Where the subscripts "b" and "s" denote bending and the transverse shear, respectively.

As mentioned in Section 2.2, the bending stiffness term is obtained using the exact integration of the membrane-bending strain energy while the shear stiffness term is obtained using the reduced integration technique [SHE 07, DUR 10]. As $g(y)$ is a quadratic polynomial, the order of $g^2(y)$ is four. So, its integration over the thickness needs five integration points along the local "y" direction. In fact, it is not really a drawback because this kind of element is intended for non-linear material computations which impose at least five through-thickness integration points [SAN 11]. It should be noticed that the shear factor $5/6$ comes from the integration of $g^2(y)$ in pure elastic examples (Figure 2.7).

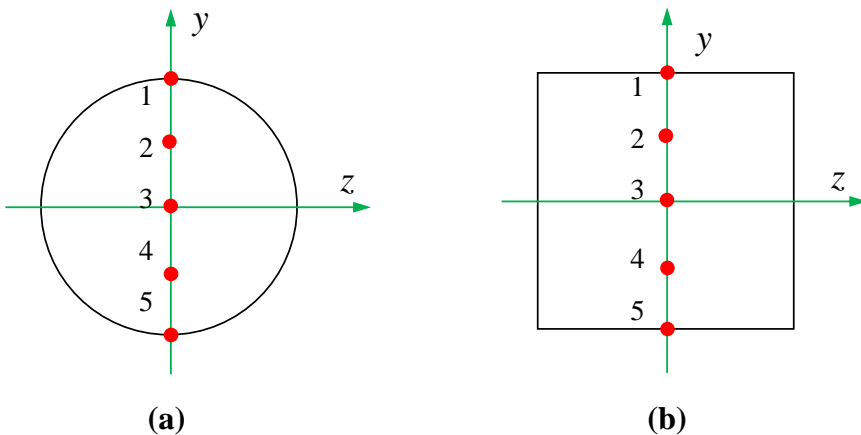


Figure 2.7 – Five through-thickness integration points [ABA 13]. (a). 2D circular cross section. (b). 2D rectangular cross section.

2.5 Extension to 3D beam element with deformable section

In this section, a behavior which remains elastic and isotropic is used but without the plane stress assumption and the goal is to extend it into full 3D elasticity. The strain

2. Development of the new 3D beam element

components for 3D should be ε_{xx} , ε_{yy} , ε_{zz} , $2\varepsilon_{xy}$, $2\varepsilon_{xz}$, $2\varepsilon_{yz}$, which means that we should add the components ε_{zz} , $2\varepsilon_{xz}$, $2\varepsilon_{yz}$ based on the 2D beam element described in Section 2.4. Compared with the 2D beam elements, the main novelty consists in the addition of extra degrees of freedom on the central node, which can represent the thickness and width changes.

2.5.1 Geometry and kinematics

One could think that going from 2D to 3D only needs to add two more degrees of freedom through width, which could be named w_2^+ and w_2^- . Unfortunately, this modification is not convenient because doing so induces ε_{yy} and ε_{zz} being independent. Such consequence is not physically admissible. For that, four other degrees of freedom are introduced to make sure that we have enough information to build the shape function and make ε_{yy} and ε_{zz} coupled together. In this way, the new 3D beam element formulation should include these main features as follows: each element has two end nodes which are treated by combining Saint-Venant and Timoshenko hypothesis; the transverse strains of both thickness and width direction are introduced based on the additional central node. The transverse strain distributions are linear, and the formulation of displacement is completely quadratic by adding the terms coupling the deformation in both transverse directions; fully 3D constitutive law can be used directly. Under this theory, the proposed 3D beam element is firstly built with 2 end nodes with 6 degrees of freedom ($u_{xi}, u_{yi}, u_{zi}, \alpha_{xi}, \alpha_{yi}, \alpha_{zi}$), with shear deformation and including Saint-Venant torsional effects. As described in Figure 2.8, a central node with 8 degrees of freedom is added to describe the transverse deformation. Corresponding degrees of freedom are described latter.

Working in the local frame (x, y, z) with the original coordinates $O (0, 0, 0)$, the displacements field for a point \mathbf{P} of coordinates (x, y, z) can be obtained (local coordinate frame x, y, z is only a translation of global frame X, Y, Z). As a result, the displacement field of the proposed 3D beam can be written as:

$$\vec{u}_P = \begin{bmatrix} u_x + \alpha_y \cdot z - \alpha_z \cdot y \\ v(x, y, z) - \alpha_x \cdot z \\ w(x, y, z) + \alpha_x \cdot y \end{bmatrix}; \quad \begin{array}{l} x \in [-L/2, L/2] \\ y \in [-h/2, h/2] \\ z \in [-b/2, b/2] \end{array} \quad (2.45)$$

For the new 3D beam element, length is noted as L ($x_1 = -L/2$, $x_2 = 0$, $x_3 = L/2$), thickness is h and width is b , an approximation of the shape of the deformed cross-section with quadratic polynomials with respect to y and z is proposed. So we assume $v(x, y, z)$ and $w(x, y, z)$ as follows:

$$v(x, y, z) = v(x, 0, 0) + a_0 y + a_1 y^2 + a_2 yz + a_3 z^2 \quad (2.46)$$

$$w(x, y, z) = w(x, 0, 0) + c_0 z + c_1 z^2 + c_2 yz + c_3 y^2 \quad (2.47)$$

Where $a_0, a_1, a_2, a_3, c_0, c_1, c_2, c_3$ are coefficients, which can be solved in terms of nodal variables.

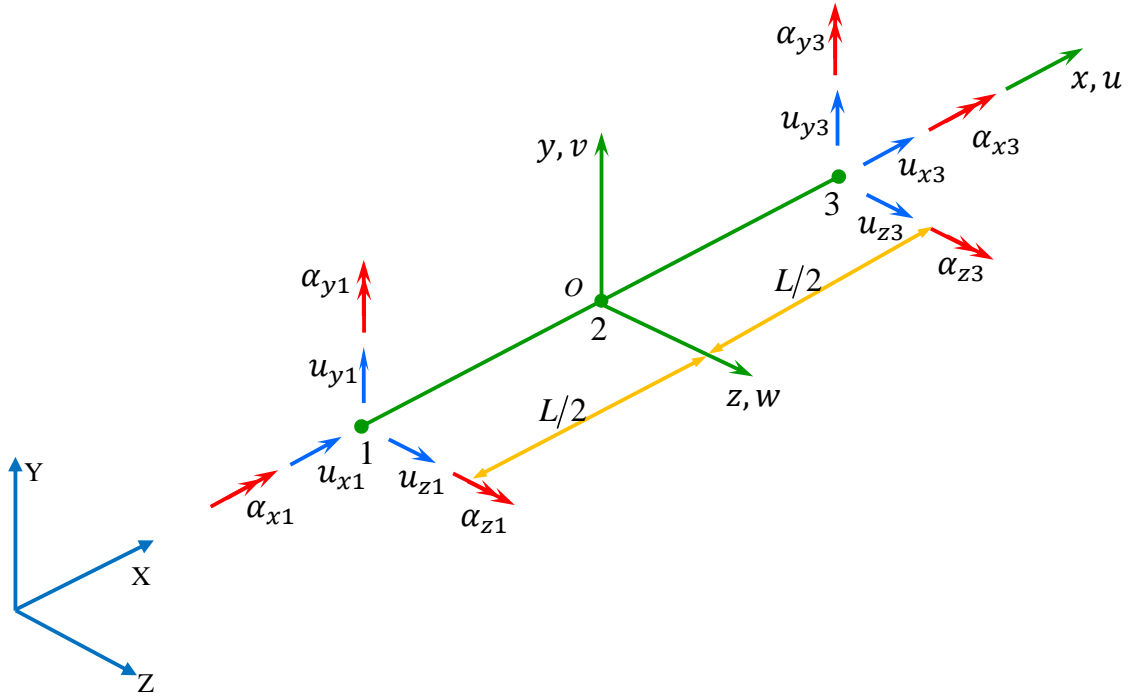


Figure 2.8 – Additional of a central node based 3D Timoshenko beam.

Thus, the three strain components ϵ_{xx} , ϵ_{yy} and ϵ_{zz} could be of the same order with respect to y and z , and they are coupled in the term related to the trace using a 3D Hooke's constitutive law. Since $\epsilon_{xx} = u'_x + \alpha'_y z - \alpha'_z y$ is linear with respect to both y and z , ϵ_{yy} and ϵ_{zz} should also be linear with respect to both y and z to avoid the so-called "Poisson locking" phenomenon. With the Equation (2.46) and (2.47), $\epsilon_{yy} = a_0 + 2a_1y + a_2z$ and $\epsilon_{zz} = c_0 + 2c_1z + c_2y$ have the same polynomial form as ϵ_{xx} .

2.5.2 Shape functions and gradient matrix

In order to solve the coefficients $a_0, a_1, a_2, a_3, c_0, c_1, c_2, c_3$, we introduced 8 degrees of freedom to the central node, four relative translations in thickness direction namely $v_a^+, v_b^+, v_c^+, v_d^+$ and four in width direction namely $w_a^+, w_b^+, w_c^+, w_d^+$ respectively, which are shown in Figure 2.9.

Denoting v_c^t , v_a^t and v_b^t the normal displacement of top surface facing node 2, v_c^b the normal displacement of bottom surface facing node 2. The superscript "t" represents the top surface, and the "b" represents the bottom surface. The subscript "a", "b", "c", "d" represent the number of the degree of freedom corresponding to the Figure 2.9. Here, we define the relative displacements as:

$$\begin{aligned} v_c^+ &= v_c^t - v(0,0,0), & v_c^- &= v_c^b - v(0,0,0) \\ v_a^+ &= v_a^t - v(0,0,0), & v_b^+ &= v_b^t - v(0,0,0) \end{aligned} \quad (2.48)$$

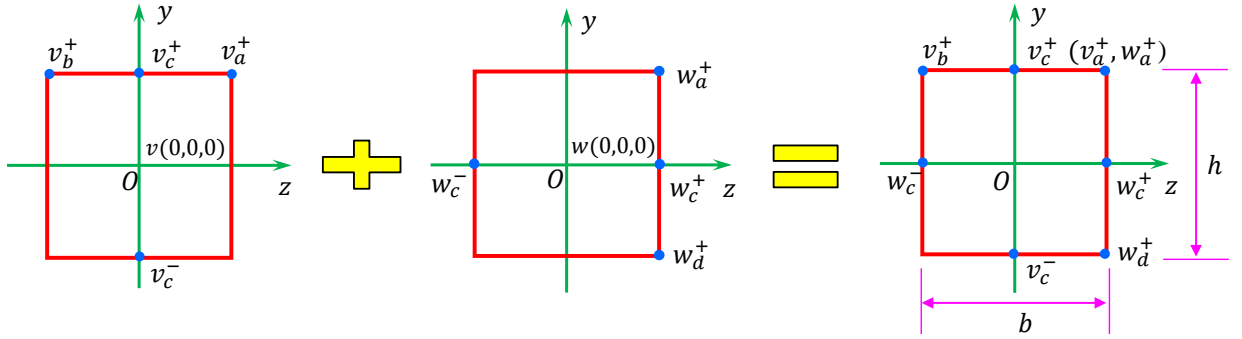


Figure 2.9 – Presentation of the additional node with 8 degrees of freedom.

By imposing $v_c^t = v(0, \frac{h}{2}, 0)$, $v_c^b = v(0, -\frac{h}{2}, 0)$, $v_a^t = v(0, \frac{h}{2}, \frac{b}{2})$, $v_b^t = v(0, \frac{h}{2}, -\frac{b}{2})$ and $v(0,0,0) = \frac{(u_{y1} + u_{y3})}{2}$ and submitting these information into Equation (2.46), we can obtain the deformation function in thickness:

$$\begin{aligned} V_1 &= \frac{y}{h} + \frac{2y^2}{h^2} - \frac{4z^2}{b^2}, \quad V_2 = -\frac{y}{h} + \frac{2y^2}{h^2} \\ V_3 &= \frac{2yz}{bh} + \frac{2z^2}{b^2}, \quad V_4 = -\frac{2yz}{bh} + \frac{2z^2}{b^2} \end{aligned} \quad (2.49)$$

Similarly, the deformation function in width direction can be expressed as:

$$w(x, y, z) = w(x, 0, 0) + W_1 w_c^+ + W_2 w_c^- + W_3 w_a^+ + W_4 w_d^+ \quad (2.50)$$

Where:

$$\begin{aligned} W_1 &= \frac{z}{b} + \frac{2z^2}{b^2} - \frac{4y^2}{h^2}, \quad W_2 = -\frac{z}{b} + \frac{2z^2}{b^2} \\ W_3 &= \frac{2yz}{bh} + \frac{2y^2}{h^2}, \quad W_4 = -\frac{2yz}{bh} + \frac{2y^2}{h^2} \end{aligned} \quad (2.51)$$

One thing should be noticed here is that $\sum_{i=1}^4 V_i = \frac{4y^2}{h^2} \neq 1$, $\sum_{i=1}^4 W_i = \frac{4z^2}{h^2} \neq 1$, which is the same situation described in Section 2.4.1. The fact that the sum of shape functions is not constant, but quadratic through the thickness and width respectively, means the partition of unity is not satisfied. This is not a drawback because the transverse displacement is expected to vary quadratically so that ε_{xx} , ε_{yy} and ε_{zz} have the same evolution through thickness and they are coupled in the term related to the trace using a 3D Hooke's constitutive law.

For node 1 and node 3, we assume the simple linear shape function H_1 and H_3 (as described in Section 2.4.2) for the variables $u_x, u_y, u_z, \alpha_x, \alpha_y, \alpha_z$:

$$\begin{aligned} u_x &= H_1 u_{x1} + H_3 u_{x3}, \quad u_y = H_1 u_{y1} + H_3 u_{y3}, \quad u_z = H_1 u_{z1} + H_3 u_{z3} \\ \alpha_x &= H_1 \alpha_{x1} + H_3 \alpha_{x3}, \quad \alpha_y = H_1 \alpha_{y1} + H_3 \alpha_{y3}, \quad \alpha_z = H_1 \alpha_{z1} + H_3 \alpha_{z3} \end{aligned} \quad (2.52)$$

Due to the strain-displacement relation, the strains of the proposed 3D beam element can be expressed:

$$[\boldsymbol{\varepsilon}] = [B] \{d^e\} \quad (2.53)$$

Where:

$$[B]_{6 \times 20} = \begin{bmatrix} H'_1 & 0 & 0 & 0 & zH'_1 & -yH'_1 & 0 & 0 & 0 & 0 \\ 0 & 0 & 0 & 0 & 0 & 0 & \frac{\partial V_1}{\partial y} & \frac{\partial V_2}{\partial y} & \frac{\partial V_3}{\partial y} & \frac{\partial V_4}{\partial y} \\ 0 & 0 & 0 & 0 & 0 & 0 & 0 & 0 & 0 & 0 \\ 0 & H'_1 & 0 & -zH'_1 & 0 & -H_1 & 0 & 0 & 0 & 0 \\ 0 & 0 & H'_1 & yH'_1 & H_1 & 0 & 0 & 0 & 0 & 0 \\ 0 & 0 & 0 & 0 & 0 & 0 & \frac{\partial V_1}{\partial z} & \frac{\partial V_2}{\partial z} & \frac{\partial V_3}{\partial z} & \frac{\partial V_4}{\partial z} \end{bmatrix} \quad (2.54)$$

$$\begin{bmatrix} 0 & 0 & 0 & 0 & H'_3 & 0 & 0 & 0 & zH'_3 & -yH'_3 \\ 0 & 0 & 0 & 0 & 0 & 0 & 0 & 0 & 0 & 0 \\ \frac{\partial W_1}{\partial z} & \frac{\partial W_2}{\partial z} & \frac{\partial W_3}{\partial z} & \frac{\partial W_4}{\partial z} & 0 & 0 & 0 & 0 & 0 & 0 \\ 0 & 0 & 0 & 0 & 0 & H'_3 & 0 & -zH'_3 & 0 & -H'_3 \\ 0 & 0 & 0 & 0 & 0 & 0 & H'_3 & yH'_3 & H'_3 & 0 \\ \frac{\partial W_1}{\partial z} & \frac{\partial W_2}{\partial z} & \frac{\partial W_3}{\partial z} & \frac{\partial W_4}{\partial z} & 0 & 0 & 0 & 0 & 0 & 0 \end{bmatrix}$$

$$[\boldsymbol{\varepsilon}] = [\varepsilon_{xx} \ \varepsilon_{yy} \ \varepsilon_{zz} \ \gamma_{yz} \ \gamma_{xz} \ \gamma_{xy}]^T \quad (2.55)$$

$$\{d^e\} = [u_{x1} \ u_{y1} \ u_{z1} \ \alpha_{x1} \ \alpha_{y1} \ \alpha_{z1} \ v_c^+ \ v_c^- \ v_a^+ \ v_b^+ \\ w_c^+ \ w_c^- \ w_a^+ \ w_d^+ \ u_{x3} \ u_{y3} \ u_{z3} \ \alpha_{x3} \ \alpha_{y3} \ \alpha_{z3}] \quad (2.56)$$

Same situation as the enhanced 2D beam element described previously, the usual shear factor is not used directly, and $2\varepsilon_{xy}, 2\varepsilon_{xz}, 2\varepsilon_{yz}$ becoming:

$$2\varepsilon_{xy} = g_y \gamma_{xy}, \quad 2\varepsilon_{xz} = g_z \gamma_{xz}, \quad 2\varepsilon_{yz} = g_z \gamma_{yz} \\ g_y = \frac{5}{4}(1 - 4 \frac{y^2}{h^2}), \quad g_z = \frac{5}{4}(1 - 4 \frac{z^2}{b^2}) \quad (2.57)$$

2.5.3 Stiffness matrix and integration strategy

Since the transverse strain component ε_{yy} and ε_{zz} are introduced, full 3D constitutive law can be used. Take isotropic material for example, the 3D constitutive matrix $[D]$:

$$[D] = \frac{E}{(1+\nu)(1-2\nu)} \begin{bmatrix} 1-\nu & \nu & \nu & 0 & 0 & 0 \\ \nu & 1-\nu & \nu & 0 & 0 & 0 \\ \nu & \nu & 1-\nu & 0 & 0 & 0 \\ 0 & 0 & 0 & \frac{1-2\nu}{2} & 0 & 0 \\ 0 & 0 & 0 & 0 & \frac{1-2\nu}{2} & 0 \\ 0 & 0 & 0 & 0 & 0 & \frac{1-2\nu}{2} \end{bmatrix} \quad (2.58)$$

As a result, the element stiffness matrix can be expressed as:

$$[K^e] = \int_{\Omega_e} [B]^T [D] [B] d\Omega \quad (2.59)$$

in which Ω_e denotes the element domain.

In order to avoid the shear locking, we use the same method described previously, splitting the integral of the element stiffness matrix $[K^e]$ into two parts: one that arises from the membrane-bending energy called bending stiffness matrix $[K_b^e]$ and one from the shear energy called shear stiffness matrix $[K_s^e]$:

$$[K^e] = [K_b^e] + [K_s^e] \quad (2.60)$$

Where the subscripts "b" and "s" indicate bending and the transverse shear, respectively.

For bending stiffness term:

$$[K_b^e] = \int_{\Omega_e} [B_b]^T [D_b] [B_b] d\Omega \quad (2.61)$$

Where:

$$[D_b] = \frac{E}{(1+\nu)(1-2\nu)} \begin{bmatrix} 1-\nu & \nu & \nu \\ \nu & 1-\nu & \nu \\ \nu & \nu & 1-\nu \end{bmatrix}, [B_b] = \begin{bmatrix} B(1,:) \\ B(2,:) \\ B(3,:) \end{bmatrix} \quad (2.62)$$

For shear stiffness term:

$$[K_s^e] = \int_{\Omega_e} [B_s]^T [D_s] [B_s] d\Omega \quad (2.63)$$

Where:

$$[D_s] = \begin{bmatrix} G & 0 & 0 \\ 0 & G & 0 \\ 0 & 0 & G \end{bmatrix}, G = \frac{E}{2(1+\nu)}, [B_s] = \begin{bmatrix} g_y \cdot B(4,:) \\ g_z \cdot B(5,:) \\ g_z \cdot B(6,:) \end{bmatrix} \quad (2.64)$$

In the matrix $[B_b]$ and $[B_s]$, $B(i,:)$ presents the i th ($i=1,2,\dots,6$) row of the matrix $[B]$. When it comes to the integration, as both $g(y)$, $g(z)$ are quadratic polynomial, the orders of $g^2(y)$ and $g^2(z)$ are four. So, that integration over the thickness and the width both need five integration points along each integration direction. The integration points for both circular cross-section and rectangular cross section can be seen in Figure 2.10.

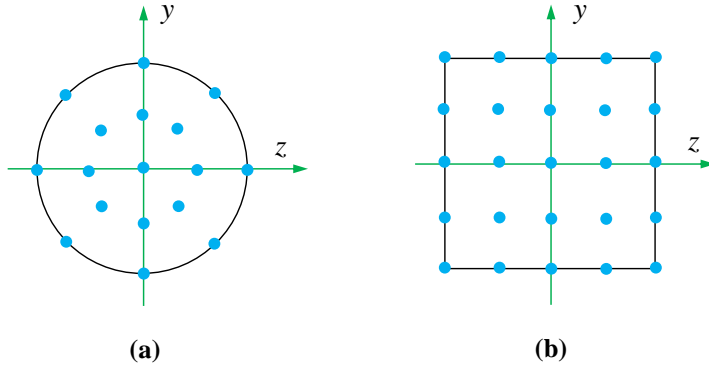


Figure 2.10 – Integration points [ABA 13]. (a). Circular cross section.(b). Rectangular cross section.

2.6 Numerical validation for linear small strain conditions

In this section, a series of examples are used to prove that the results obtained with the proposed 3D elements are similar to those given by the solid elements from ABAQUS/Standard. A FEM code has been developed in Matlab, and a mesh of 10 elements for cantilever is used for calculations as shown in Figure 2.11(a). Then the results are compared with corresponding values from ABAQUS/Standard 3D simulations which uses C3D8I element (incompatible mode eight-node brick element) for calculating the same example. In this case, at least 640 elements are needed so that we can have five nodes along the "y" and "z" directions respectively, the mesh model is shown in Figure 2.11(b). The reason is that the solid element adopts bilinear interpolation while the proposed 3D beam adopts quadratic polynomials interpolation in the cross section and five integration points are needed both along "y" and "z" direction.

In these examples, we consider a cantilever beam with length $l = 10\text{mm}$ and width $b = 1\text{mm}$ and thickness $h = 1\text{mm}$. Material parameters are $E = 2.1 \times 10^5 \text{ MPa}$, $\nu = 0.3$. The cantilever beam is subjected to the action of axial force P , bending moment M , shear force F , and transverse compression Q , respectively.

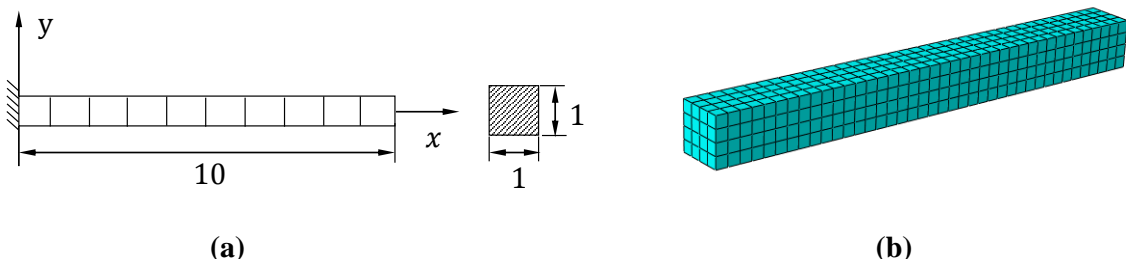


Figure 2.11 – Mesh model. (a).In Matlab. (b). In Abaqus.

2.6.1 Tension

In this example, a cantilever beam is subjected to an axial load of 500N at the right end to demonstrate the ability of the element to simulate the section shape under tension. The results given by the proposed 3D beam element in Matlab and solid element in ABAQUS/Standard can be seen in Figure 2.12(a). The largest displacement U_x given by Matlab for the node at the right end is 0.0238 mm which corresponds to the theoretical value given by P/El . In Figure 2.12(a), the two results are so close that it is difficult to distinguish them, so we define the difference between the two results as errors, that is $U_xError = U_{xAbaqus} - U_{xMatlab}$ which are more intuitive to express the results, as shown in Figure 2.12(b). From Figure 2.12(b), we can see that all the errors have a magnitude of the order of 10^{-5} mm and the relative errors are of the order of 0.37% which remain stable except the values near the boundary. This relative error is very small, it could be related to the difference in element size along x-axis between the two models.

For the simple case, the stiffness matrix can be calculated, and the symbolic equation can be solved, we obtain some conclusions such as: $v_c^+ = -v_c^-$, $v_a^+ = v_b^+$, $w_c^+ = -w_c^-$, $w_a^+ = w_d^+$ and the values of v_c^+ , v_a^+ , w_c^+ , w_a^+ are constant along the positions of x axis, so we use four series of values corresponding to v_c^+ , v_a^+ , w_c^+ , w_a^+ , instead of eight to describe the deformation of the section, which are listed in Table 2.1. From Table 2.1, it can be seen that the results are consistent except for the first value near the boundary which is not listed in the table. That is to say the proposed 3D beam element can be applied in tension simulation.

Table 2.1 – Cross section deformation comparison of ABAQUS and Matlab under tension

	v_c^+	v_a^+	w_c^+	w_a^+
Abaqus(mm)	-0.00035714	-0.00035714	0.00035714	0.00035714
Matlab(mm)	-0.00035714	-0.00035714	-0.00035714	0.00035714

2.6.2 Pure bending

We consider a cantilever beam subjected to a constant moment $M=500$ Nmm at the right end, which demonstrates the ability of the element to simulate the deformation occurring in the cross section under the action of bending moment (Figure 2.13). Let U_y be the displacement along y axis, the distributions of U_y for the centroidal axis can be seen in Figure 2.14(a), there's a little difference between the results from ABAQUS and Matlab. The main reason is that since the solid element doesn't have rotational degree of freedom, a bending moment can't be directly applied to it. Instead, we applied a linear variation distribution force though thickness in the cross section. Due to this reason, the results from ABAQUS and Matlab can't be exactly the same since the solid element can't avoid the transverse shear locking completely while the proposed 3D beams elements can. The errors of U_y are defied as $U_yError = U_{yAbaqus} - U_{yMatlab}$, and the biggest value achieves

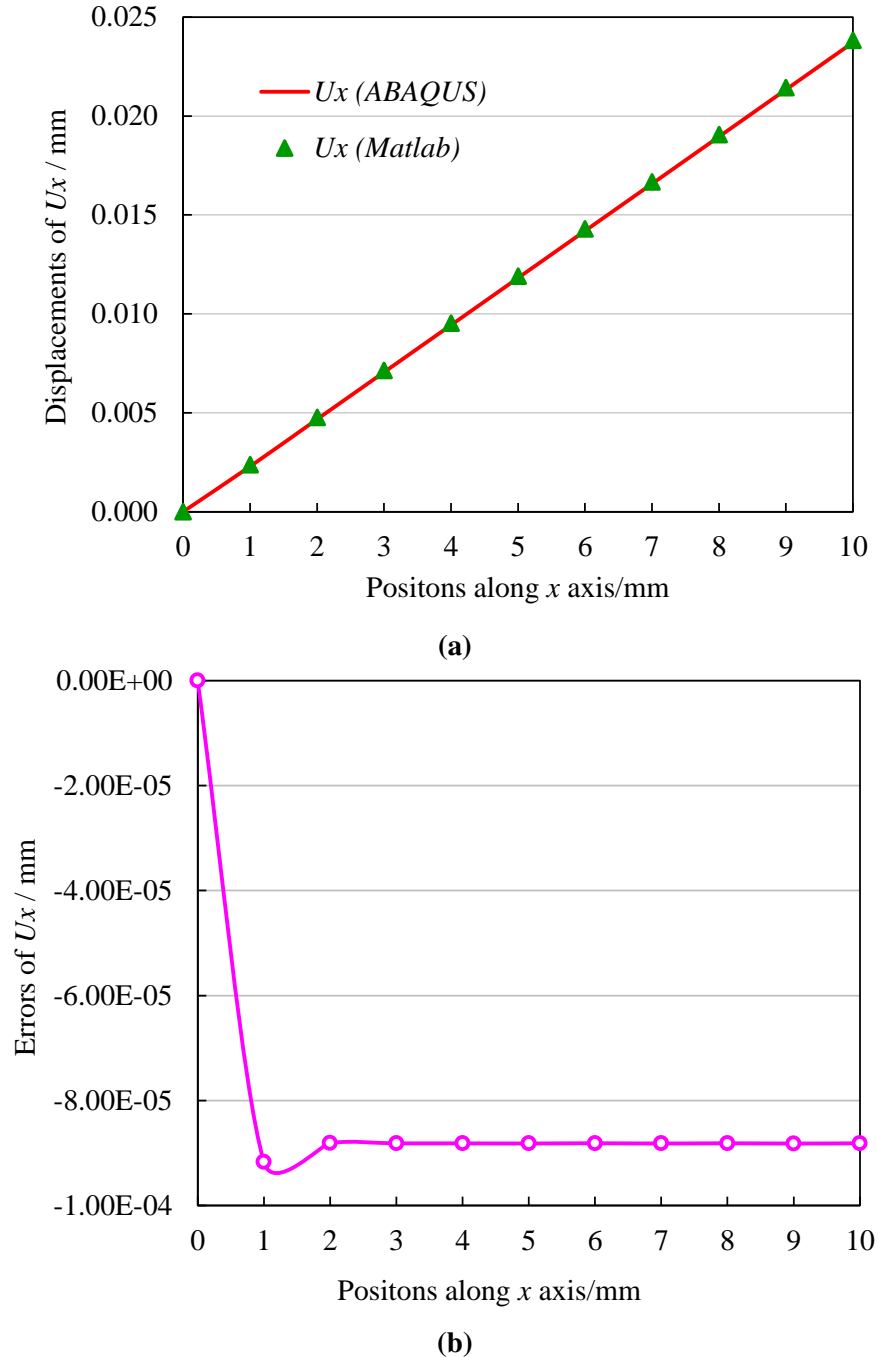


Figure 2.12 – Results comparison of ABAQUS and Matlab under tension. (a). Distribution of displacement U_x . (b). Distribution of displacement errors U_{xError} .

2. Development of the new 3D beam element

0.021 mm at the end of the cantilever which can be seen in Figure 2.14(b). For the simple case, by solving the symbolic equation, we can obtain the conclusions such as $v_c^+ = -v_c^-$, $v_a^+ = v_b^+$, $w_c^+ = -w_c^-$, $w_a^+ = -w_d^+$. After deformation, the cross section changes into trapezoid, with parabolic curve for the top and bottom edges, as shown in Figure 2.15(a). From the numerical results, there's $v_a^+ = 0$, $w_c^+ = 0$ in both ABAQUS and Matlab. Thus, we just need to compare the values of v_c^+ and w_a^+ , the distribution is shown in Figure 2.15(a). The results show that the relative displacements of v_c^+ and w_a^+ , in both thickness and width directions are almost constant except the value near boundary. The results from ABAQUS and Matlab are very close, and the same definition method of U_y is used to define the errors of v_c^+ and w_a^+ , which are shown in Figure 2.15(b). Except the big difference near the boundary, all the errors distribution is of the order of 10^{-5} mm in magnitude, and the relative error is of the order of 1%.

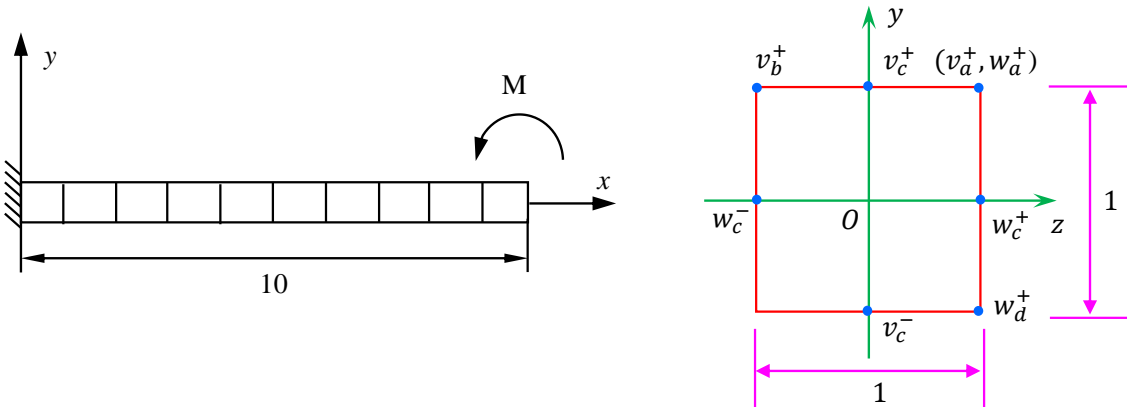


Figure 2.13 – A cantilever beam subjected to a constant moment

Furthermore, in order to verify the validation of the new 3D beam element under pure bending, 3D Timoshenko beam element (B31) is also chosen in ABAQUS/Standard to simulate the same example, with the same discretization along x axis as shown in Figure 2.11(a). One thing should be noticed here is that B31 beam element can't describe the cross section changes, so we just compare the displacement U_y and their errors of the centroidal axis. The results can be seen in Figure 2.16, the values of U_y are quite the same (Figure 2.16a), and the errors of U_y are nearly zeros with a little fluctuation (Figure 2.16b). However, all the errors are of the order of 10^{-7} mm in magnitude which may be caused by the different solving accuracy in ABAQUS/Standard and Matlab. Compared with the biggest displacement at the end of the cantilever 1.4286 mm, this fluctuation is small enough to be neglected, which proves the consistency of both two results.

It shows that the results of the proposed 3D beam element concerning U_y are closer to B31 elements of Abaqus than to the solid elements (C3D8I). The main reason lies that the solid element can't avoid the transverse shear locking completely while the proposed 3D beams elements and B31 elements can avoid.

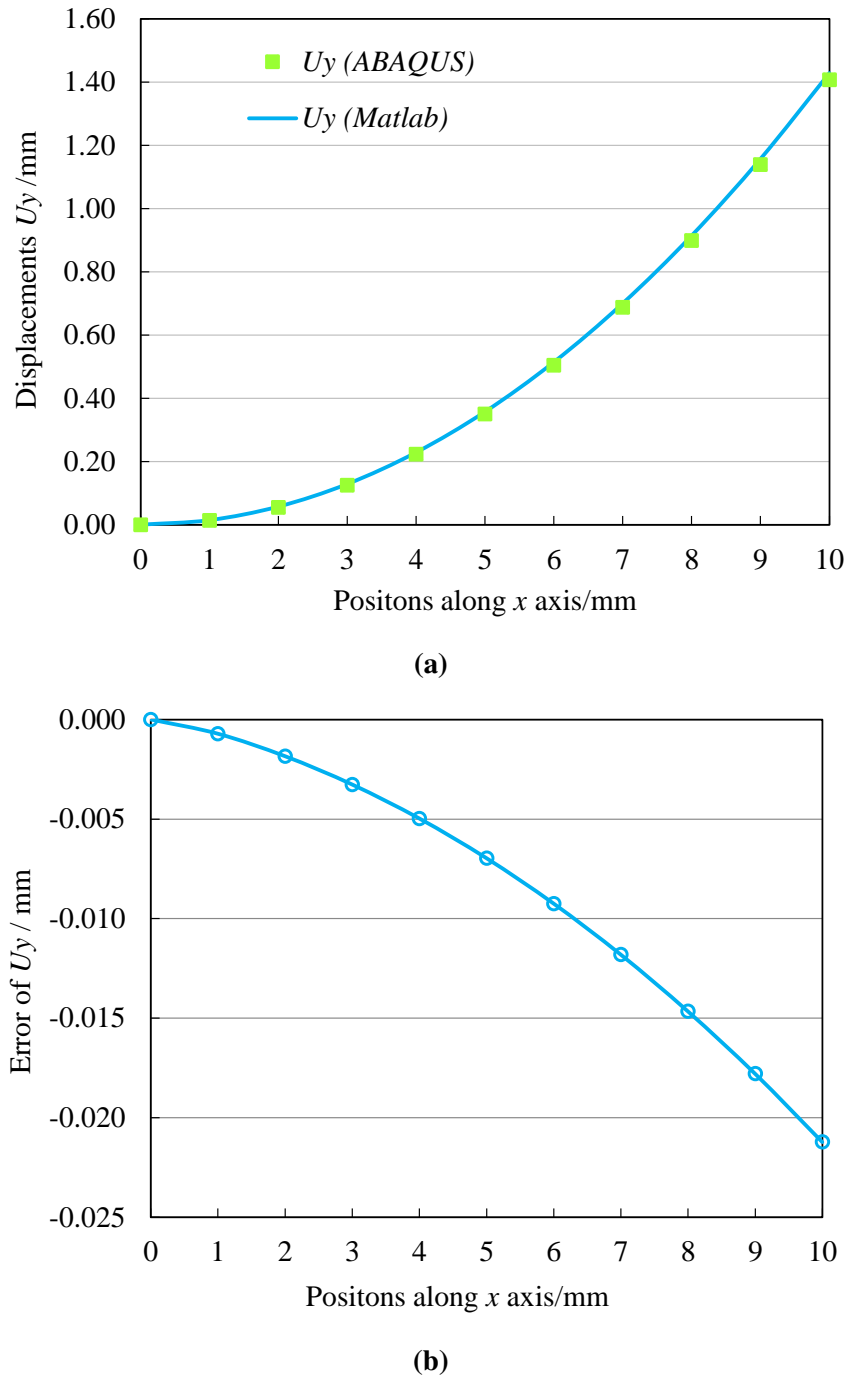


Figure 2.14 – Results comparison of ABAQUS and Matlab under pure bending. (a). Displacement U_y of the centroidal axis. (b). Distribution of displacement errors U_yError .

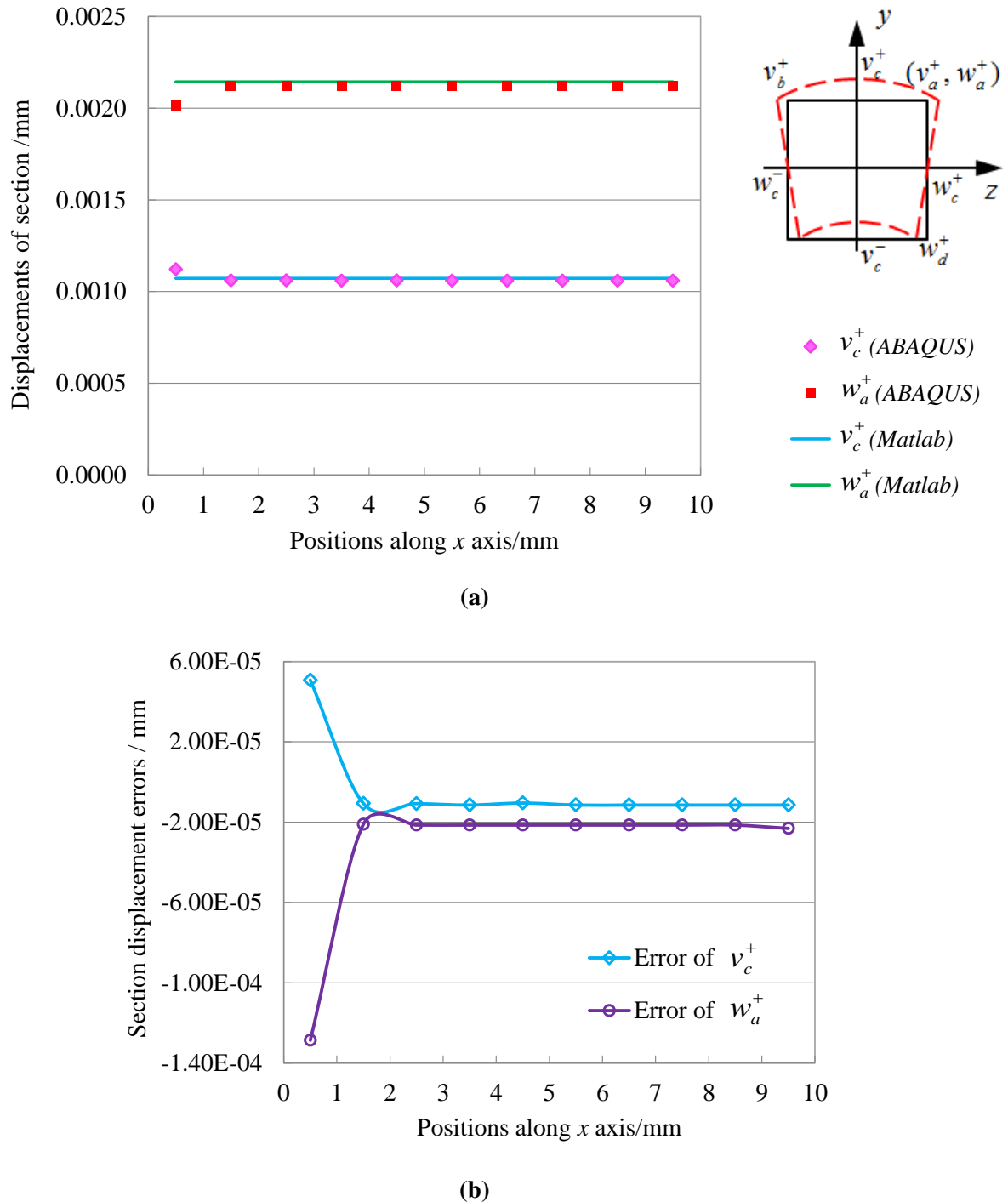


Figure 2.15 – Results comparison of ABAQUS and Matlab under pure bending. (a). Displacement distribution of cross section. (b). Displacement errors of cross section.

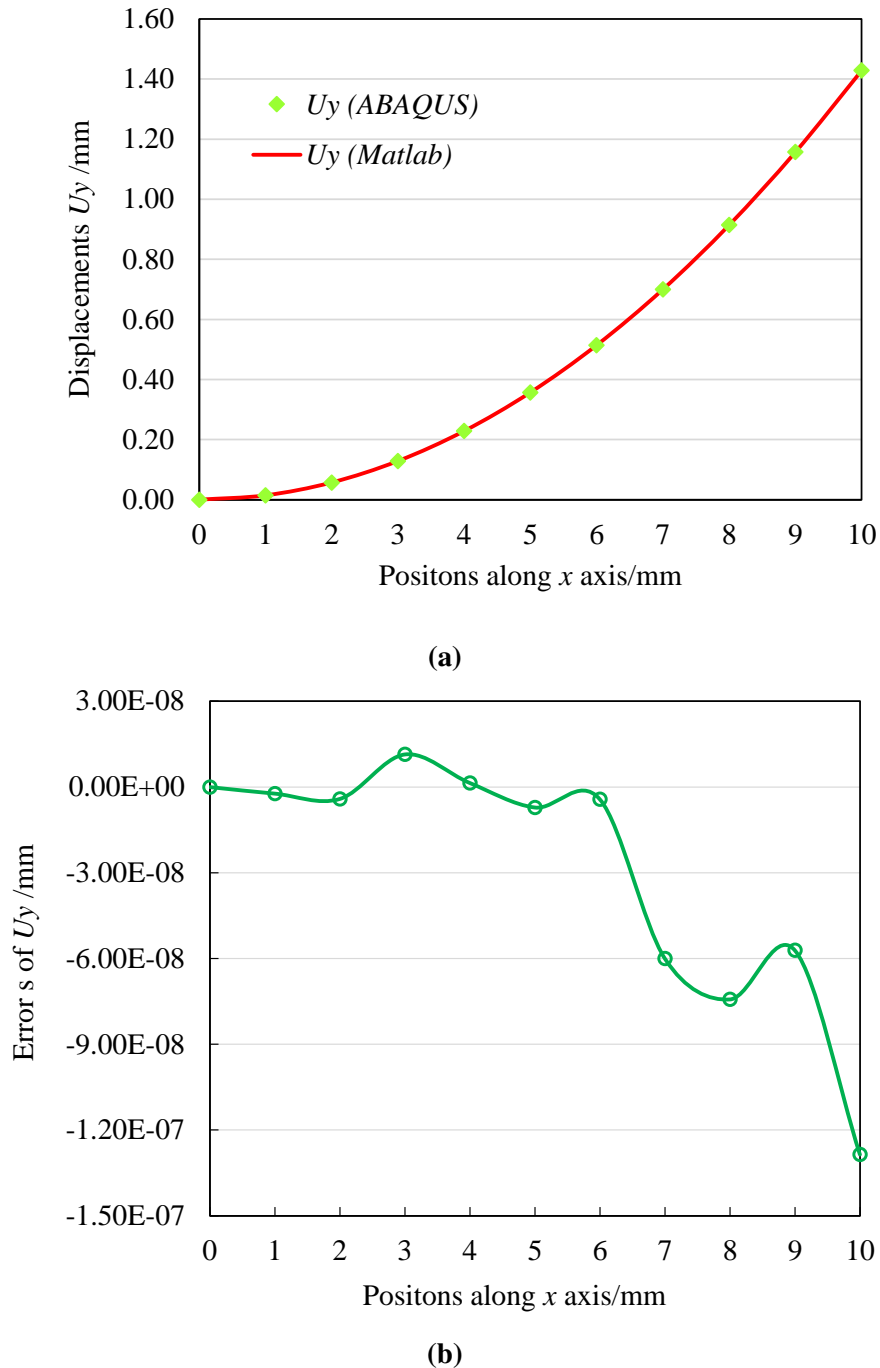


Figure 2.16 – Results comparison of ABAQUS and Matlab under tension. (a). Displacement U_y of the centroidal axis. (b). Error of U_y for the centroidal axis.

2.6.3 Shear + bending

In this example, we discuss a cantilever beam subjected to a concentrated force $F=-100$ N at the right end (Figure 2.17). The concentrated force not only has the effect of bending but also the effect of shear. The comparisons of results between ABAQUS and Matlab are shown in Figure 2.18. We can see that the results comparisons are better than that of pure bending. The errors of U_y (U_yError) for the centroidal axis between the two results can be seen in Figure 2.18(b). The errors distribution is linear and the biggest value lies at the end of the cantilever beam, which is 0.0137 mm. Compared with the biggest displacement at the end of the cantilever 1.915mm, the relative error is 0.7% which is in the accepted range of error, which may be caused by the different discretization along x axis. Besides comparison of U_y , we also compare the deformation of the cross section, and the results are almost the same. Similarly to the Section 2.6.2, the following conclusions can be drawn: $v_c^+ = -v_c^-$, $v_a^+ = v_b^+ = 0$, $w_c^+ = -w_c^- = 0$, $w_a^+ = -w_d^+$. Thus, we just need to compare the value of v_c^+ and w_a^+ , which can be seen in Figure 2.19(a). The two results are very close except the values at the boundary. The same definition method of U_yError is used to define the errors of v_c^+ and w_a^+ , the results are shown in Figure 2.19(b). All the errors are nearly zeros (at the order of 10^{-7} mm in magnitude) except for the values near boundary, which proves the proposed 3D beam element can be used to simulate the beam deformation under concentrated force and could obtain good results.

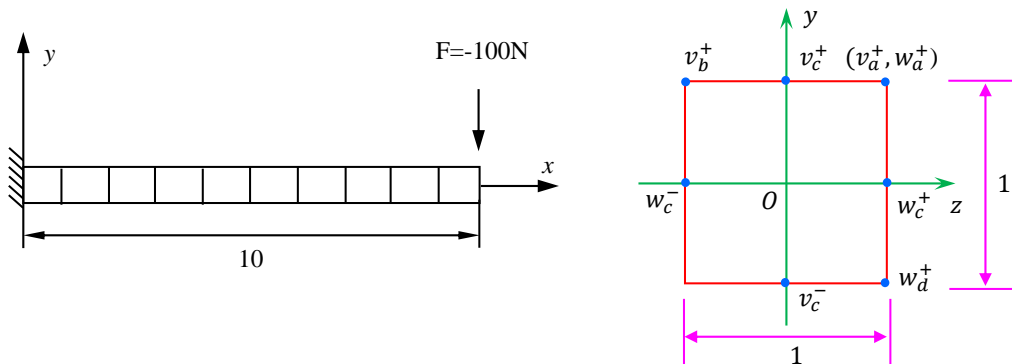


Figure 2.17 – A cantilever beam subjected to a concentrated force.

The absolute value of the relative displacements v_c^+ and w_a^+ in both thickness and width directions change with the positions along x axis and become smaller and smaller. For that reason, we chose the middle plane to observe the deformation law precisely. Due to a special feature of the proposed element (the values of $v_c^+, v_a^+, w_c^+, w_a^+$ are obtained at midpoint of the element), the plane at the position $x=5.5$ mm is chosen. The isovalues of U_y on deformed configuration of the cross section can be seen in Figure 2.20, of which Figure 2.20(a) is the results from ABAQUS/Standard while Figure 2.20(b) is the results from Matlab. The values for all integration points are almost the same and the shapes of deformed configurations are close, which means using the proposed 3D elements can achieve good results as respected.

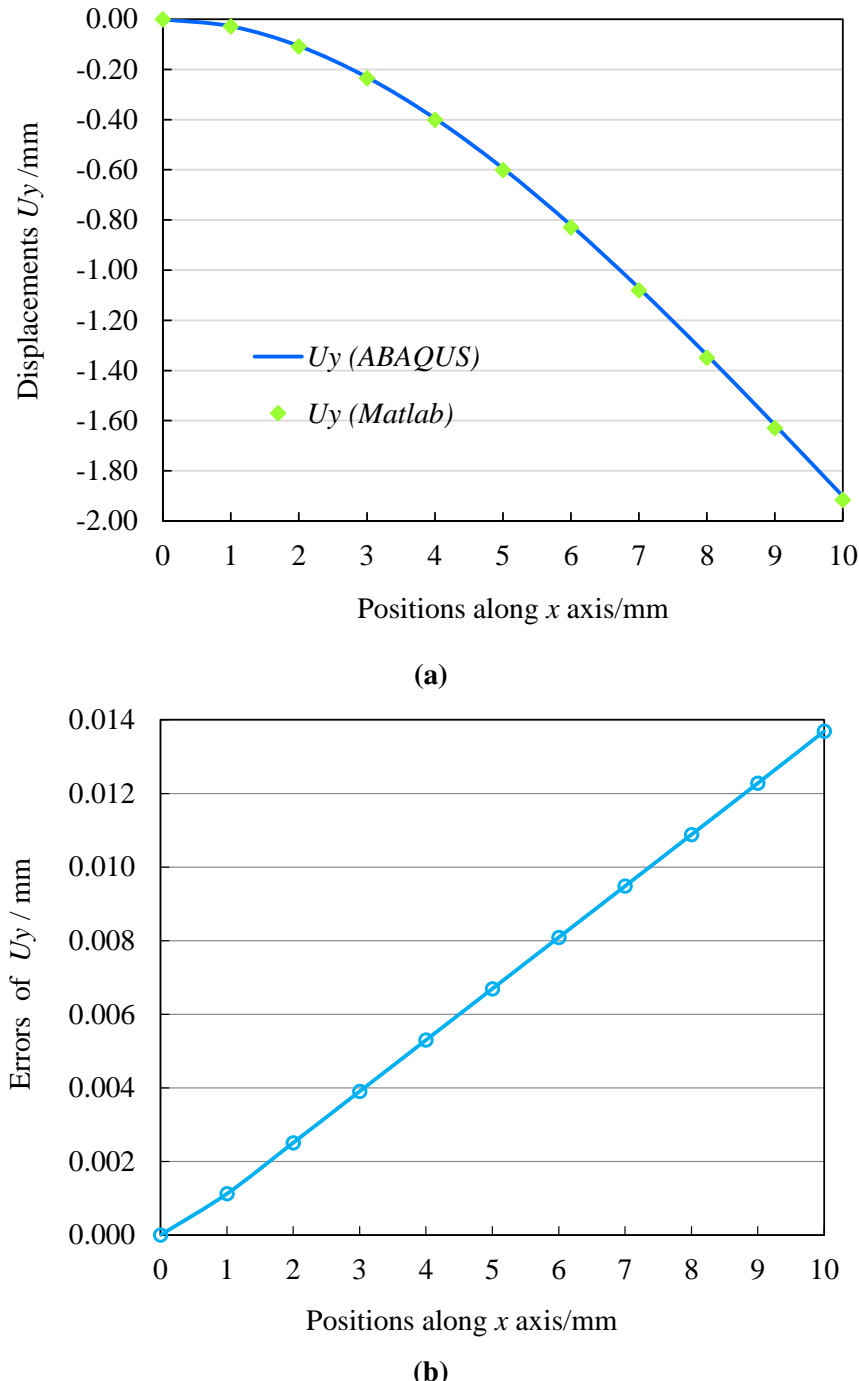


Figure 2.18 – Results comparison of ABAQUS and Matlab. (a). Displacement U_y of the centroidal axis. (b). Distribution of displacement errors U_yError .

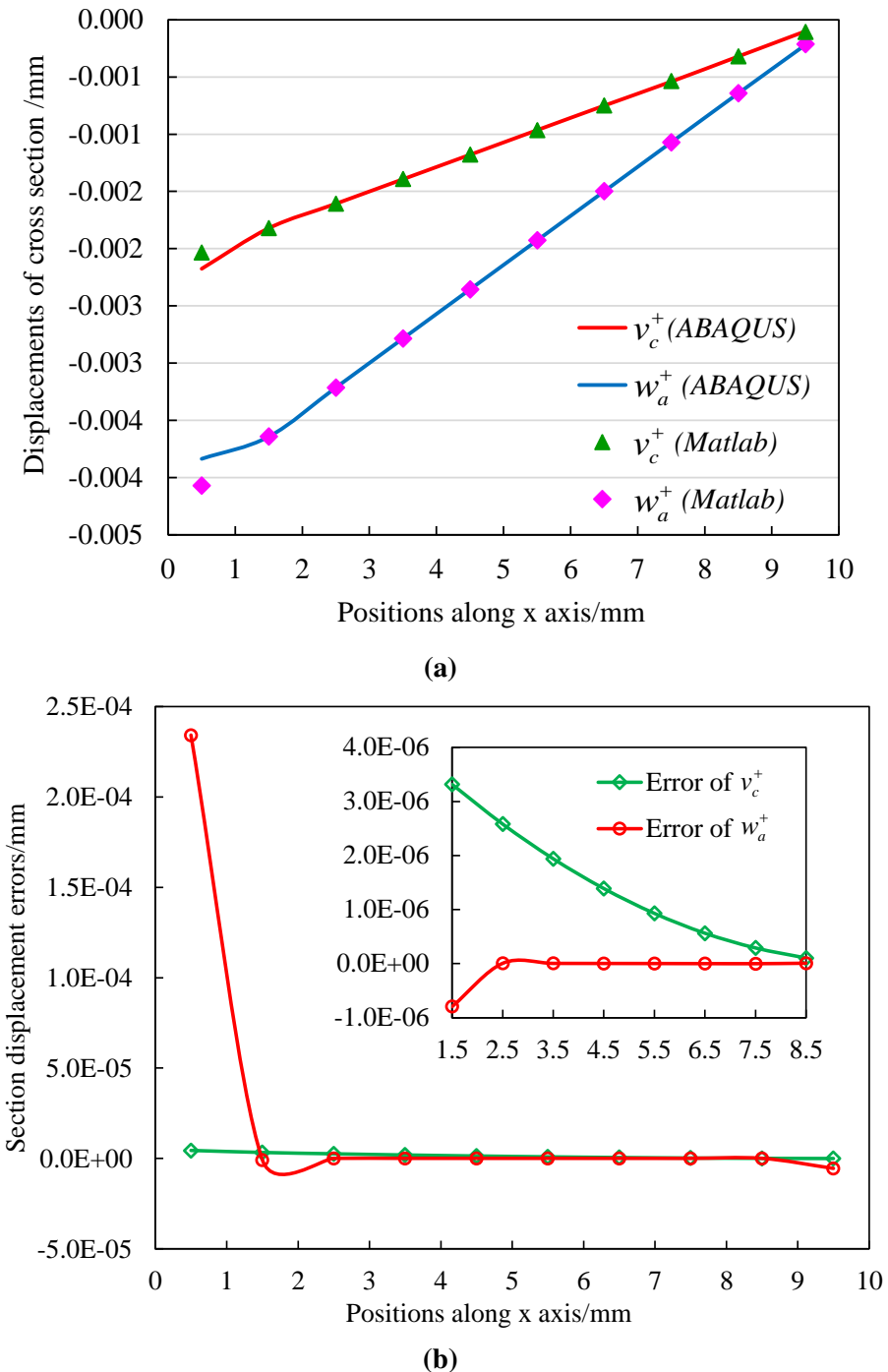


Figure 2.19 – Results comparison of ABAQUS and Matlab. (a). Relative displacement of cross section. (b). Displacement errors of cross section.

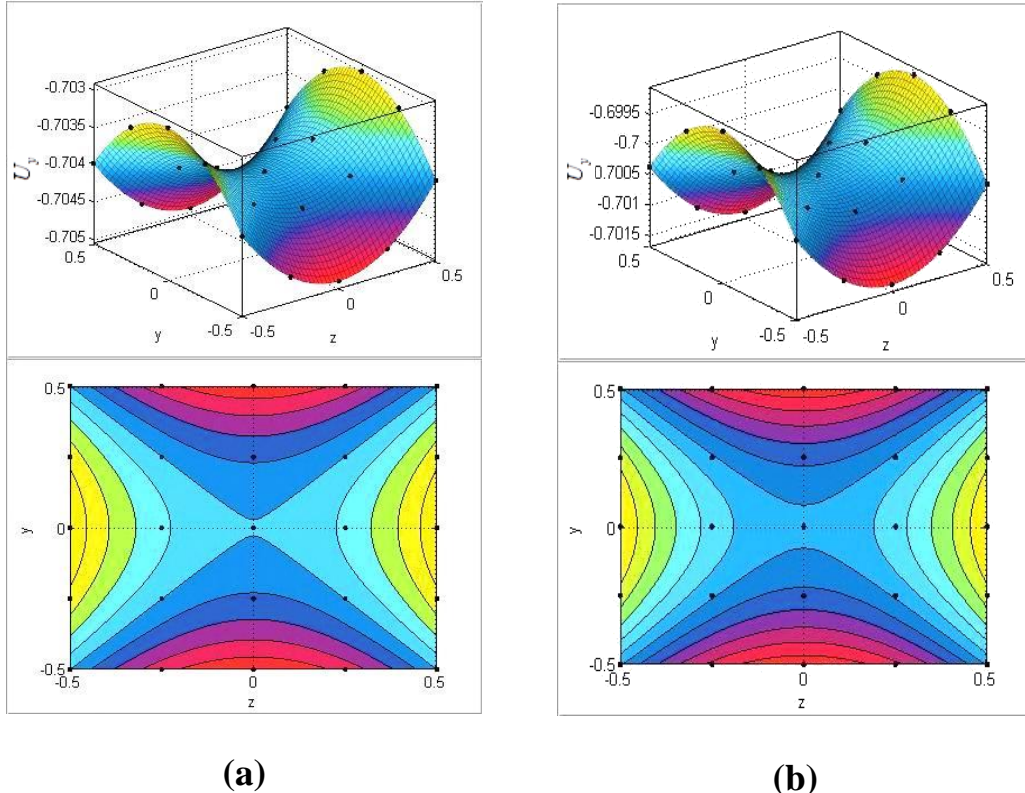


Figure 2.20 – Isovalues of U_y on deformed configuration of cross section at $x=5.5$ mm given by ABAQUS and MATLAB .

2.6.4 Transverse compression

Here, we consider a cantilever beam subjected to a uniformly distributed load $Q=50\text{N/mm}$ to demonstrate the ability of 3D beam element to simulate the section deformation occurring under the action of compression. The calculation model in Matlab is shown as Figure 2.21. For the proposed 3D beam element, we set the same boundary conditions, actually only the mid-line is fixed. For simulation in ABAQUS, much more elements in transverse direction are needed with the discretization shown in Figure 2.11(b) to simulate the same example. In order to set the same boundary conditions to compare the results of solid element and proposed elements, we take 1/4 of beam model in ABAQUS and set the symmetric boundary conditions. Under the action of compression, we can obtain the conclusions: $v_c^+ = -v_c^-$, $v_a^+ = v_b^+$, $w_c^+ = -w_c^-$, $w_a^+ = w_d^+$, and the values of v_c^+ , v_a^+ , w_c^+ , w_a^+ are constant along the positions of x axis, the results are listed in Table 2.2. From which, it can be seen that the proposed 3D beam elements can be used to obtain the same results as those given by solid elements in ABAQUS. Such results show, if needed, that the 8 extra degrees of freedom are sufficient to introduce the coupling between ϵ_{yy} and ϵ_{zz} .

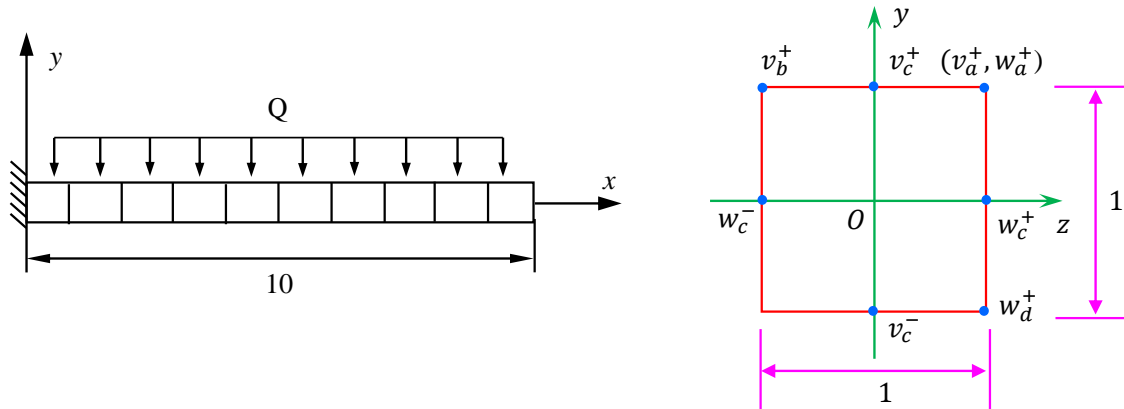


Figure 2.21 – Cantilever under transverse compression.

Table 2.2 – Cross section deformation comparison of results from ABAQUS and Matlab under transverse compaction

	v_c^+	v_a^+	w_c^+	w_a^+
Abaqus(mm)	-0.00011905	-0.00011905	0.00003571	0.00003571
Matlab(mm)	-0.00011905	-0.00011905	0.00003571	0.00003571

2.6.5 Torsion

Here, the cantilever beam is subjected by constant torsion moment $T=500$ Nmm, the calculation model is shown in Figure 2.22. Boundary conditions are $u_{x1} = u_{y1} = u_{z1} = \alpha_{x1} = \alpha_{y1} = \alpha_{z1} = 0$. For the beam elements in Abaqus, we meet the same question as pure bending that the beam element can't bear the torsion directly, so we apply a force couple at the end cross section of the beam instead. When cantilever under action of torsion, there is $\epsilon_{yy} = 0$, $\epsilon_{zz} = 0$. By solving the calculation model in Matlab, we can obtain some conclusions such as $v_c^+ = v_c^- = v_a^+ = v_b^+ = 0$, $w_c^+ = w_c^- = w_a^+ = w_d^+ = 0$.

Compared with the results in Abaqus, it's true that the cross sections just rotate an angle around x axis, there's no relative displacement in thickness and width direction. The results of displacement in Abaqus will be transferred into rotation angles so that we can compare the difference. The results from both Abaqus and Matlab are listed in Figure 2.23(a), where, we can see that the two results are very similar, the error of rotation angle α_x can be seen in Figure 2.23(b), which shows no big difference.

2.7 The advantages of the new 3D beam compared with solid element

All of our examples are compared with the solid element C3D8I in Abaqus. The element C3D8I has 8 nodes, each node has 3 degrees of freedoms, and the total number of the

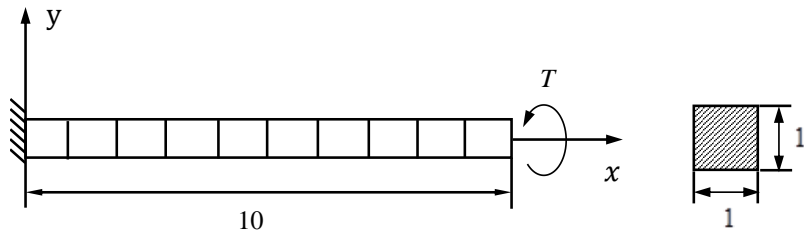


Figure 2.22 – Cantilever under torsion.

degrees of freedoms is 24. It adopts reduced integration with 1 integration point per element. In order to obtain the accurate results, in each layer, at least four elements are needed. In this way, the total degrees of freedoms involved in the calculation is: $(4 \times 4 \times 40) \times 24 = 15360$, while using the new 3D beam, the total degrees of freedoms is: $10 \times 20 = 200$. By using less elements, less degrees of freedoms, we can obtain the same accurate results. This is the largest advantages of the new 3D beam. Since using less degrees of freedoms, the calculation time is assumed to be shorter. But there's some difficulty in comparing the CPU time at the moment since it has many other influence factors. In commercial software Abaqus, it adopts many optimization algorithm, and the new 3D beam element is developed in Matlab, the calculation speed in Matlab can't be the same with Abaqus. Comparison the CPU time is a good idea, maybe after the whole work, we can improve and optimize algorithm, then compare the CPU time of the two calculation methods.

2.8 Conclusions and developments

In this chapter, a new 3D beam element with deformable section has been proposed. It was inspired by the evolution of an enriched shell element that has been firstly introduced in a 2D beam element in order to validate the interest of such technique. The new beam element is an evolution of a 2 nodes Timoshenko beam element with an extra node at mid length. That extra node allows the introduction of 3 extra strain components: ϵ_{yy} , ϵ_{zz} and $2\epsilon_{yz}$ so that full 3D stress/strain constitutive relations can be used. For that, 8 degrees of freedom are required. The proposed element has been introduced in a Matlab finite element code and a series of validation cases have been treated and compared with 3D ABAQUS/Standard simulations. The results obtained are in good agreement and encouraging.

The results presented in this chapter are only the first step of a more ambitious work. Indeed, the final goal is to use those elements to model yarns in a textile composite pre-form. For that purpose, the two following steps are: (1) carrying out validation for large displacements/small strains; (2) introducing contract between 3D beam to beam in the next chapters.

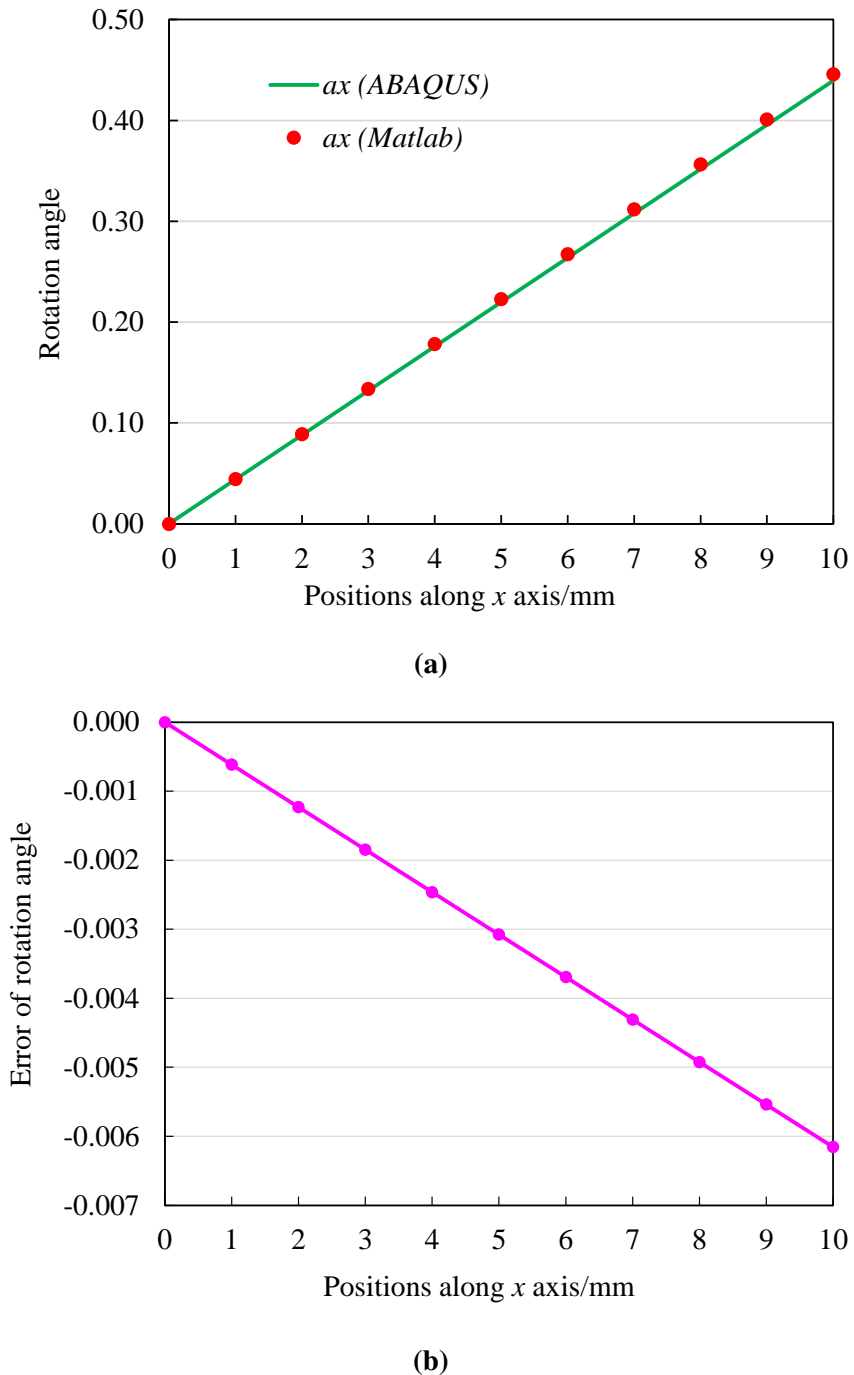


Figure 2.23 – Rotation angle comparisons with ABAQUS and MATLAB. (a). Rotation angle α_x . (b). Error of rotation angle α_x .

Chapter 3

Analysis of large displacements/small strains behavior

Modelling fabric process at the mesoscopic (i.e. the yarn) scale can be able to give realistic and physically fabric shape predictions. For that, we proposed a new 3D beam element with section changes while breaking out from classical beam hypothesis, which can describe the compression and shape change of the yarn. The proposed element has been developed into a finite element code using Matlab which is extensively described in the previous chapter. A series of validation cases for linear small strain conditions have been realized and compared with 3D ABAQUS/Standard simulations. However, the results presented before are only the first step of a more ambitious work. The final aim we want to achieve is using these elements to model yarns in a textile composite preform. For this purpose, the present chapter aims to carry out validation for large displacements (which also refer to large rotations) and small strains. As previously, we start from 2D beam element, after the validation, then extend it into 3D case.

3.1 Introduction and review of literature

If the rotations are large while the mechanical strains (those that cause stresses) are small, then a large rotation procedure must be used. The development of new and efficient formulations for the nonlinear analysis of beam structures has attracted the study of many researchers in recent years, and different alternative formulation strategies and procedures have been presented to accommodate large rotation capability during the large deformation process [CHU 72, BEL 73, BEL 77, REM 79, BAT 79, PAP 81, WEN 83, MEE 84, HSI 87]. These formulations can be divided into three categories: Total Lagrangian (TL) formulation, Updated Lagrangian (UL) formulation and Corotational (CR) formulation. It should be noted that within the corotating system either a TL or a UL formulation, or even a formulation based on a small deflection theory may be employed. The large number of publications on the nonlinear analysis of beam structures is, at least partially, due to the fact that various kinematic nonlinear formulations can be employed. It seems that large

3. Analysis of large displacements/small strains behavior

rotations in plane frames present no major problem. Hsiao and Hou [HSI 87] introduced a simple and effective corotational formulation of beam element and numerical procedure, which can remove the restriction of small rotations between two successive increments for the large displacement analysis of plane frames using incremental-iterative methods. Unfortunately, the method presented in [HSI 87] cannot be applied to three dimensional frames. The difficulty of obtaining effective solutions is particularly pronounced in the analysis of spatial beam structures; a general three dimensional nonlinear formulation is not a simple extension of a two dimensional formulation, because large rotations in three dimensional analysis are not true vector quantities; that is, they do not comply with the rules of vector operations and the result will in general depend on the order in which the rotations are taken. This point has been thoroughly discussed by Argyris [ARG 75] and Wempner [WEM 69].

The problem of large rotations on space structures has received wide attention in the literature. Many different strategies based on the TL, the UL, or the CR formulations have been reported, those of [BEL 73, BEL 77, ARG 75, WEM 69, RAM 77, HOR 78, BAT 80, HUG 81, ARG 79, SUR 83, HSI 87] being only a small fraction of the total. Hughes and Liu [HUG 81] developed a specialized shell element which can handle arbitrarily large rotations. Argyris has covered the subject of corotational coordinates extensively including a lengthy discourse on the subject of large rotations [ARG 79, ARG 82]. Belytschko et al [BEL 77, BEL 79] have applied corotational formulation to the dynamic analysis of space frames where arbitrarily large rotations can be expected. Horrigmoe and Bergan [HOR 78] have successfully applied a corotational approach to their shell elements. Rankin and Brogan [RAN 86] have introduced a corotational procedure which may enable existing shell element formulations to be used in problems that contain arbitrarily large rotations. Recently, Hsiao [HSI 87] has proposed a motion process for triangular shell elements to remove the restriction of small rotations between two successive increments for nonlinear shell analysis using incremental-iterative methods. The wide range of numerical examples studied in [BEL 73, BEL 77, ARG 75, WEM 69, RAM 77, HOR 78, BAT 80, HUG 81, ARG 79, SUR 83, HSI 87] indicate that the corotation approach, first described by Argyris et al [ARG 64], may be very useful in the analysis of spatial structures containing arbitrarily large rotations. However, most strategies based on the corotational formulation suffer from one inherent drawback: they are restricted to small rotations between two successive load increments during the deformation process. This limitation arises because the incremental nodal rotations are considered to be vector quantities. Although the method introduced in [HSI 87] may remove this restriction for triangular shell elements, unfortunately, this method cannot be applied to the space beam elements, because, unlike the shell elements, the element coordinate of the space beam elements cannot be determined using only nodal coordinates.

In this chapter, we first present the large displacement formulation of the new 3D beam element with section changes. Starting from the basic continuum mechanics virtual work theorem, an updated Lagrangian (U.L.) and a total Lagrangian (T.L.) formulation are presented, which allow very large displacements and rotations, and materially nonlinear conditions. Based on the two methods, an effective numerical method is chosen. Next,

we describe some important aspects pertaining to the formulation, implementation and usage of the element. Finally, we present in this chapter the results of a number of sample analyses that demonstrate the versatility and effectiveness of the element.

3.2 Incremental T.L. and U.L. continuum mechanics formulations

Consider the motion of a body in a fixed Cartesian coordinate frame, as shown in Figure 3.1, in which all kinematic and static variables are defined. The coordinates describing the configuration of the body at time 0 are ${}^0x_1, {}^0x_2, {}^0x_3$, at time t are ${}^tx_1, {}^tx_2, {}^tx_3$ and at time $t + \Delta t$ are ${}^{t+\Delta t}x_1, {}^{t+\Delta t}x_2, {}^{t+\Delta t}x_3$, where the left superscripts refer to the configuration of the body and the subscripts to the coordinate axes. The notation for the displacements of the body is similar to the notation for the coordinates. At time t , the displacements are ${}^tu_i, i = 1, 2, 3$, and at time $t + \Delta t$, the displacements are ${}^{t+\Delta t}u_i, i = 1, 2, 3$. During motion of the body, its volume, surface area, mass density, stresses and strains are changing continuously. The specific mass, area and volume of the body at times 0, t and $t + \Delta t$ are denoted by ${}^0\rho, {}^t\rho$ and ${}^{t+\Delta t}\rho$, ${}^0A, {}^tA$ and ${}^{t+\Delta t}A$ and ${}^0V, {}^tV$ and ${}^{t+\Delta t}V$ respectively.

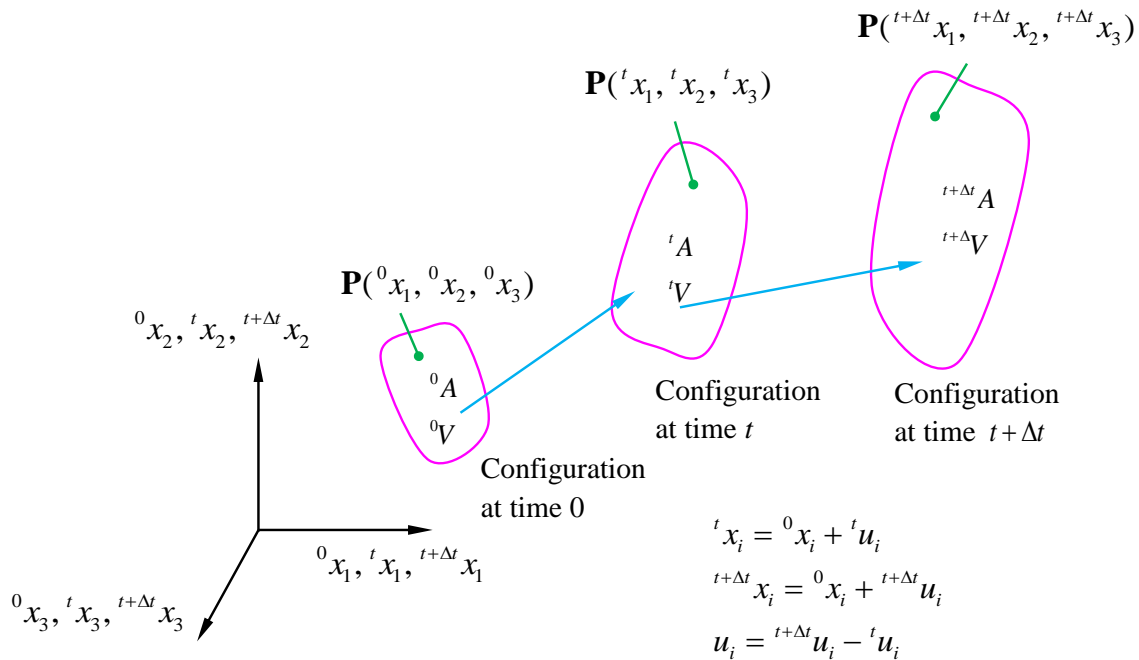


Figure 3.1 – Motion of body in Cartesian coordinate frame [BAT 75].

Consider the large displacement motion of a general body as a function of time and assume that the solutions for the static and kinematic variables are known for the discrete time points, 0, Δt , $2\Delta t, \dots, t$. The basic aim of the analysis is to establish an equation of virtual work from which the unknown static and kinematic variables in the configuration

at time $t + \Delta t$ be solved. Since the displacement-based finite element procedure shall be employed for numerical solution, we use the principle of virtual displacements to express the equilibrium of the body. In this chapter, we present the large displacement formulation of the new 3D beam element. In essence, the large displacement motion of a general body can be considered as a function of time. For example, at time $t + \Delta t$, the equation of the principle of virtual displacements can be expressed as [BAT 75]:

$$\int_{t+\Delta t V}^{t+\Delta t} t^{+\Delta t} \tau_{ij} \delta_{t+\Delta t} e_{ij}^{t+\Delta t} dv = t^{+\Delta t} R \quad (3.1)$$

Where $t^{+\Delta t} R$ is the external virtual work expression:

$$t^{+\Delta t} R = \int_{t+\Delta t A}^{t+\Delta t} t^{+\Delta t} t_k \delta u_k^{t+\Delta t} dA + \int_{t+\Delta t V}^{t+\Delta t} t^{+\Delta t} \rho^{t+\Delta t} f_k \delta u_k^{t+\Delta t} dV \quad (3.2)$$

In Equation (3.1) and (3.2), δu_k is a (virtual) displacement variation measured in the configuration at $t + \Delta t$, $\delta_{t+\Delta t} e_{ij}$ are the corresponding (virtual) strain variations measured in the configuration at $t + \Delta t$, $t^{+\Delta t} t_k$ and $t^{+\Delta t} f_k$ ($k = 1, 2, 3$) are the surface and body force components per unit mass at time $t + \Delta t$ measured in configuration at time $t + \Delta t$, $t^{+\Delta t} \tau_{ij}$ are the Cartesian stresses components of the Cauchy stress tensor at time $t + \Delta t$.

It shows that the Equation (3.1) is a highly non-linear equation in terms of the displacements, which can't be solved directly since the configuration at time $t + \Delta t$ is unknown. A solution can be obtained by referring all variables to a known previously calculated equilibrium configuration. To linearize the equation of the principle of virtual displacements and solve the static and kinematic variables of the body at time $t + \Delta t$, two different formulations can be employed: total Lagrangian (T.L.) formulation and updated Lagrangian (U.L.) formulation [BAT 75, BAT 80], which are presented in the following sections.

3.2.1 Total Lagrangian (T.L.) formulation

For total Lagrangian (T.L.) formulation, all static and kinematic variables are referred to the initial configuration at time $t = 0$, Considering the equilibrium of the body at time $t + \Delta t$, the principle of virtual displacements is expressed as:

$$\int_{0V}^{t+\Delta t} {}_0^t S_{ij} \delta {}_0^{t+\Delta t} \epsilon_{ij}^0 dv = t^{+\Delta t} R \quad (3.3)$$

Where, ${}^{t+\Delta t} {}_0 S$ and ${}^{t+\Delta t} {}_0 \epsilon_{ij}$ are the components of the 2nd Piola-Kirchhoff stress tensor and Green-Lagrange strain tensor in the configuration at time $t + \Delta t$ referred to the initial configuration, which are defined as Equation (3.4) and (3.5), ${}^0 V$ is the initial volume of the body, $t^{+\Delta t} R$ is the external virtual work due to surface tractions and body forces, as defined in Equation (3.6):

$${}^{t+\Delta t} {}_0 S_{ij} = \frac{{}^0 \rho}{t^{+\Delta t} \rho} {}_{t+\Delta t} {}_0 x_{i,k} {}^{t+\Delta t} \tau_{kl} {}_{t+\Delta t} {}_0 x_{j,l} \quad (3.4)$$

$${}^{t+\Delta t}{}_0\boldsymbol{\varepsilon}_{ij} = \frac{1}{2} \left({}^{t+\Delta t}{}_0u_{i,j} + {}^{t+\Delta t}{}_0u_{j,i} + \sum_{k=1}^3 {}^{t+\Delta t}{}_0u_{k,i} {}^{t+\Delta t}{}_0u_{k,j} \right) \quad (3.5)$$

$${}^{t+\Delta t}\boldsymbol{R} = \int_{0A} {}^{t+\Delta t}{}_0t_k \delta u_k {}^0dA + \int_{0V} {}^0\boldsymbol{\rho} {}^{t+\Delta t}{}_0f_k \delta u_k {}^0dV \quad (3.6)$$

Where ${}_{t+\Delta t}{}^0x_{i,j} = \partial^0x_i/\partial^{t+\Delta t}x_j$ and ${}^{t+\Delta t}\boldsymbol{\tau}_{kl}$ are the components of the Cauchy stress tensor at time $t + \Delta t$.

Since the stresses and strains ${}^{t+\Delta t}{}_0S_{ij}$ and ${}^{t+\Delta t}{}_0\boldsymbol{\varepsilon}_{ij}$ are unknown, for solution, the following incremental are used:

$${}^{t+\Delta t}{}_0S_{ij} = {}^t{}_0S_{ij} + {}_0S_{ij} \quad (3.7)$$

$${}^{t+\Delta t}{}_0\boldsymbol{\varepsilon}_{ij} = {}^t{}_0\boldsymbol{\varepsilon}_{ij} + {}_0\boldsymbol{\varepsilon}_{ij} \quad (3.8)$$

Where ${}^t{}_0S_{ij}$ and ${}^t{}_0\boldsymbol{\varepsilon}_{ij}$ are the known 2nd Piola-Kirchhoff stresses and Green-Lagrange strains in the configuration at time t , ${}_0S_{ij}$ and ${}_0\boldsymbol{\varepsilon}_{ij}$ are the 2nd Piola-Kirchhoff stresses and Green-Lagrange strains incremental measured in the initial configuration. It follows from Equation (3.8) that $\delta {}^{t+\Delta t}{}_0\boldsymbol{\varepsilon}_{ij} = \delta {}_0\boldsymbol{\varepsilon}_{ij}$. The strain components can be separated into linear and nonlinear parts:

$${}_0\boldsymbol{\varepsilon}_{ij} = {}_0\boldsymbol{e}_{ij} + {}_0\boldsymbol{\eta}_{ij} \quad (3.9)$$

Where ${}_0\boldsymbol{e}_{ij}$ and ${}_0\boldsymbol{\eta}_{ij}$ are the Cartesian components of the linear and nonlinear strain increments in the initial configuration, respectively.

The constitutive relations ${}_0S_{ij} = {}_0C_{ijrs} {}_0\boldsymbol{\varepsilon}_{rs}$, the approximations ${}_0S_{ij} = {}_0C_{ijrs} {}_0\boldsymbol{e}_{rs}$ and $\delta {}_0\boldsymbol{\varepsilon}_{ij} = \delta {}_0\boldsymbol{e}_{ij}$ are used to transform and linearize Equation (3.3). Finally, Equation (3.3) can be rearranged as:

$$\int_{0V} {}_0C_{ijrs} {}_0\boldsymbol{e}_{rs} \delta {}_0\boldsymbol{e}_{ij} {}^0dV + \int_{0V} {}^t{}_0S_{ij} \delta {}_0\boldsymbol{\eta}_{ij} {}^0dV = {}^{t+\Delta t}\boldsymbol{R} - \int_{0V} {}^t{}_0S_{ij} \delta {}_0\boldsymbol{e}_{ij} {}^0dV \quad (3.10)$$

Where ${}_0C_{ijrs}$ is the component of tangent constitutive tensor at time $t = 0$.

3.2.2 Updated Lagrangian (U.L.) formulation

The updated Lagrangian (U.L.) formulation is based on the same procedures that are used in the T. L. formulation, but in the solution all static and kinematic variables are referred to the last calculated configuration at time t . And, in the U.L. formulation, at time $t + \Delta t$, the equation of the principle of virtual displacements is expressed as:

$$\int_{tV} {}^{t+\Delta t}{}_t\boldsymbol{S} \delta {}^{t+\Delta t}{}_t\boldsymbol{\varepsilon}_{ij} {}^t dV = {}^{t+\Delta t}\boldsymbol{R} \quad (3.11)$$

Where tV is the current volume of the body at time t , ${}^{t+\Delta t}{}_tS$ and ${}^{t+\Delta t}{}_t\epsilon_{ij}$ are the components of the 2nd Piola-Kirchhoff stress tensor and Green-Lagrange strain tensor referred to the initial configuration at time t , which are defined by Equations (3.7) and (3.8) respectively, if the superscript and subscript "0" is replaced by " t " and displacements are measured in the configuration at time t . In the U.L. formulation, the same incremental stress and strain decompositions as in the T.L. formulation are employed, but all variables are referred to the configuration at time t . Thus, corresponding to Equation (3.11), the linearized equilibrium equation is in the U.L. formulation:

$$\int_{{}^tV} {}^tC_{ijrs} {}_t\epsilon_{rs} \delta_t \epsilon_{ij} {}^t dV + \int_{{}^tV} {}^t\tau_{ij} \delta_t \eta_{ij} {}^t dV = {}^{t+\Delta t}R - \int_{{}^tV} {}^t\tau_{ij} \delta_t \epsilon_{ij} {}^t dV \quad (3.12)$$

Where ${}^t\tau_{ij}$ is the Cartesian components of the Cauchy stress tensor at time t , ${}_t\epsilon_{ij}$ and ${}_t\eta_{ij}$ are the Cartesian components of the linear and nonlinear strain increments, respectively. ${}_tC_{ijrs}$ is the components of tangent constitutive tensor at time t relating small strain increments to the corresponding stress increments.

3.3 Calculation formulation chosen

3.3.1 U.L. and T.L. formulations of general 3D beam element

The general three dimensional straight beam element is formulated based on the continuum mechanics theory summarized above. The element has two nodes with 6 degrees of freedom per node, and can transmit axial force, shear forces, bending moments and torque. In Equations (3.10) and (3.12), the incremental equilibrium equations of a body in motion are given corresponding to the global coordinate frame ${}^tX_i(\tau = 0, t)$. Considering a typical beam element, it is more effective to first evaluate the finite element matrices corresponding to the local principal axes ${}^t x_i$, as shown in Figure 3.2, and then transform the resulting matrices to correspond to the global Cartesian coordinate axes prior to the element assemblage process [BAT 76]. The finite element matrices corresponding to the axes ${}^t x_i$ are simply obtained by measuring all static and kinematic quantities in this coordinate system. Thus, using Equations (3.10), we can obtain the T.L. formulation considering a single beam element for static analysis:

$$({}^t_0\mathbf{K}_L + {}^t_0\mathbf{K}_{NL})\mathbf{U} = {}^{t+\Delta t}\mathbf{R} - {}^t_0\mathbf{F} \quad (3.13)$$

Where ${}^t_0\mathbf{K}_L$ is linear strain stiffness matrices, ${}^t_0\mathbf{K}_{NL}$ is nonlinear strain stiffness matrices; ${}^{t+\Delta t}\mathbf{R}$ is the vector of externally applied element nodal loads at time $t + \Delta t$, ${}^t_0\mathbf{F}$ is vectors of nodal point forces equivalent to the element stresses at time t and \mathbf{U} is the vector of incremental nodal displacements.

In Equation (3.13), ${}^t_0\mathbf{K}_L\mathbf{U}$, ${}^t_0\mathbf{K}_{NL}\mathbf{U}$ and ${}^t_0\mathbf{F}$ are obtained from the finite element evaluation of $\int_{{}^tV} {}^t_0C_{ijrs} {}_0\epsilon_{rs} \delta_0 \epsilon_{ij} {}^0 dV$, $\int_{{}^tV} {}^t_0S_{ij} \delta_0 \eta_{ij} {}^0 dV$ and $\int_{{}^tV} {}^t_0S_{ij} \delta_0 \epsilon_{ij} {}^0 dV$ respectively. The vector ${}^{t+\Delta t}\mathbf{R}$ is obtained from the finite element evaluation of Equation (3.6) in the usual way.

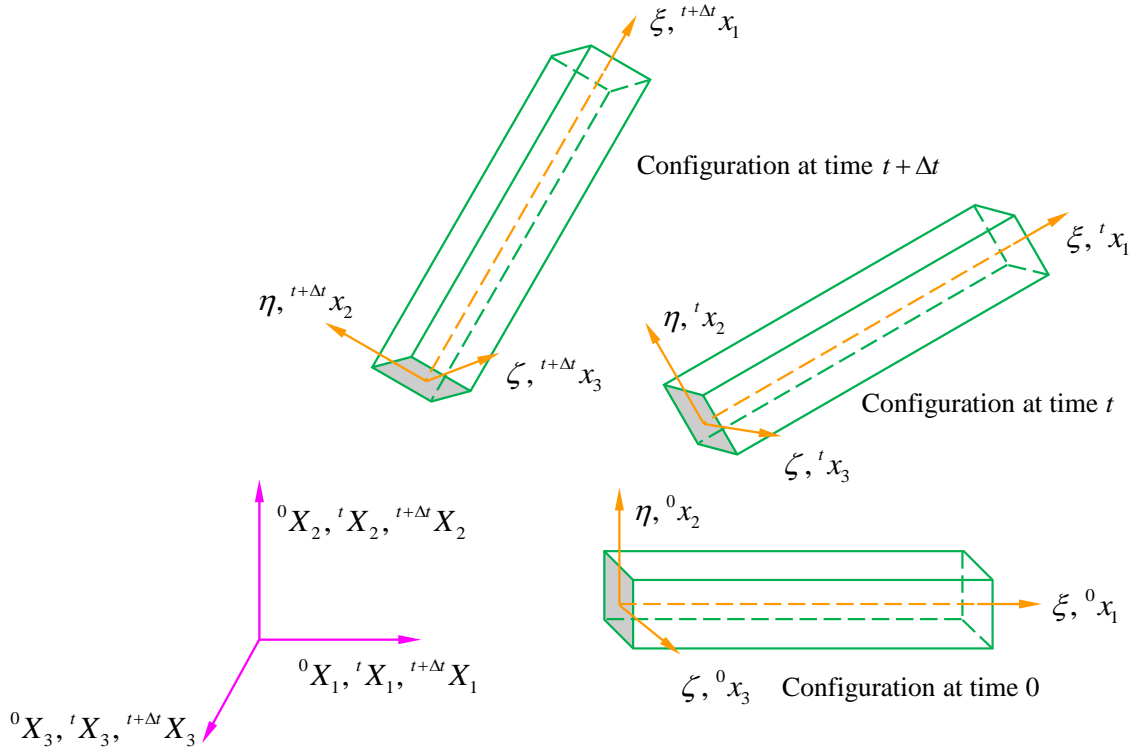


Figure 3.2 – Motion of the 3D beam element and its local coordinate axes shown in global coordinate frame [BAT 76].

$${}^t_0\mathbf{K}_L = \int_{0V} {}^t_0\mathbf{B}_L^T {}_0\mathbf{C}_0^t {}_0\mathbf{B}_L {}^0 dV \quad (3.14)$$

$${}^t_0\mathbf{K}_{NL} = \int_{0V} {}^t_0\mathbf{B}_{NL}^T {}_0\mathbf{S}_0^t {}_0\mathbf{B}_{NL} {}^0 dV \quad (3.15)$$

$${}^t_0\mathbf{F} = \int_{0V} {}^t_0\mathbf{B}_L^T {}_0\hat{\mathbf{S}} {}^0 dV \quad (3.16)$$

In the above equations, ${}^t_0\mathbf{B}_L$ and ${}^t_0\mathbf{B}_{NL}$ are linear and non-linear strain displacement transformation matrices, ${}_0\mathbf{C}$ tangent constitutive matrix, ${}_0\mathbf{S}$ is a matrix of 2nd Piola-Kirchhoff stresses, and ${}_0\hat{\mathbf{S}}$ is a vector of these stresses. All matrix elements correspond to the configuration at time t and are defined with respect to the configuration at time 0.

Similarly, the finite element solution of Equation (2.12), which was obtained using the U.L. formulation, results into:

$$({}^t_0\mathbf{K}_L + {}^t_0\mathbf{K}_{NL})\mathbf{U} = {}^{t+\Delta t}\mathbf{R} - {}^t_0\mathbf{F} \quad (3.17)$$

Where:

$${}^t_0\mathbf{K}_L = \int_{tV} {}^t_0\mathbf{B}_L^T {}_t\mathbf{C}_t^t {}_t\mathbf{B}_L {}^t dV \quad (3.18)$$

$${}^t\mathbf{K}_{NL} = \int_V {}^t\mathbf{B}_{NL}^T {}^t\boldsymbol{\tau} {}^t\mathbf{B}_{NL} {}^t dV \quad (3.19)$$

$${}^t\mathbf{F} = \int_V {}^t\mathbf{B}_L^T {}^t\hat{\boldsymbol{\tau}} {}^t dV \quad (3.20)$$

In Equations (3.18) to (3.20), ${}^t\mathbf{B}_L^T$ and ${}^t\mathbf{B}_{NL}^T$ are the linear and non-linear strain-displacement transformation respectively, ${}^t\mathbf{C}$ is the material property matrix defined with respect to the configuration at time t . ${}^t\boldsymbol{\tau}$ is a Cauchy stress matrix and ${}^t\hat{\boldsymbol{\tau}}$ is a vector of Cauchy stresses in the configuration at time t measured in the configuration at time t . It should be noted that the element matrices in Equations (3.13) to (3.20) are functions of the natural element coordinates and that the volume integrations are performed using a coordinate change from Cartesian to natural coordinates [ZIE 71].

3.3.2 The calculation method chosen

Although the total and updated Lagrangian formulations are superficially quite different, it will be shown that the underlying mechanics of the two formulations are identical; furthermore, expressions in the total Lagrangian formulation can be transformed to updated Lagrangian expressions and vice versa. The major difference between the two formulations is in the point of view: in the total Lagrangian formulation variables are described in the original configuration, in the updated Lagrangian formulation they are described in the current configuration. Different stress and deformation measures are typically used in these two formulations. For example, the total Lagrangian formulation customarily uses a total measure of strain, whereas the updated Lagrangian formulation often uses a rate measure of strain.

An advantage of the T.L. formulation is that the derivatives of the interpolation functions are with respect to the initial configuration, and therefore only need be formed once, if they are stored on back-up storage for use in all load steps. However, in practice, the use of tape or disc to store and retrieve the required derivatives in each step may be more costly than simply to recalculate them. It could be stated in general that, the strain displacement matrix (i.e. the matrix containing the derivatives of the interpolation functions) is more complicated in the Total Lagrangian formulation because the effect of the term involves the initial strain effect.

Various applications of both formulations in the analysis of continuum problems are presented in [BAT 75, CHA 88, FEL 73, SHA 71, STA 06], it shows that both the T.L. and U.L. formulations include all nonlinear effects due to large displacements, large strains and material non-linearities. And the two formulations can give the same numerical results while the constitutive tensors are defined appropriately. Indeed, the choice for a total Lagrangian or an updated Lagrangian formulation should be decided only by the relative numerical effectiveness of the formulations.

In this chapter, in order to simplify the kinematic formulation and obtain a more effective numerical solution, a nonlinear theory of deformation based on the updated Lagrangian method is chosen. The work employs small strain theory on each element like

the corotational technique, and only the unit vectors of the cross sections are employed instead of the complicated three dimensional rotational vectors or angles. The enhanced 3D beam element has been implemented in the Matlab program, and a series of sample analyses are carried out, and the results are systematically compared with the corresponding values of ABAQUS/Standard 3D simulations.

3.4 Properties of isotropic and orthotropic materials

The materials are classified based on the behavior for a particular loading condition, which include: anisotropic materials, isotropic materials, transversely isotropic materials, orthotropic materials and monoclinic materials. In this chapter, we mainly use the isotropic materials and orthotropic materials. In an anisotropic material, there are no planes of material property symmetry. So, there are 21 independent elastic constants in the stress-strain relationship as given in Equation (3.21), and material properties are directionally dependent.

$$\left\{ \begin{array}{l} \sigma_x \\ \sigma_y \\ \sigma_z \\ \tau_{yz} \\ \tau_{zx} \\ \tau_{xy} \end{array} \right\} = \left[\begin{array}{cccccc} C_{11} & C_{12} & C_{13} & C_{14} & C_{15} & C_{16} \\ C_{21} & C_{22} & C_{23} & C_{24} & C_{25} & C_{26} \\ C_{31} & C_{32} & C_{33} & C_{34} & C_{35} & C_{36} \\ C_{41} & C_{42} & C_{43} & C_{44} & C_{45} & C_{46} \\ C_{51} & C_{52} & C_{53} & C_{54} & C_{55} & C_{56} \\ C_{61} & C_{62} & C_{63} & C_{64} & C_{65} & C_{66} \end{array} \right] \left\{ \begin{array}{l} \epsilon_x \\ \epsilon_y \\ \epsilon_z \\ \gamma_{yz} \\ \gamma_{zx} \\ \gamma_{xy} \end{array} \right\} \quad (3.21)$$

Isotropic material:

In an isotropic material, properties are the same in all directions (axial, lateral, and in between). Thus, the material contains an infinite number of planes of material property symmetry passing through a point, i.e., material properties are directionally independent. So, there are two independent elastic constants.

$$\left\{ \begin{array}{l} \sigma_x \\ \sigma_y \\ \sigma_z \\ \tau_{yz} \\ \tau_{zx} \\ \tau_{xy} \end{array} \right\} = \left[\begin{array}{ccccc} C_{11} & C_{12} & C_{12} & 0 & 0 \\ C_{12} & C_{11} & C_{12} & 0 & 0 \\ C_{12} & C_{12} & C_{11} & 0 & 0 \\ 0 & 0 & 0 & \frac{C_{11} - C_{12}}{2} & 0 \\ 0 & 0 & 0 & 0 & \frac{C_{11} - C_{12}}{2} \\ 0 & 0 & 0 & 0 & 0 \end{array} \right] \left\{ \begin{array}{l} \epsilon_x \\ \epsilon_y \\ \epsilon_z \\ \gamma_{yz} \\ \gamma_{zx} \\ \gamma_{xy} \end{array} \right\} \quad (3.22)$$

Tensile normal stresses applied in any direction on an isotropic material cause only elongation in the direction of the applied stresses and contractions in the two transverse directions. It will not produce any shear strain in any form in the material. Similarly, shear stresses produce only corresponding shear strains not normal strains.

Orthotropic materials:

There are three mutually orthogonal planes of material property symmetry in an orthotropic material. Fiber-reinforced composites, in general, contain the three orthogonal planes of material property symmetry and are classified as orthotropic materials. The intersections of these three planes of symmetry are called the principal material directions.

The material behavior is called as special orthotropic, when the normal stresses are applied in the principal material directions. Otherwise, it is called as general orthotropic which behaves almost equivalent to anisotropic material. There are nine independent elastic constants in the stiffness matrix as given below for a special orthotropic material.

$$\left\{ \begin{array}{l} \sigma_x \\ \sigma_y \\ \sigma_z \\ \tau_{yz} \\ \tau_{zx} \\ \tau_{xy} \end{array} \right\} = \left[\begin{array}{cccccc} c_{11} & c_{12} & c_{13} & 0 & 0 & 0 \\ c_{12} & c_{22} & c_{23} & 0 & 0 & 0 \\ c_{13} & c_{23} & c_{33} & 0 & 0 & 0 \\ 0 & 0 & 0 & c_{44} & 0 & 0 \\ 0 & 0 & 0 & 0 & c_{55} & 0 \\ 0 & 0 & 0 & 0 & 0 & c_{66} \end{array} \right] \left\{ \begin{array}{l} \epsilon_x \\ \epsilon_y \\ \epsilon_z \\ \gamma_{yz} \\ \gamma_{zx} \\ \gamma_{xy} \end{array} \right\} \quad (3.23)$$

From the stress-strain relationship it is clear that normal stresses applied in one of the principal material directions on an orthotropic material cause elongation in the direction of the applied stresses and contractions in the other two transverse directions. However, normal stresses applied in any directions other than the principal material directions create both extensional and shear deformations.

3.5 Formulation for large rotations/small strains behavior

3.5.1 Small rotation theory

If the rotations are large but the mechanical strains (those that cause stresses) are small, then a large rotation procedure should be used. In order to simplify the kinematic formulation and obtain a more effective numerical solution, a nonlinear theory of deformation based on the updated Lagrangian method is chosen. Here, we employ small rotation theory at each increment, and then update the rotation vector at the end of each increment. The small rotation theory is shown in Figure 3.3, a vector \vec{V}_n is rotated through $\Delta\vec{\theta}$ to become a vector \vec{V}_{n+1} , we could therefore write:

$$\vec{V}_{n+1} = \vec{V}_n + \Delta\vec{V} = \vec{V}_n + (\Delta\vec{\theta} \wedge \vec{V}_n) \quad (3.24)$$

3.5.2 Motion decomposition of rotation vector

The plane motion of a rigid body can be divided into the translation along with the original point and the rotation around the original point. Under this theory, the movement of vector \vec{AB} can be divided into the translational motion from \vec{AB} to $\vec{A'B'}$ and the rotation from $\vec{A'B'}$ to $\vec{A''B''}$ as shown in Figure 3.4.

$$\begin{aligned}\overrightarrow{B'B'} &= \Delta\vec{\theta} \wedge \overrightarrow{A'B'} \\ \overrightarrow{BB''} &= \overrightarrow{BB'} + \overrightarrow{B'B''} = \overrightarrow{AA'} + \overrightarrow{B'B''} = \vec{u}_A + (\Delta\vec{\theta} \wedge \overrightarrow{A'B'})\end{aligned}\quad (3.25)$$

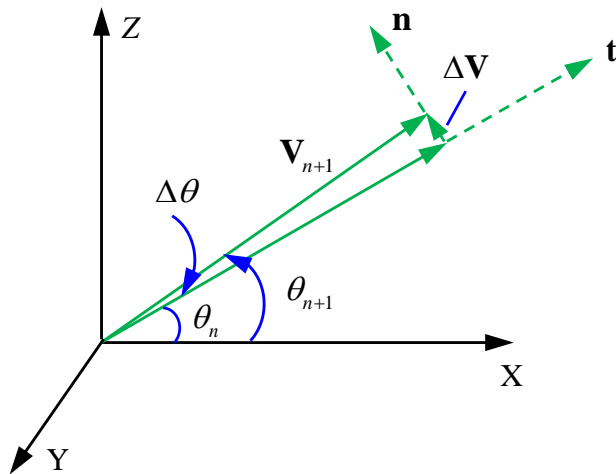


Figure 3.3 – Description of small rotation theory.

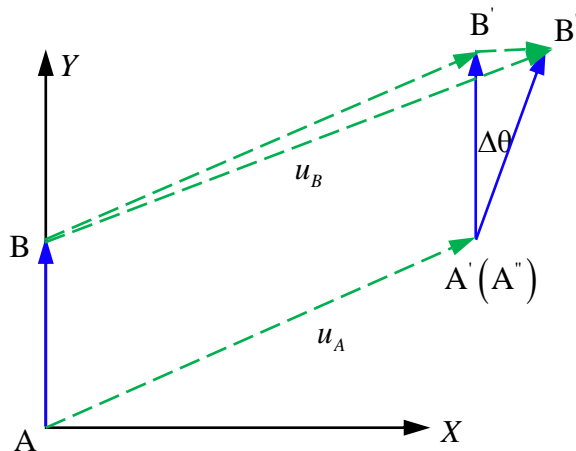


Figure 3.4 – Motion decomposition of rotational vector.

3.5.3 Updated Lagrangian formulation for rotation vector of 2D beam element

Figure 3.5 shows the motion of the rotation vector of 2D beam element and its local coordinate shown in global coordinate frame (${}^tX, {}^tY$), $t = 0, t, t + \Delta t$. Considering a 2D beam element, it is more effective to first evaluate the rotation vector corresponding to the local principal axes (${}^t\eta, {}^t\xi$) of the element, and then transform the results to correspond to the global coordinate frame. According to the theories presented previously, we can obtain the Updated Lagrangian formulation for the rotation vector, which can be expressed as:

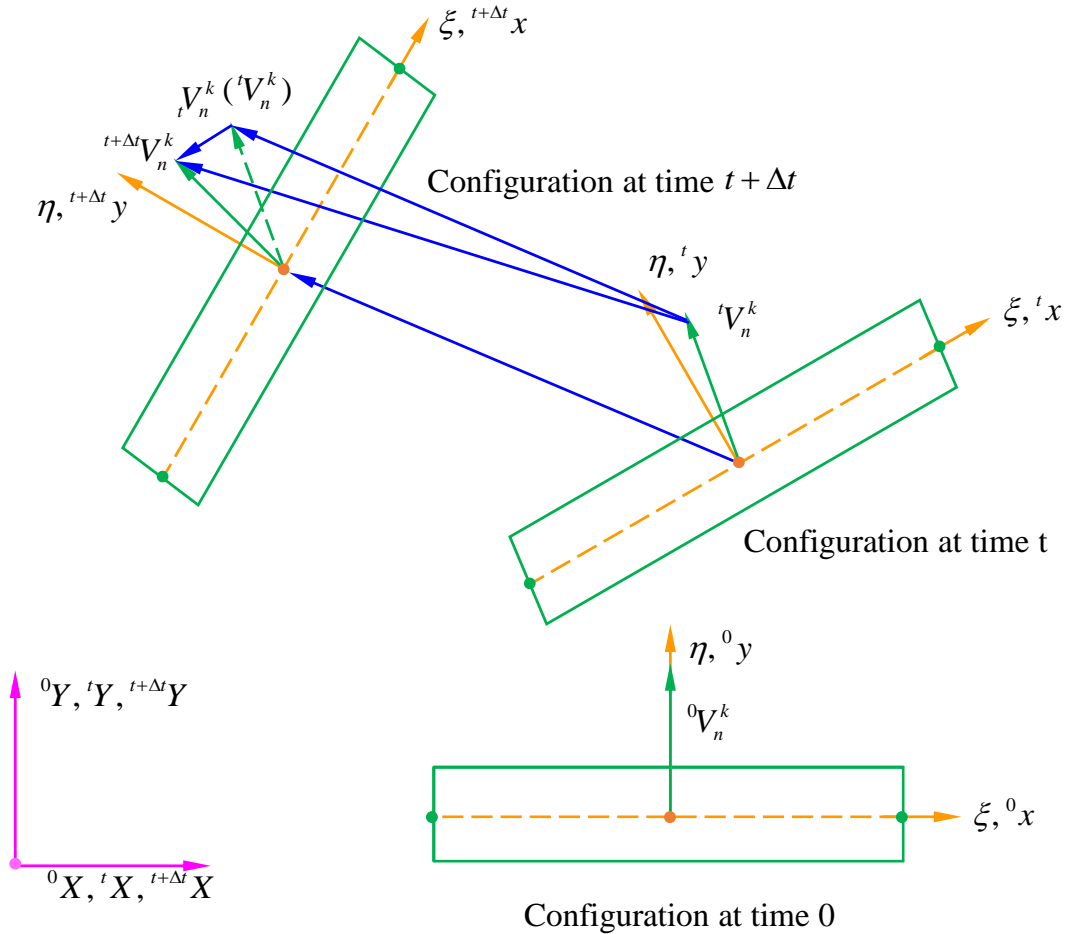


Figure 3.5 – Motion decomposition of rotational vector.

$$\begin{aligned}
 {}^{t+Δt} \vec{V}_n &= {}^t \vec{V}_n + {}_t \vec{V}_n \\
 {}_t \vec{V}_n &= {}_t \vec{\theta} \wedge {}^t \vec{V}_n \\
 {}_t \vec{\theta} &= {}^{t+Δt} \vec{\theta}_n - {}_t \vec{\theta}_n
 \end{aligned} \tag{3.26}$$

Where ${}^{t+Δt} \vec{V}_n$ is the rotation vector \vec{V}_n in the configuration at time $t + \Delta t$ measured

in the configuration at time t , while ${}^t\vec{V}_n^k$ is the rotation vector in configuration at time t referred to the configuration at time t , in fact ${}^t\vec{V}_n^k = {}^t\vec{V}_n^k$. The same notation definitions are used for rotation angle $\vec{\theta}$. In analogy to the notation used for coordinates and displacements, a left superscript indicates in which configuration the quantity (body force, surface traction, stress, ...) occurs while a left subscript indicates with respect to which configuration the quantity is measured.

3.5.4 Incremental displacement field of classical 2D beam

In this way, the incremental displacement field for classical 2D beam can be written by:

$${}_t\vec{u}_B = {}_t\vec{u}_A + {}^t y \cdot ({}_t\vec{\theta} \wedge {}^t\vec{V}_n) \quad (3.27)$$

Where B denotes the point located off the centroidal axis of beam and A is the corresponding point on the centroidal axis. After deformation, due to the effect of shear and torsion, the unit vector ${}^t\vec{V}_n$ will not be vertical, which can be divided into two components ${}^t\vec{V}_{nx}$, ${}^t\vec{V}_{ny}$ in direction of axis ${}^t x$ and ${}^t y$ separately. This is same for ${}_t\vec{u}_A$ and ${}_t\vec{u}_B$. The incremental displacement field can be rewritten as:

$${}_t\vec{u}_B = \begin{cases} {}_t u_{Ax} - {}_t \theta \cdot {}^t y \cdot {}^t V_{ny} \\ {}_t u_{Ay} + {}_t \theta \cdot {}^t y \cdot {}^t V_{nx} \end{cases} \quad (3.28)$$

For classical 2D beam element with two nodes numbered 1 and 2, length is denoted as L . Here, the deformation functions are related to the local coordinate frame $({}^t x, {}^t y)$. The interpolation functions can be expressed as:

$$\begin{aligned} {}_t u_{Ax} &= H_1(\xi) \cdot {}_t u_{1x} + H_2(\xi) \cdot {}_t u_{2x} \\ {}_t u_{Ay} &= H_1(\xi) \cdot {}_t u_{1y} + H_2(\xi) \cdot {}_t u_{2y} \\ {}_t \theta &= H_1(\xi) \cdot {}_t \theta^1 + H_2(\xi) \cdot {}_t \theta^2 \\ {}^t \vec{V}_n &= H_1(\xi) \cdot {}^t \vec{V}_n^1 + H_2(\xi) \cdot {}^t \vec{V}_n^2 \\ {}^t V_{nx} &= H_1(\xi) \cdot {}^t V_{nx}^1 + H_2(\xi) \cdot {}^t V_{nx}^2 \\ {}^t V_{ny} &= H_1(\xi) \cdot {}^t V_{ny}^1 + H_2(\xi) \cdot {}^t V_{ny}^2 \end{aligned} \quad (3.29)$$

Where ${}_t u_{ix}$, ${}_t u_{iy}$, ${}_t \theta^i$ and ${}^t \vec{V}_n^i$ denote the quantities at node i ($i = 1, 2$), $H_1(\xi)$ and $H_2(\xi)$ are interpolation functions, and $H_1(\xi) = 1/2(1 - \xi)$, $H_2(\xi) = 1/2(1 + \xi)$.

At the end of each increment, the unit vector ${}^t \vec{V}_n^i$ will be updated by: ${}^{t+\Delta t} \vec{V}_n^i = {}^t \vec{V}_n^i + ({}^t \vec{\theta} \wedge {}^t \vec{V}_n^i)$.

3.5.5 Incremental displacement field of classical 3D beam

What makes the 3D beam element different from 2D beam element is the number of the unit vectors chosen. For example, a 3D beam element with 2 nodes numbered 1 and 2, two unit vectors \vec{V}_s and \vec{V}_t located in the middle cross section of the element are employed

which can be interpolated by the unit vectors $\vec{V}_s^1, \vec{V}_s^2, \vec{V}_t^1, \vec{V}_t^2$ located at node 1 and node 2 respectively, as shown in Figure 3.6. It presents a 3D Timoshenko beam element with 2 nodes, each node has 6 degrees of freedoms, 3 translations and 3 rotations.

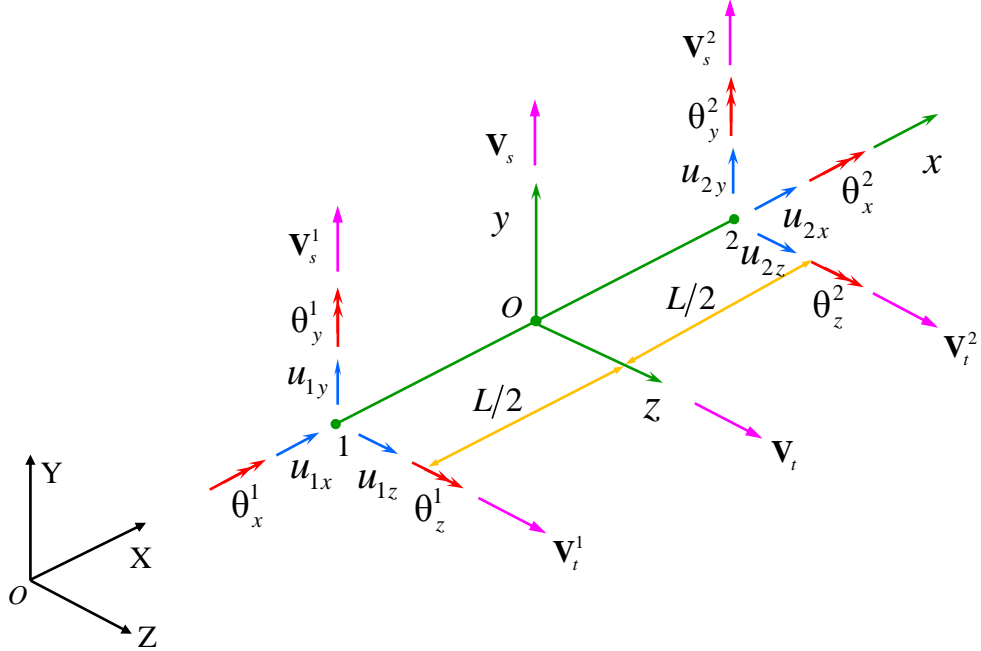


Figure 3.6 – Presentation of the 3D Timoshenko beam element in initial configuration.

$$\begin{aligned}\vec{V}_s &= H_1(\xi) \cdot \vec{V}_s^1 + H_2(\xi) \cdot \vec{V}_s^2 \\ \vec{V}_t &= H_1(\xi) \cdot \vec{V}_t^1 + H_2(\xi) \cdot \vec{V}_t^2\end{aligned}\quad (3.30)$$

Where, $H_1(\xi) = 1/2(1 - \xi)$, $H_2(\xi) = 1/2(1 + \xi)$.

Denoting point B located off the centroidal axis while point A is the corresponding point located on the centroidal axis. The incremental displacement field of classical 3D beam element can be written as:

$${}_t\vec{u}_B = {}_t\vec{u}_A + {}^t y \cdot {}_t\vec{\theta} \wedge {}^t\vec{V}_s + {}^t z \cdot {}_t\vec{\theta} \wedge {}^t\vec{V}_t \quad (3.31)$$

One thing needs to be noticed is that there are different coordinates in the process of derivation, (X, Y, Z) is the global coordinates, (x, y, z) is the local coordinates while (ξ, η, ζ) is the dimensionless local coordinates. After deformation, due to the effect of shear and torsion, the rotation vectors ${}^t\vec{V}_s$ and ${}^t\vec{V}_t$ are not vertical, which can be divided into three components: ${}^t\vec{V}_{tx}, {}^t\vec{V}_{ty}, {}^t\vec{V}_{tz}$, along ${}^t x, {}^t y, {}^t z$ direction respectively. The interpolation functions are in the same form as Equation (3.29).

The incremental displacement field of 3D beam element for large displacement/small strain at each increment can be rearranged as:

$${}^t\vec{u}_B = \begin{cases} {}^t u_{Ax} + \sum_{i=1}^2 \{ H_i \cdot {}^t y \cdot ({}^t \theta_y^i \cdot {}^t V_{sz}^i - {}^t \theta_z^i \cdot {}^t V_{sy}^i) + H_i \cdot {}^t z \cdot ({}^t \theta_y^i \cdot {}^t V_{tz}^i - {}^t \theta_z^i \cdot {}^t V_{ty}^i) \} \\ {}^t u_{Ay} + \sum_{i=1}^2 \{ H_i \cdot {}^t y \cdot ({}^t \theta_z^i \cdot {}^t V_{sx}^i - {}^t \theta_x^i \cdot {}^t V_{sz}^i) + H_i \cdot {}^t z \cdot ({}^t \theta_z^i \cdot {}^t V_{tx}^i - {}^t \theta_x^i \cdot {}^t V_{tz}^i) \} \\ {}^t u_{Az} + \sum_{i=1}^2 \{ H_i \cdot {}^t y \cdot ({}^t \theta_x^i \cdot {}^t V_{sy}^i - {}^t \theta_y^i \cdot {}^t V_{sx}^i) + H_i \cdot {}^t z \cdot ({}^t \theta_x^i \cdot {}^t V_{ty}^i - {}^t \theta_y^i \cdot {}^t V_{tx}^i) \} \end{cases} \quad (3.32)$$

Where ${}^t V_{sx}^i, {}^t V_{sy}^i, {}^t V_{sz}^i, {}^t V_{tx}^i, {}^t V_{ty}^i, {}^t V_{tz}^i$ are the components of ${}^t \vec{V}_s^i$ and ${}^t \vec{V}_t^i$ (located at node i) in ${}^t x, {}^t y, {}^t z$ axis separately, and ${}^t \theta_x^i, {}^t \theta_y^i, {}^t \theta_z^i$ are the components of angle ${}^t \vec{\theta}^i$ rotated by ${}^t x, {}^t y, {}^t z$ axis separately. ${}^t u_{Ax}, {}^t u_{Ay}, {}^t u_{Az}$ are three components of ${}^t u_A$ along axis ${}^t x, {}^t y, {}^t z$. At the end of each increment, the unit vectors ${}^t \vec{V}_s^i$ and ${}^t \vec{V}_t^i$ will be updated by:

$$\begin{aligned} {}^{t+\Delta t} \vec{V}_s^i &= {}^t \vec{V}_s^i + ({}^t \vec{\theta}^i \wedge {}^t \vec{V}_s^i) \\ {}^{t+\Delta t} \vec{V}_t^i &= {}^t \vec{V}_t^i + ({}^t \vec{\theta}^i \wedge {}^t \vec{V}_t^i) \end{aligned} \quad (3.33)$$

3.5.6 Incremental displacement field for enhanced 2D beam elements

In chapter 2, the enhanced 2D beam element has been built by introducing a central node to an initially two nodes element, as shown in Figure 2.6, nodes 1 and 3 have 3 degrees of freedoms $u_i, v_i, \theta^i, (i = 1, 3)$, as nodal variables. For large rotations/ small strains behavior, a unit vector \vec{V}_n , located at node 2 is introduced based on the enhanced 2D beam element, as shown in Figure 3.7, and \vec{V}_n can be interpolated by the unit vectors located at node 1 and node 3 in the form: $\vec{V}_n = H_1(\xi) \cdot \vec{V}_n^1 + H_3(\xi) \cdot \vec{V}_n^3$.

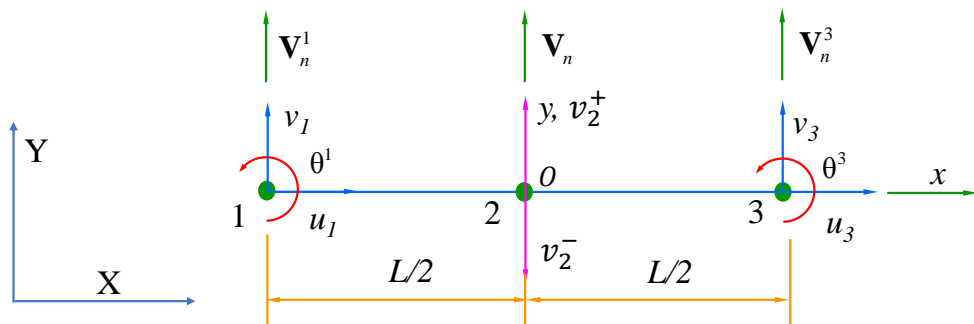


Figure 3.7 – Presentation of the enhanced 2D beam element with large rotation in initial configuration.

After addition of the unit vector \vec{V}_n , the quadratic polynomial $v(x, y)$ in thickness direction will be different from the Equation (2.30), which can be expressed in the following form:

$$v(x, y) = v(x, 0) + \Delta\theta \cdot y \cdot V_{nx} + b_0 y + c_0 y^2 \quad (3.34)$$

Where, b_0 and c_0 are coefficients, which can be solved in terms of nodal variables corresponding to node 2, and $v(x, 0)$ is transverse displacement of the mean axis.

The method to solve the coefficients b_0 and c_0 is the same as described in Section 2.4.1. The final function for $v(x, y)$ can be expressed in terms of nodal variables v_2^+, v_2^- :

$$v(x, y) = v(x, 0) + V_1(y)v_2^+ + V_2(y)v_2^- \quad (3.35)$$

Where, $V_1(y)$ and $V_2(y)$ are shape functions in thickness direction, which can be expressed as:

$$\begin{aligned} V_1(y) &= \frac{y}{h} + \frac{2y^2}{h^2} \\ V_2(y) &= -\frac{y}{h} + \frac{2y^2}{h^2} \end{aligned} \quad (3.36)$$

For convenience of calculations, $V_1(y)$ and $V_2(y)$ should be mapped from the physical coordinate system to the natural coordinate system. So we have the shape function like this:

$$\begin{aligned} V_1(\eta) &= \frac{1}{2}(\eta + \eta^2) \\ V_2(\eta) &= -\frac{1}{2}(\eta - \eta^2) \end{aligned} \quad (3.37)$$

The derivation of shape function $V_1(\eta)$ and $V_2(\eta)$ can be expressed as:

$$\begin{aligned} V'_1(\eta) &= \frac{1}{2}(1 + 2\eta) \\ V'_2(\eta) &= -\frac{1}{2}(1 - 2\eta) \end{aligned} \quad (3.38)$$

Then, the incremental displacement field for the enhanced 2D beam with large rotation/ small strain at each increment can be written as:

$${}^t\vec{u}_B = \begin{cases} {}^t u_x - {}^t \theta \cdot \frac{{}^t h}{2} \eta \cdot {}^t V_{ny} \\ {}^t u_y + V_1 \cdot {}^t v_2^+ + V_2 \cdot {}^t v_2^- \end{cases} \quad (3.39)$$

Defining ${}^t u_{Bx}$ and ${}^t u_{By}$ are two components of the displacement ${}^t \vec{u}_B$ along axis ${}^t x$ and axis ${}^t y$ in configuration at time t respectively. Due to the strain-displacement relation, we can get the incremental strain expression:

$${}^t \bar{\epsilon}_{xx} = \frac{\partial {}^t u_{Bx}}{\partial {}^t x}, {}^t \bar{\epsilon}_{yy} = \frac{\partial {}^t u_{By}}{\partial {}^t y}, 2 {}^t \bar{\epsilon}_{xy} = \frac{\partial {}^t u_{Bx}}{\partial {}^t y} + \frac{\partial {}^t u_{By}}{\partial {}^t x} \quad (3.40)$$

To obtain the displacement derivatives corresponding to the axis ${}^t x$ and ${}^t y$, we need to translate the formulation from dimensionless local coordinates (ξ, η) . We now employ the chain rule and Jacobian transformation, there is:

$$\begin{bmatrix} \frac{\partial_t u_{Bx}}{\partial^t x} & \frac{\partial_t u_{By}}{\partial^t y} \\ \frac{\partial_t u_{Bx}}{\partial^t y} & \frac{\partial_t u_{By}}{\partial^t x} \end{bmatrix} = \begin{bmatrix} \frac{\partial \xi}{\partial^t x} & \frac{\partial \eta}{\partial^t x} \\ \frac{\partial \xi}{\partial^t y} & \frac{\partial \eta}{\partial^t y} \end{bmatrix} \begin{bmatrix} \frac{\partial_t u_{Bx}}{\partial \xi} & \frac{\partial_t u_{By}}{\partial \xi} \\ \frac{\partial_t u_{Bx}}{\partial \eta} & \frac{\partial_t u_{By}}{\partial \eta} \end{bmatrix} = {}^t \mathbf{J}^{-1} \begin{bmatrix} \frac{\partial_t u_{Bx}}{\partial \xi} & \frac{\partial_t u_{By}}{\partial \xi} \\ \frac{\partial_t u_{Bx}}{\partial \eta} & \frac{\partial_t u_{By}}{\partial \eta} \end{bmatrix} \quad (3.41)$$

Where Jacobian matrix ${}^t \mathbf{J}$ contains the derivatives of the current coordinates $({}^t x, {}^t y)$ with respect to the dimensionless local coordinates (ξ, η) , ${}^t J_{ij}^{-1}$ is the element (i, j) of the matrix ${}^t \mathbf{J}^{-1}$:

Substituting Equation (3.41) into (3.40), finally we obtain the incremental strain expression as the following:

$$\begin{aligned} {}^t \bar{\epsilon}_{xx} &= {}^t J_{11}^{-1} \cdot \frac{\partial_t u_{Bx}}{\partial \xi} + {}^t J_{12}^{-1} \cdot \frac{\partial_t u_{Bx}}{\partial \eta} \\ {}^t \bar{\epsilon}_{yy} &= {}^t J_{21}^{-1} \cdot \frac{\partial_t u_{By}}{\partial \xi} + {}^t J_{22}^{-1} \cdot \frac{\partial_t u_{By}}{\partial \eta} \\ {}^t \bar{\epsilon}_{xy} &= {}^t J_{21}^{-1} \cdot \frac{\partial_t u_{Bx}}{\partial \xi} + {}^t J_{22}^{-1} \cdot \frac{\partial_t u_{Bx}}{\partial \eta} + {}^t J_{11}^{-1} \cdot \frac{\partial_t u_{By}}{\partial \xi} + {}^t J_{12}^{-1} \cdot \frac{\partial_t u_{By}}{\partial \eta} \end{aligned} \quad (3.42)$$

Which can be rearranged as:

$$\begin{aligned} {}^t \bar{\epsilon} &= \begin{bmatrix} {}^t \bar{\epsilon}_{xx} \\ {}^t \bar{\epsilon}_{yy} \\ {}^t \bar{\epsilon}_{xy} \end{bmatrix} \\ &= \begin{bmatrix} {}^t J_{11}^{-1} \cdot H'_1 & 0 & {}^t A_1 & 0 & 0 & {}^t J_{11}^{-1} \cdot H'_3 & 0 & {}^t A_3 \\ 0 & {}^t J_{21}^{-1} \cdot H'_1 & 0 & {}^t J_{22}^{-1} \cdot V'_1 & {}^t J_{22}^{-1} \cdot V'_2 & 0 & {}^t J_{21}^{-1} \cdot H'_3 & 0 \\ {}^t J_{21}^{-1} \cdot H'_1 & {}^t J_{11}^{-1} \cdot H'_1 & {}^t B_1 & {}^t J_{12}^{-1} \cdot V'_1 & {}^t J_{12}^{-1} \cdot V'_2 & {}^t J_{21}^{-1} \cdot H'_3 & {}^t J_{11}^{-1} \cdot H'_3 & {}^t B_3 \end{bmatrix} \begin{Bmatrix} {}^t u_1 \\ {}^t v_1 \\ {}^t \theta_1 \\ {}^t v_2^+ \\ {}^t v_2^- \\ {}^t u_3 \\ {}^t v_3 \\ {}^t \theta_3 \end{Bmatrix} \\ &= {}^t \bar{\mathbf{B}} {}^t \mathbf{u} \end{aligned} \quad (3.43)$$

The bar ($\bar{\bullet}$) denotes the qualities (\bullet) measured in the $({}^t x, {}^t y)$ coordinate frame. In this way, ${}^t \bar{\epsilon}$ is the vector of incremental strain, ${}^t \bar{\mathbf{B}}$ is the strain-displacement transformation matrix, and ${}^t \mathbf{u}$ is the vector of incremental nodal displacements, all of which are measured in the $({}^t x, {}^t y)$ coordinate frame.

$$\begin{aligned} {}^t A_i &= -({}^t J_{11}^{-1} \cdot H'_i \cdot \frac{h}{2} \eta \cdot {}^t V_{ny}^i + {}^t J_{12}^{-1} \cdot H_i \cdot \frac{h}{2} \cdot {}^t V_{ny}^i); \quad i = 1, 3 \\ {}^t B_i &= -{}^t J_{21}^{-1} \cdot H'_i \cdot \frac{h}{2} \eta \cdot {}^t V_{ny}^i - {}^t J_{22}^{-1} \cdot H_i \cdot \frac{h}{2} \cdot {}^t V_{ny}^i; \quad i = 1, 3 \end{aligned} \quad (3.44)$$

As mentioned previously, the shear strain remains unchanged except that the usual shear factor is not used directly, so $2_t\bar{\epsilon}_{xy}$ becoming:

$$2_t\bar{\epsilon}_{xy} = {}^t g_{yt} \bar{\gamma}_{xy}, {}^t g_y = \frac{5}{4} \left(1 - 4 \frac{{}^t y^2}{h^2}\right) \quad (3.45)$$

In the U.L. formulations, a transformation matrix ${}^t \mathbf{T}$ that relates displacements measured in the current configuration to displacements measured in the original configuration is needed.

$$\mathbf{U} = {}^t \mathbf{T}^T {}_t \mathbf{u} \quad (3.46)$$

Where \mathbf{U} is the vector of incremental nodal displacements in the global coordinate frame, and the transformation matrix ${}^t \mathbf{T}$ is evaluated using Euler angles which define the rotations of the beam, which will be introduced later.

3.6 Extend to enhanced 3D beam elements with large rotation/ small strain behavior

We have built the enhanced 3D beam element in Chapter 2, a central node with 8 degrees of freedom is introduced to the classical 3D beam element with two end nodes, each node has 6 degrees of freedom ($u_{xi}, u_{yi}, u_{zi}, \theta_{xi}, \theta_{yi}, \theta_{zi}$), as shown in Figure 2.8. For large rotations/ small strains behavior, the difference is that two unit vectors \vec{V}_s and \vec{V}_t of the cross-sections are employed at the position of node 2, which can be interpolated by the unit vectors $\vec{V}_s^1, \vec{V}_s^3, \vec{V}_t^1, \vec{V}_t^3$ located node 1 and node 3.

$$\begin{aligned} \vec{V}_s &= H_1(\xi) \cdot \vec{V}_s^1 + H_3(\xi) \cdot \vec{V}_s^3 \\ \vec{V}_t &= H_1(\xi) \cdot \vec{V}_t^1 + H_3(\xi) \cdot \vec{V}_t^3 \end{aligned} \quad (3.47)$$

Figure 3.8 presents the enhanced 3D beam element with large rotation by introducing two unit vectors \vec{V}_s and \vec{V}_t . As defined previously, (X, Y, Z) is the global coordinates, (x, y, z) is the local coordinates, while ξ, η, ζ is the dimensionless local coordinates. After deformation, the unit vectors \vec{V}_s and \vec{V}_t can be divided into three components $\vec{V}_{sx}, \vec{V}_{sy}, \vec{V}_{sz}$ and $\vec{V}_{tx}, \vec{V}_{ty}, \vec{V}_{tz}$. The interpolation functions are in the same form as Equation (3.29).

Since the unit vectors are introduced, the deformation functions $v(x, y, z)$ and $w(x, y, z)$ is different form Equation (2.46) and (2.47), which are assumed as follows:

$$\begin{aligned} v(x, y, z) &= v(x, 0, 0) + y \cdot (\theta_z \cdot V_{sx} - \{\theta_x \cdot V_{sz}\}) \\ &\quad + z \cdot (\theta_z \cdot V_{tx} - \theta_x \cdot V_{tz}) + a_0 y + a_1 y^2 + a_2 yz + a_3 z^2 \end{aligned} \quad (3.48)$$

$$\begin{aligned} w(x, y, z) &= w(x, 0, 0) + y \cdot (\theta_x \cdot V_{sy} - \theta_y \cdot V_{sx}) \\ &\quad + z \cdot (\theta_x \cdot V_{ty} - \theta_y \cdot V_{tx}) + c_0 z + c_1 z^2 + c_2 yz + c_3 y^2 \end{aligned} \quad (3.49)$$

Where, $a_0, a_1, a_2, a_3, c_0, c_1, c_2, c_3$ are coefficients, which can be solved in terms of nodal variables. The solving methods are the same as described in Section 2.5.2. Finally,

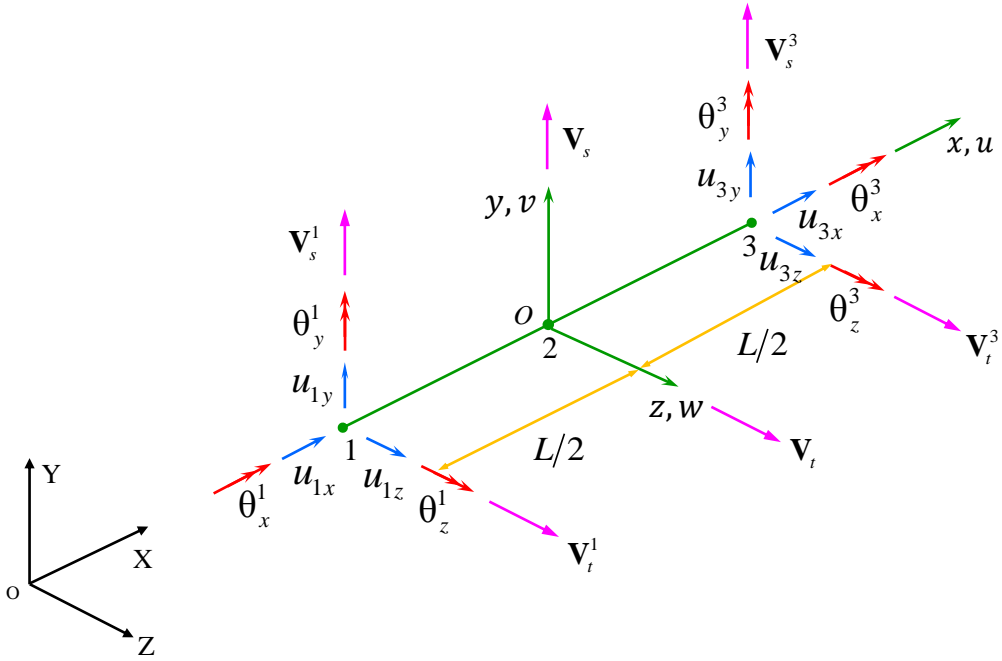


Figure 3.8 – Presentation of the enhanced 3D beam element with large rotation at initial configuration.

we obtain the deformation function in thickness in the dimensionless local coordinates (ξ, η, ζ) :

$$v(x, y, z) = v(x, 0, 0) + \frac{b}{2} \zeta \cdot (1 - \eta) \cdot (\Delta \theta_z \cdot V_{tx} - \Delta \theta_x \cdot V_{tz}) + V_1 v_c^+ + V_2 v_c^- + V_3 v_a^+ + V_4 v_b^+ \quad (3.50)$$

Where:

$$\begin{aligned} V_1 &= \frac{1}{2} (\eta + \eta^2) - \zeta^2, V_2 = -\frac{1}{2} (\eta - \eta^2) \\ V_3 &= \frac{1}{2} (\eta \zeta + \zeta^2), V_4 = -\frac{1}{2} (\eta \zeta - \zeta^2) \end{aligned} \quad (3.51)$$

Similarly, the deformation function in width direction can be expressed as:

$$w(x, y, z) = w(x, 0, 0) + \frac{h}{2} \eta \cdot (1 - \zeta) \cdot (\theta_x \cdot V_{sy} - \theta_y \cdot V_{sx}) + W_1 w_c^+ + W_2 w_c^- + W_3 w_a^+ + W_4 w_d^+ \quad (3.52)$$

Where:

$$\begin{aligned} W_1 &= \frac{1}{2} (\zeta + \zeta^2) - \eta^2, W_2 = -\frac{1}{2} (\zeta - \zeta^2) \\ W_3 &= \frac{1}{2} (\eta \zeta + \eta^2), W_4 = -\frac{1}{2} (\eta \zeta - \eta^2) \end{aligned} \quad (3.53)$$

In the end, the kinematic formulation of the enhanced 3D beam element at each incre-

ment can be written as follows:

$$\begin{aligned} {}^t\vec{u}_B = & \left\{ \begin{array}{l} {}^t u_x + \sum_{i=1}^3 \left\{ H_i \cdot \frac{h}{2} \eta \cdot ({}^t \theta_y^i \cdot {}^t V_{sz}^i - {}^t \theta_z^i \cdot {}^t V_{sy}^i) + H_i \cdot \frac{b}{2} \zeta \cdot ({}^t \theta_y^i \cdot {}^t V_{tz}^i - {}^t \theta_z^i \cdot {}^t V_{ty}^i) \right\} \\ {}^t u_y + \sum_{i=1}^3 \left\{ H_i \cdot \frac{b}{2} \zeta \cdot (1 - \eta) \cdot ({}^t \theta_z^i \cdot {}^t V_{tx}^i - {}^t \theta_x^i \cdot {}^t V_{tz}^i) \right\} + V_{1t} v_c^+ + V_{2t} v_c^- + V_{3t} v_a^+ + V_{4t} v_b^+ \\ {}^t u_z + \sum_{i=1}^3 \left\{ H_i \cdot \frac{h}{2} \eta \cdot (1 - \zeta) \cdot ({}^t \theta_x^i \cdot {}^t V_{sy}^i - {}^t \theta_y^i \cdot {}^t V_{sx}^i) \right\} + W_{1t} w_c^+ + W_{2t} w_c^- + W_{3t} w_a^+ + W_{4t} w_d^+ \end{array} \right\} \end{aligned} \quad (3.54)$$

To obtain the displacement derivatives corresponding to the axis ${}^t x, {}^t y, {}^t z$, we need to translate the formulation from dimensionless local coordinates (ξ, η, ζ) to the local coordinates $({}^t x, {}^t y, {}^t z)$. Defining ${}^t u_{Bx}, {}^t u_{By}, {}^t u_{Bz}$ are three components of the incremental displacement ${}^t \vec{u}_B$ along axis ${}^t x, {}^t y, {}^t z$ respectively. Employing the chain rule and Jacobian transformation, there is :

$$\begin{bmatrix} \frac{\partial {}^t u_{Bx}}{\partial {}^t x} & \frac{\partial {}^t u_{By}}{\partial {}^t x} & \frac{\partial {}^t u_{Bz}}{\partial {}^t x} \\ \frac{\partial {}^t u_{Bx}}{\partial {}^t y} & \frac{\partial {}^t u_{By}}{\partial {}^t y} & \frac{\partial {}^t u_{Bz}}{\partial {}^t y} \\ \frac{\partial {}^t u_{Bx}}{\partial {}^t z} & \frac{\partial {}^t u_{By}}{\partial {}^t z} & \frac{\partial {}^t u_{Bz}}{\partial {}^t z} \end{bmatrix} = {}^t \mathbf{J}^{-1} \begin{bmatrix} \frac{\partial {}^t u_{Bx}}{\partial \xi} & \frac{\partial {}^t u_{By}}{\partial \xi} & \frac{\partial {}^t u_{Bz}}{\partial \xi} \\ \frac{\partial {}^t u_{Bx}}{\partial \eta} & \frac{\partial {}^t u_{By}}{\partial \eta} & \frac{\partial {}^t u_{Bz}}{\partial \eta} \\ \frac{\partial {}^t u_{Bx}}{\partial \zeta} & \frac{\partial {}^t u_{By}}{\partial \zeta} & \frac{\partial {}^t u_{Bz}}{\partial \zeta} \end{bmatrix} \quad (3.55)$$

Due to the strain-displacement relation, we can get the incremental strain expression in local coordinate:

$$\begin{aligned} {}^t \bar{\epsilon}_{xx} &= \frac{\partial {}^t u_{Bx}}{\partial {}^t x} = {}^t J_{11}^{-1} \cdot \frac{\partial {}^t u_{Bx}}{\partial \xi} + {}^t J_{12}^{-1} \cdot \frac{\partial {}^t u_{Bx}}{\partial \eta} + {}^t J_{13}^{-1} \cdot \frac{\partial {}^t u_{Bx}}{\partial \zeta} \\ {}^t \bar{\epsilon}_{yy} &= \frac{\partial {}^t u_{By}}{\partial {}^t y} = {}^t J_{21}^{-1} \cdot \frac{\partial {}^t u_{By}}{\partial \xi} + {}^t J_{22}^{-1} \cdot \frac{\partial {}^t u_{By}}{\partial \eta} + {}^t J_{23}^{-1} \cdot \frac{\partial {}^t u_{By}}{\partial \zeta} \\ {}^t \bar{\epsilon}_{zz} &= \frac{\partial {}^t u_{Bz}}{\partial {}^t z} = {}^t J_{31}^{-1} \cdot \frac{\partial {}^t u_{Bz}}{\partial \xi} + {}^t J_{32}^{-1} \cdot \frac{\partial {}^t u_{Bz}}{\partial \eta} + {}^t J_{33}^{-1} \cdot \frac{\partial {}^t u_{Bz}}{\partial \zeta} \\ 2 {}^t \bar{\epsilon}_{xy} &= \frac{\partial {}^t u_{Bx}}{\partial {}^t y} + \frac{\partial {}^t u_{By}}{\partial {}^t x} \\ &= {}^t J_{21}^{-1} \cdot \frac{\partial {}^t u_{Bx}}{\partial \xi} + {}^t J_{22}^{-1} \cdot \frac{\partial {}^t u_{Bx}}{\partial \eta} + {}^t J_{23}^{-1} \cdot \frac{\partial {}^t u_{Bx}}{\partial \zeta} + {}^t J_{11}^{-1} \cdot \frac{\partial {}^t u_{By}}{\partial \xi} + {}^t J_{12}^{-1} \cdot \frac{\partial {}^t u_{By}}{\partial \eta} + {}^t J_{13}^{-1} \cdot \frac{\partial {}^t u_{By}}{\partial \zeta} \\ 2 {}^t \bar{\epsilon}_{xz} &= \frac{\partial {}^t u_{Bx}}{\partial {}^t z} + \frac{\partial {}^t u_{Bx}}{\partial {}^t x} \\ &= {}^t J_{31}^{-1} \cdot \frac{\partial {}^t u_{Bx}}{\partial \xi} + {}^t J_{32}^{-1} \cdot \frac{\partial {}^t u_{Bx}}{\partial \eta} + {}^t J_{33}^{-1} \cdot \frac{\partial {}^t u_{Bx}}{\partial \zeta} + {}^t J_{11}^{-1} \cdot \frac{\partial {}^t u_{Bz}}{\partial \xi} + {}^t J_{12}^{-1} \cdot \frac{\partial {}^t u_{Bz}}{\partial \eta} + {}^t J_{13}^{-1} \cdot \frac{\partial {}^t u_{Bz}}{\partial \zeta} \\ 2 {}^t \bar{\epsilon}_{yz} &= \frac{\partial {}^t u_{By}}{\partial {}^t z} + \frac{\partial {}^t u_{Bz}}{\partial {}^t y} \\ &= {}^t J_{31}^{-1} \cdot \frac{\partial {}^t u_{By}}{\partial \xi} + {}^t J_{32}^{-1} \cdot \frac{\partial {}^t u_{By}}{\partial \eta} + {}^t J_{33}^{-1} \cdot \frac{\partial {}^t u_{By}}{\partial \zeta} + {}^t J_{21}^{-1} \cdot \frac{\partial {}^t u_{Bz}}{\partial \xi} + {}^t J_{22}^{-1} \cdot \frac{\partial {}^t u_{Bz}}{\partial \eta} + {}^t J_{23}^{-1} \cdot \frac{\partial {}^t u_{Bz}}{\partial \zeta} \end{aligned} \quad (3.56)$$

The incremental strains of the proposed 3D beam element can be expressed in a simple way:

$${}_t\bar{\boldsymbol{\epsilon}} = {}_t\bar{\mathbf{B}} {}_t\mathbf{u} \quad (3.57)$$

Where,

$${}_t\bar{\boldsymbol{\epsilon}} = \begin{bmatrix} {}_t\bar{\epsilon}_{xx} & {}_t\bar{\epsilon}_{yy} & {}_t\bar{\epsilon}_{zz} & {}_t\bar{\gamma}_{yz} & {}_t\bar{\gamma}_{xz} & {}_t\bar{\gamma}_{xy} \end{bmatrix}^T \quad (3.58)$$

$${}_t\mathbf{u} = \left\{ {}_tu_{1x} \ {}_tu_{1y} \ {}_tu_{1z} \ {}_t\theta_x^1 \ {}_t\theta_y^1 \ {}_t\theta_z^1 \ {}_tv_c^+ \ {}_tv_c^- \ {}_tv_a^+ \ {}_tv_b^+ \right. \\ \left. {}_tw_c^+ \ {}_tw_c^- \ {}_tw_a^+ \ {}_tw_d^+ \ {}_tu_{3x} \ {}_tu_{3y} \ {}_tu_{3z} \ {}_t\theta_x^3 \ {}_t\theta_y^3 \ {}_t\theta_z^3 \right\}^T \quad (3.59)$$

Where ${}_t\bar{\boldsymbol{\epsilon}}$ is the incremental strain vector, ${}_t\bar{\mathbf{B}}$ is the strain-displacement transformation matrix, and ${}_t\mathbf{u}$ is the vector of incremental nodal displacements, all of these quantities are measured in the $({}^tx, {}^ty, {}^tz)$ coordinate frame. Since the explicit form of the expression of matrix gradient ${}_t\bar{\mathbf{B}}$ is very long and it is not presented here, which can be seen in the Appendix A.

As described previously, the usual shear factor is not used directly, and $2{}_t\epsilon_{xy}, 2{}_t\epsilon_{xz}, 2{}_t\epsilon_{yz}$ become:

$$2{}_t\bar{\epsilon}_{xy} = {}^tg_{yt}\bar{\gamma}_{xy}, 2{}_t\bar{\epsilon}_{xz} = {}^tg_{zt}\bar{\gamma}_{xz}, 2{}_t\bar{\epsilon}_{yz} = {}^tg_{zt}\bar{\gamma}_{yz} \\ {}^tg_y = \frac{5}{4}(1 - \eta^2), {}^tg_z = \frac{5}{4}(1 - \zeta^2) \quad (3.60)$$

Since the transverse strain components ${}_t\bar{\epsilon}_{yy}$, ${}_t\bar{\epsilon}_{zz}$ and $2{}_t\bar{\epsilon}_{yz}$ are introduced, the full 3D stress/strain constitutive relations can be used.

The reference coordinate system used in the U.L. formulation is defined by the principal axes of the beam element in the position at time t $({}^tx, {}^ty, {}^tz)$

Therefore, the local stiffness matrix and the nodal point force vector are referred to this coordinate frame. These matrices are transformed to the global coordinate frame using:

$$\begin{aligned} {}_t\mathbf{K} &= {}^t\mathbf{T}^T {}_t\bar{\mathbf{K}} {}^t\mathbf{T} \\ {}_t\mathbf{F} &= {}^t\mathbf{T}^T {}_t\bar{\mathbf{F}} \\ \mathbf{U} &= {}^t\mathbf{T}^T {}_t\mathbf{u} \\ {}^t\mathbf{T} &= {}^t\bar{\mathbf{T}} {}^0\mathbf{T} \end{aligned} \quad (3.61)$$

In Equation (3.61), the bar ($\bar{\bullet}$) denotes the qualities (\bullet) measured in the $({}^tx, {}^ty, {}^tz)$ coordinate frame. ${}_t\mathbf{K}$ and ${}_t\bar{\mathbf{K}}$ are linear strain incremental stiffness matrices measured in global frame and local frame at time t respectively; ${}_t\mathbf{F}$ and ${}_t\bar{\mathbf{F}}$ are vectors of nodal point forces referred to global frame and local frame at time t , \mathbf{U} and ${}_t\mathbf{u}$ are the vector of incremental nodal displacements measured in global and local frame respectively. ${}^t\bar{\mathbf{T}}$ is the transformation matrix relating the coordinate frames $({}^tx, {}^ty, {}^tz)$ and $({}^0x, {}^0y, {}^0z)$, ${}^0\mathbf{T}$ is the transformation matrix that expresses the nodal point displacements measured in the beam local coordinate frame $({}^0x, {}^0y, {}^0z)$ in terms of the global nodal point displacements.

$${}^t\bar{\mathbf{K}}_L = \int_{tV} {}^t\bar{\mathbf{B}}^T {}^t\bar{\mathbf{C}} {}^t\bar{\mathbf{B}}^t dV \quad (3.62)$$

$${}^t\bar{\mathbf{F}} = \int_{tV} {}^t\bar{\mathbf{B}}^T {}^t\hat{\mathbf{T}} {}^t dV \quad (3.63)$$

In Equations (3.62) and (3.63), ${}^t\bar{\mathbf{B}}^T$ is the linear strain-displacement transformation, ${}^t\bar{\mathbf{C}}$ is the material property matrix defined with respect to the configuration at time t , ${}^t\hat{\mathbf{T}}$ is a vector of Cauchy stresses in the configuration at time t , all of these quantities are referred to the coordinate frame $({}^t x, {}^t y, {}^t z)$.

For the enhanced 3D beam, transformation matrix ${}^t\bar{\mathbf{T}}$ is evaluated using Euler angles which define the rotations of the beam. The components of the matrix ${}^t\bar{\mathbf{T}}$ are then constructed from the direction cosines of the axes ${}^t x, {}^t y, {}^t z$ with respect to the axes ${}^0 x, {}^0 y, {}^0 z$. We have:

$${}^t\bar{\mathbf{T}} = \begin{bmatrix} {}^t\bar{\mathbf{T}}_\alpha & 0 & 0 & 0 & 0 \\ 0 & {}^t\bar{\mathbf{T}}_\alpha & 0 & 0 & 0 \\ 0 & 0 & {}^t\bar{\mathbf{T}}_\beta & 0 & 0 \\ 0 & 0 & 0 & {}^t\bar{\mathbf{T}}_\alpha & 0 \\ 0 & 0 & 0 & 0 & {}^t\bar{\mathbf{T}}_\alpha \end{bmatrix} \quad (3.64)$$

Where, ${}^t\bar{\mathbf{T}}_\beta$ is an identity matrix of order 8×8 while ${}^t\bar{\mathbf{T}}_\alpha$ is a matrix of order 3×3 .

The orthogonal matrix, ${}^t\bar{\mathbf{T}}_\alpha$ may be composed in various ways. Here, we shall adopt the usage of three Euler's angles ϕ, θ, ψ , that represent rotations about the x, y, z axes, respectively. For any single rotation about the x, y, z , one may assign as ${}^t\bar{\mathbf{T}}_\alpha$ the following ${}^t\mathbf{T}_\alpha^x(\phi)$, ${}^t\mathbf{T}_\alpha^y(\theta)$ or ${}^t\mathbf{T}_\alpha^z(\psi)$ matrices, respectively:

$$\begin{aligned} {}^t\mathbf{T}_\alpha^x(\phi) &= \begin{bmatrix} 1 & 0 & 0 \\ 0 & \cos\phi & \sin\phi \\ 0 & -\sin\phi & \cos\phi \end{bmatrix} \\ {}^t\mathbf{T}_\alpha^y(\theta) &= \begin{bmatrix} \cos\theta & 0 & -\sin\theta \\ 0 & 1 & 0 \\ \sin\theta & 0 & \cos\theta \end{bmatrix} \\ {}^t\mathbf{T}_\alpha^z(\psi) &= \begin{bmatrix} \cos\psi & \sin\psi & 0 \\ -\sin\psi & \cos\psi & 0 \\ 0 & 0 & 1 \end{bmatrix} \end{aligned} \quad (3.65)$$

However, a generic orthogonal transformation will be composed as a rotation by the angle ψ about the z -axis, followed by a rotation by the angle θ about the y -axis (in its new position x', y', z'), followed by a rotation by the angle ϕ about the x -axis (in its new position x'', y'', z''), see Figure 3.9. Thus, the final resulting system is $\bar{x}, \bar{y}, \bar{z}$. In this case, the orthogonal matrix ${}^t\bar{\mathbf{T}}_\alpha$ takes the form:

$${}^t\bar{\mathbf{T}}_\alpha = {}^t\mathbf{T}_\alpha^x(\phi) \cdot {}^t\mathbf{T}_\alpha^y(\theta) {}^t \cdot \mathbf{T}_\alpha^z(\psi) \quad (3.66)$$

$${}^t\bar{\mathbf{T}}_\alpha = \begin{bmatrix} \cos\theta\cos\psi & \cos\theta\sin\psi & -\sin\theta \\ \sin\phi\sin\theta\cos\psi - \cos\phi\sin\psi & \sin\phi\sin\theta\sin\psi + \cos\phi\cos\psi & \sin\phi\cos\theta \\ \cos\phi\sin\theta\cos\psi + \sin\phi\sin\psi & \cos\phi\sin\theta\sin\psi - \sin\phi\cos\psi & \cos\phi\cos\theta \end{bmatrix} \quad (3.67)$$

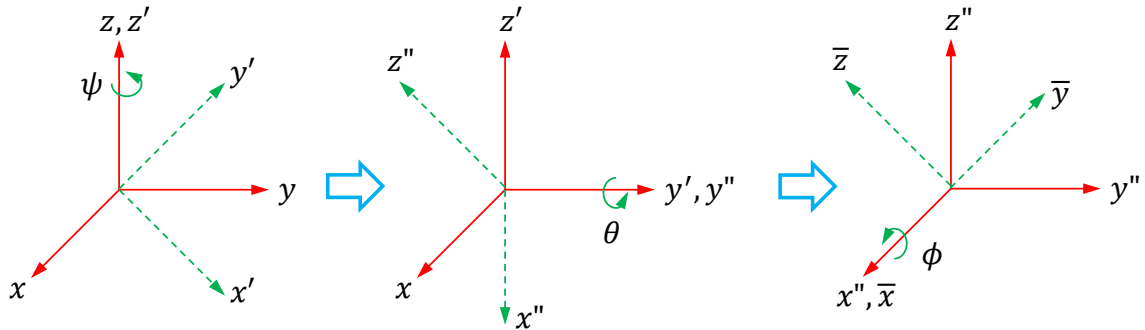


Figure 3.9 – Definition of Euler's angles.

3.7 Numerical studies

The updated Lagrangian-based new 3D beam element was implemented in the computer program MATLAB and a number of numerical examples analyses were carried out, and the results are systematically compared with corresponding values of ABAQUS/Standard 3D simulations. We report here the results of some of the analyses. Since large displacement/ large rotation has nothing to do with the uniaxial tension and pure transverse compression behavior, such as the examples described in section 2.6.1 and section 2.6.4, which won't be listed here. In this chapter, some typical examples are chosen to show the bending, shear and torsion performance with large displacements/ small strains. Two problems were analyzed: first, a moderate displacement analysis of a clamped cantilever with one transverse concentrated end load and two transverse concentrated end loads were carried out respectively; second, a large displacement analysis of a clamped cantilever subjected to two concentrated end forces. In order to verify the general applicability of the new beam element, two materials are used for simulations: isotropic and orthotropic materials.

In these examples, we consider a cantilever beam with length $l = 10\text{mm}$, width $b = 1\text{mm}$ and thickness $h = 1\text{mm}$. The cantilever was modelled using 10 beam elements for calculations as shown in Figure 2.11(a). Then the results are compared with corresponding values from ABAQUS/Standard 3D simulations (using C3D8I element) for calculating the same example. Since for large displacement analysis, the mesh model shown in Figure 2.11(b) can't achieve the calculation accuracy, much more elements are needed, which has $10 \times 10 \times 100 = 10000$ elements.

3.7.1 Large displacement/rotation analysis of a cantilever with isotropic material

In this section, the material was assumed to be linear elastic, material parameters are $E = 1 \times 10^5 \text{ MPa}$, $\nu = 0.3$. A series of examples are carried out to test the new 3D beam element, some of them are reported here.

3.7.1.1 Cantilever bending analysis 1

In this example, we consider a cantilever beam subjected to the action of a concentrated force $F_y = -50\text{N}$ at the right end. Since the concentrated force is in y direction, the displacement in z direction is 0, but there is small displacement in x direction. Figure 3.10 gives the results comparisons of the displacements of centroidal axis, all the unit of the results are expressed in the order of mm (In this thesis, unless specifically mentioned, all the displacements are measured in mm). It can be seen that the two results are almost the same. The biggest displacement in y direction is -1.930 mm using the new 3D beam element while the value is -1.925 mm in ABAQUS. Since the solid element C3D8I doesn't have the rotational degree of freedom, the rotation angle of the centroidal axis around z axis are measured using the FEM code developed in Matlab, which can be seen in Figure 3.11, the maximum rotation angle is about 16.60° . We also compare the displacement distribution of cross section obtained from ABAQUS and Matlab, as shown in Figure 3.12. All the results are in good agreement, Figure 3.12(a) shows the distribution of v_c^+ and v_c^- , there's no big difference between the two results. For v_a^+ and v_b^+ , we observed from the results of both ABAQUS and Matlab, there always exists $v_a^+ = v_b^+$, so only the distribution of v_a^+ is compared, which is shown in Figure 3.12(b), we can see that the two results are consistent. Figure 3.13(a) shows the distribution of w_c^+ and w_c^- , the values are in order of 10^{-5} mm in magnitude, which are small enough to neglect the errors between ABAQUS and Matlab. Finally, the distribution of w_a^+ and w_d^+ is shown in Figure 3.13(b), which also shows good consistent.

3.7.1.2 Cantilever bending analysis 2

The moderate displacement analysis of a clamped cantilever with one transverse concentrated end load doesn't show any big problem. Here, we continue the bending analysis in section 3.7.1.1, the difference is that two transverse concentrated end loads in y direction and z direction respectively are employed at the same time, $F_y = F_z = -50\text{N}$.

Since the concentrated forces are applied in both two transverse directions, from the results obtained from both ABAQUS and Matlab, there's $U_y = U_z$ for the centroidal axis. Figure 3.14 just shows the comparisons of the displacements in x and y directions of centroidal axis, the results are almost the same. The biggest displacement in y direction is -1.866 mm using the new 3D beam element while the value is -1.844 mm in ABAQUS. We also compare the distribution of v_c^+ and v_c^- , v_a^+ and v_b^+ , w_c^+ and w_c^- , w_a^+ and w_d^+ , which can be seen in Figure 3.15 and 3.16. All the results from ABAQUS and Matlab are consistent, which show no big difference.

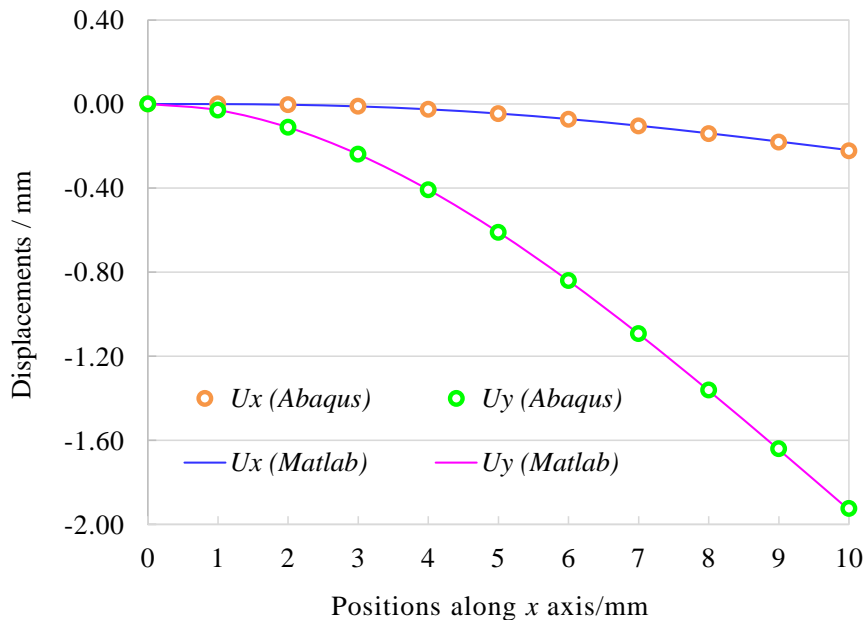


Figure 3.10 – Displacements of the centroidal axis in x and y direction.

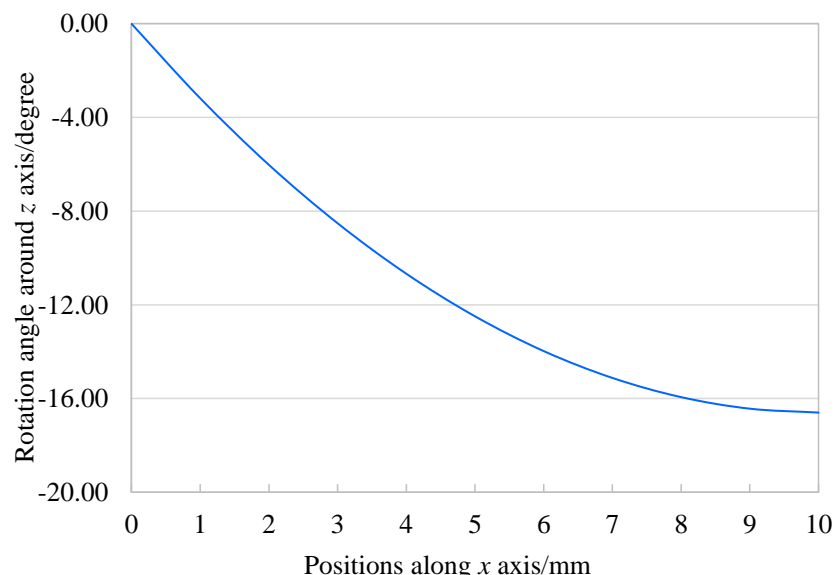


Figure 3.11 – Rotations angles of the centroidal axis around z axis.

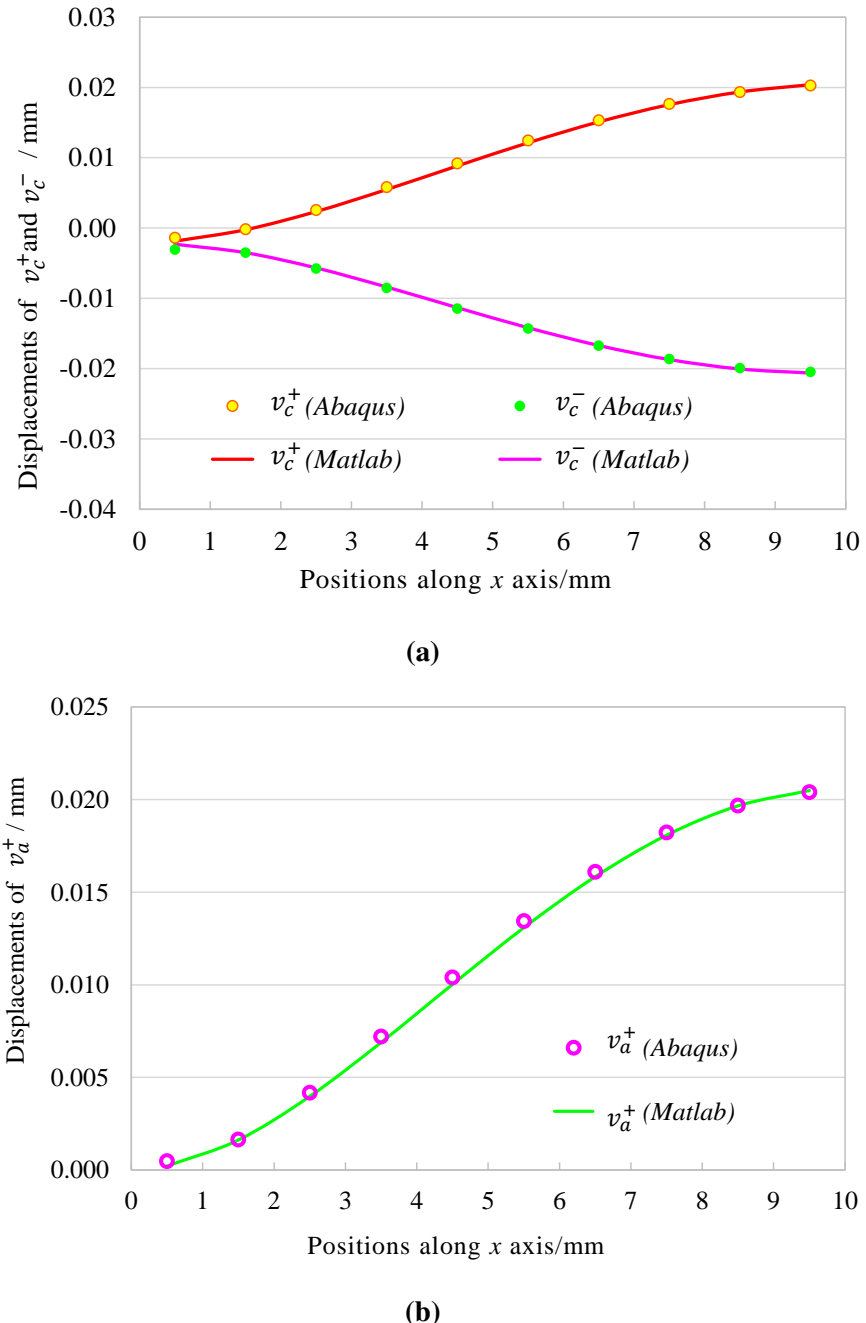


Figure 3.12 – Comparisons of the displacement distribution of cross section. (a). Distribution of v_c^+ and v_c^- . (b). Distribution of v_a^+ .

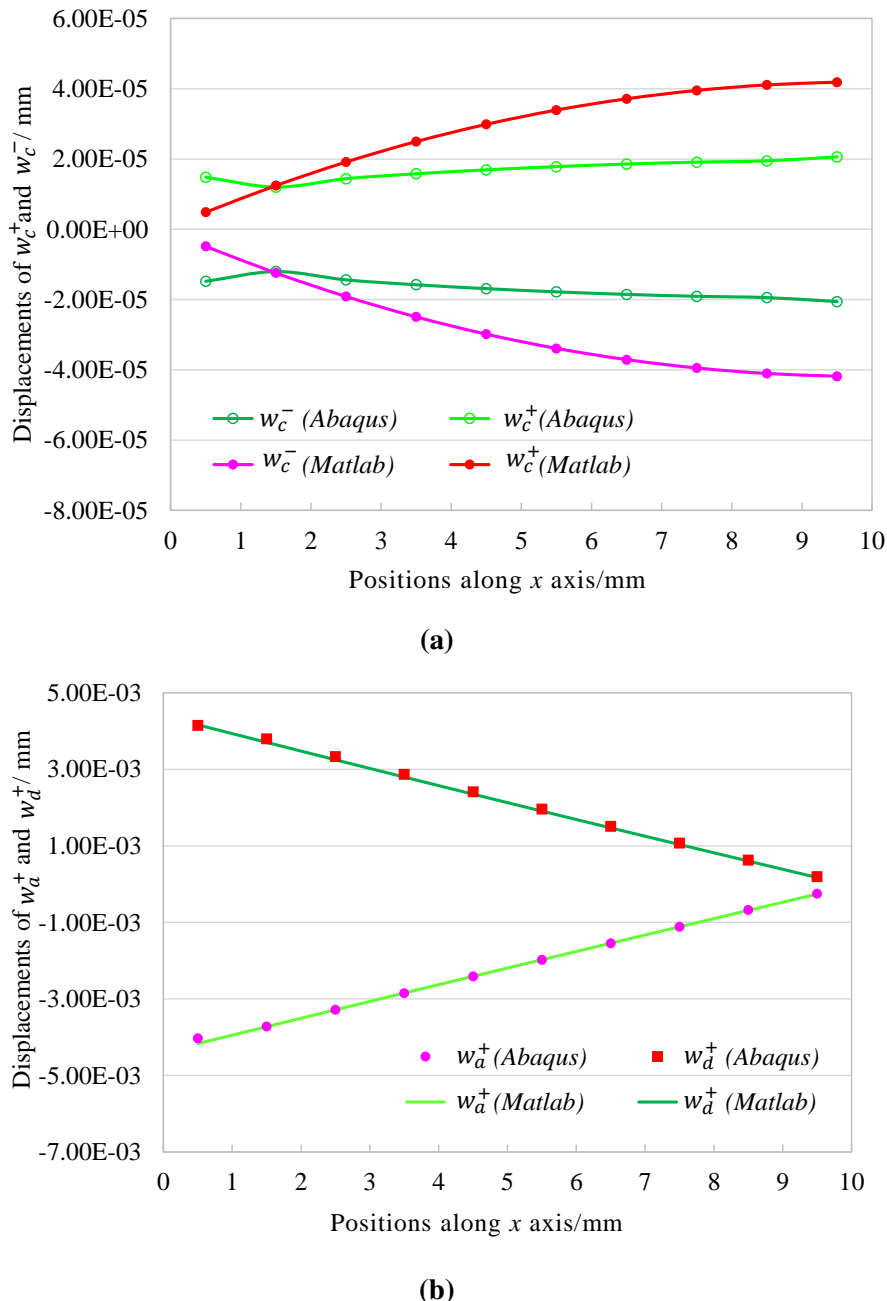


Figure 3.13 – Comparisons of the displacement distribution of cross section. (a). Distribution of w_c^+ and w_c^- . (b). Distribution of w_a^+ and w_d^+ .

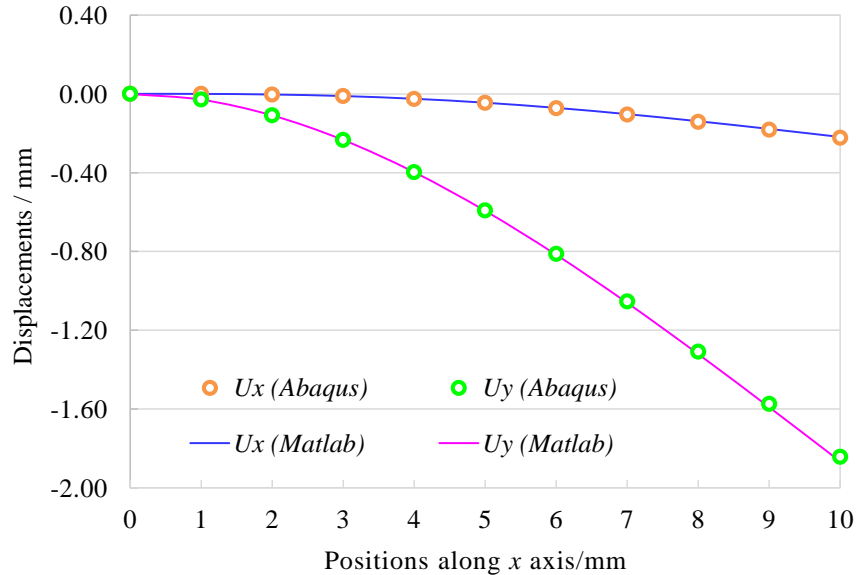


Figure 3.14 – Displacements of the centroidal axis in x and y direction.

3.7.1.3 Cantilever bending analysis 3

The moderate displacement analysis of a clamped cantilever with two transverse concentrated end loads is also in good consistent with the results from ABAQUS. In this example, we continue the bending analysis in section 3.7.1.2, and apply $F_y = F_z = -200N$ simultaneously. Since there exists $U_y = U_z$ for the centroidal axis, it just needs to compare the displacements in x and y directions, which can be seen in Figure 3.17. The biggest displacement in y direction is -4.530 mm using the new 3D beam element while the value is -4.513 mm in ABAQUS. The relative error is of order of 0.38%, which is very small. Figure 3.18 shows the the rotation angle of the centroidal axis around zaxis measured using the FEM code developed in Matlab, the maximum rotation angle is about 43° . Figure 3.19 and 3.20 give the comparisons of the distribution of v_c^+ and v_c^- , $v_a^+ = v_b^+$, w_c^+ and w_c^- , w_a^+ and w_d^+ . For the large displacement analysis, the values are close and the change trend are similar. We use 10000 elements in 3D ABAQUS/Standard simulations while 10 elements are used to solve the same problem. The calculations efficiency has improved greatly. The assumptions of the new 3D beam element is quite different from the solid element C3D8I, it certainly will cause some errors during the calculations, and the relative errors are controlled under 20% .

3.7.2 Large displacement/rotation analysis of a cantilever with orthotropic material

In this section, the material was assumed to be orthotropic, the engineering constants are: $E_1 = 2 \times 10^5 MPa$, $E_2 = E_3 = 1 \times 10^5 MPa$, $\nu_{12} = \nu_{13} = 0.25$, $G_{12} = G_{13} = 5 \times$

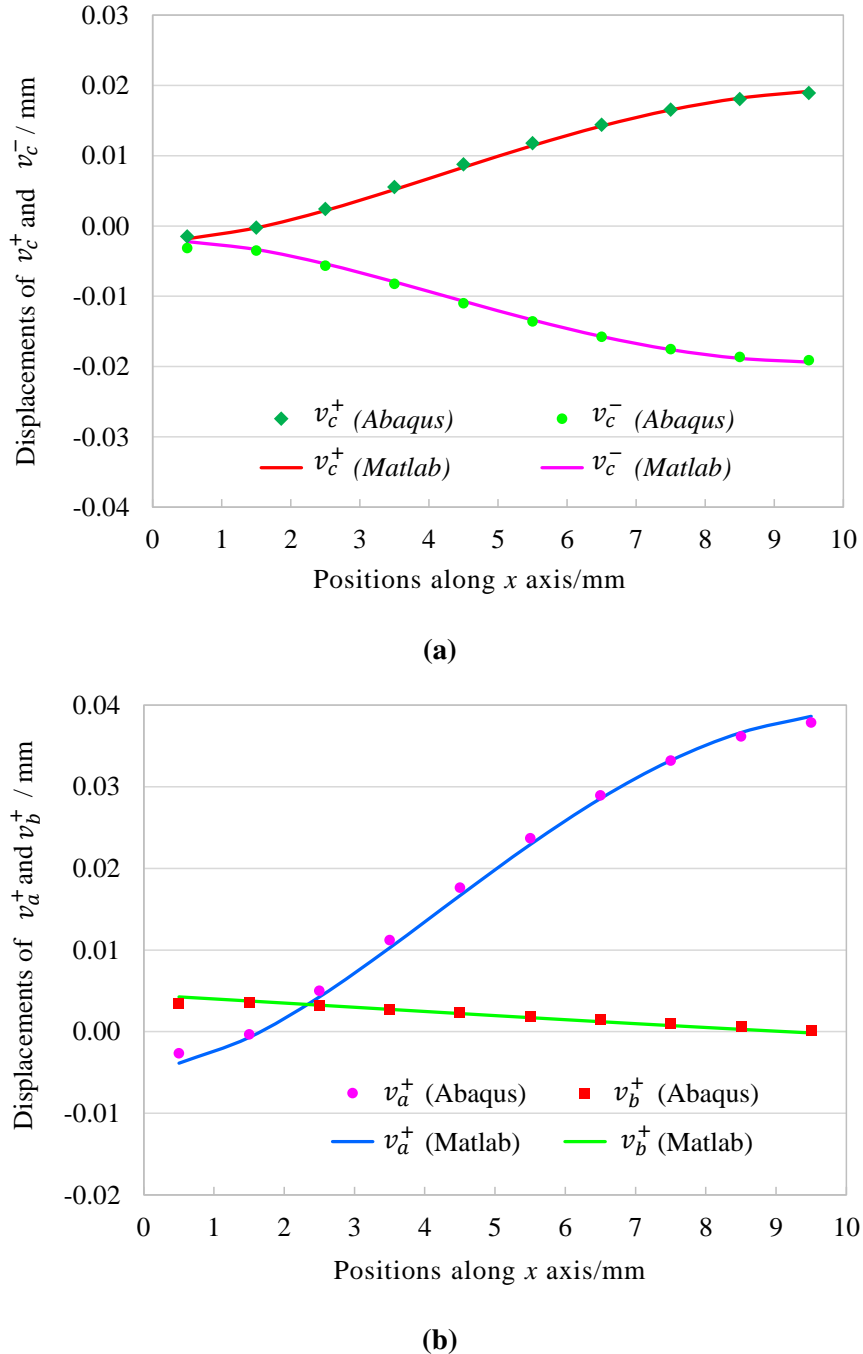


Figure 3.15 – Comparisons of the displacement distribution of cross section. (a). Distribution of v_c^+ and v_c^- . (b). Distribution of v_a^+ and v_b^+ .

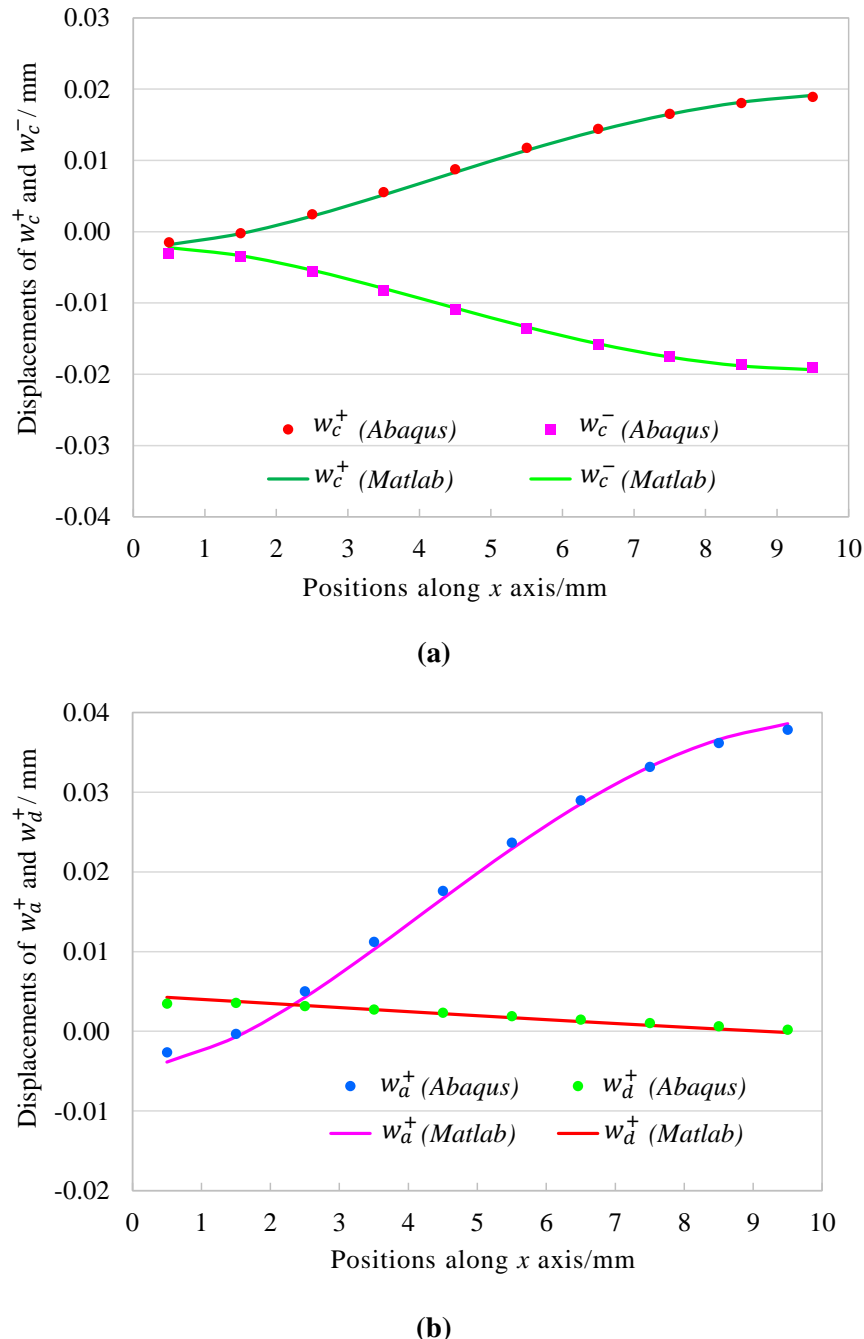


Figure 3.16 – Comparisons of the displacement distribution of cross section. (a). Distribution of w_c^+ and w_c^- . (b). Distribution of w_a^+ and w_d^+ .

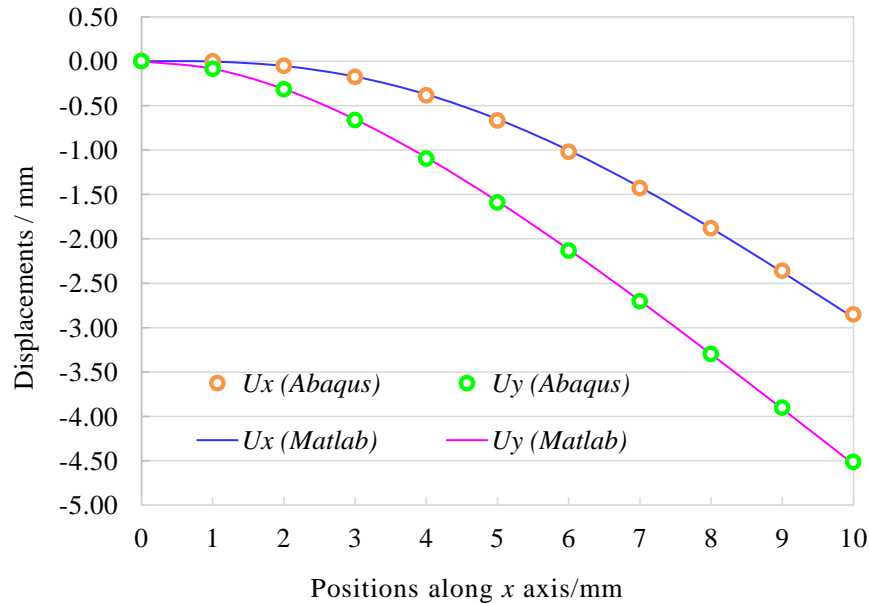


Figure 3.17 – Displacements of the centroidal axis in x and y direction.

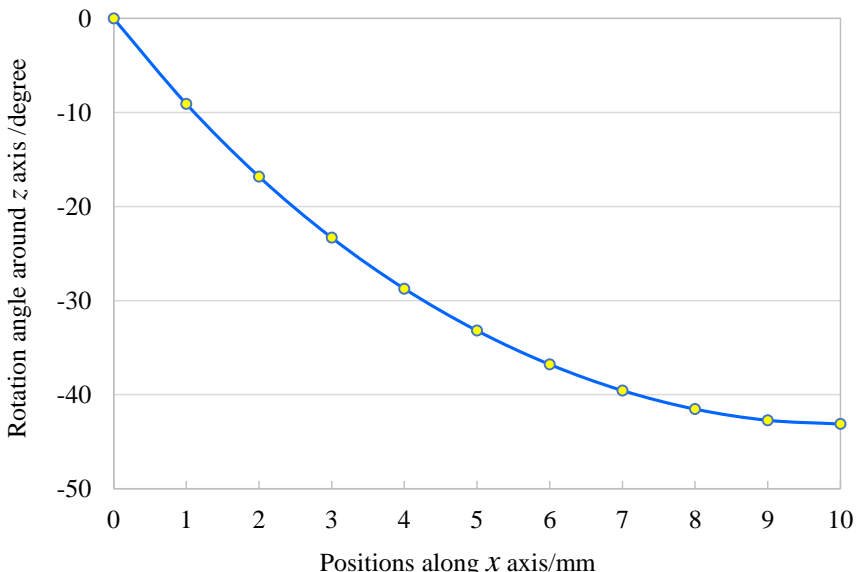


Figure 3.18 – Rotations angles of the centroidal axis around z axis.

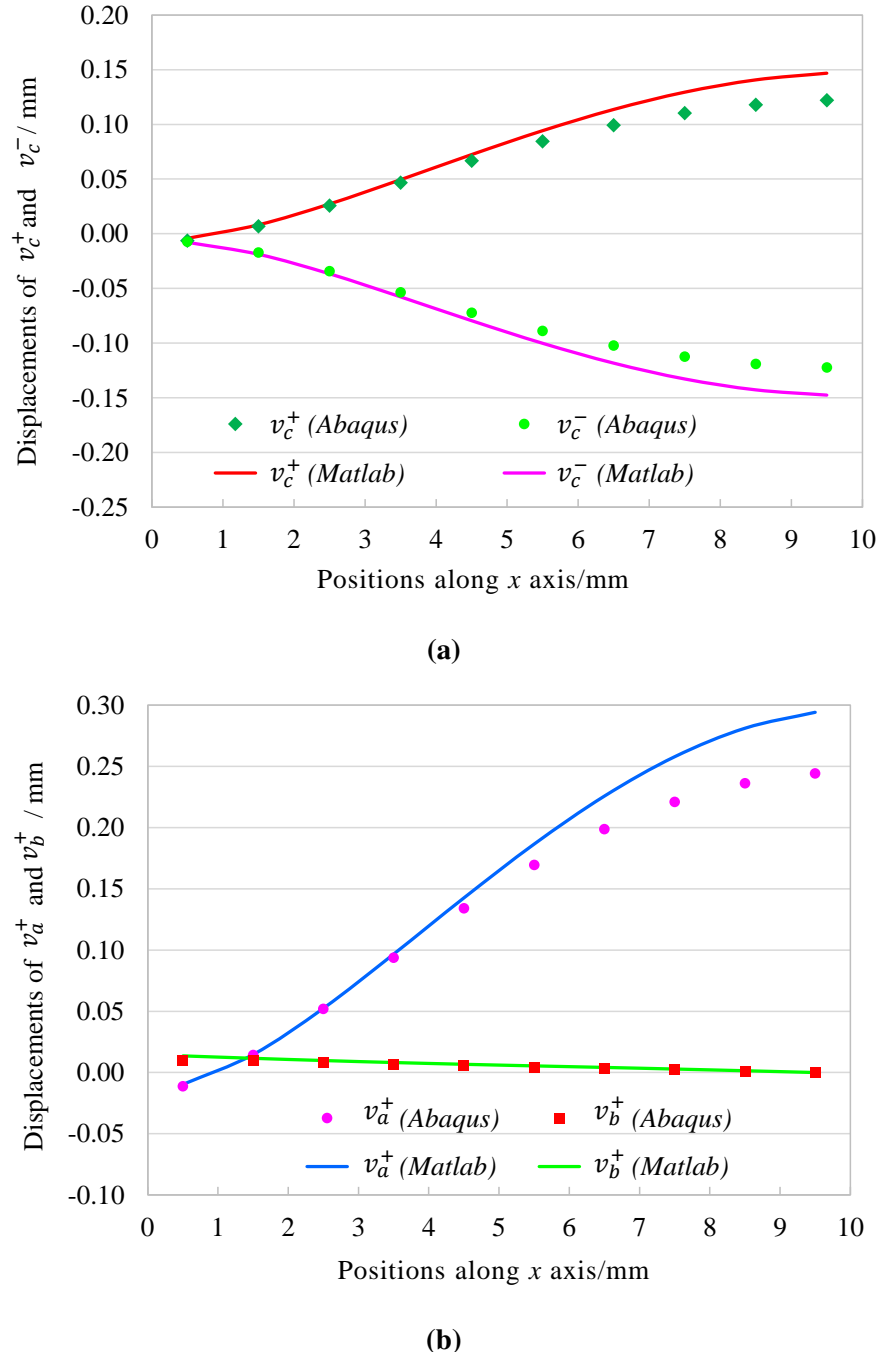


Figure 3.19 – Comparisons of the displacement distribution of cross section. (a). Distribution of v_c^+ and v_c^- . (b). Distribution of v_a^+ and v_b^+ .

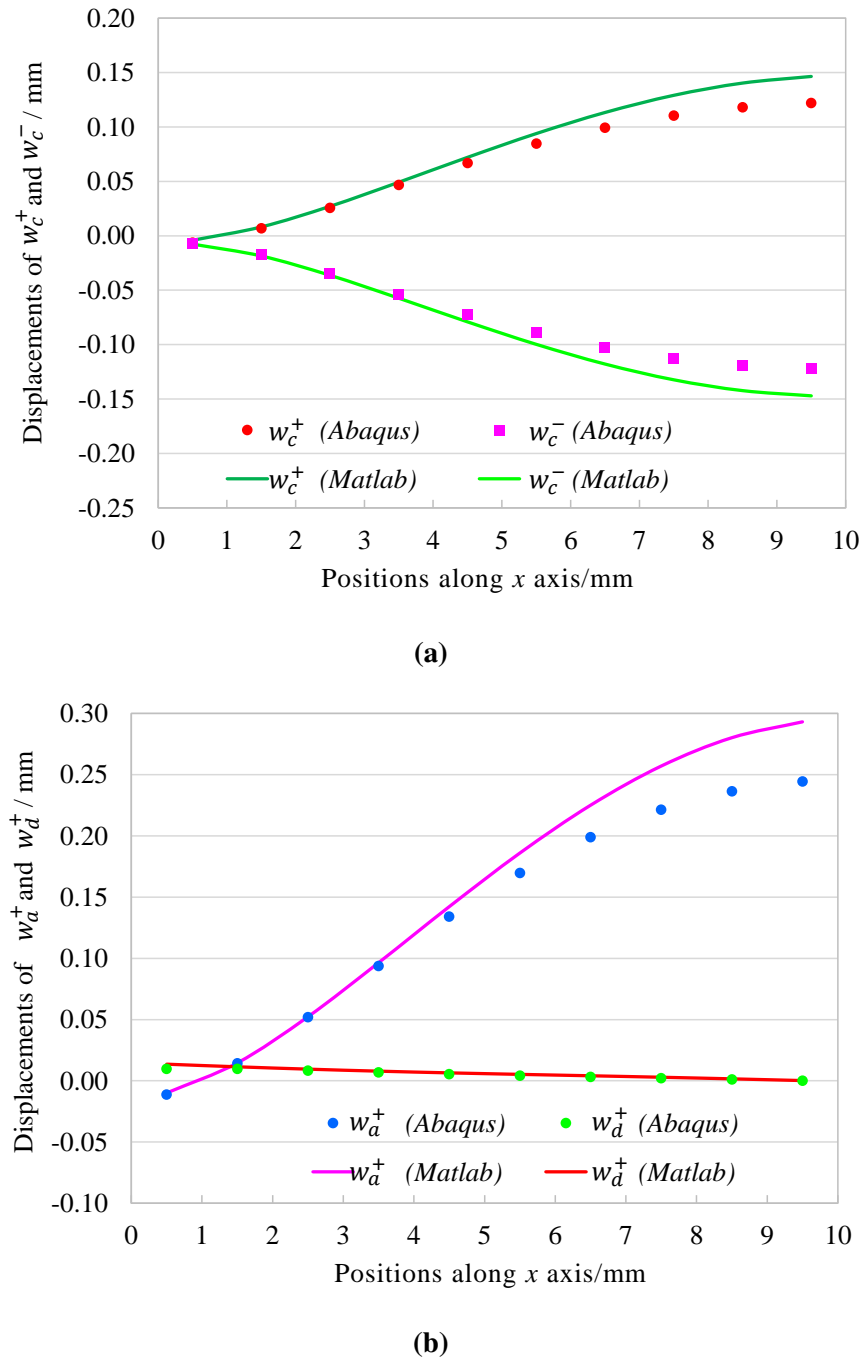


Figure 3.20 – Comparisons of the displacement distribution of cross section. (a). Distribution of w_c^+ and w_c^- . (b). Distribution of w_a^+ and w_d^+ .

10^4 MPa , $G_{23} = E_2/2(1 + v_{23})$, . A series of examples are carried out to test the new 3D beam element used for orthotropic material with large displacement behavior, one typical example is chosen to report here. Two transverse concentrated end loads in y and z direction are applied at the meantime: $F_y = F_z = -300 \text{ N}$. Figure 3.21 shows the comparisons of the displacements in x and y directions of centroidal axis, the results are almost the same. The biggest displacement in y direction is -4.024 mm using the new 3D beam element while the value is -4.060 mm in ABAQUS. The distributions of v_c^+ and v_c^- , v_a^+ and v_b^+ , w_c^+ and w_c^- , w_a^+ and w_d^+ can be seen in Figure 3.22 and 3.23, from which we can see that all the results from ABAQUS and Matlab are consistent while existing some errors, and all of the relative errors are controlled under 20%.

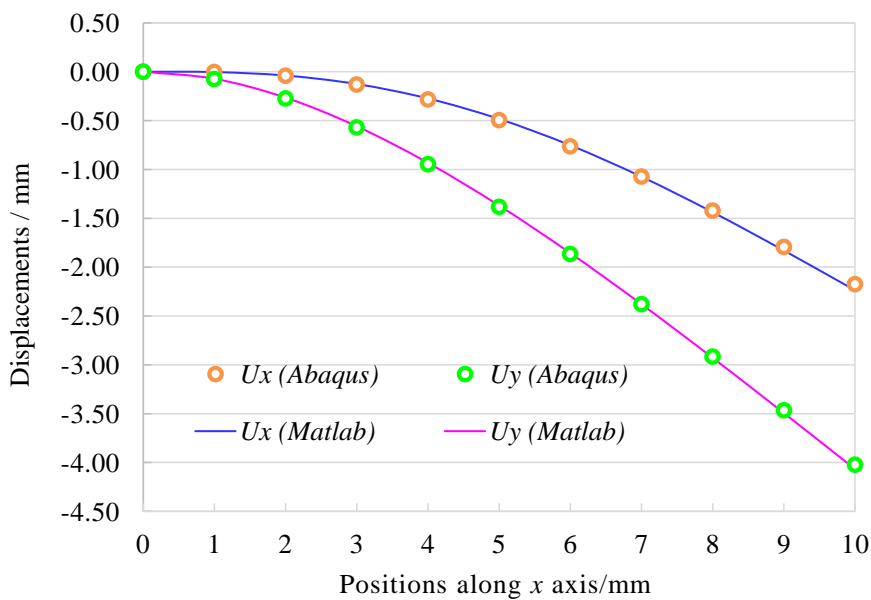


Figure 3.21 – Displacements of the centroidal axis in x and y direction.

3.8 Conclusions and future developments

In this chapter, the large displacements/ small strains formulation of the enhanced 3D beam element with section changes has been developed. And the formulation has been introduced in a Matlab finite element code and a series of validation cases have been treated and compared with 3D ABAQUS/Standard simulations. The results obtained are in good agreement and encouraging, which are the follow-up work of the reference [GAO 16]. Indeed, the final goal is to use those elements to model yarns in a textile composite preform. The results presented in this chapter are only the second step, and the following steps are: introducing contact behavior to the enhanced 3D beam to beam contact.

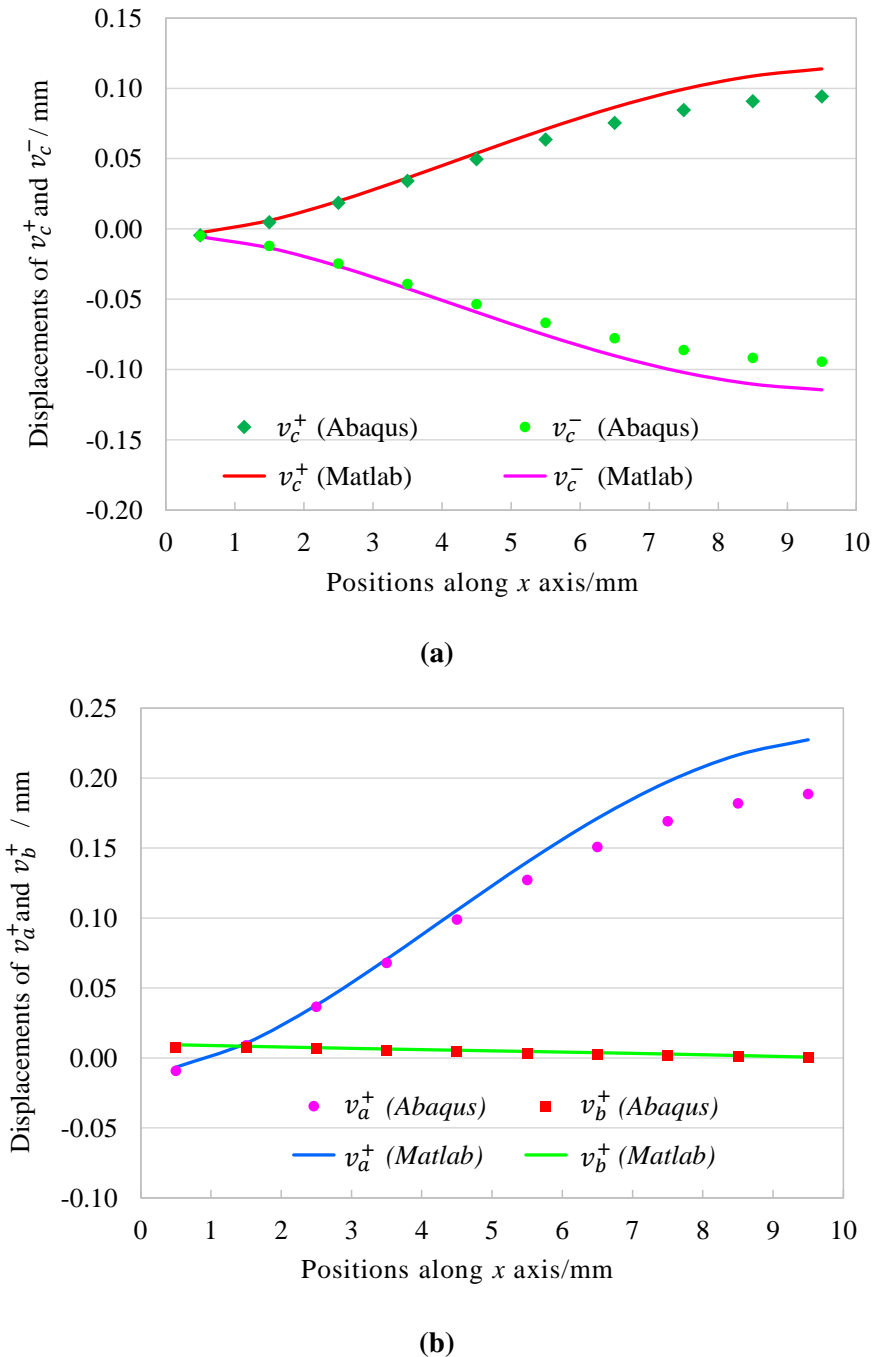


Figure 3.22 – Comparisons of the displacement distribution of cross section. (a). Distribution of v_c^+ and v_c^- . (b). Distribution of v_a^+ and v_b^+ .

3. Analysis of large displacements/small strains behavior

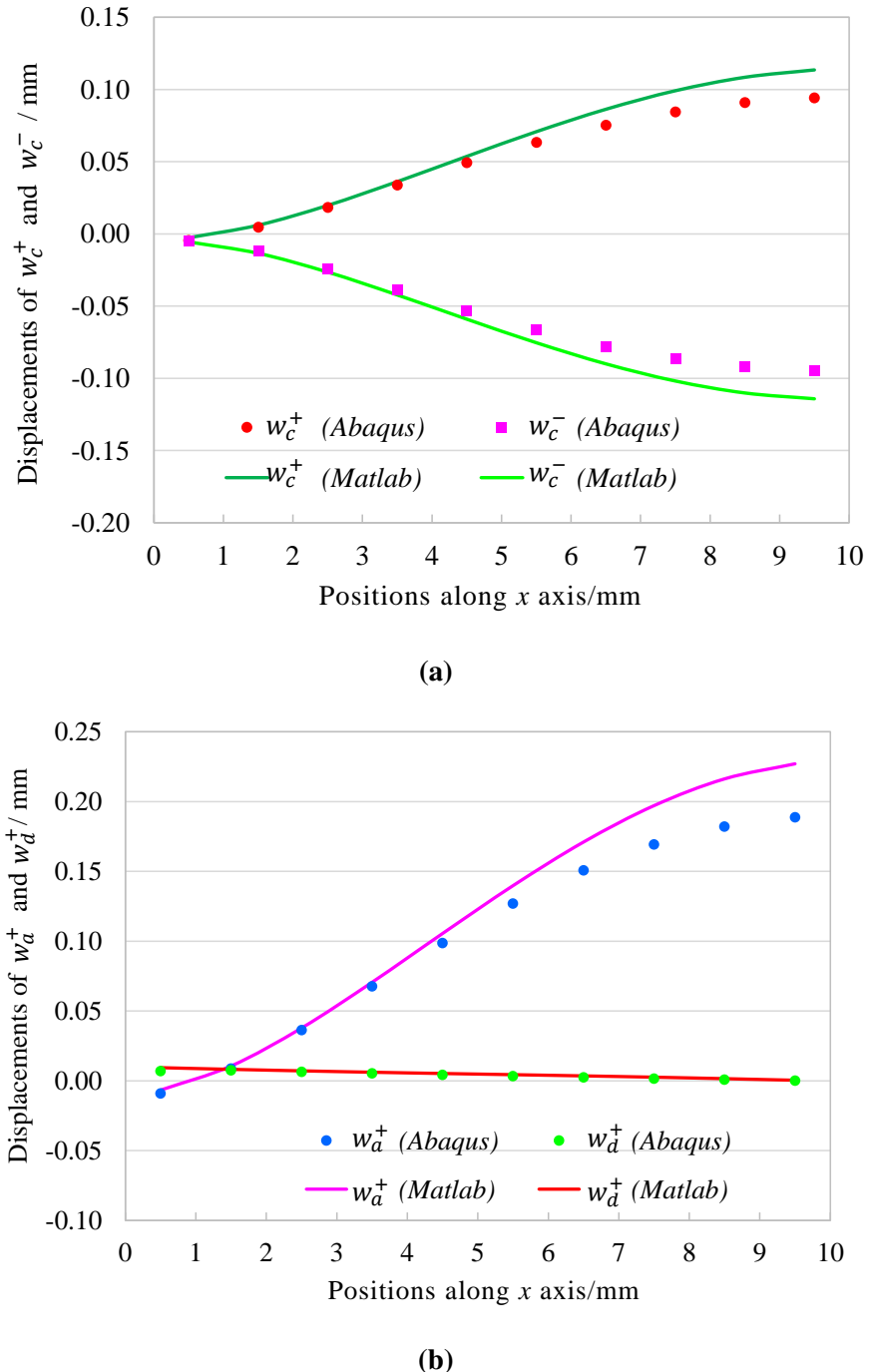


Figure 3.23 – Comparisons of the displacement distribution of cross section. (a). Distribution of w_c^+ and w_c^- . (b). Distribution of w_a^+ and w_d^+ .

Chapter 4

Enhanced 3D beam to beam contact

4.1 Introduction and review of the related work

Contact and related phenomena occurring at the interface of two bodies are encountered at every step of everyday life, in nature and in engineering. They are so common that usually one does not think about them, despite the fact one takes advantage of their effects.

The numerical treatment of contact problems between deformable bodies has a long history. Solution of this type of problem requires the scheme for solving variational inequalities, which result from inequality contact constraints. This end can be achieved in several ways. Lagrange multiplier and penalty parameter methods known from optimization theory [LUE 84] gained the most extensive use, mathematical background can be also seen in [KIK 88]. The solution in the frame of mathematical programming can be obtained as well [KLA 86].

First papers dealing with application of the finite element method in the contact analysis with large strains involved can be found in [CUR 88, SIM 92, WRI 92]. Among many other known publications it is worth to mention two, almost simultaneously published, monographs by Laursen [LAU 02] and by Wriggers [WRI 06]. They include a thorough presentation of mathematical background of numerical contact formulation, physical models of phenomena at the contact interfaces and the theoretical considerations are illustrated by numerical results concerning many practical cases of contacting bodies.

The rapid development of computer technology enabled the analysis of variety of more and more complicated contact cases involving e.g. large deformations or thermo-mechanical coupling. Numerous papers dealing with contact problems between general 2D or 3D bodies, with or without friction can be named [CUR 88, PAR 89, WRI 90, WRI 94, LAU 93]. Maker and Laursen [MAK 94] analyzed contact between a rod-like object and a continuous medium.

The beam to beam contact is a special case of a 3D bodies contact. One might think of contact between moving elements of machines, woven fabrics and textiles, sport racquet stringing or, finally, a multi-degree twists of strands in steel cables or electric conductors. Especially the last case of beam-to-beam contact poses a great challenge because it requires an advanced numerical model including effects of coupling of displacements,

temperature, electric current and magnetic field. Beam contact is characterized by some features, which demand a different approach than in the case of typical solids. That's the reason why the scarcity of this research is a much smaller number of practical applications than in the case of typical solids, where application of simpler analysis including beam contact finite elements can be profitable.

This research on beam contact was started by Wriggers and Zavarise [WRI 97, ZAV 00], analyzing the contact between beams having a simple circular cross section without and with Coulomb friction, respectively. And the research continued in [LIT 02b, LIT 02a], where beam to beam contact has been investigated in the case of frictionless and frictional contact for beams of rectangular cross section. The further development concerned inclusion of thermal and electric coupling [BOS 05]. Some subsequent research was also devoted to smoothing procedures for 3D curves representing axes of beams in contact [LIT 07a, LIT 07b]. A rigorous approach to the question of point-wise contact was also suggested by Konyukhov and Schweizerhof in [KON 10]. There the authors focused their interest on the closest-point projection procedure, which for the beam-to-beam contact leads to the orthogonality conditions [WRI 97]. The same authors used their approach to analyze the problem of rope wound around a cylinder and the question of knot-tightening [KON 11b]. The latter issue was also considered and solved by Durville in [DUR 05, DUR 12]. Litewka [LIT 13, LIT 15] has investigated point-wise beam-to-beam contact finite elements used in cases when beams get in contact at very acute angles.

However, the literature concerning contact between beam to beam with deformable cross section is not so broad. The problems of this type can be found frequently in practice, such as woven fabrics, and racquet stringing. To the authors'knowledge, there exist only few contributions [KAW 14, KAW 15], in which contact between 3D beams with deformable circular cross sections is analyzed, dealing with the question of cross section deformations at the contact zone. However, there are still many issues that might be addressed. For the contact between 3D beams with deformable rectangular cross section, there's no related literature yet. In this thesis, the challenge is that a more complicated case of a contact finite element for 3D beams with rectangular cross-section is considered. The element is reported previously in chapter 2 and chapter 3, beam deformations are taken into account, and the appropriate kinematic variables for normal contact together with their finite element approximation are derived in this chapter. Basing on the weak form for normal contact and its linearization, the tangent stiffness matrix and the residual vector are derived. The new element is tested using author's computer programs implanted in Matlab, a couple of examples are carried out and the results are compared with that of the solid element C3D8I in ABAQUS/Standard simulations.

4.2 Frictionless Contact between Solids

Let us consider two bodies, B_1 and B_2 , shown in Figure 4.1 [LIT 10], which undergo deformation f , such that any arbitrary points on their surfaces, described in the initial

configuration with position vectors \mathbf{X}_1^0 and \mathbf{X}_2^0 undergo displacements \mathbf{U}_1 and \mathbf{U}_2 . In the current configuration they are defined by the position vectors \mathbf{X}_1 and \mathbf{X}_2 , which can be expressed by the formula:

$$f : \begin{cases} \mathbf{X}_1 = \mathbf{X}_1^0 + \mathbf{U}_1 \\ \mathbf{X}_2 = \mathbf{X}_2^0 + \mathbf{U}_2 \end{cases} \quad (4.1)$$

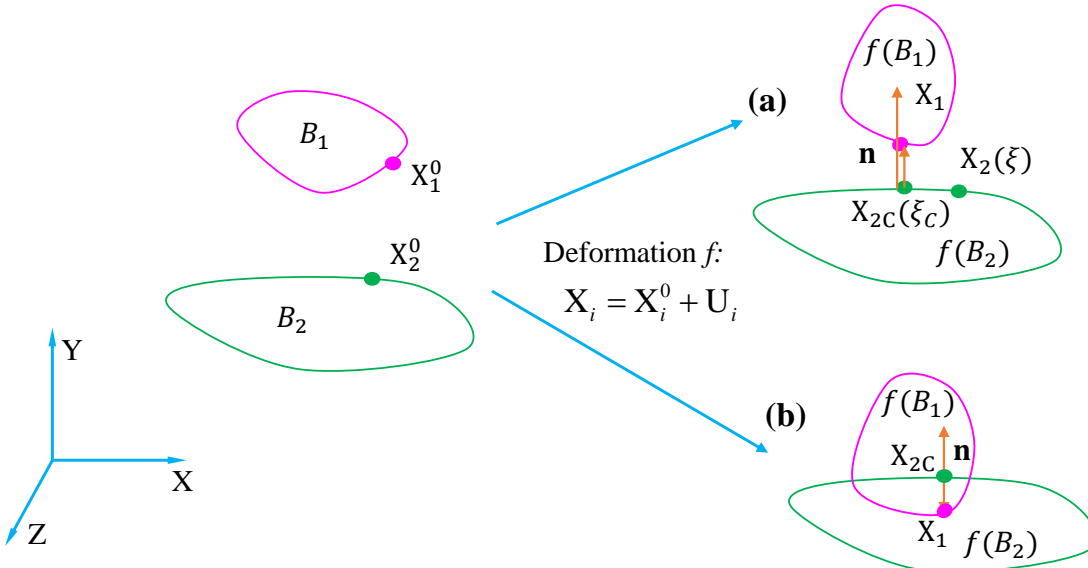


Figure 4.1 – Deformation of two bodies and penetration function: (a) separate bodies. (b) penetration [LIT 10].

Contact only has the relationship with the points on surface of the bodies and its formulation is practically independent with a physical model of the body material. That is why the phenomena occurring inside the bodies are not dealt with here. It is only assumed that the deformation f leads to large displacements in both bodies. Solution of a problem in the theory of elasticity concerning the two bodies involves finding a minimum of the potential energy functional Π .

$$\min \Pi = \min (\Pi_1 + \Pi_2) \quad (4.2)$$

Theoretically, in the deformation process f , a situation presented in Figure 4.1(b) may occur, when the bodies intersect mutually. Obviously, in reality such a state is not allowed. To exclude such a possibility, unilateral constraints are introduced. They are formulated using a penetration function (or a gap function) g_N . To this end, one of the bodies B_1 is distinguished as a slave body. Then the points \mathbf{X}_1 and \mathbf{X}_{2C} are obtained, as in Figure 4.1. The location of the point \mathbf{X}_{2C} is expressed in terms of local surface coordinates $\xi = \xi_C$. Then the penetration function is defined as:

$$g_N = \mathbf{n} \circ (\mathbf{X}_1 - \mathbf{X}_{2C}) \quad (4.3)$$

Where the unit outward normal vector \mathbf{n} on the surface of body B_2 is introduced (Figure 4.1) and " \circ " denotes the scalar product of vectors. The value of function g_N provides the distance between the points in the case of penetration.

Preserving the condition of non-penetrability requires that the penetration function remains non-negative

$$g_N \geq 0 \quad (4.4)$$

The condition expressed by Equation (4.4) constitutes an inequality constraint, which must be included in the minimization of the Equation (4.2). It should be emphasized, that the inequality Equation (4.4) concerns all possible point pairs \mathbf{X}_1 and \mathbf{X}_{2C} .

If the condition of Equation (4.4) is accompanied by the constraint of contact normal force, which can only be compressive:

$$F_N \leq 0 \quad (4.5)$$

Then the complete set of the classical Hertz-Signorini-Moreau conditions for the frictionless contact is obtained, together with the equality:

$$F_N g_N = 0 \quad (4.6)$$

According to Equation (4.5), in the case of contact the penetration is zero and the contact force is negative, while in the case of separation the gap is positive and the contact force is zero [MOR 11]. These are the conditions of unilateral contact [JOH 74, KIK 88], called also the Kuhn-Tucker conditions in the theory of optimization. The relations yielding from contact, presented above, introduce only geometric constraints, which may be called a low precision contact. In some cases it is necessary to consider high precision contact, which requires introduction of physical law for the microscale phenomena at rough contacting surfaces. In the present work, considerations are limited to the low precision contact.

4.3 Finite element method in contact analysis

The constraints in the Equation (4.4) are in general related to each point lying on the surface of the slave body and its projection on the surface of the master body. Various types of contact finite elements can be used depending on the character of deformation and the spatial dimension. The simplest possible element is the node-to-node element, which can be used in 2D and 3D analysis, as shown in Figure 4.2(a). The restriction is that it only can be applied in the cases with small displacements and small strains. No distinction between master and slave bodies is necessary in this case. When it comes to large displacements, especially large relative displacements between the bodies, node-to-segment and node-to-surface should be used, which are presented in Figure 4.2(b) and 4.2(c). The case of contacting beams is different from the elements mentioned, the contact points do not coincide with slave nodes but lie between the nodes on both beams,

see in Figure 4.2(d). In this case, the distinction between the slave and the master is not introduced, either.

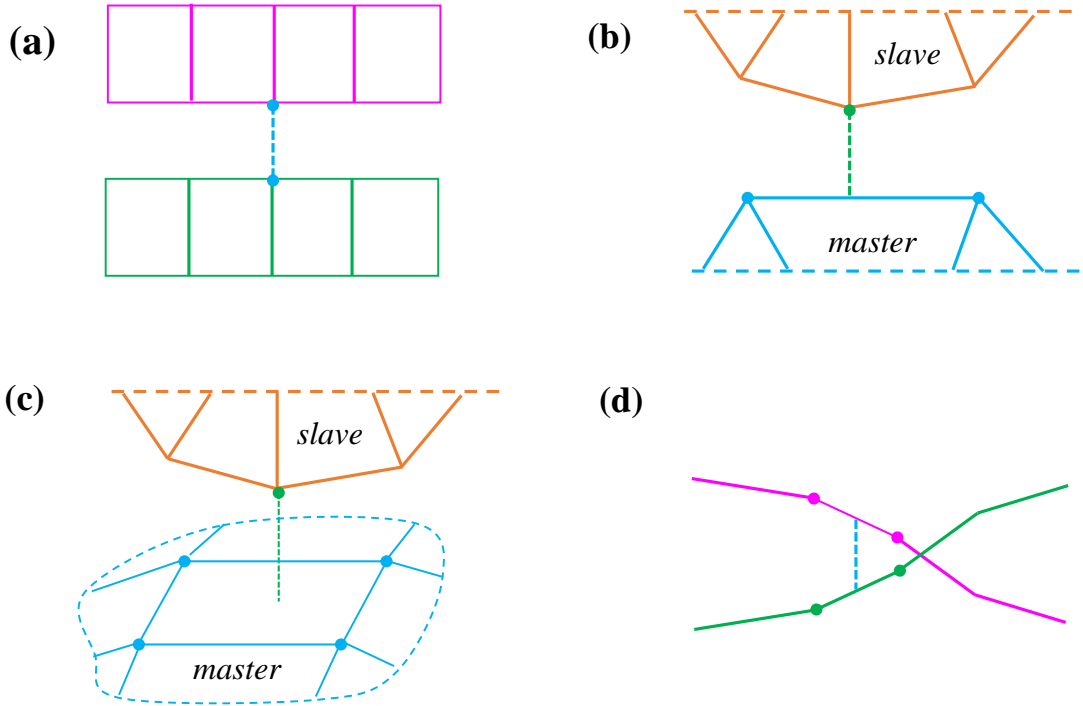


Figure 4.2 – Contact finite elements: (a) node-to-node. (b) node-to-segment. (c) node-to-surface. (d) beam-to-beam [LIT 10].

Incremental-iterative solution of the functional minimization by the finite element method at each iteration (for a pair of separated bodies A and B) takes the following matrix form, shown in Equation (4.7), which actually represents two uncoupled sets of equation.

$$\begin{bmatrix} \mathbf{K}_A & \mathbf{0} \\ \mathbf{0} & \mathbf{K}_B \end{bmatrix} \begin{bmatrix} \Delta \mathbf{U}_A \\ \Delta \mathbf{U}_B \end{bmatrix} + \begin{bmatrix} \mathbf{R}_A \\ \mathbf{R}_B \end{bmatrix} = \begin{bmatrix} \mathbf{0} \\ \mathbf{0} \end{bmatrix} \quad (4.7)$$

The situation is different, if additional terms, resulting from the constraint fulfillment using the penalty method or the Lagrange multiplier method are introduced to Π_c . For the case of penalty method, the related tangent stiffness matrix and the residual vector can be written as:

$$\mathbf{K}_N = \begin{bmatrix} \mathbf{K}_{NAA} & \mathbf{K}_{NAB} \\ \mathbf{K}_{NBA} & \mathbf{K}_{NBB} \end{bmatrix}, \mathbf{R}_N = \begin{bmatrix} \mathbf{R}_{NA} \\ \mathbf{R}_{NB} \end{bmatrix} \quad (4.8)$$

and for the Lagrange multiplier method as:

$$\mathbf{K}_N = \begin{bmatrix} \mathbf{K}_{NAA} & \mathbf{K}_{NAB} & \mathbf{K}_{NA\lambda} \\ \mathbf{K}_{NBA} & \mathbf{K}_{NBB} & \mathbf{K}_{NB\lambda} \\ \mathbf{K}_{NA\lambda} & \mathbf{K}_{NB\lambda} & \mathbf{0} \end{bmatrix}, \mathbf{R}_N = \begin{bmatrix} \mathbf{R}_{NA} \\ \mathbf{R}_{NB} \\ \mathbf{R}_{N\lambda} \end{bmatrix} \quad (4.9)$$

If the matrices and vectors above are introduced to the finite element formulation, the coupled set of equation for penalty method can be expressed as:

$$\begin{bmatrix} (\mathbf{K}_A + \mathbf{K}_{NAA}) & \mathbf{K}_{NAB} \\ \mathbf{K}_{NBA} & \mathbf{K}_B + \mathbf{K}_{NBB} \end{bmatrix} \begin{bmatrix} \Delta \mathbf{U}_A \\ \Delta \mathbf{U}_B \end{bmatrix} + \begin{bmatrix} \mathbf{R}_A + \mathbf{R}_{NA} \\ \mathbf{R}_B + \mathbf{R}_{NB} \end{bmatrix} = \begin{bmatrix} \mathbf{0} \\ \mathbf{0} \end{bmatrix} \quad (4.10)$$

and for the Lagrange multiplier method, one gets:

$$\begin{bmatrix} (\mathbf{K}_A + \mathbf{K}_{NAA}) & \mathbf{K}_{NAB} & \mathbf{K}_{NA\lambda} \\ \mathbf{K}_{NBA} & (\mathbf{K}_B + \mathbf{K}_{NBB}) & \mathbf{K}_{NB\lambda} \\ \mathbf{K}_{NA\lambda} & \mathbf{K}_{NB\lambda} & \mathbf{0} \end{bmatrix} \begin{bmatrix} \Delta \mathbf{U}_A \\ \Delta \mathbf{U}_B \\ \Delta \lambda \end{bmatrix} + \begin{bmatrix} \mathbf{R}_A + \mathbf{R}_{NA} \\ \mathbf{R}_B + \mathbf{R}_{NB} \\ \mathbf{R}_{N\lambda} \end{bmatrix} = \begin{bmatrix} \mathbf{0} \\ \mathbf{0} \\ \mathbf{0} \end{bmatrix} \quad (4.11)$$

Taking contact into account in the finite element analysis leads in a natural way to a connection of the contacting bodies into one entity. For this new body, one tangent stiffness matrix and one residual vector can be calculated, since the resulting sets of Equations (4.10) or (4.11) are coupled, contrary to Equation (4.7).

4.4 Weak formulation and kinematic variables of contact contribution

The basis to define the penetration function for two beams in the point-wise contact is finding a pair of two closest points lying on two curves, as shown in Figure 4.3. In the case of beams with circular cross sections the points are to belong to curves representing beam axes, while for beams with rectangular cross sections the points lie on edges. Location of an arbitrary point on the curve is defined by a local curvilinear coordinate, ξ_m or ξ_s , respectively. The subscripts "m" and "s" does not mean the distinction between master and slave beam. As mentioned previously, in the case of the beam to beam contact such a distinction is not necessary since both beams are treated equivalently.

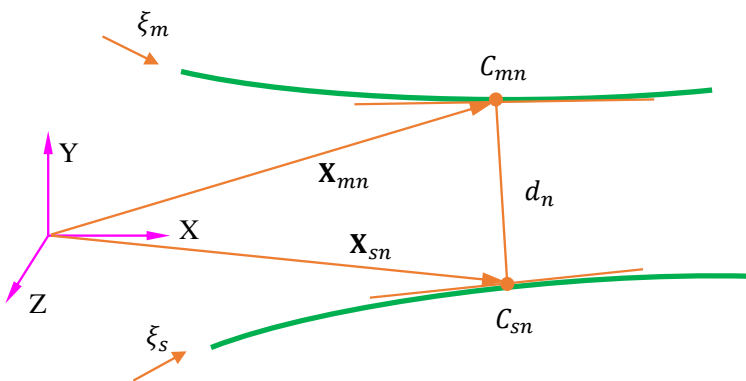


Figure 4.3 – The closest points on two curves.

We consider a pair of beam edges with initial position vectors \mathbf{X}_m^0 and \mathbf{X}_s^0 undergoing displacements \mathbf{U}_m and \mathbf{U}_s to give the current position vectors.

$$\mathbf{X}_i = \mathbf{X}_i^0 + \mathbf{U}_i, \quad i = m, s \quad (4.12)$$

The vital problem is to find the closest points C_{mn} and C_{sn} on the beam edges, which are represented by their coordinates ξ_m and ξ_s . A thorough discussion of the closest points' projection can be found in the papers by Konyuhov and Schweizerhof [KON 08, KON 11a]. The position vectors $\mathbf{X}_{mn}, \mathbf{X}_{sn}$ of the closest points C_{mn} and C_{sn} on the curves must fulfil the orthogonality conditions [LIT 10]:

$$\begin{aligned} (\mathbf{X}_{mn} - \mathbf{X}_{sn}) \cdot \mathbf{X}_{mn,n} &= 0 \\ (\mathbf{X}_{mn} - \mathbf{X}_{sn}) \cdot \mathbf{X}_{sn,s} &= 0 \end{aligned} \quad (4.13)$$

Where the common notation for the partial derivatives with respect to the local coordinates ξ_m and ξ_s was introduced: $(\cdot)_{,i} = \partial(\cdot)/\partial\xi_i$, $i = m, s$.

Linearization of the orthogonality conditions gives the local coordinates increments $\Delta\xi_m, \Delta\xi_s$:

$$\begin{bmatrix} \mathbf{X}_{m,m} \cdot \mathbf{X}_{m,m} + (\mathbf{X}_m - \mathbf{X}_s) \cdot \mathbf{X}_{m,mm} & -\mathbf{X}_{m,m} \cdot \mathbf{X}_{s,s} \\ \mathbf{X}_{m,m} \cdot \mathbf{X}_{s,s} & -\mathbf{X}_{s,s} \cdot \mathbf{X}_{s,s} + (\mathbf{X}_m - \mathbf{X}_s) \cdot \mathbf{X}_{s,ss} \end{bmatrix} \begin{bmatrix} \Delta\xi_m \\ \Delta\xi_s \end{bmatrix} = \begin{bmatrix} -(\mathbf{X}_m - \mathbf{X}_s) \cdot \mathbf{X}_{m,m} \\ -(\mathbf{X}_m - \mathbf{X}_s) \cdot \mathbf{X}_{s,s} \end{bmatrix} \quad (4.14)$$

For a pair of beams in contact, the strain energy can be split into three parts, which correspond to the energy of each beam Π_m , Π_s , and the energy of contact contribution Π_c :

$$\Pi = \Pi_m + \Pi_s + \Pi_c \quad (4.15)$$

The contact contribution used penalty method is expressed as:

$$\Pi_N^\varepsilon = \frac{1}{2} \varepsilon_N g_N^2 \quad (4.16)$$

And in Lagrange multiplier method:

$$\Pi_N^\lambda = \lambda_N g_N \quad (4.17)$$

Where, the superscript ε relates to the penalty method, and λ relates to the Lagrange multiplier method. ε_N is the penalty parameter, λ_N is the Lagrange multiplier, and g_N is the penetration function defined as:

$$g_N = \|\mathbf{X}_{mn} - \mathbf{X}_{sn}\| \quad (4.18)$$

Where \mathbf{X}_{mn} and \mathbf{X}_{sn} are position vectors of the contacting points.

For a single active pair, the additional component of the functional variation can be expressed as:

$$\delta\Pi_N^\varepsilon = \delta\left(\frac{1}{2} \varepsilon_N g_N^2\right) = \varepsilon_N g_N \delta g_N \quad (4.19)$$

$$\delta\Pi_N^\lambda = \delta(\lambda_N g_N) = \lambda_N \delta g_N + \delta\lambda_N g_N \quad (4.20)$$

If contact occurs and the contact contribution terms must be taken into account, the solution is an extremal value of Π , which leads to the requirement which leads to the requirement $\delta\Pi = 0$. Hence we have to compute for the penalty method and for the Lagrange multiplier method:

$$\delta\Pi^\varepsilon = \delta\Pi_m + \delta\Pi_s + \varepsilon_N g_N \delta g_N = 0 \quad (4.21)$$

$$\delta\Pi^\lambda = \delta\Pi_m + \delta\Pi_s + \delta\lambda_N g_N + \lambda_N \delta g_N = 0 \quad (4.22)$$

The Newton iteration scheme for the solution of non-linear equation requires linearization:

$$\Delta\delta\Pi^\varepsilon = \Delta\delta\Pi_m + \Delta\delta\Pi_s + \varepsilon_N \Delta g_N \delta g_N + \varepsilon_N g_N \Delta\delta g_N \quad (4.23)$$

$$\Delta\delta\Pi^\lambda = \Delta\delta\Pi_m + \Delta\delta\Pi_s + \delta\lambda_N \Delta g_N + \Delta\lambda_N \delta g_N + \lambda_N \Delta\delta g_N \quad (4.24)$$

Since we are only interested here in the contact contribution, the following terms, associated with Π_c , have to be computed and expressed in a suitable way as functions of the displacement field: $g_N, \delta g_N, \Delta g_N, \Delta\delta g_N$ [WRI 97, LIT 02b, LIT 10]. From the penetration function g_N , we can obtain:

$$\delta g_N = (\delta\mathbf{X}_{mn} - \delta\mathbf{X}_{sn})^T \cdot \mathbf{n} \quad (4.25)$$

Here, the normal vector \mathbf{n} has been introduced:

$$\mathbf{n} = \frac{\mathbf{X}_{mn} - \mathbf{X}_{sn}}{\|\mathbf{X}_{mn} - \mathbf{X}_{sn}\|} \quad (4.26)$$

After some algebra calculations,

$$\delta g_N = (\delta\mathbf{U}_{mn} - \delta\mathbf{U}_{sn})^T \cdot \mathbf{n} \quad (4.27)$$

Note that the linearization of the gap function Δg_N has the same structure as δg_N :

$$\Delta g_N = (\Delta\mathbf{U}_{mn} - \Delta\mathbf{U}_{sn})^T \cdot \mathbf{n} \quad (4.28)$$

The linearization of Δg_N yields:

$$\Delta\delta g_N = (\Delta\delta\mathbf{X}_{mn} - \Delta\delta\mathbf{X}_{sn})^T \cdot \mathbf{n} + (\delta\mathbf{X}_{mn} - \delta\mathbf{X}_{sn})^T \cdot \Delta\mathbf{n} \quad (4.29)$$

$$\text{and } \Delta\mathbf{n} = \frac{1}{g_N} [\mathbf{1} - \mathbf{n} \otimes \mathbf{n}] [\Delta\mathbf{X}_{mn} - \Delta\mathbf{X}_{sn}].$$

Thus by taking into account normality conditions, we can rewrite $\Delta\delta g_N$:

$$\begin{aligned} \Delta\delta g_N &= (\delta\mathbf{U}_{mn,m} \Delta\xi_{mn} - \delta\mathbf{U}_{sn,n} \Delta\xi_{sn}) \cdot \mathbf{n} + (\Delta\mathbf{U}_{mn,m} \delta\xi_{mn} - \Delta\mathbf{U}_{sn,n} \delta\xi_{sn}) \cdot \mathbf{n} \\ &\quad + (\mathbf{X}_{mn,mn} \Delta\xi_{mn} \delta\xi_{sn} - \mathbf{X}_{sn,ss} \Delta\xi_{sn} \delta\xi_{sn}) \cdot \mathbf{n} \\ &\quad + \frac{1}{g_N} (\delta\mathbf{U}_{mn} + \mathbf{X}_{mn,m} \delta\xi_{mn} - \delta\mathbf{U}_{sn} - \mathbf{X}_{sn,s} \delta\xi_{sn}) \\ &\quad \cdot (\mathbf{1} - \mathbf{n} \otimes \mathbf{n}) (\Delta\mathbf{U}_{mn} + \mathbf{X}_{mn,m} \Delta\xi_{mn} - \Delta\mathbf{U}_{sn} - \mathbf{X}_{sn,s} \Delta\xi_{sn}) \end{aligned} \quad (4.30)$$

For the explicit expression of kinematic variables, the variation and the linearization of the local coordinates $\delta\xi_{mn}, \delta\xi_{sn}, \Delta\xi_{mn}, \Delta\xi_{sn}$, must be derived, too. They can be obtained from the linearization and the variation of the orthogonality conditions of Equation (4.13) at ξ_{mn} and ξ_{sn} and obtain:

$$\begin{aligned} [\Delta\mathbf{U}_{mn} + \mathbf{X}_{mn,m}\Delta\xi_{mn} - \Delta\mathbf{U}_{sn} - \mathbf{X}_{sn,s}\Delta\xi_{sn}] \cdot \mathbf{X}_{mn,m} + (\mathbf{X}_{mn} - \mathbf{X}_{sn}) \cdot [\Delta\mathbf{U}_{mn,m} + \mathbf{X}_{mn,mm}\Delta\xi_{mn}] &= 0 \\ [\Delta\mathbf{U}_{mn} + \mathbf{X}_{mn,m}\Delta\xi_{mn} - \Delta\mathbf{U}_{sn} - \mathbf{X}_{sn,s}\Delta\xi_{sn}] \cdot \mathbf{X}_{sn,s} + (\mathbf{X}_{mn} - \mathbf{X}_{sn}) \cdot [\Delta\mathbf{U}_{sn,s} + \mathbf{X}_{sn,ss}\Delta\xi_{sn}] &= 0 \end{aligned} \quad (4.31)$$

This equation can be rearranged in matrix form as:

$$\begin{bmatrix} \Delta\xi_{mn} \\ \Delta\xi_{sn} \end{bmatrix} = \mathbf{A}^{-1} \left(\mathbf{B} \begin{bmatrix} \Delta\mathbf{U}_{mn} \\ \Delta\mathbf{U}_{sn} \end{bmatrix} + \mathbf{C} \begin{bmatrix} \Delta\mathbf{U}_{mn,m} \\ \Delta\mathbf{U}_{sn,s} \end{bmatrix} \right) \quad (4.32)$$

Where

$$\begin{aligned} \mathbf{A} &= \begin{bmatrix} \mathbf{X}_{mn,m} \cdot \mathbf{X}_{mn,m} + \mathbf{X}_{ms} \cdot \mathbf{X}_{mn,mm} & -\mathbf{X}_{mn,m} \cdot \mathbf{X}_{sn,s} \\ \mathbf{X}_{mn,m} \cdot \mathbf{X}_{sn,s} & -\mathbf{X}_{sn,s} \cdot \mathbf{X}_{sn,s} + \mathbf{X}_{ms} \cdot \mathbf{X}_{sn,ss} \end{bmatrix} \\ \mathbf{B} &= \begin{bmatrix} -\mathbf{X}_{mn,m}^T & \mathbf{X}_{mn,m}^T \\ -\mathbf{X}_{sn,s}^T & \mathbf{X}_{sn,s}^T \end{bmatrix}, \mathbf{C} = \begin{bmatrix} -\mathbf{X}_{ms}^T & \mathbf{0} \\ \mathbf{0} & -\mathbf{X}_{ms}^T \end{bmatrix}, \mathbf{X}_{ms} = \mathbf{X}_{mn} - \mathbf{X}_{sn} \end{aligned} \quad (4.33)$$

Similarly, the variations of the local coordinates follow from:

$$\begin{bmatrix} \delta\xi_{mn} \\ \delta\xi_{sn} \end{bmatrix} = \mathbf{A}^{-1} \left(\mathbf{B} \begin{bmatrix} \delta\mathbf{U}_{mn} \\ \delta\mathbf{U}_{sn} \end{bmatrix} + \mathbf{C} \begin{bmatrix} \delta\mathbf{U}_{mn,m} \\ \delta\mathbf{U}_{sn,s} \end{bmatrix} \right) \quad (4.34)$$

4.5 Contact search

In the contact search both beams are treated equivalently, no distinction between slave and master is introduced and the contact points must be located simultaneously on both beams. In the case of the rectangular cross section the problem is more complicated. The contact may occur between the curves representing the longitudinal edges of real beams [LIT 02b, LIT 10], several different configurations are possible, as shown in Figure 4.4. The contact-search strategy used in the present analysis is based on several assumptions:

- (1) Contact between beams is pointwise, i.e. the case of parallel beams getting into contact is not covered;
- (2) Cross sections of contacting beams undergo some deformations, they still remain plane but not necessarily perpendicular to the respective beam axes;
- (3) Contact occurs between edges of beams, for each pair of beams no more than two edges of one beam can contact with no more than two edges of the second beam. This means that the configuration shown in Figure 4.4(d) is not considered since very large deformation leads to winding of one beam around another.

With the pair of the closest points C_{mn} and C_{sn} found (Figure 4.3), one can calculate the distance d_N between them:

$$d_N = \|\mathbf{X}_{mn} - \mathbf{X}_{sn}\| \quad (4.35)$$

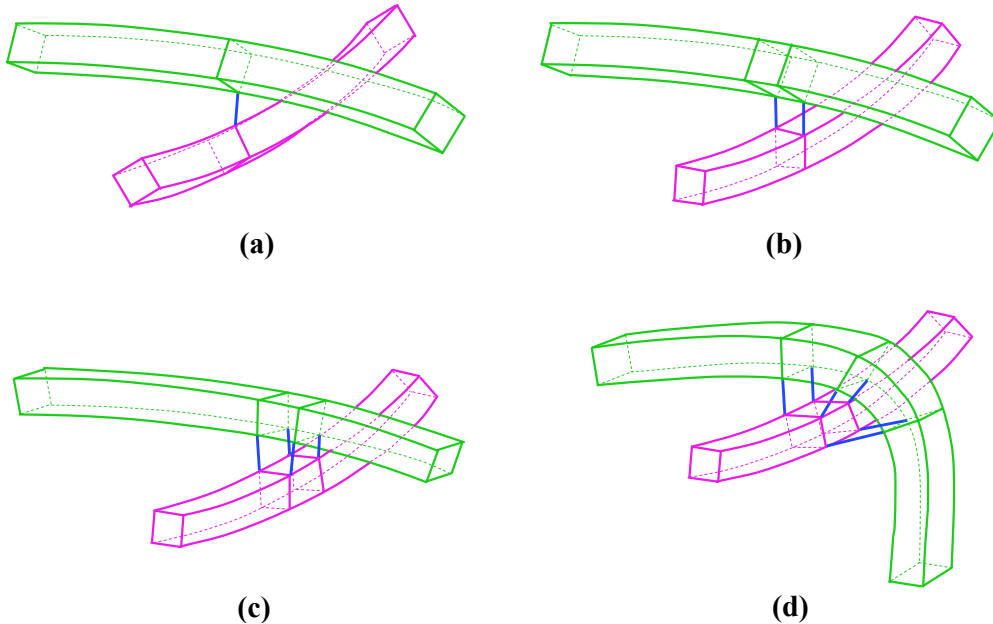


Figure 4.4 – Contact between edges of beams with rectangular cross-sections. (a) One pair. (b) Two pairs. (c) Four pairs. (d) More than four pairs [LIT 02b].

For the beams with rectangular cross-section, where d_N represents the distance between the beam edges, this value is simultaneously equal to the penetration function:

$$g_N = d_N \quad (4.36)$$

In the case of beams with rectangular cross sections, Equation (4.36) is always positive. In order to define a special criterion for this case, two beams named m and s separately, as shown in Figure 4.5.

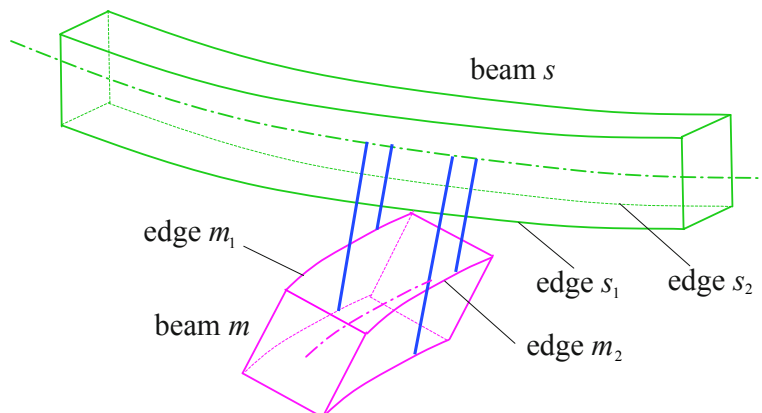


Figure 4.5 – Search of the closest edges [LIT 10].

The linearization of the orthogonality conditions and the Newton method are used to perform the search for the closest points between edges.

- 1) The search for the closest points is carried out between four edges of beam m and the axis of beam s , and two closest edges from beam m (m_1 and m_2) are selected.
- 2) The roles of the beams are exchanged and two edges, s_1 and s_2 , which are the closest edges of beam s with respect to the axis of beam m , are found.
- 3) The closest points are found for four pairs of the edges $m_1 - s_1$, $m_1 - s_2$, $m_2 - s_1$ and $m_2 - s_2$. For all these pairs, the contact criterion is checked.

The contact criterion takes the form as follows, the following vectors shown in Figure 4.6 are introduced [LIT 02b, LIT 10]:

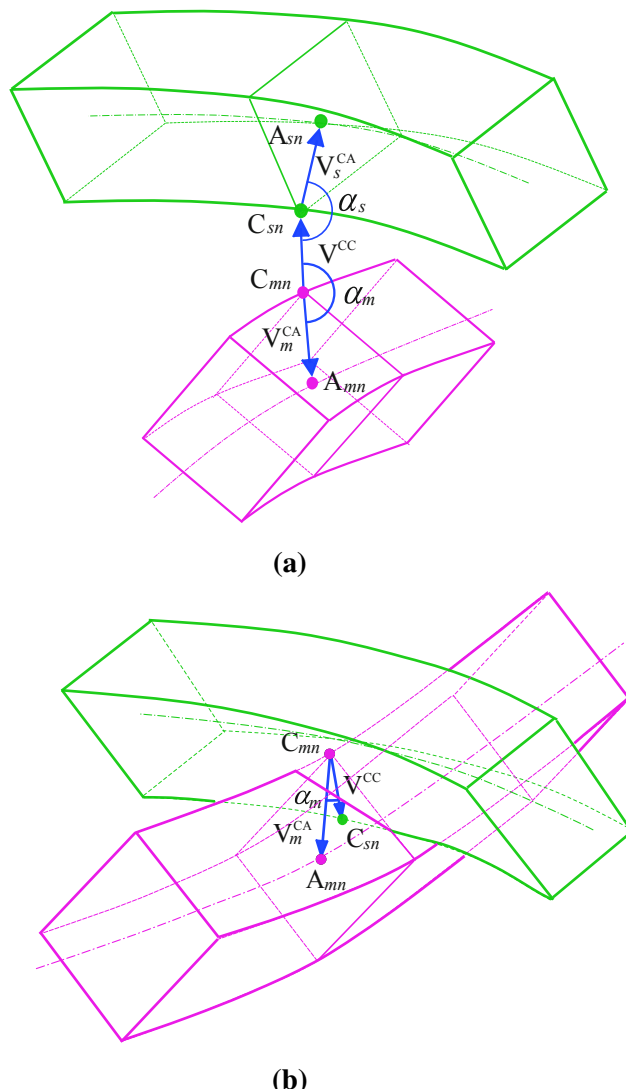


Figure 4.6 – Contact criterion for beams with rectangular cross sections. (a) Separation. (b) Penetration. [LIT 02b, LIT 10]

1) The vector between the closest points C_{mn} and C_{sn} on the beam edges:

$$\mathbf{V}^{CC} = \mathbf{X}_{sn} - \mathbf{X}_{mn} \quad (4.37)$$

2) The vector between C_{mn} and the corresponding point A_{mn} located on beam axis m :

$$\mathbf{V}_m^{CA} = \mathbf{X}_{mA} - \mathbf{X}_{mn} \quad (4.38)$$

3) The vector between C_{sn} and the corresponding point A_{sn} located on beam axis s :

$$\mathbf{V}_s^{CA} = \mathbf{X}_{sA} - \mathbf{X}_{sn} \quad (4.39)$$

The angles α_m and α_s between these vectors can be defined as:

$$\begin{aligned} \alpha_m &= \angle(\mathbf{V}^{CC}, \mathbf{V}_m^{CA}) \\ \alpha_s &= \angle(-\mathbf{V}^{CC}, \mathbf{V}_s^{CA}) \end{aligned} \quad (4.40)$$

It can be noticed in Figure 4.6, the angles α_m and α_s are obtuse when the two beams are separate while acute in the case of penetration. Hence, the contact criterion for the beams with rectangular cross sections can be defined as:

$$\begin{aligned} \cos \alpha_m < 0 &\quad \text{and} \quad \cos \alpha_s < 0 \quad \Rightarrow \text{Separate bodies} \\ \cos \alpha_m > 0 &\quad \text{and} \quad \cos \alpha_s > 0 \quad \Rightarrow \text{Penetration} \end{aligned} \quad (4.41)$$

4.6 Finite element formulation of contact contribution

In the case of beams with rectangular cross sections, the further stages must involve finding the possible contact candidates among beam edges. To this end, the coordinates of points lying on these edges (edges 1, 2, 3, 4) must be expressed by means of nodal displacements of the beam element, shown in Figure 4.7. Here, the shape functions for the beam finite element based on Updated Lagrangian formulation presented in chapter 3 is used. To determine displacements of a point C on the beam edge using Equation (3.54), one must substitute for the coordinates η and ζ the appropriate values:

$$\begin{aligned} \text{Edge 1 : } \vec{u}_{B1} &= \vec{u}_B(\eta = 1, \zeta = 1) \\ \text{Edge 2 : } \vec{u}_{B2} &= \vec{u}_B(\eta = 1, \zeta = -1) \\ \text{Edge 3 : } \vec{u}_{B3} &= \vec{u}_B(\eta = -1, \zeta = -1) \\ \text{Edge 4 : } \vec{u}_{B4} &= \vec{u}_B(\eta = -1, \zeta = 1) \end{aligned} \quad (4.42)$$

Substitution of $\eta = 0, \zeta = 0$ allows for calculation of the displacements of a point located on the beam axis.

All the kinematic variables derived in Section 4.4 can now be expressed in terms of nodal displacements of two beam elements, within which the current contact points are

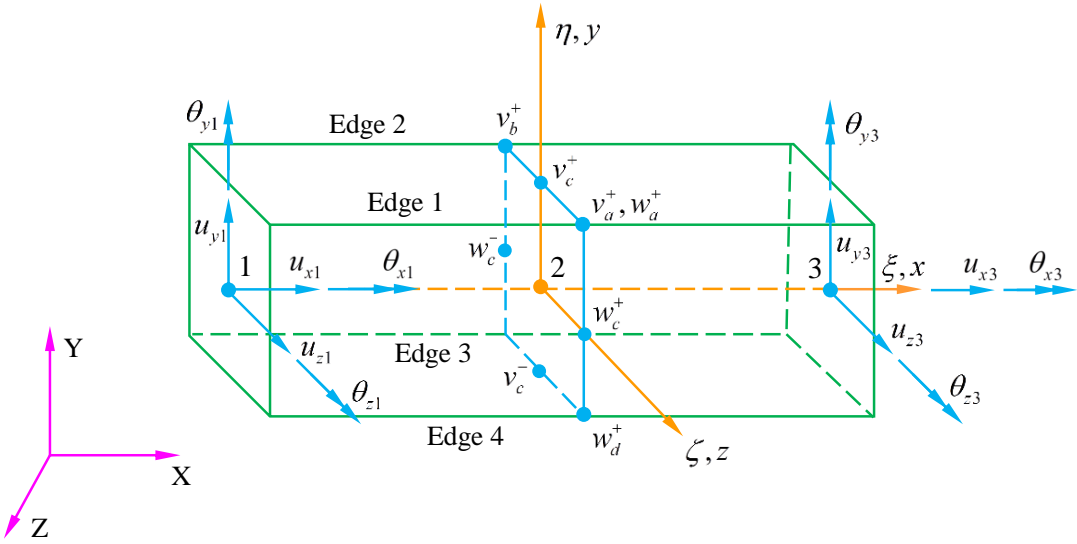


Figure 4.7 – Illustration of the beam finite element with rectangular cross section.

located. The nodal displacements in respective element local coordinates (see Figure 4.7) can be grouped into the following vectors:

$$\begin{aligned} \mathbf{u}_M &= \{ u_{x1m} \ u_{y1m} \ u_{z1m} \ \theta_{x1m} \ \theta_{y1m} \ \theta_{z1m} \ v_{cm}^+ \ v_{cm}^- \ v_{am}^+ \ v_{bm}^+ \\ &\quad w_{cm}^+ \ w_{cm}^- \ w_{am}^+ \ w_{dm}^+ \ u_{x3m} \ u_{y3m} \ u_{z3m} \ \theta_{x3m} \ \theta_{y3m} \ \theta_{z3m} \}^T \quad (4.43) \\ \mathbf{u}_S &= \{ u_{x1s} \ u_{y1s} \ u_{z1s} \ \theta_{x1s} \ \theta_{y1s} \ \theta_{z1s} \ v_{cs}^+ \ v_{cs}^- \ v_{as}^+ \ v_{bs}^+ \\ &\quad w_{cs}^+ \ w_{cs}^- \ w_{as}^+ \ w_{ds}^+ \ u_{x3s} \ u_{y3s} \ u_{z3s} \ \theta_{x3s} \ \theta_{y3s} \ \theta_{z3s} \}^T \end{aligned}$$

In Section 4.4, the contact contributions from Equation (4.21) to (4.30) are expressed in terms of nodal displacements. It is done by using the representation of edge functions evaluated at the closest points. This yields the additional terms to be incorporated into the tangent stiffness matrix and residual vector within the Newton iterations scheme. To this end, the variation and linearization of the displacement vectors \mathbf{U}_{mn} and \mathbf{U}_{sn} as well as their derivatives with respect to the local coordinates ξ_m and ξ_s need to be determined. For the values in local coordinate system (ξ, η, ζ) , one can write down:

$$\begin{aligned} \Delta \mathbf{u}_{mn} &= \frac{\partial \mathbf{u}_{mn}}{\partial \mathbf{u}_M} \Delta \mathbf{u}_M = \mathbf{D}_{mn} \cdot \Delta \mathbf{u}_M \\ \Delta \mathbf{u}_{sn} &= \frac{\partial \mathbf{u}_{sn}}{\partial \mathbf{u}_S} \Delta \mathbf{u}_S = \mathbf{D}_{sn} \cdot \Delta \mathbf{u}_S \end{aligned} \quad (4.44)$$

$$\begin{aligned} \delta \mathbf{u}_{mn} &= \frac{\partial \mathbf{u}_{mn}}{\partial \mathbf{u}_M} \delta \mathbf{u}_M = \mathbf{D}_{mn} \cdot \delta \mathbf{u}_M \\ \delta \mathbf{u}_{sn} &= \frac{\partial \mathbf{u}_{sn}}{\partial \mathbf{u}_S} \delta \mathbf{u}_S = \mathbf{D}_{sn} \cdot \delta \mathbf{u}_S \end{aligned} \quad (4.45)$$

$$\begin{aligned}\Delta \mathbf{u}_{mn,m} &= \frac{\partial \mathbf{u}_{mn,m}}{\partial \mathbf{u}_M} \Delta \mathbf{u}_M = \mathbf{E}_{mn} \cdot \Delta \mathbf{u}_M \\ \Delta \mathbf{u}_{sn,s} &= \frac{\partial \mathbf{u}_{sn,s}}{\partial \mathbf{u}_S} \Delta \mathbf{u}_S = \mathbf{E}_{sn} \cdot \Delta \mathbf{u}_S\end{aligned}\quad (4.46)$$

$$\begin{aligned}\delta \mathbf{u}_{mn,m} &= \frac{\partial \mathbf{u}_{mn,m}}{\partial \mathbf{u}_M} \delta \mathbf{u}_M = \mathbf{E}_{mn} \cdot \delta \mathbf{u}_M \\ \delta \mathbf{u}_{sn,s} &= \frac{\partial \mathbf{u}_{sn,s}}{\partial \mathbf{u}_S} \delta \mathbf{u}_S = \mathbf{E}_{sn} \cdot \delta \mathbf{u}_S\end{aligned}\quad (4.47)$$

The matrices \mathbf{D}_{mn} , \mathbf{D}_{sn} , \mathbf{E}_{mn} , \mathbf{E}_{sn} can be derived by tedious differentiation of the displacement approximation with respect to the local coordinates. Results of these calculations are presented in Appendix B.

Transformation of the Equation (4.44) to (4.47) from local coordinate system to the global coordinates yields the following relations:

$$\begin{aligned}\Delta \mathbf{U}_{mn} &= (\mathbf{T}_m^T \mathbf{D}_{mn} \mathbf{T}_{12m}) \Delta \mathbf{U}_M = \mathbf{G}_{mn} \Delta \mathbf{U}_M \\ \Delta \mathbf{U}_{sn} &= (\mathbf{T}_s^T \mathbf{D}_{sn} \mathbf{T}_{12s}) \Delta \mathbf{U}_S = \mathbf{G}_{sn} \Delta \mathbf{U}_S\end{aligned}\quad (4.48)$$

$$\begin{aligned}\delta \mathbf{U}_{mn} &= \mathbf{G}_{mn} \delta \mathbf{U}_M \\ \delta \mathbf{U}_{sn} &= \mathbf{G}_{sn} \delta \mathbf{U}_S\end{aligned}\quad (4.49)$$

$$\begin{aligned}\Delta \mathbf{U}_{mn,m} &= (\mathbf{T}_m^T \mathbf{E}_{mn} \mathbf{T}_{12m}) \Delta \mathbf{U}_M = \mathbf{H}_{mn} \Delta \mathbf{U}_M \\ \Delta \mathbf{U}_{sn,s} &= (\mathbf{T}_s^T \mathbf{E}_{sn} \mathbf{T}_{12s}) \Delta \mathbf{U}_S = \mathbf{H}_{sn} \Delta \mathbf{U}_S\end{aligned}\quad (4.50)$$

$$\begin{aligned}\delta \mathbf{U}_{mn,m} &= \mathbf{H}_{mn} \delta \mathbf{U}_M \\ \delta \mathbf{U}_{sn,s} &= \mathbf{H}_{sn} \delta \mathbf{U}_S\end{aligned}\quad (4.51)$$

Where the transformation matrix \mathbf{T}_{12m} , \mathbf{T}_{12s} are defined by Equation (3.64), in which \mathbf{T}_m , \mathbf{T}_s are defined as \mathbf{T}_α ($\alpha = m$ or s).

The linearization of the local coordinates of the contact points can be expressed by means of the nodal displacements as:

$$\begin{bmatrix} \Delta \xi_{mn} \\ \Delta \xi_{sn} \end{bmatrix} = \mathbf{A}^{-1} \left(\mathbf{B} \begin{bmatrix} \mathbf{G}_{mn} & \mathbf{0} \\ \mathbf{0} & \mathbf{G}_{sn} \end{bmatrix} + \mathbf{C} \begin{bmatrix} \mathbf{H}_{mn} & \mathbf{0} \\ \mathbf{0} & \mathbf{H}_{sn} \end{bmatrix} \right) \begin{bmatrix} \Delta \mathbf{U}_M \\ \Delta \mathbf{U}_S \end{bmatrix} = \mathbf{F} \begin{bmatrix} \Delta \mathbf{U}_M \\ \Delta \mathbf{U}_S \end{bmatrix} \quad (4.52)$$

Where,

$$\mathbf{F} = \mathbf{A}^{-1} \begin{bmatrix} (-\mathbf{X}_{mn,m}^T \cdot \mathbf{G}_{mn} - \mathbf{X}_{ms}^T \cdot \mathbf{H}_{mn}) & \mathbf{X}_{mn,m}^T \cdot \mathbf{G}_{sn} \\ -\mathbf{X}_{sn,s}^T \cdot \mathbf{G}_{mn} & (\mathbf{X}_{sn,s}^T \cdot \mathbf{G}_{sn} - \mathbf{X}_{ms}^T \cdot \mathbf{H}_{sn}) \end{bmatrix}, \mathbf{X}_{ms} = \mathbf{X}_{mn} - \mathbf{X}_{sn} \quad (4.53)$$

Similarly, the variations of the local coordinates are given by:

$$\begin{bmatrix} \delta\xi_{mn} \\ \delta\xi_{sn} \end{bmatrix} = \mathbf{F} \begin{bmatrix} \delta\mathbf{U}_M \\ \delta\mathbf{U}_S \end{bmatrix} \quad (4.54)$$

Furthermore, to simplify the notation the following matrix is introduced

$$\mathbf{L} = [\mathbf{G}_{mn} \ -\mathbf{G}_{sn}] + [\mathbf{X}_{mn,m} \ -\mathbf{X}_{sn,s}] \mathbf{F} \quad (4.55)$$

Having discretized the kinematic variables, finally the residual vector and the tangent stiffness matrix for the contact element can be calculated for both formulations: the penalty method and the Lagrange multipliers method. The contact contributions within penalty and Lagrange multiplier methods, resulting from Equation (4.21) to (4.24) can now be expressed as:

$$\Delta\delta\Pi_N^\epsilon = (\delta\mathbf{U}_M^T, \delta\mathbf{U}_S^T) [\mathbf{K}_N^\epsilon] (\Delta\mathbf{U}_M, \Delta\mathbf{U}_S)^T \quad (4.56)$$

$$\Delta\delta\Pi_N^\lambda = (\delta\mathbf{U}_M^T, \delta\mathbf{U}_S^T, \delta\lambda_N) [\mathbf{K}_N^\lambda] (\Delta\mathbf{U}_M, \Delta\mathbf{U}_S, \delta\lambda_N)^T \quad (4.57)$$

$$\delta\Pi_N^\epsilon = (\delta\mathbf{U}_M^T, \delta\mathbf{U}_S^T) [\mathbf{R}_N^\epsilon] \quad (4.58)$$

$$\delta\Pi_N^\lambda = (\delta\mathbf{U}_M^T, \delta\mathbf{U}_S^T, \delta\lambda_N) [\mathbf{R}_N^\lambda] \quad (4.59)$$

Finally, with matrices $\mathbf{G}, \mathbf{H}, \mathbf{F}, \mathbf{L}$ and the normal vector \mathbf{n} defined previously, the residual vector and symmetric tangent stiffness matrix for the penalty method has the following form:

$$\mathbf{K}_N^\epsilon = \epsilon_N \mathbf{K}_1 + \epsilon_N g_N \mathbf{K}_2 \quad (4.60)$$

$$\mathbf{R}_N^\epsilon = \epsilon_N g_N \mathbf{R}_1 \quad (4.61)$$

where:

$$\mathbf{R}_1 = \begin{bmatrix} \mathbf{G}_{mn}^T \mathbf{n} \\ -\mathbf{G}_{sn}^T \mathbf{n} \end{bmatrix} \quad (4.62)$$

$$\mathbf{K}_1 = \mathbf{R}_1 \otimes \mathbf{R}_1 \quad (4.63)$$

$$\begin{aligned} \mathbf{K}_2 = & \begin{bmatrix} \mathbf{H}_{mn}^T \mathbf{n} & \mathbf{0} \\ \mathbf{0} & -\mathbf{H}_{sn}^T \mathbf{n} \end{bmatrix} \mathbf{F} + \mathbf{F}^T \begin{bmatrix} \mathbf{n}^T \mathbf{H}_{mn} & \mathbf{0} \\ \mathbf{0} & -\mathbf{n}^T \mathbf{H}_{sn} \end{bmatrix} \\ & + \mathbf{F}^T \begin{bmatrix} \mathbf{n}^T \mathbf{X}_{mn,mm} & \mathbf{0} \\ \mathbf{0} & -\mathbf{n}^T \mathbf{X}_{sn,ss} \end{bmatrix} \mathbf{F} + \frac{1}{g_N} \mathbf{L}^T (\mathbf{1} - \mathbf{n} \cdot \mathbf{n}^T) \mathbf{L} \end{aligned} \quad (4.64)$$

while for the Lagrange multipliers method one gets

$$\mathbf{K}_N^\lambda = \begin{bmatrix} \lambda_N \mathbf{K}_2 & \mathbf{R}_1 \\ \mathbf{R}_1^T & \mathbf{0} \end{bmatrix} \quad (4.65)$$

$$\mathbf{R}_N^\lambda = \begin{bmatrix} \lambda_N \mathbf{R}_1 \\ g_N \end{bmatrix} \quad (4.66)$$

4.7 Smooth contact between enhanced 3D beam contact

4.7.1 3D curve smoothing using Hermite polynomial

A proper representation of surface geometry for bodies undergoing contact and sliding is a very important aspect of modeling in the finite element method. The fundamental issue is to ensure continuity and smoothness. In the case when a contact point moves from one element to another, the quadratic convergence of the Newton-Raphson method is affected. Hence, in the analysis of contact between beams with rectangular cross-sections, shape functions in the form of the third-order polynomials are used to provide the C^1 continuity of curves representing edges of beams. These functions are taken directly from the formulation of the beam finite elements. There are several methods of construction of a smooth curve. They involve two types of polynomial representation of a 3D curve, the Hermite's polynomials and the Bezier's curves, as well as two types of curve layout related to the beam nodes, the inscribed curve method and the node-preserving method [LIT 07a, LIT 07b, LIT 10]. Here, we adopt the inscribed curve method.

The suggested procedure of smoothing a curve in 3D is based only on current position vectors of nodes of beam elements discretizing a pair of contacting beams. Firstly, a contact search routine, presented in Section 4.5, preselects contact candidates, i.e. the closest beam elements. In this approach the smooth contact segments are constructed on two pairs of the adjacent closest beam elements. So, in fact, for each beam a pair of the closest elements has to be found. Then each of these pairs undergoes the smoothing. In the case of inscribed curve method, a segment of C^1 continuous curve is constructed using three adjacent nodes, as shown in Figure 4.8. This curve is formulated parametrically with the local coordinate ξ_m or ξ_s ranging from -1 to 1 . In the following, the subscript "m" or "s" will be skipped for the sake of notation brevity. Any point on the curve can be defined by its position vector:

$$\mathbf{A} = (X, Y, Z)^T \quad (4.67)$$

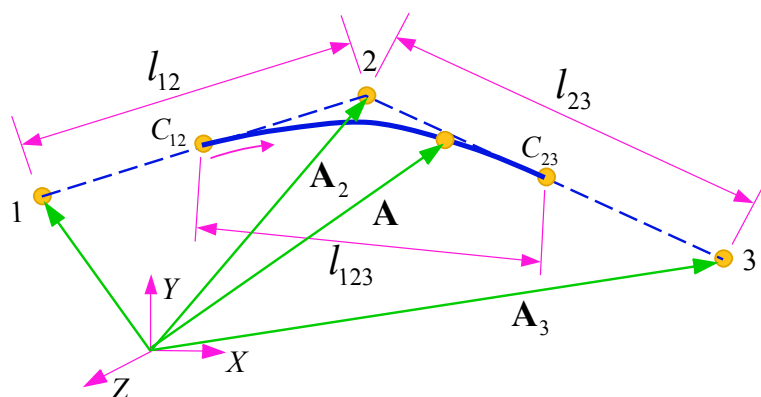


Figure 4.8 – Construction of inscribed curve segment.

Hermite's polynomials are used to define the curve mathematically, for an arbitrary point on the curve, it can be expressed by:

$$\begin{aligned} X &= a_1\xi^3 + b_1\xi^2 + c_1\xi + d_1 \\ Y &= a_2\xi^3 + b_2\xi^2 + c_2\xi + d_2 \\ Z &= a_3\xi^3 + b_3\xi^2 + c_3\xi + d_3 \end{aligned} \quad (4.68)$$

In the vector form, Equation (4.68) can be written down as:

$$\begin{aligned} X &= [a_1 \ b_1 \ c_1 \ d_1] [\xi^3 \ \xi^2 \ \xi \ 1]^T = \alpha_1 \cdot \xi \\ Y &= [a_2 \ b_2 \ c_2 \ d_2] [\xi^3 \ \xi^2 \ \xi \ 1]^T = \alpha_2 \cdot \xi \\ Z &= [a_3 \ b_3 \ c_3 \ d_3] [\xi^3 \ \xi^2 \ \xi \ 1]^T = \alpha_3 \cdot \xi \end{aligned} \quad (4.69)$$

The position vectors for three nodes of two adjacent beam elements involved in the smoothing procedure are written in the form:

$$\begin{aligned} \mathbf{A}_1 &= (X_1, Y_1, Z_1)^T \\ \mathbf{A}_2 &= (X_2, Y_2, Z_2)^T \\ \mathbf{A}_3 &= (X_3, Y_3, Z_3)^T \end{aligned} \quad (4.70)$$

The boundary conditions required to determine the coefficients of Hermite's polynomial in Equation (4.69), which ensure that the curve passes through the mid points C_{12} and C_{23} , and forcing it to be tangent to the straight line segments, there is:

$$\begin{aligned} \xi = -1 \Rightarrow X &= X_{12} = \frac{X_1 + X_2}{2}, \quad Y = Y_{12} = \frac{Y_1 + Y_2}{2}, \quad Z = Z_{12} = \frac{Z_1 + Z_2}{2} \\ \xi = 1 \Rightarrow X &= X_{23} = \frac{X_2 + X_3}{2}, \quad Y = Y_{23} = \frac{Y_2 + Y_3}{2}, \quad Z = Z_{23} = \frac{Z_2 + Z_3}{2} \\ \xi = -1 \Rightarrow \frac{\partial X}{\partial \xi} &= \varphi_{12X} = \frac{X_2 - X_1}{2l_{12}}l_{123}, \quad \frac{\partial Y}{\partial \xi} = \varphi_{12Y} = \frac{Y_2 - Y_1}{2l_{12}}l_{123}, \quad \frac{\partial Z}{\partial \xi} = \varphi_{12Z} = \frac{Z_2 - Z_1}{2l_{12}}l_{123} \\ \xi = 1 \Rightarrow \frac{\partial X}{\partial \xi} &= \varphi_{23X} = \frac{X_3 - X_2}{2l_{23}}l_{123}, \quad \frac{\partial Y}{\partial \xi} = \varphi_{23Y} = \frac{Y_3 - Y_2}{2l_{23}}l_{123}, \quad \frac{\partial Z}{\partial \xi} = \varphi_{23Z} = \frac{Z_3 - Z_2}{2l_{23}}l_{123} \end{aligned} \quad (4.71)$$

The straight line distances $1 - 2$, $2 - 3$ and $C_{12} - C_{23}$ are present. They are denoted by l_{12} , l_{23} and l_{123} respectively, and can be calculated as:

$$\begin{aligned} l_{12} &= \|\mathbf{A}_2 - \mathbf{A}_1\| \\ l_{23} &= \|\mathbf{A}_3 - \mathbf{A}_2\| \\ l_{123} &= \left\| \frac{\mathbf{A}_2 + \mathbf{A}_3}{2} - \frac{\mathbf{A}_1 + \mathbf{A}_2}{2} \right\| \end{aligned} \quad (4.72)$$

Expressing the polynomial coefficients in the vector α_1 in terms of the coordinates and the slopes of the center points:

$$\alpha_1 = \frac{1}{4} \begin{bmatrix} 1 & -1 & 1 & 1 \\ 0 & 0 & -1 & 1 \\ -3 & 3 & -1 & -1 \\ 2 & 2 & 1 & -1 \end{bmatrix} \begin{bmatrix} X_{c12} \\ X_{c23} \\ \Phi_{c12X} \\ \Phi_{c23X} \end{bmatrix} = B_1 \begin{bmatrix} X_{c12} \\ X_{c23} \\ \Phi_{c12X} \\ \Phi_{c23X} \end{bmatrix} \quad (4.73)$$

Finally, the polynomial coefficients in the vector α_1 can be expressed in terms of components of the position vectors:

$$\alpha_1 = B_1 \frac{1}{2} \begin{bmatrix} 1 & 1 & 0 \\ 0 & 1 & 1 \\ -\frac{l_{123}}{l_{12}} & \frac{l_{123}}{l_{12}} & 0 \\ 0 & -\frac{l_{123}}{l_{23}} & \frac{l_{123}}{l_{23}} \end{bmatrix} \begin{bmatrix} X_1 \\ X_2 \\ X_3 \end{bmatrix} = B_1 B_2 \begin{bmatrix} X_1 \\ X_2 \\ X_3 \end{bmatrix} \quad (4.74)$$

Similarly, for vector α_2, α_3 , there is:

$$\alpha_2 = B_1 B_2 \begin{bmatrix} Y_1 \\ Y_2 \\ Y_3 \end{bmatrix}, \alpha_3 = B_1 B_2 \begin{bmatrix} Z_1 \\ Z_2 \\ Z_3 \end{bmatrix} \quad (4.75)$$

It is possible to express the position vector of any point on the smooth curve in terms of the nodal coordinates:

$$\begin{aligned} X &= \xi \cdot \left[B_1 B_2 (X_1, X_2, X_3)^T \right] \\ Y &= \xi \cdot \left[B_1 B_2 (Y_1, Y_2, Y_3)^T \right] \\ Z &= \xi \cdot \left[B_1 B_2 (Z_1, Z_2, Z_3)^T \right] \end{aligned} \quad (4.76)$$

4.7.2 Finite element discretization of smooth contact

Application of Equation (4.76) for the position vectors of the points on smooth curve, presented in Section 4.7.1, in the modeling of axes of two contacting beams with rectangular cross-sections leads to the formulation of smooth beam contact finite elements. Each of these elements involves nodes of two pairs of adjacent beam finite elements. Since the proposed curve approximations do not depend on nodal rotations but only linear displacements. Hence, the involved degrees of freedom of the contact element will be 18 displacements of 6 end nodes involved (3 per contacting beam), which can be assembled in the following way:

$$\begin{aligned} q = \{ &u_{x1m} \ u_{y1m} \ u_{z1m} \ u_{x3m} \ u_{y3m} \ u_{z3m} \ u_{x5m} \ u_{y5m} \ u_{z5m} \\ &u_{x1s} \ u_{y1s} \ u_{z1s} \ u_{x3s} \ u_{y3s} \ u_{z3s} \ u_{x5s} \ u_{y5s} \ u_{z5s} \}^T = \{ u_M^T, u_S^T \}^T \end{aligned} \quad (4.77)$$

Discretization of the kinematic variables presented in Sections 4.6 is carried out in the same way for the presented smooth elements. The same notation for the matrices can be

applied and all the relations remain unchanged. The differences are how to determine the matrices \mathbf{G}_{mn} and \mathbf{G}_{sn} in Equation (4.48) and (4.49), \mathbf{H}_{mn} and \mathbf{H}_{sn} in (4.50) and (4.51). Their components should be calculated as partial derivatives with respect to the nodal displacements and their derivatives. These calculations are carried out using the symbolic algebra program Matlab. Due to the very complex character of the Equation (4.76), the explicit representation of these matrices is too long to be presented here. Hence, instead of presenting the matrices themselves, we present the commands of Matlab worksheet in Appendix C, which allow for calculation of these matrices and creation of an output ready-to-use Matlab computer code.

In the case of inscribed curve representation, each of these matrices has dimensions 3×9 , which influences the dimensions of all further matrices included in the residual vectors and the tangent stiffness matrices of the contact beam finite elements. The matrix \mathbf{F} in Equation (4.52) used to calculate the linearization and variation of the local coordinates has the dimensions 2×18 . The auxiliary matrix \mathbf{L} given in Equation (4.55) is a 3×18 matrix. Finally, the 18×18 tangent stiffness matrices and the 18 component residual vectors for contact elements can be determined.

4.8 Numerical examples

Since the final goal of the present work is to use the new 3D beam element to model and simulate the behavior of the yarn in a unit cell (shown in Figure 4.9), which includes three kinds of contact, as introduced in Section 4.5: (1) one pairs of points (Figure 4.4a), (2) edge to edge (Figure 4.4b), (3) surface to surface (Figure 4.4c).

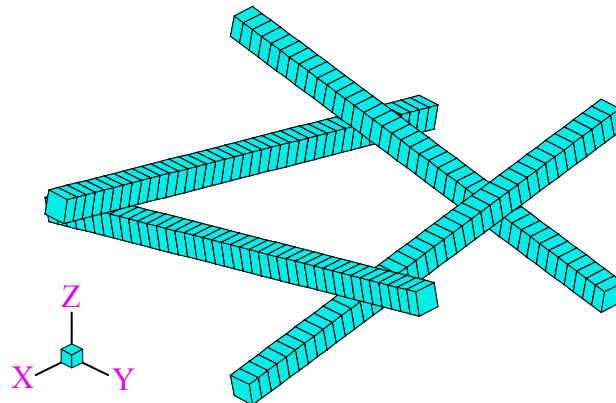


Figure 4.9 – Illustration of unit cell with rectangular cross-section.

In this section, three numerical examples of the frictionless contact between new 3D beams with rectangular cross sections are presented. All of the three examples are solved using penalty method. It is well known, that the Penalty method requires a proper value of the penalty parameter to avoid the ill-conditioning of tangent stiffness matrix and fulfill

the constraint conditions. The purpose of the presented examples is a qualitative analysis of contact and checking the correctness and the effectiveness of the proposed 3D beam finite element, the contact numerical algorithm is modified base that of [LIT 10], hence, the physical solution of the problems is of a smaller importance.

For the model in Matlab, each beam has 10 elements while for the beam model in Abaqus, the mesh model is the same as Figure 2.11 (b), at least 640 elements for each beam are used for the same calculation. And the results using the enhanced 3D beam element from Matlab program and those from Abaqus using C3D8I element are compared systematically. The following data are used in the calculations: $E = 1 \times 10^5 \text{ MPa}$, $\nu = 0.3$, cross section dimensions $b = h = 1 \text{ mm}$, length 10mm.

4.8.1 Example 1: point to point contact

In this example, contact between two cantilever beams shown in Figure 4.10 is analyzed. There is only one pair of contact points. For beam m, the free end is subjected to a concentrated force $F = -70 \text{ N}$ in y direction, applied in 70 increments. And penalty parameter is $\epsilon_N = 3000$.

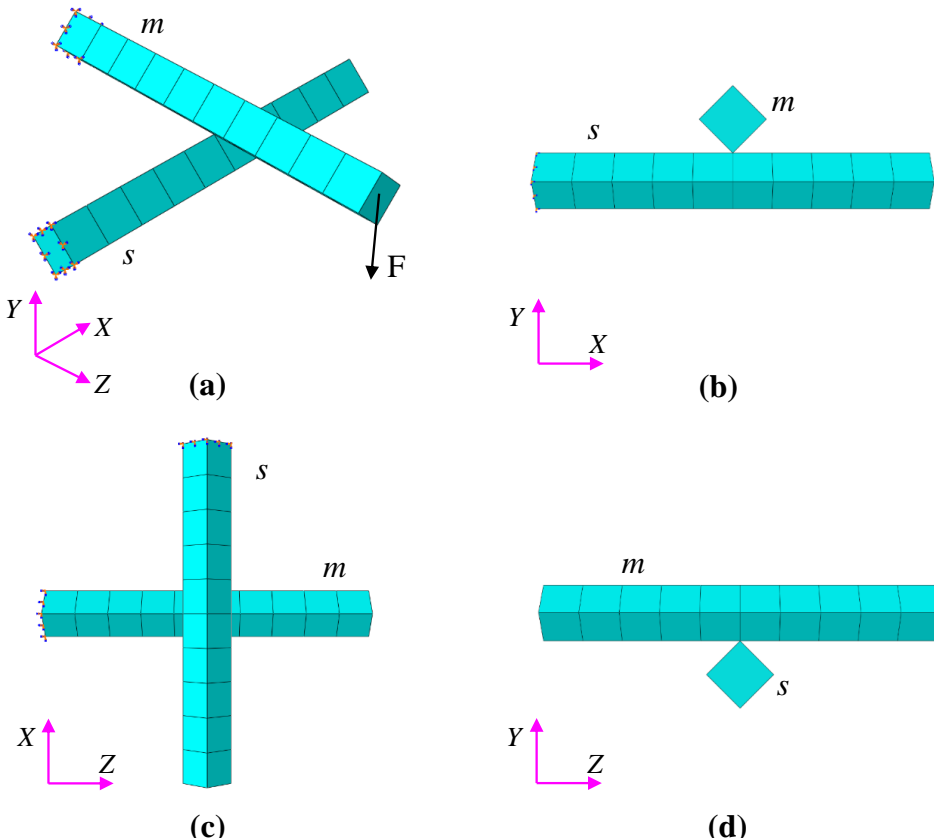


Figure 4.10 – Initial configuration of contact between one pair of points. (a). 3D view. (b). Plane XY. (c). Plane XZ. (d). Plane YZ.

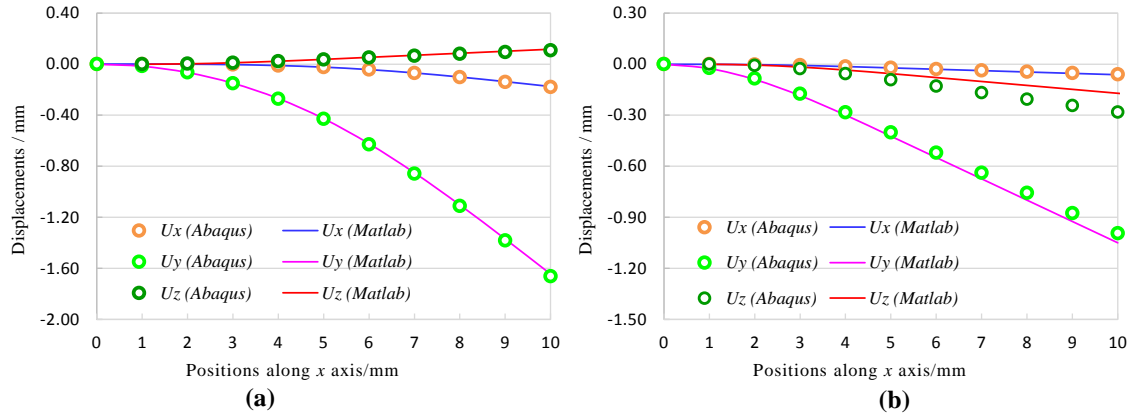


Figure 4.11 – Displacements of the centroidal axis in three directions. (a) Beam m . (b) Beam s .

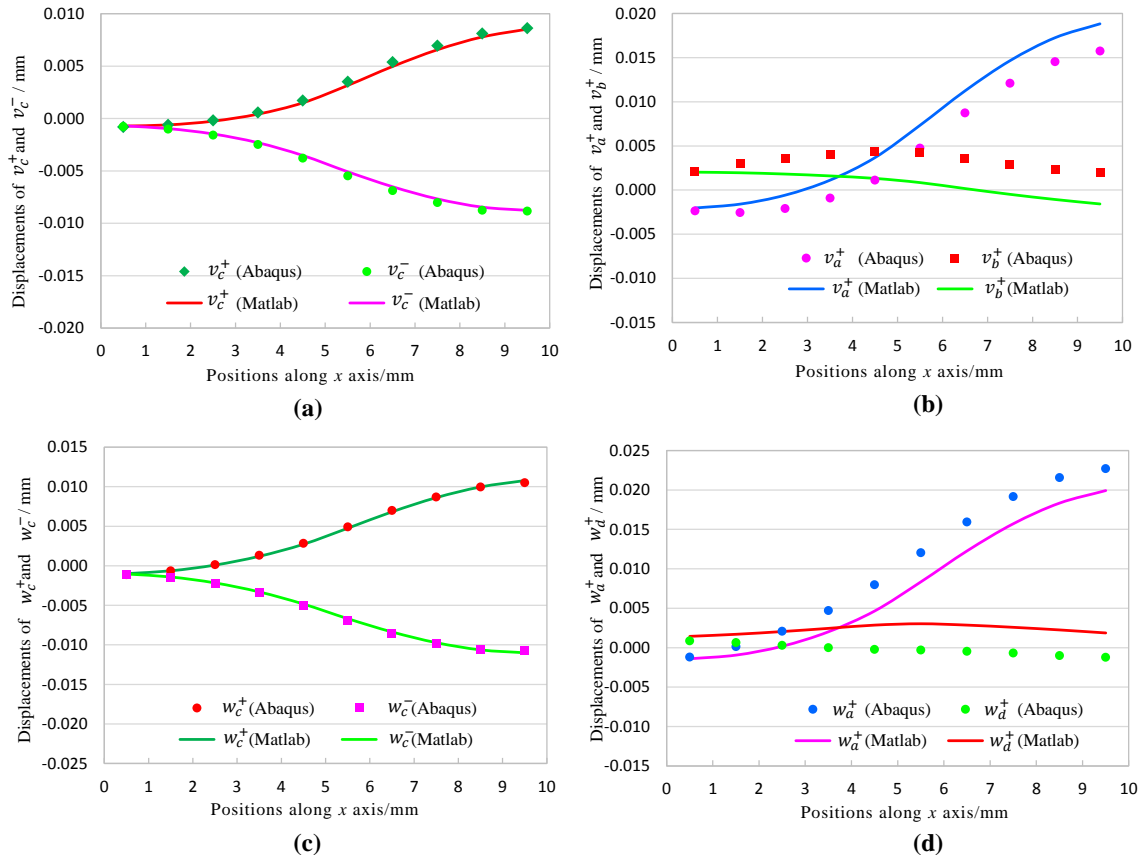


Figure 4.12 – Displacement distribution comparisons of cross section of beam m . (a). Distribution of v_c^+ and v_c^- . (b). Distribution of v_a^+ and v_b^+ . (c). Distribution of w_c^+ and w_c^- . (d). Distribution of w_a^+ and w_d^+ .

Figure 4.11 gives the results of the comparisons of the displacements of centroidal

4. Enhanced 3D beam to beam contact

axis of beam m and beam s separately. For beam m , the displacements in x, y, z directions from both Matlab and Abaqus are quite the same. While for beam s , the displacements in x and y direction from the two results are almost the same, but there's a little difference for the values in z direction.

We also compare the displacement distributions of cross section obtained from Abaqus and Matlab, as shown in Figure 4.12 (beam m) and Figure 4.13 (beam s). From Figure 4.12, we can see that the distributions of v_c^+ and v_c^- , w_c^+ and w_c^- of beam m from both Abaqus and Matlab are quite the same, shown in Figure 4.12(a) and 4.12(c). For distributions of v_a^+ and v_b^+ , w_a^+ and w_d^+ , the values are close and the change trend are similar (see Figure 4.12b and 4.12d), which don't show big difference. From Figure 4.13, we can see the distributions of v_c^+ and v_c^- , w_c^+ and w_c^- of beam s from both Abaqus and Matlab are close (Figure 4.13a and 4.13c), and the values of v_a^+ and v_b^+ , w_a^+ and w_d^+ of both two results have similar change trend though exist some errors (see Figure 4.13b and 4.13d).

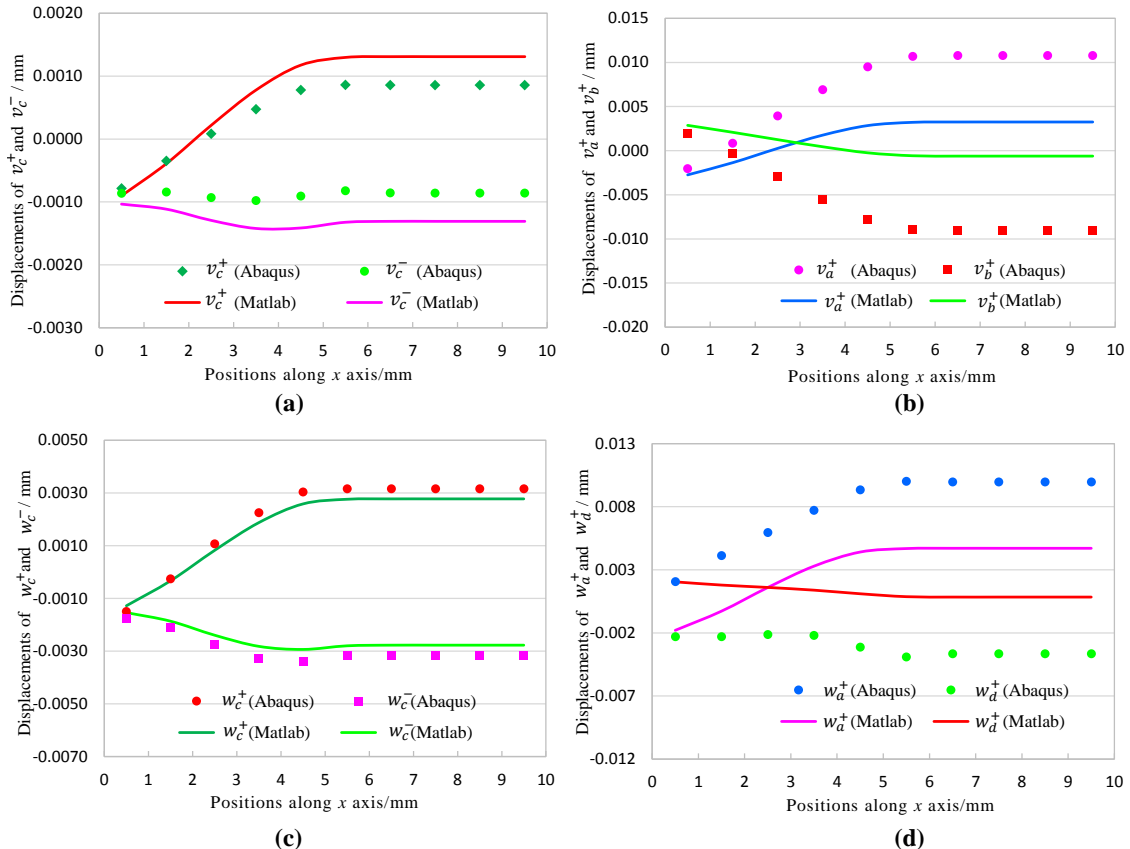


Figure 4.13 – Displacement distribution comparisons of cross section of beam s . (a). Distribution of v_c^+ and v_c^- . (b). Distribution of v_a^+ and v_b^+ . (c). Distribution of w_c^+ and w_c^- . (d). Distribution of w_a^+ and w_d^+ .

From the observation, we can see that all the results for beam m are very good while existing some errors for beam s , the problem isn't the beam element itself, but the contact

algorithm calculation method and how to transfer the contact force to the transverse cross section. The contact algorithm is just an approximation, which may be different from that in commercial software Abaqus. Another reason may be that the shape function ($v(x, y, z)$ and $w(x, y, z)$) in Equation (2.46) and (2.47) of the enhanced 3D beam element aren't totally complete quadratic since we don't have enough information for building the completely quadratic polynomial. Therefore, while subjected contact force in the point on the edge of beam s , the cross section doesn't deform symmetrically.

4.8.2 Example 2: edge to edge contact

In this example, we consider a pair of beam with edge to edge contact, shown in Figure 4.14. The free end of beam m is subjected to a concentrated force $F = -70N$ in y direction, applied in 70 increments, and the penalty parameter $\epsilon_N = 3000$.

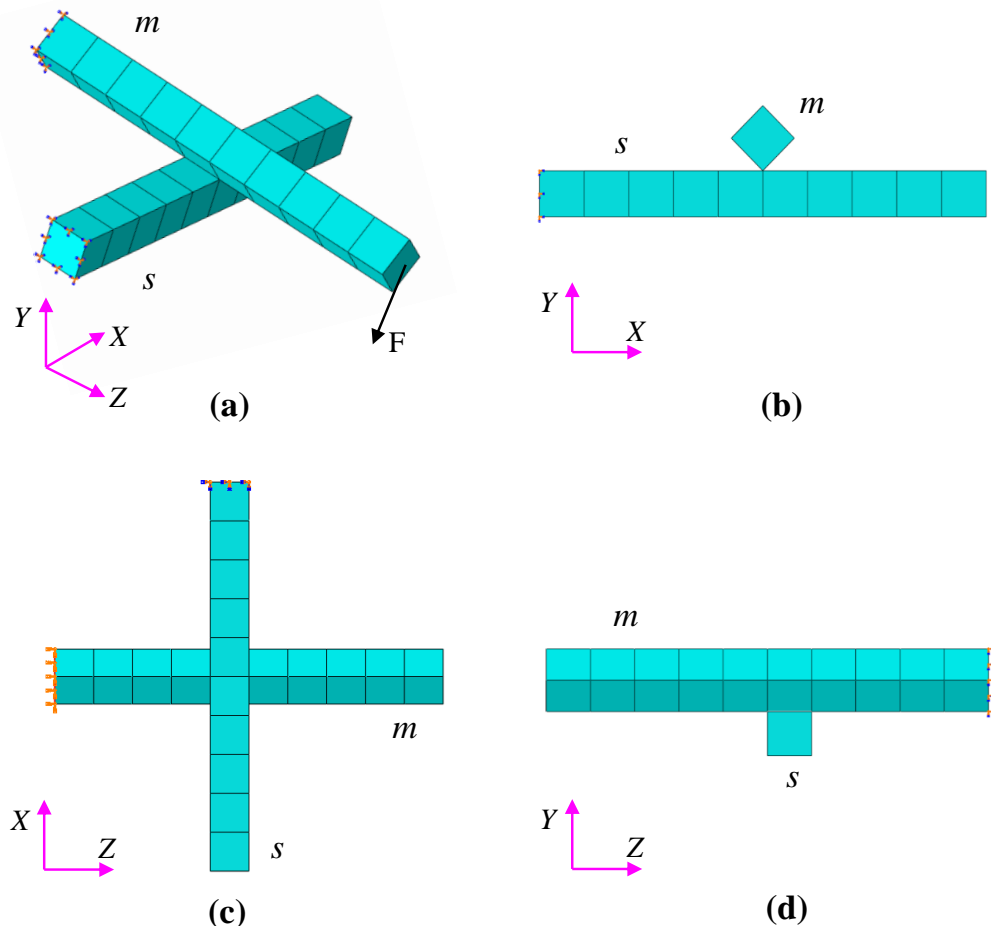


Figure 4.14 – Initial configuration of contact between edge to edge. (a). 3D view. (b). Plane XY. (c). Plane XZ. (d). Plane YZ.

4. Enhanced 3D beam to beam contact

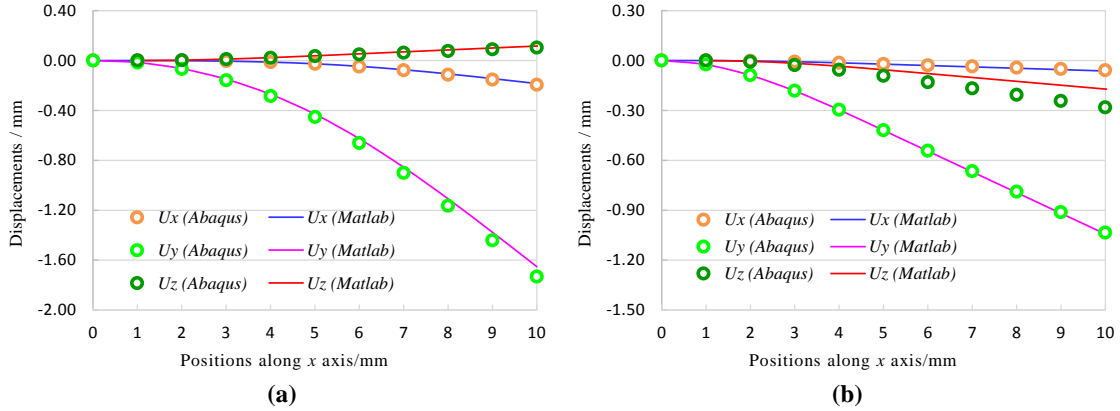


Figure 4.15 – Displacements of the centroidal axis in three directions. (a) Beam *m*. (b) Beam *s*.

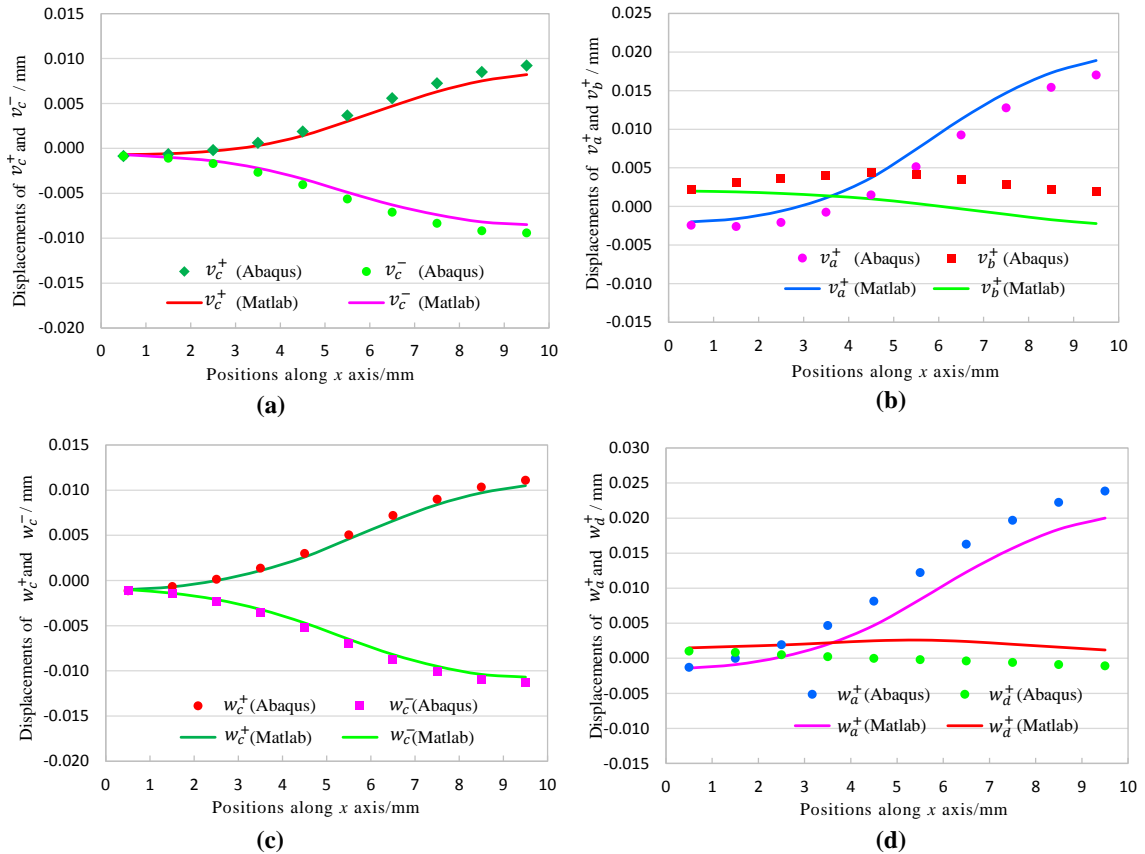


Figure 4.16 – Displacement distribution comparisons of cross section of beam *m*. (a). Distribution of v_c^+ and v_c^- . (b). Distribution of v_a^+ and v_b^+ . (c). Distribution of w_c^+ and w_c^- . (d). Distribution of w_a^+ and w_d^+ .

The results of the comparisons of the displacements of centroidal axis of beam m and beam s can be seen in Figure 4.15. From Figure 4.15(a), we can see that the displacements of beam m obtained using the enhanced 3D beam element are quite the same as the results from Abaqus 3D simulations. However, there exists some errors for the displacements of beam s in z direction while the values in x and y directions are almost the same, see in Figure 4.15(b). Figure 4.16 and Figure 4.17 show the displacement distributions of cross section of beam m and beam s obtained from Abaqus and Matlab, respectively. All the comparisons for beam m is better than those of beam s , the possible reason is explained in Section 4.8.1.

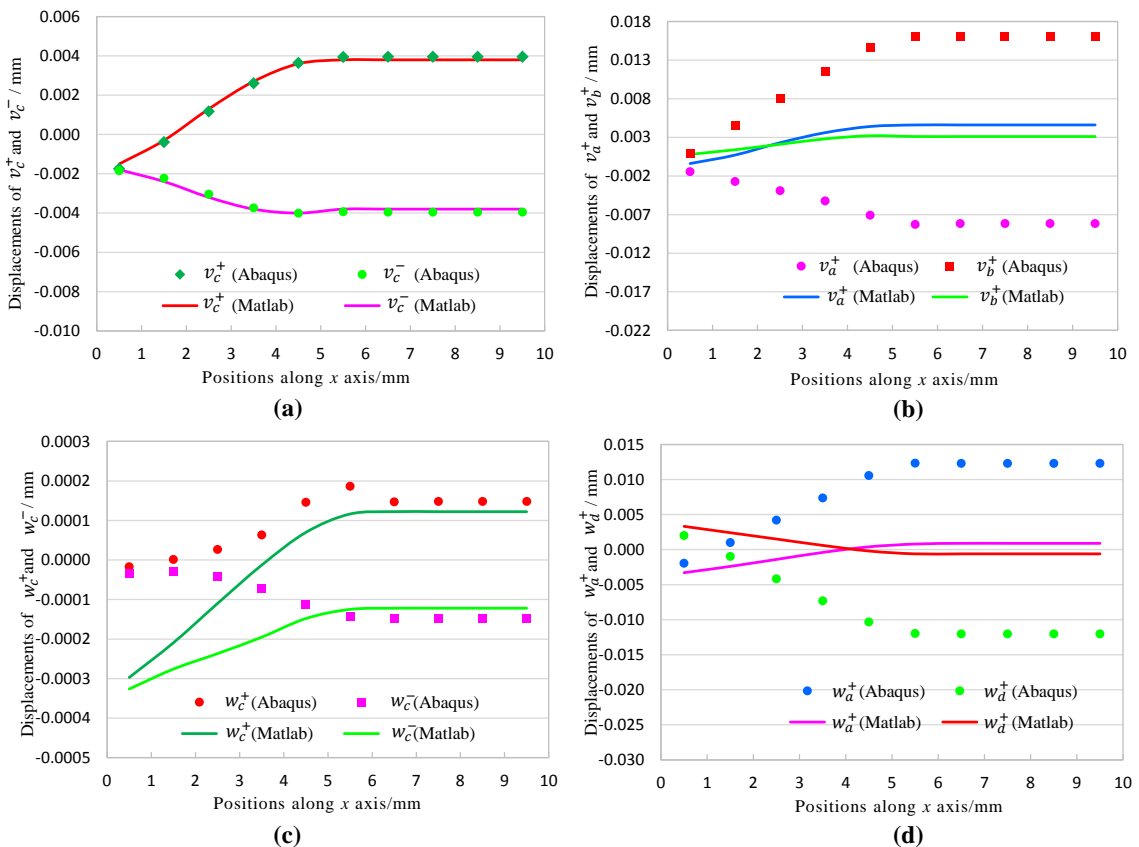


Figure 4.17 – Displacement distribution comparisons of cross section of beam s . (a). Distribution of v_c^+ and v_c^- . (b). Distribution of v_a^+ and v_b^+ . (c). Distribution of w_c^+ and w_c^- . (d). Distribution of w_a^+ and w_d^+ .

4.8.3 Example 3: surface to surface contact

Here, a pair of beams with surface to surface contact is considered, as shown in Figure 4.18. The free end of beam m is subjected to a concentrated force $F = -70N$ in y direction, applied in 70 increments, and the penalty parameter $\varepsilon_N = 500$.

4. Enhanced 3D beam to beam contact

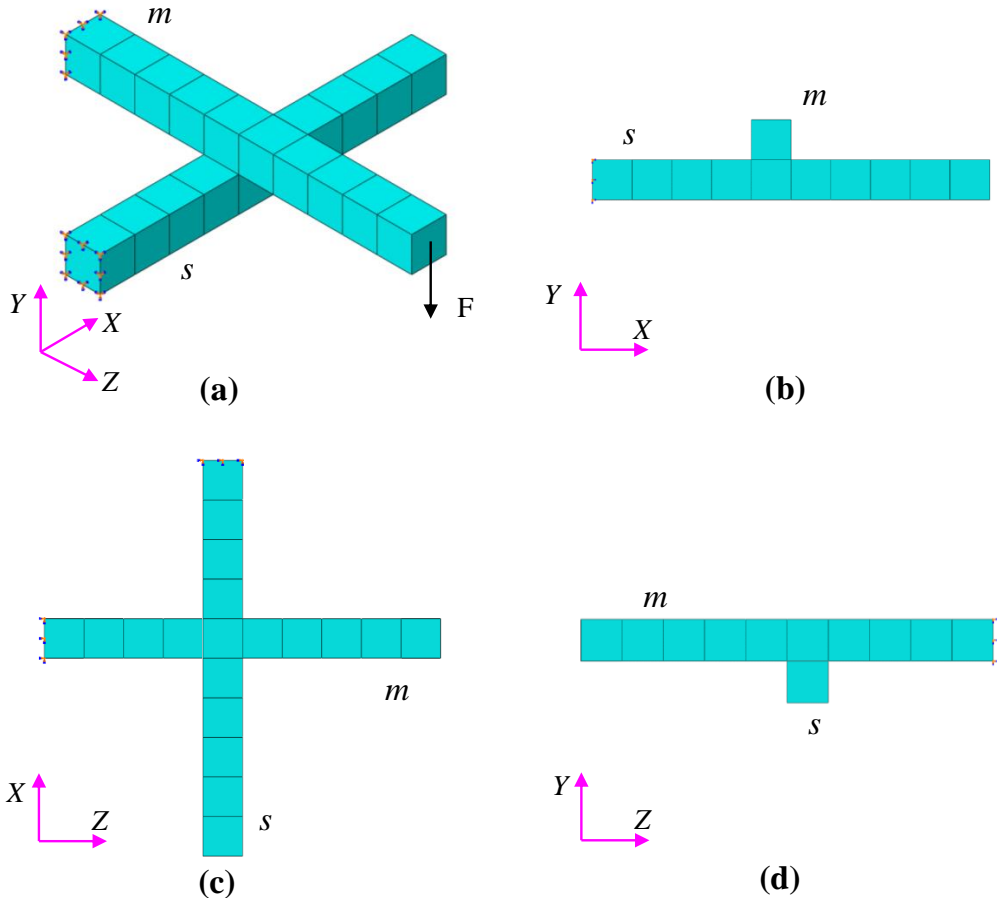


Figure 4.18 – Initial configuration of contact between surface to surface. (a). 3D view. (b). Plane XY. (c). Plane XZ. (d). Plane YZ.

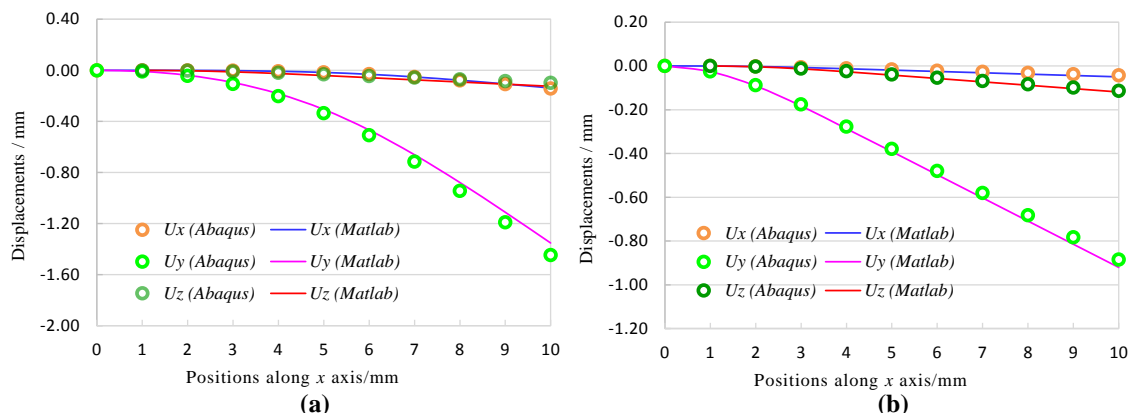


Figure 4.19 – Displacements of the centroidal axis in three directions. (a) Beam *m*. (b) Beam *s*.

Figure 4.19 shows the results of the comparisons of the displacements of centroidal axis of beam m and beam s respectively, from which we can see that the displacements of beam m and s obtained using the enhanced 3D beam element are quite the same as the results from Abaqus 3D simulations. The displacement distributions of cross section of beam m and beam s obtained from Abaqus and Matlab are shown in Figure 4.20 and Figure 4.21 respectively. The results are not good except the distributions of v_c^+ and v_c^- for both beam m and s . The possible reason may be the same as explained in Section 4.8.1. Another reason may be the number of the elements, since there are at least 640 elements for each beam in Abaqus while just 10 elements used in Matlab.

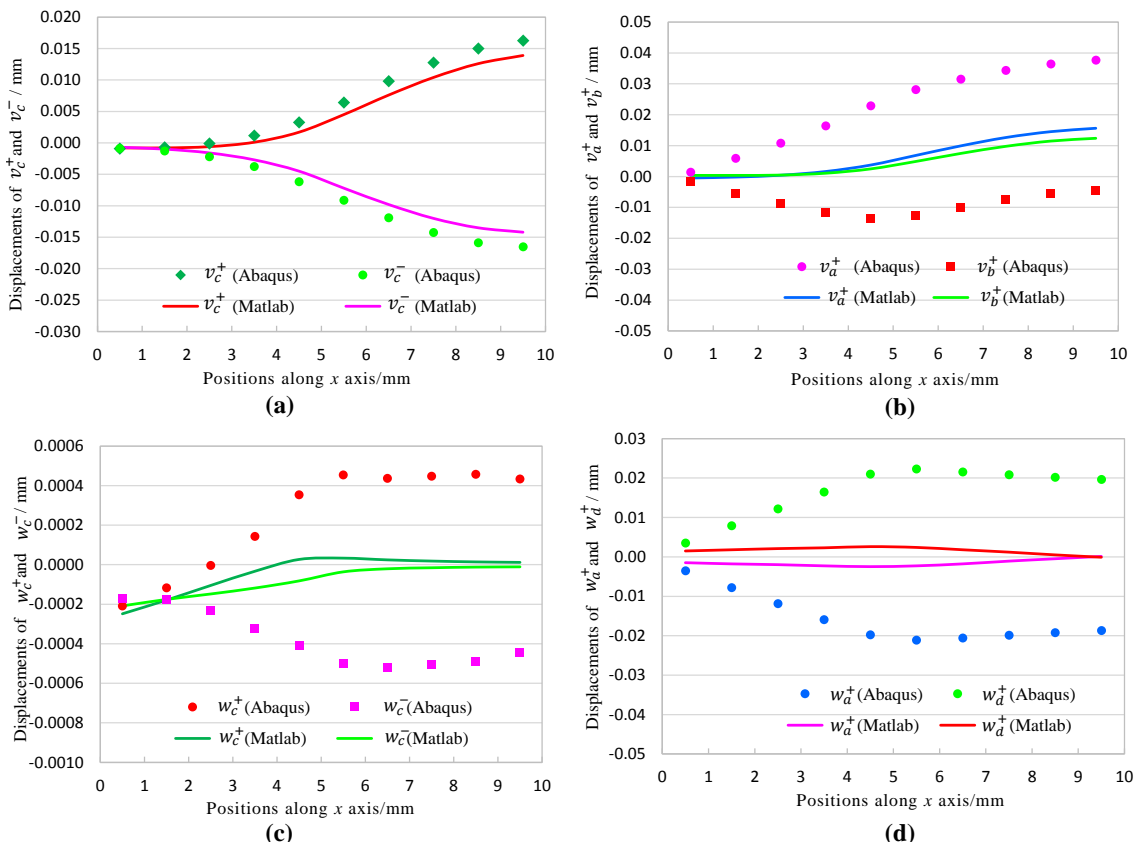


Figure 4.20 – Displacement distribution comparisons of cross section of beam m . (a). Distribution of v_c^+ and v_c^- . (b). Distribution of v_a^+ and v_b^+ . (c). Distribution of w_c^+ and w_c^- . (d). Distribution of w_a^+ and w_d^+ .

4.9 Conclusions and future developments

In this chapter, the contact behavior is introduced and validation for new 3D beam to beam contact with rectangular cross section is carried out. The contact formulation is derived on the basis of Penalty formulation and Updated Lagrangian formulation using physical

4. Enhanced 3D beam to beam contact

shape functions with shear effect included. An effective contact search algorithm, which is necessary to determine an active set for the contact contribution treatment, is elaborated. And a consistent linearization of contact contribution is derived and expressed in suitable matrix form, which is easy to use in FEM approximation. Finally, some numerical examples are presented which are only qualitative analysis of contact and checking the correctness and the effectiveness of the proposed 3D beam element. Hence, the results from the program implanted in Matlab is not totally the same as those from ABAQUS, which will be improved in the future work. In the next step, we should further improve the enhanced 3D beam element and the contact formulation. And the simulations base on Updated Lagrangian formulation should be carried out and compared with the results from those based on Penalty formulation.

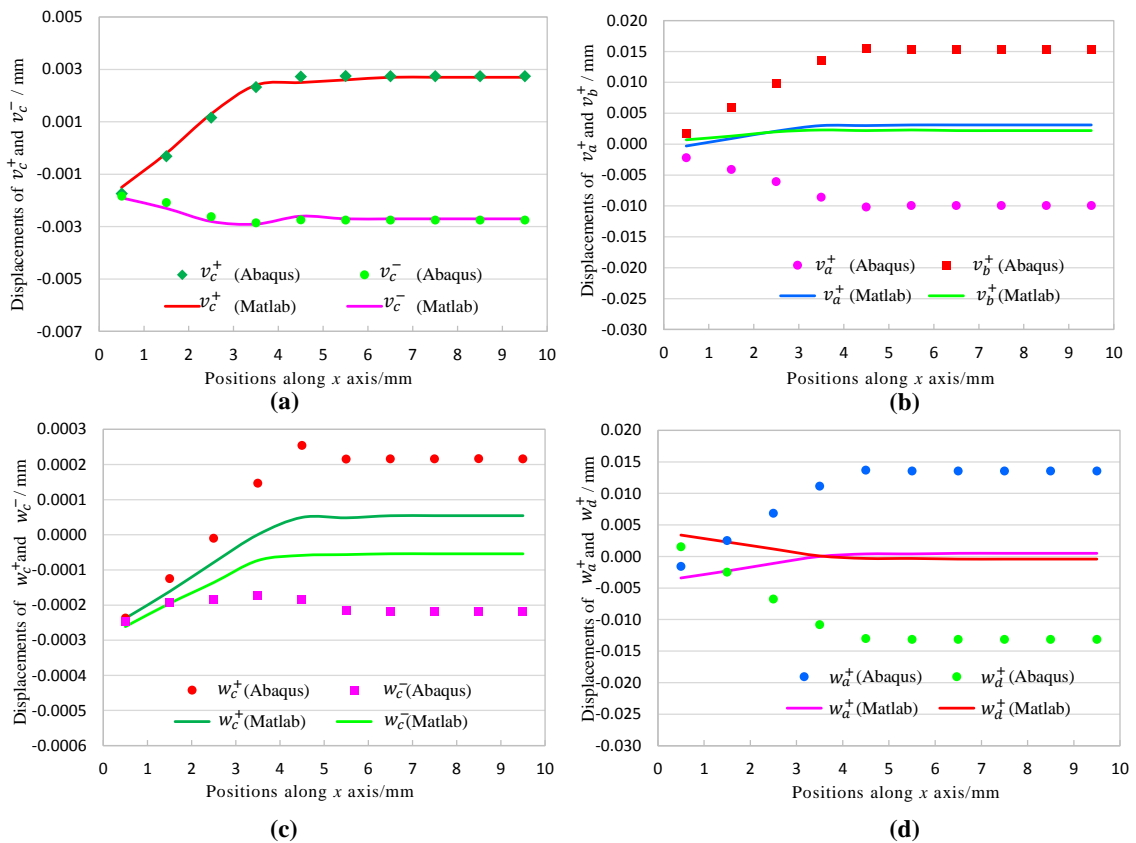


Figure 4.21 – Displacement distribution comparisons of cross section of beam s . (a). Distribution of v_c^+ and v_c^- . (b). Distribution of v_a^+ and v_b^+ . (c). Distribution of w_c^+ and w_c^- . (d). Distribution of w_a^+ and w_d^+ .

Conclusions and perspectives

This thesis is devoted to propose a new 3D beam element with deformable section while breaking from classical beam hypothesis. The idea is inspired by the evolution of an enriched shell element which has been firstly introduced in a 2D beam element in order to validate the interest of such technique.

The new beam element is an evolution of a two nodes Timoshenko beam element with an extra node located at mid-length. In this way, the new 3D beam element formulation should include these main features as follows: each element has two end nodes which are treated by combining Saint-Venant and Timoshenko hypothesis; the transverse strains of both thickness and width direction are introduced based on the additional central node. The transverse strain distributions are linear, and the formulation of displacement is completely quadratic by adding the terms coupling the deformation in both transverse directions; fully 3D constitutive law can be used directly since three extra strain components ϵ_{yy} , ϵ_{zz} and $2\epsilon_{yz}$ are introduced. The proposed element has been introduced in a Matlab finite element code and a series of linear/small strain cases have been realized and the results are systematically compared with the corresponding values from ABAQUS/Standard 3D simulations. Both results obtained are in good agreement and quite the same. Such results show, if needed, that the 8 extra degrees of freedom are sufficient to introduce the coupling between ϵ_{yy} and ϵ_{zz} .

The second step is to introduce the orthotropic behavior and carry out validation for large displacements/small strains based on Updated Lagrangian Formulation. A series of numerical analyses are carried out, the results from Matlab using the enhanced 3D beam element are quite the same with those from ABAQUS/Standard 3D simulations, which shows that the enhanced 3D element can provide an excellent numerical performance under large displacement condition (large rotation).

Contact behavior is introduced based on the basis of Penalty Formulation and Updated Lagrangian formulation using physical shape functions with shear effect included. An effective contact search algorithm is elaborated. And a consistent linearization of contact contribution is derived and expressed in suitable matrix form, which is easy to use in FEM approximation. Finally, some numerical examples are presented: point to point contact, edge to edge contact and surface to surface contact. The results obtained from Matlab and ABAQUS/Standard 3D simulations are similar though some errors exist, which don't show big difference. However, the results of contact shown in the present work are only qualitative analysis of contact and checking the correctness and the effectiveness of the proposed 3D beam element, the physical solution of the problems is of a smaller

importance. Hence, the results from the program implanted in Matlab is not totally the same as those from ABAQUS, which will be improved in the future work.

Perspectives

The final goal of the present work is to use the new 3D beam elements to model yarns in a textile composite preform. Therefore, besides the major conclusions obtained in this thesis, additional investigations can be done in the future works. A summary of these is presented below:

- Improve the contact algorithm so that the contact force can be transferred effectively.
- The simulations of contact behavior base on Updated Lagrangian formulation should be carried out and compared with the results from that based on Penalty formulation.
- Introduce the contract behavior into a unit cell simulation. The model can be built in Abaqus or TexGen, and then imported into Matlab for calculations using the new 3D beam element.
- Introduce the friction behavior into the contact model which is much closer to the realistic.
- Improve and optimize algorithm used so that we can compare the CPU time with that of ommercial software Abaqus.
- Realize the visualizations, which can show the results intuitively.

Appendices

Appendix A

Strain-displacement transformation matrix B

The explicit form of the expression of strain-displacement transformation matrix ${}^t\bar{\mathbf{B}}$ in Equation (3.57) in Section 3.7 is very long. In order to simplify the notation, bar over the symbols, superscript "t" and subscript "t" used previously are dropped here. Symbol \mathbf{B} is used for short, which can be expressed as follows:

$$[B]_{6 \times 20} = \begin{bmatrix} R_{11}H'_1 & 0 & 0 & 0 & A_{y1} & A_{z1} & 0 & 0 & 0 & 0 \\ 0 & R_{21}H'_1 & 0 & B_{x1} & 0 & B_{z1} & B_{v1} & B_{v2} & B_{v3} & B_{v4} \\ 0 & 0 & R_{31}H'_1 & C_{x1} & C_{y1} & 0 & 0 & 0 & 0 & 0 \\ R_{21}H'_1 & R_{11}H'_1 & 0 & D_{x1} & D_{y1} & D_{z1} & D_{v1} & D_{v2} & D_{v3} & D_{v4} \\ R_{31}H'_1 & 0 & R_{11}H'_1 & E_{x1} & E_{y1} & E_{z1} & 0 & 0 & 0 & 0 \\ 0 & R_{31}H'_1 & R_{21}H'_1 & F_{x1} & F_{y1} & F_{z1} & F_{v1} & F_{v2} & F_{v3} & F_{v4} \end{bmatrix} \quad (A.1)$$

$$\begin{bmatrix} 0 & 0 & 0 & 0 & R_{11}H'_3 & 0 & 0 & 0 & A_{y3} & A_{z3} \\ 0 & 0 & 0 & 0 & 0 & R_{21}H'_3 & 0 & B_{x3} & 0 & B_{z3} \\ C_{w1} & C_{w2} & C_{w3} & C_{w4} & 0 & 0 & R_{31}H'_3 & C_{x3} & C_{y1} & C_{z3} \\ 0 & 0 & 0 & 0 & R_{21}H'_3 & R_{11}H'_3 & 0 & D_{x3} & D_{y1} & D_{z3} \\ E_{w1} & E_{w2} & E_{w3} & E_{w4} & R_{31}H'_3 & 0 & R_{11}H'_3 & E_{x3} & E_{y1} & E_{z3} \\ F_{w1} & F_{w2} & F_{w3} & F_{w4} & 0 & R_{31}H'_3 & R_{21}H'_3 & F_{x3} & F_{y1} & F_{z3} \end{bmatrix}$$

Other simplifying notations used in Equation (A.1) are:

$$A_{yi} = R_{11} \cdot (H'_i \cdot \frac{h}{2} \eta \cdot V_{sz}^i + H'_i \cdot \frac{b}{2} \zeta \cdot V_{tz}^i) + R_{12} \cdot H_i \cdot \frac{h}{2} \cdot V_{sz}^i + R_{13} \cdot H_i \cdot \frac{b}{2} \cdot V_{tz}^i; \quad i = 1, 3$$

$$A_{zi} = -R_{11} \cdot (H'_i \cdot \frac{h}{2} \eta \cdot V_{sy}^i + H'_i \cdot \frac{b}{2} \zeta \cdot V_{ty}^i) - R_{12} \cdot H_i \cdot \frac{h}{2} \cdot V_{sy}^i - R_{13} \cdot H_i \cdot \frac{b}{2} \cdot V_{ty}^i; \quad i = 1, 3$$

A. Strain-displacement transformation matrix B

$$B_{xi} = -R_{21} \cdot H'_i \cdot \frac{b}{2} \zeta \cdot (1 - \eta) \cdot V_{tz}^i + R_{22} \cdot H_i \cdot \frac{b}{2} \cdot \zeta \cdot V_{tz}^i - R_{23} \cdot H_i \cdot \frac{b}{2} \cdot (1 - \eta) \cdot V_{tx}^i; \quad i = 1, 3$$

$$B_{zi} = R_{21} \cdot H'_i \cdot \frac{b}{2} \zeta \cdot (1 - \eta) \cdot V_{tx}^i - R_{22} \cdot H_i \cdot \frac{b}{2} \cdot \zeta \cdot V_{tx}^i + R_{23} \cdot H_i \cdot \frac{b}{2} \cdot (1 - \eta) \cdot V_{tx}^i; \quad i = 1, 3$$

$$B_{vj} = R_{22} \frac{\partial V_j}{\partial \eta} + R_{23} \frac{\partial V_j}{\partial \zeta}; \quad j = 1, 2, 3, 4$$

$$C_{xi} = R_{31} \cdot H'_i \cdot \frac{h}{2} \eta \cdot (1 - \zeta) \cdot V_{sy}^i + R_{32} \cdot H_i \cdot \frac{h}{2} \cdot (1 - \zeta) \cdot V_{sy}^i - R_{33} \cdot H_i \cdot \frac{h}{2} \eta \cdot V_{sy}^i; \quad i = 1, 3$$

$$C_{yi} = -R_{31} \cdot H'_i \cdot \frac{h}{2} \eta \cdot (1 - \zeta) \cdot V_{sx}^i - R_{32} \cdot H_i \cdot \frac{h}{2} \cdot (1 - \zeta) \cdot V_{sx}^i + R_{33} \cdot H_i \cdot \frac{h}{2} \eta \cdot V_{sx}^i; \quad i = 1, 3$$

$$C_{wj} = R_{32} \frac{\partial W_j}{\partial \eta} + R_{33} \frac{\partial W_j}{\partial \zeta}; \quad j = 1, 2, 3, 4$$

$$D_{xi} = -R_{11} \cdot H'_i \cdot \frac{b}{2} \zeta \cdot (1 - \eta) \cdot V_{tz}^i + R_{12} \cdot H_i \cdot \frac{b}{2} \cdot \zeta \cdot V_{tz}^i - R_{13} \cdot H_i \cdot \frac{b}{2} \cdot (1 - \eta) \cdot V_{tz}^i; \quad i = 1, 3$$

$$D_{yi} = R_{21} \cdot (H'_i \cdot \frac{h}{2} \eta \cdot V_{sz}^i + H'_i \cdot \frac{b}{2} \zeta \cdot V_{tz}^i) + R_{22} \cdot H_i \cdot \frac{h}{2} \cdot V_{sz}^i + R_{23} \cdot H_i \cdot \frac{b}{2} \cdot V_{tz}^i; \quad i = 1, 3$$

$$D_{zi} = -R_{21} \cdot (H'_i \cdot \frac{h}{2} \eta \cdot V_{sy}^i + H'_i \cdot \frac{b}{2} \zeta \cdot V_{ty}^i) - R_{22} \cdot H_i \cdot \frac{h}{2} \cdot V_{sy}^i - R_{23} \cdot H_i \cdot \frac{b}{2} \cdot V_{ty}^i + \dots$$

$$R_{11} \cdot H'_i \cdot \frac{b}{2} \zeta \cdot (1 - \eta) \cdot V_{tx}^i - R_{12} \cdot H_i \cdot \frac{b}{2} \zeta \cdot V_{tx}^i + R_{13} \cdot H_i \cdot \frac{b}{2} \cdot (1 - \eta) \cdot V_{tx}^i; \quad i = 1, 3$$

$$D_{vj} = R_{12} \frac{\partial V_j}{\partial \eta} + R_{13} \frac{\partial V_j}{\partial \zeta}; \quad j = 1, 2, 3, 4$$

$$E_{xi} = R_{11} \cdot H'_i \cdot \frac{h}{2} \eta \cdot (1 - \zeta) \cdot V_{sy}^i + R_{12} \cdot H_i \cdot \frac{h}{2} \cdot (1 - \zeta) \cdot V_{sy}^i - R_{13} \cdot H_i \cdot \frac{h}{2} \eta \cdot V_{sy}^i; \quad i = 1, 3$$

$$E_{yi} = R_{31} \cdot (H'_i \cdot \frac{h}{2} \eta \cdot V_{sz}^i + H'_i \cdot \frac{b}{2} \zeta \cdot V_{tz}^i) + R_{32} \cdot H_i \cdot \frac{h}{2} \cdot V_{sz}^i + R_{33} \cdot H_i \cdot \frac{b}{2} \cdot V_{tz}^i \dots$$

$$R_{11} \cdot H'_i \cdot \frac{h}{2} \eta \cdot (1 - \zeta) \cdot V_{sx}^i - R_{12} \cdot H_i \cdot \frac{h}{2} \cdot (1 - \zeta) \cdot V_{sx}^i + R_{13} \cdot H_i \cdot \frac{h}{2} \eta \cdot V_{sx}^i; \quad i = 1, 3$$

$$E_{zi} = -R_{31} \cdot (H_i' \cdot \frac{h}{2} \eta \cdot V_{sy}^i + H_i' \cdot \frac{b}{2} \zeta \cdot V_{ty}^i) - R_{32} \cdot H_i \cdot \frac{h}{2} \cdot V_{sy}^i - R_{33} \cdot H_i \cdot \frac{b}{2} \cdot V_{ty}^i ; \quad i = 1, 3$$

$$E_{wj} = R_{12} \frac{\partial W_j}{\partial \eta} + R_{13} \frac{\partial W_j}{\partial \zeta}; \quad j = 1, 2, 3, 4$$

$$F_{xi} = -R_{31} \cdot H_i' \cdot \frac{b}{2} \zeta \cdot (1 - \eta) \cdot V_{tz}^i + R_{32} \cdot H_i \cdot \frac{b}{2} \cdot \zeta \cdot V_{tz}^i - R_{33} \cdot H_i \cdot \frac{b}{2} \cdot (1 - \eta) \cdot V_{tz}^i + \dots$$

$$R_{21} \cdot H_i' \cdot \frac{h}{2} \eta \cdot (1 - \zeta) \cdot V_{sy}^i + R_{22} \cdot H_i \cdot \frac{h}{2} \cdot (1 - \zeta) \cdot V_{sy}^i - R_{23} \cdot H_i \cdot \frac{h}{2} \eta \cdot V_{sy}^i; \quad i = 1, 3$$

$$F_{yi} = -R_{21} \cdot H_i' \cdot \frac{h}{2} \eta \cdot (1 - \zeta) \cdot V_{sx}^i - R_{22} \cdot H_i \cdot \frac{h}{2} \cdot (1 - \zeta) \cdot V_{sx}^i + R_{23} \cdot H_i \cdot \frac{h}{2} \eta \cdot V_{sx}^i; \quad i = 1, 3$$

$$F_{zi} = R_{31} \cdot H_i' \cdot \frac{b}{2} \zeta \cdot (1 - \eta) \cdot V_{tx}^i - R_{32} \cdot H_i \cdot \frac{b}{2} \zeta \cdot V_{tx}^i + R_{33} \cdot H_i \cdot \frac{b}{2} \cdot (1 - \eta) \cdot V_{tx}^i ; \quad i = 1, 3$$

$$F_{vj} = R_{32} \frac{\partial V_j}{\partial \eta} + R_{33} \frac{\partial V_j}{\partial \zeta}; \quad j = 1, 2, 3, 4$$

$$F_{wj} = R_{22} \frac{\partial W_j}{\partial \eta} + R_{23} \frac{\partial W_j}{\partial \zeta}; \quad j = 1, 2, 3, 4$$

A. Strain-displacement transformation matrix B

Appendix B

Calculations of matrix D and E

B.1 Calculation of matrix D

The matrices \mathbf{D}_{mn} and \mathbf{D}_{sn} in Equation (4.44) and Equation (4.45), all of dimensions (3×20) , can be derived by tedious differentiation of the displacement approximation with respect to the local coordinates. In the case of the beam-to-beam contact, since both two beams are treated equivalently, the subscripts "m" and "s" does not mean the distinction between master and slave beam. The matrices \mathbf{D}_{mn} and \mathbf{D}_{sn} have the same form, in order to simplify the notation, subscript "mn" and "sn" used previously are dropped here. So, matrix \mathbf{D} can be expressed as follows:

$$[\mathbf{D}]_{3 \times 20} = \begin{bmatrix} H_1 & 0 & 0 & 0 & A_{y1} & A_{z1} & 0 & 0 & 0 & 0 \\ 0 & H_1 & 0 & B_{x1} & 0 & B_{z1} & V_1 & V_2 & V_2 & V_4 \\ 0 & 0 & H_1 & C_{x1} & C_{y1} & 0 & 0 & 0 & 0 & 0 \\ 0 & 0 & 0 & 0 & H_3 & 0 & 0 & 0 & A_{y3} & A_{z3} \\ 0 & 0 & 0 & 0 & 0 & H_3 & 0 & B_{x3} & 0 & B_{z3} \\ W_1 & W_2 & W_3 & W_4 & 0 & 0 & H_3 & C_{x3} & C_{y3} & 0 \end{bmatrix} \quad (B.1)$$

Other simplifying notations used in Equation (B.1) are:

$$A_{yi} = H_i \cdot \frac{h}{2} \eta \cdot V_{sy}^i + H_i \cdot \frac{b}{2} \zeta \cdot V_{ty}^i; \quad i = 1, 3$$

$$A_{zi} = -H_i \cdot \frac{h}{2} \eta \cdot V_{sy}^i - H_i \cdot \frac{b}{2} \zeta \cdot V_{ty}^i; \quad i = 1, 3$$

$$B_{xi} = -H_i \cdot \frac{b}{2} \zeta \cdot (1 - \eta) \cdot V_{tz}^i; \quad i = 1, 3$$

$$B_{zi} = H_i \cdot \frac{b}{2} \zeta \cdot (1 - \eta) \cdot V_{tx}^i; \quad i = 1, 3$$

$$C_{xi} = H_i \cdot \frac{h}{2} \eta \cdot (1 - \zeta) \cdot V_{sy}^i; \quad i = 1, 3$$

$$C_{yi} = -H_i \cdot \frac{h}{2} \eta \cdot (1 - \zeta) \cdot V_{sx}^i; \quad i = 1, 3$$

B.2 Calculation of matrix E

Similarly, for the matrices \mathbf{E}_{mn} and \mathbf{E}_{sn} in Equation (4.46) and Equation (4.47), dropping the subscript "mn" and "sn" used previously, which can be expressed as:

$$[\mathbf{E}]_{3 \times 20} = \begin{bmatrix} H'_1 & 0 & 0 & 0 & A_{y1,\xi} & A_{z1,\xi} & 0 & 0 & 0 & 0 \\ 0 & H'_1 & 0 & B_{x1,\xi} & 0 & B_{z1,\xi} & 0 & 0 & 0 & 0 \\ 0 & 0 & H'_1 & C_{x1,\xi} & C_{y1,\xi} & 0 & 0 & 0 & 0 & 0 \\ 0 & 0 & 0 & 0 & H'_3 & 0 & 0 & 0 & A_{y3,\xi} & A_{z3,\xi} \\ 0 & 0 & 0 & 0 & 0 & H'_3 & 0 & B_{x3,\xi} & 0 & B_{z3,\xi} \\ 0 & 0 & 0 & 0 & 0 & 0 & H'_3 & C_{x3,\xi} & C_{y3,\xi} & 0 \end{bmatrix} \quad (B.2)$$

Where $(\)_{,\xi} = \partial(\)/\partial \xi$, and other simplifying notations used in Equation (B.2) are:

$$A_{yi,m} = H'_i \cdot \frac{h}{2} \eta \cdot V_{sz}^i + H'_i \cdot \frac{b}{2} \zeta \cdot V_{tz}^i; \quad i = 1, 3$$

$$A_{zi,m} = -H'_i \cdot \frac{h}{2} \eta \cdot V_{sy}^i - H'_i \cdot \frac{b}{2} \zeta \cdot V_{ty}^i; \quad i = 1, 3$$

$$B_{xi,m} = -H'_i \cdot \frac{b}{2} \zeta \cdot (1 - \eta) \cdot V_{tz}^i; \quad i = 1, 3$$

$$B_{zi,m} = H'_i \cdot \frac{b}{2} \zeta \cdot (1 - \eta) \cdot V_{tx}^i; \quad i = 1, 3$$

$$C_{xi,m} = H'_i \cdot \frac{h}{2} \eta \cdot (1 - \zeta) \cdot V_{sy}^i; \quad i = 1, 3$$

$$C_{yi,m} = -H'_i \cdot \frac{h}{2} \eta \cdot (1 - \zeta) \cdot V_{sx}^i; \quad i = 1, 3$$

Appendix C

Matrices **G** and **H** in Smoothing Procedures

The symbolic algebra computer program Matlab is used to calculate the components of the matrix **G** and **H** present in the formulation of the contact between the beams modelled by smooth 3D curves in Equation (4.48) to (4.51), with a description in Section 4.7.2. Here, the commands of Matlab worksheet are given which allow for calculation and creation of an output ready-to-use Matlab computer code for computing the matrix **G** and **H**. The results themselves are quite long and complicated which are not given here. Note that the presented worksheet commands are only valid for the inscribed curve Hermite smooth contact finite element.

```
syms X1 Y1 Z1 X2 Y2 Z2 X3 Y3 Z3 xsi L123 L12 L23

% the position vectors for three nodes of two adjacent beam elements
A1=[X1;Y1;Z1];
A2=[X2;Y2;Z2];
A3=[X3;Y3;Z3];

% the straight line distances in Equation (4.72)
L12=sqrt((X2-X1)^2+(Y2-Y1)^2+(Z2-Z1)^2);
L23=sqrt((X3-X2)^2+(Y3-Y2)^2+(Z3-Z2)^2);
L123=0.5*sqrt((X3-X1)^2+(Y3-Y1)^2+(Z3-Z1)^2);

% matrix B1 and B2 used in Equation (4.73) and Equation (4.74)
B1=1/4*[1 -1 1 1;0 0 -1 1;-3 3 -1 -1;2 2 1 -1];
B2=1/2*[1 1 0; 0 1 1; -L123/L12 L123/L12 0; 0 -L123/L23 L123/L23];

% polynomial coefficients vector in Equation (4.74) and Equation (4.75)
a1=B1*B2*[X1;X2;X3];
a2=B1*B2*[Y1;Y2;Y3];
a3=B1*B2*[Z1;Z2;Z3];

%the vector of nodal position
q=[A1;A2;A3];
```

C. Matrices G and H in Smoothing Procedures

```
% calculation of matrix G
for i=1:9
    g1(1,i)=xsi^3*diff(a1(1),q(i))+xsi^2*diff(a1(2),q(i))+...
        +xsi*diff(a1(3),q(i))+diff(a1(4),q(i));
    g2(1,i)=xsi^3*diff(a2(1),q(i))+xsi^2*diff(a2(2),q(i))+...
        +xsi*diff(a2(3),q(i))+diff(a2(4),q(i));
    g3(1,i)=xsi^3*diff(a3(1),q(i))+xsi^2*diff(a3(2),q(i))+...
        +xsi*diff(a3(3),q(i))+diff(a3(4),q(i));
end
G=[g1;g2;g3]

% calculation of matrix H
for i=1:9
    h1(1,i)=3*xsi^2*diff(a1(1),q(i))+2*xsi*diff(a1(2),q(i))+...
        +diff(a1(3),q(i));
    h2(1,i)=3*xsi^2*diff(a2(1),q(i))+2*xsi*diff(a2(2),q(i))+...
        +diff(a2(3),q(i));
    h3(1,i)=3*xsi^2*diff(a3(1),q(i))+2*xsi*diff(a3(2),q(i))+...
        +diff(a3(3),q(i));
end
H=[h1;h2;h3]
```

Bibliography

[ABA 13] ABAQUS

Abaqus analysis User's Manual, 2013.

[AIM 09] AIMENE Y., VIDAL-SALLÉ E., HAGÈGE B., SIDOROFF F., BOISSE P.

A hyperelastic approach for composite reinforcement large deformation analysis. *Journal of Composite materials*, , 2009, Sage Publications.

[ALT 13] ALTBACH H., ALTBACH J. W., KISSING W.

Mechanics of composite structural elements. Springer Science & Business Media, 2013.

[ARG 64] ARGYRIS J., KAMEL H., KELSEY S.

Matrix methods of structural analysis. a precis of recent developments(Matrix methods of structural analysis). 1964., , 1964, p. 1–164.

[ARG 75] ARGYRIS J. H., DUNNE P. C.

On the application of the natural mode technique to small strain large displacement problems. rapport, 1975.

[ARG 79] ARGYRIS J., BALMER H., DOLTSINIS J. S., DUNNE P., HAASE M., KLEIBER M., MALEJANNAKIS G., MLEJNEK H.-P., MÜLLER M., SCHARPF D.

Finite element method: the natural approach. *Computer Methods in Applied Mechanics and Engineering*, vol. 17, 1979, p. 1–106, North-Holland.

[ARG 82] ARGYRIS J.

An excursion into large rotations. *Computer methods in applied mechanics and engineering*, vol. 32, n° 1, 1982, p. 85–155, Elsevier.

[BAD 09] BADEL P., VIDAL-SALLÉ E., MAIRE E., BOISSE P.

Simulation and tomography analysis of textile composite reinforcement deformation at the mesoscopic scale. *International Journal of Material Forming*, vol. 2, n° 1, 2009, p. 189–192, Springer.

[BAL 08] BALLHAUSE D., KÖNIG M., KRÖPLIN B.

Modelling fabric-reinforced membranes with the discrete element method. *Textile Composites and Inflatable Structures II*, p. 51–67 Springer, 2008.

Bibliography

- [BAS 12] BASSA B., SABOURIN F., BRUNET M.
A new nine-node solid-shell finite element using complete 3D constitutive laws. *International Journal for Numerical Methods in Engineering*, vol. 92, n° 7, 2012, p. 589–636, Wiley Online Library.
- [BAT 75] BATHE K.-J., RAMM E., WILSON E. L.
Finite element formulations for large deformation dynamic analysis. *International Journal for Numerical Methods in Engineering*, vol. 9, n° 2, 1975, p. 353–386, Wiley Online Library.
- [BAT 76] BATHE K.
Static and Dynamic Geometric and Material Nonlinear Analysis Using ADINA, Report 82448-2, Acoustics and Vibration Laboratory. *Mechanical Engineering Department, Massachusetts Institute of Technology*, vol. 5, 1976.
- [BAT 79] BATHE K.-J., BOLOURCHI S.
Large displacement analysis of three-dimensional beam structures. *International Journal for Numerical Methods in Engineering*, vol. 14, n° 7, 1979, p. 961–986, Wiley Online Library.
- [BAT 80] BATHE K.-J., BOLOURCHI S.
A geometric and material nonlinear plate and shell element. *Computers & structures*, vol. 11, n° 1, 1980, p. 23–48, Elsevier.
- [BEL 73] BELYTSCHKO T., HSIEH B.
Non-linear transient finite element analysis with convected co-ordinates. *International Journal for Numerical Methods in Engineering*, vol. 7, n° 3, 1973, p. 255–271, Wiley Online Library.
- [BEL 77] BELYTSCHKO T., SCHWER L., KLEIN M.
Large displacement, transient analysis of space frames. *International journal for numerical methods in engineering*, vol. 11, n° 1, 1977, p. 65–84, Wiley Online Library.
- [BEL 79] BELYTSCHKO T., GLAUM L. W.
Applications of higher order corotational stretch theories to nonlinear finite element analysis. *Computers & Structures*, vol. 10, n° 1, 1979, p. 175–182, Elsevier.
- [BOI 93] BOISSE P., GELIN J., SABHI H.
Experimental study and finite element simulation of glass fiber fabric shaping process. *ASME MATER DIV PUBL MD, ASME, NEW YORK, NY, (USA)*, 1993, vol. 46, 1993, p. 587–608.
- [BOI 05] BOISSE P., ZOUARI B., GASSER A.
A mesoscopic approach for the simulation of woven fibre composite forming. *Composites science and technology*, vol. 65, n° 3, 2005, p. 429–436, Elsevier.

- [BOI 12] BOISSE P.
Composite reinforcements for optimum performance. *MRS Bulletin*, vol. 37, n° 09, 2012, p. 865–865, Cambridge Univ Press.
- [BOS 05] BOSO D., LITEWKA P., SCHREFLER B., WRIGGERS P.
A 3D beam-to-beam contact finite element for coupled electric–mechanical fields. *International journal for numerical methods in engineering*, vol. 64, n° 13, 2005, p. 1800–1815, Wiley Online Library.
- [BRI 04] BRIDGENS B., GOSLING P., BIRCHALL M.
Membrane material behaviour: concepts, practice & developments. *Structural Engineer*, vol. 82, n° 14, 2004, p. 28–33.
- [BUE 01] BUET-GAUTIER K., BOISSE P.
Experimental analysis and modeling of biaxial mechanical behavior of woven composite reinforcements. *Experimental mechanics*, vol. 41, n° 3, 2001, p. 260–269, Springer.
- [CAM 03] CAMPBELL JR F. C.
Manufacturing processes for advanced composites. Elsevier, 2003.
- [CAM 10] CAMPBELL F. C.
Structural composite materials. ASM international, 2010.
- [CAR 01] CARVELLI V., POGGI C.
A homogenization procedure for the numerical analysis of woven fabric composites. *Composites Part A: applied science and manufacturing*, vol. 32, n° 10, 2001, p. 1425–1432, Elsevier.
- [CHA 88] CHAN S. L.
Geometric and material non-linear analysis of beam-columns and frames using the minimum residual displacement method. *International Journal for Numerical Methods in Engineering*, vol. 26, n° 12, 1988, p. 2657–2669, Wiley Online Library.
- [CHE 99] CHEN B., CHOU T.-W.
Compaction of woven-fabric preforms in liquid composite molding processes: single-layer deformation. *Composites Science and Technology*, vol. 59, n° 10, 1999, p. 1519–1526, Elsevier.
- [CHU 72] CHU K., RAMPETSREITER R.
Large deflection buckling of space frames. *Journal of the Structural Division*, vol. 98, n° 12, 1972, p. 2701–2722.
- [COR 09] CORNELISSEN B., AKKERMANN R.
Analysis of yarn bending behaviour. , 2009, The British Composites Society.

Bibliography

- [CRE 06] CREECH G., PICKETT A.
Meso-modelling of non-crimp fabric composites for coupled drape and failure analysis.
Journal of materials science, vol. 41, n° 20, 2006, p. 6725–6736, Springer.
- [CUR 88] CURNIER A., ALART P.
A generalized Newton method for contact problems with friction. rapport, 1988.
- [DEB 10] DE BILBAO E., SOULAT D., HIVET G., GASSER A.
Experimental study of bending behaviour of reinforcements. *Experimental Mechanics*, vol. 50, n° 3, 2010, p. 333–351, Springer.
- [DEL 09] DE LUYCKER E.
Simulation et expérimentation en mise en forme de renforts composites 3D interlocks.
PhD thesis, 2009.
- [DON 01] DONG L., LEKAKOU C., BADER M.
Processing of composites: simulations of the draping of fabrics with updated material behaviour law. *Journal of composite materials*, vol. 35, n° 2, 2001, p. 138–163, Sage Publications.
- [DUH 06] DUHOVIC M., BHATTACHARYYA D.
Simulating the deformation mechanisms of knitted fabric composites. *Composites Part A: Applied Science and Manufacturing*, vol. 37, n° 11, 2006, p. 1897–1915, Elsevier.
- [DUR 05] DURVILLE D.
Numerical simulation of entangled materials mechanical properties. *Journal of materials science*, vol. 40, n° 22, 2005, p. 5941–5948, Springer.
- [DUR 08] DURVILLE D.
Finite element simulation of the mechanical behaviour of textile composites at the mesoscopic scale of individual fibers. *textile composites and inflatable structures II*, p. 15–34 Springer, 2008.
- [DUR 09] DURVILLE D.
Finite element simulation of textile materials at the fiber scale. *arXiv preprint arXiv:0912.1268*, , 2009.
- [DUR 10] DURVILLE D.
Simulation of the mechanical behaviour of woven fabrics at the scale of fibers. *International journal of material forming*, vol. 3, n° 2, 2010, p. 1241–1251, Springer.
- [DUR 12] DURVILLE D.
Contact-friction modeling within elastic beam assemblies: an application to knot tightening. *Computational Mechanics*, vol. 49, n° 6, 2012, p. 687–707, Springer.

[FEL 73] FELIPPA C., SHARIFI P.

Computer implementation of nonlinear finite element analysis. *Numerical solution of nonlinear structural problems*, , 1973, p. 31–49.

[FIN 04] FINCKH H.

Numerical simulation of mechanical properties of fabrics: weaving numerische simulation der mechanischen eigenschaften textiler flächengebilde - gewebeherstellung. *Proceedings of the 3rd German LS-DYNA forum 2*, 2004.

[FLO 13] FLORIMOND C.

Contributions à la modélisation mécanique du comportement de mèches de renforts tissés à l'aide d'un schéma éléments finis implicite. PhD thesis, Lyon, INSA, 2013.

[GAO 16] GAO S., LIANG B., VIDAL-SALLE E., CHINESTA F., CUETO E., ABISSET-CHAVANNE E.

Analysis of large displacements/small strains of enhanced 3D beam with section changes. *AIP Conference Proceedings*, vol. 1769 AIP Publishing, 2016, Page 170015.

[GAS 00] GASSER A., BOISSE P., HANKLAR S.

Mechanical behaviour of dry fabric reinforcements. 3D simulations versus biaxial tests. *Computational materials science*, vol. 17, n° 1, 2000, p. 7–20, Elsevier.

[GAT 10] GATOUILLAT S., VIDAL-SALLÉ E., BOISSE P.

Advantages of the meso/macro approach for the simulation of fibre composite reinforcements. *International Journal of Material Forming*, vol. 3, n° 1, 2010, p. 643–646, Springer.

[GRO 66] GROSBERG P.

The mechanical properties of woven fabrics part ii: the bending of woven fabrics. *Textile Research Journal*, vol. 36, n° 3, 1966, p. 205–211, Sage Publications.

[GRO 80] GROSBERG P., HEARLE J., THWAITES J., AMIRBAYAT J.

Mechanics of flexible fiber assemblies. *NATO ASI Series, The Netherlands*, , 1980, Page 197.

[HAM 08] HAMILA N., BOISSE P.

Simulations of textile composite reinforcement draping using a new semi-discrete three node finite element. *Composites Part B: Engineering*, vol. 39, n° 6, 2008, p. 999–1010, Elsevier.

[HAM 09] HAMILA N., BOISSE P., SABOURIN F., BRUNET M.

A semi-discrete shell finite element for textile composite reinforcement forming simulation. *International journal for numerical methods in engineering*, vol. 79, n° 12, 2009, p. 1443–1466, Wiley Online Library.

Bibliography

- [HOR 78] HORRIGMOE G., BERGAN P. G.
Nonlinear analysis of free-form shells by flat finite elements. *Computer Methods in Applied Mechanics and Engineering*, vol. 16, n° 1, 1978, p. 11–35, Elsevier.
- [HSI 87] HSIAO K. M., HOU F. Y.
Nonlinear finite element analysis of elastic frames. *Computers & structures*, vol. 26, n° 4, 1987, p. 693–701, Elsevier.
- [HUG 81] HUGHES T. J., LIU W. K.
Nonlinear finite element analysis of shells: Part I. Three-dimensional shells. *Computer methods in applied mechanics and engineering*, vol. 26, n° 3, 1981, p. 331–362, Elsevier.
- [JOH 74] JOHNSON K.
. « Contact mechanics, 1985 », 1974.
- [KAW 73a] KAWABATA S., NIWA M., KAWAI H.
3 THE FINITE-DEFORMATION THEORY OF PLAIN-WEAVE FABRICS PART I: THE BIAXIAL-DEFORMATION THEORY. *Journal of the textile institute*, vol. 64, n° 1, 1973, p. 21–46, Taylor & Francis.
- [KAW 73b] KAWABATA S., NIWA M., KAWAI H.
5 THE FINITE-DEFORMATION THEORY OF PLAIN-WEAVE FABRICS. PART III: THE SHEAR-DEFORMATION THEORY. *Journal of the textile institute*, vol. 64, n° 2, 1973, p. 62–85, Taylor & Francis.
- [KAW 14] KAWA O., LITEWKA P.
Contact between 3-D beams with deformable circular cross sections. *Recent Advances in Computational Mechanics*, T. Łodygowski, J. Rakowski, P. Litewka, Eds, , 2014, p. 183–190.
- [KAW 15] KAWA O., LITEWKA P.
Contact with Friction Between 3D Beams with Deformable Circular Cross Sections. *Engineering Transactions*, vol. 63, n° 4, 2015, p. 439–462.
- [KHA 10] KHAN M., MABROUKI T., VIDAL-SALLÉ E., BOISSE P.
Numerical and experimental analyses of woven composite reinforcement forming using a hypoelastic behaviour. Application to the double dome benchmark. *Journal of Materials Processing Technology*, vol. 210, n° 2, 2010, p. 378–388, Elsevier.
- [KIK 88] KIKUCHI N., ODEN J. T.
Contact problems in elasticity: a study of variational inequalities and finite element methods, vol. 8. siam, 1988.

[KIN 05] KING M., JEARANAISILAWONG P., SOCRATE S.

A continuum constitutive model for the mechanical behavior of woven fabrics. *International Journal of Solids and Structures*, vol. 42, n° 13, 2005, p. 3867–3896, Elsevier.

[KLA 86] KLARBRING A.

A mathematical programming approach to three-dimensional contact problems with friction. *Computer Methods in Applied Mechanics and Engineering*, vol. 58, n° 2, 1986, p. 175–200, Elsevier.

[KON 08] KONYUKHOV A., SCHWEIZERHOF K.

Covariant description for contact between arbitrary curves: general approach for beams, cables and surface edges. *8th World Congress on Computational Mechanics/5th European congress on Computational methods in Applied Sciences and Engineering Methods in Mechanics, Venice, Italy, June, 2008*.

[KON 10] KONYUKHOV A., SCHWEIZERHOF K.

Geometrically exact covariant approach for contact between curves. *Computer Methods in Applied Mechanics and Engineering*, vol. 199, n° 37, 2010, p. 2510–2531, Elsevier.

[KON 11a] KONYUKHOV A., SCHWEIZERHOF K.

On a geometrically exact theory for contact interactions. *Trends in Computational Contact Mechanics*, p. 41–56 Springer, 2011.

[KON 11b] KONYUKHOV A., SCHWEIZERHOF K., METZGER A.

On contact between curves and rigid surfaces from verification of the Euler-Eytelwein problem to knots. *Comput Plast XI: Fundam Appl COMPLAS XI*, , 2011, p. 147–158.

[LAH 04] LAHEY T., HEPPLER G.

Mechanical modeling of fabrics in bending. *Journal of applied mechanics*, vol. 71, n° 1, 2004, p. 32–40, American Society of Mechanical Engineers.

[LAU 93] LAURSEN T., SIMO J.

A continuum-based finite element formulation for the implicit solution of multibody, large deformation-frictional contact problems. *International Journal for numerical methods in engineering*, vol. 36, n° 20, 1993, p. 3451–3485, Wiley Online Library.

[LAU 02] LAURSEN T. A.

. « Computational Contact and Impact Mechanics: Fundamentals of Modelling Interfacial Phenomena in Nonlinear Finite Element Analysis », 2002.

[LIA 14] LIANG B., HAMILA N., PEILLON M., BOISSE P.

Analysis of thermoplastic prepreg bending stiffness during manufacturing and of its influence on wrinkling simulations. *Composites Part A: Applied Science and Manufacturing*, vol. 67, 2014, p. 111–122, Elsevier.

Bibliography

- [LIT 02a] LITEWKA P., WRIGGERS P.
Frictional contact between 3D beams. *Computational mechanics*, vol. 28, n° 1, 2002, p. 26–39, Springer.
- [LIT 02b] LITEWKA P., WRIGGERS P.
Contact between 3D beams with rectangular cross-sections. *International journal for numerical methods in engineering*, vol. 53, n° 9, 2002, p. 2019–2041, Wiley Online Library.
- [LIT 07a] LITEWKA P.
Hermite polynomial smoothing in beam-to-beam frictional contact. *Computational Mechanics*, vol. 40, n° 5, 2007, p. 815–826, Springer.
- [LIT 07b] LITEWKA P.
Smooth frictional contact between beams in 3D. *IUTAM Symposium on Computational Methods in Contact Mechanics* Springer, 2007, p. 157–176.
- [LIT 10] LITEWKA P.
Finite element analysis of beam-to-beam contact, vol. 53. Springer Science & Business Media, 2010.
- [LIT 13] LITEWKA P.
Enhanced multiple-point beam-to-beam frictionless contact finite element. *Computational Mechanics*, vol. 52, n° 6, 2013, p. 1365–1380, Springer.
- [LIT 15] LITEWKA P.
Numerical analysis of frictionless contact between almost conforming beams. *Building Information Modeling: Framework for Structural Design*, , 2015, Page 191, CRC Press.
- [LOM 07] LOMOV S. V., IVANOV D. S., VERPOEST I., ZAKO M., KURASHIKI T., NAKAI H., HIROSAWA S.
Meso-FE modelling of textile composites: Road map, data flow and algorithms. *Composites Science and Technology*, vol. 67, n° 9, 2007, p. 1870–1891, Elsevier.
- [LUE 84] LUENBERGER D. G., YE Y. et al.
Linear and nonlinear programming, vol. 2. Springer, 1984.
- [MAK 94] MAKER B., LAURSEN T.
A finite element formulation for rod/continuum interactions: The one-dimensional slideline. *International journal for numerical methods in engineering*, vol. 37, n° 1, 1994, p. 1–18, Wiley Online Library.
- [MEE 84] MEEK J., TAN H. S.
Geometrically nonlinear analysis of space frames by an incremental iterative technique. *Computer methods in applied mechanics and engineering*, vol. 47, n° 3, 1984, p. 261–282, Elsevier.

- [MIA 08] MIAO Y., ZHOU E., WANG Y., CHEESEMAN B. A.
Mechanics of textile composites: Micro-geometry. *Composites Science and Technology*, vol. 68, n° 7, 2008, p. 1671–1678, Elsevier.
- [MOR 11] MOREAU J. J.
On unilateral constraints, friction and plasticity. *New variational techniques in mathematical physics*, p. 171–322 Springer, 2011.
- [MUK 01] MUKHERJEE S., PRATHAP G.
Analysis of shear locking in Timoshenko beam elements using the function space approach. *Communications in numerical methods in engineering*, vol. 17, n° 6, 2001, p. 385–393, Wiley Online Library.
- [NGU 13] NGUYEN Q., VIDAL-SALLÉ E., BOISSE P., PARK C., SAOUAB A., BRÉARD J., HIVET G.
Mesoscopic scale analyses of textile composite reinforcement compaction. *Composites Part B: Engineering*, vol. 44, n° 1, 2013, p. 231–241, Elsevier.
- [PAP 81] PAPADRAKAKIS M.
Post-buckling analysis of spatial structures by vector iteration methods. *Computers & structures*, vol. 14, n° 5-6, 1981, p. 393–402, Elsevier.
- [PAR 89] PARISCH H.
A consistent tangent stiffness matrix for three-dimensional non-linear contact analysis. *International Journal for Numerical Methods in Engineering*, vol. 28, n° 8, 1989, p. 1803–1812, Wiley Online Library.
- [PEN 05] PENG X., CAO J.
A continuum mechanics-based non-orthogonal constitutive model for woven composite fabrics. *Composites part A: Applied Science and manufacturing*, vol. 36, n° 6, 2005, p. 859–874, Elsevier.
- [POP 66] POPPER P. G.
Mechanics of bending of fiber assemblies. PhD thesis, Massachusetts Institute of Technology, 1966.
- [PRA 82] PRATHAP G., BHASYAM G.
Reduced integration and the shear flexible beam element. *International Journal for Numerical Methods in Engineering*, vol. 18, n° 2, 1982, p. 195–210, Wiley Online Library.
- [PRO 11] PRODROMOU A. G., LOMOV S. V., VERPOEST I.
The method of cells and the mechanical properties of textile composites. *Composite structures*, vol. 93, n° 4, 2011, p. 1290–1299, Elsevier.

Bibliography

[RAM 77] RAMM E.

A plate/shell element for large deflections and rotations. *Formulations and computational algorithms in finite element analysis*, , 1977, p. 264–293, MIT Press Cambridge, MA.

[RAN 86] RANKIN C., BROGAN F.

An element independent corotational procedure for the treatment of large rotations. *Journal of pressure vessel technology*, vol. 108, n° 2, 1986, p. 165–174, American Society of Mechanical Engineers.

[RAO 00] RAO Y., FARRIS R. J.

A modeling and experimental study of the influence of twist on the mechanical properties of high-performance fiber yarns. *Journal of applied polymer science*, vol. 77, n° 9, 2000, p. 1938–1949, Wiley Online Library.

[REM 79] REMSETH S.

Nonlinear static and dynamic analysis of framed structures. *Computers & Structures*, vol. 10, n° 6, 1979, p. 879–897, Elsevier.

[ROG 89] ROGERS T.

Rheological characterization of anisotropic materials. *Composites*, vol. 20, n° 1, 1989, p. 21–27, Elsevier.

[SAN 11] SANSALONE M., SABOURIN F., BRUNET M.

A new shell formulation using complete 3D constitutive laws. *International Journal for Numerical Methods in Engineering*, vol. 86, n° 6, 2011, p. 688–716, Wiley Online Library.

[SAU 98] SAUNDERS R., LEKAKOU C., BADER M.

Compression and microstructure of fibre plain woven cloths in the processing of polymer composites. *Composites Part A: Applied Science and Manufacturing*, vol. 29, n° 4, 1998, p. 443–454, Elsevier.

[SHA 71] SHARIFI P., POPOV E. P.

Nonlinear buckling analysis of sandwich arches. *Journal of the Engineering Mechanics Division*, vol. 97, n° 5, 1971, p. 1397–1412, ASCE.

[SHAH 07] SHAHKARAMI A., VAZIRI R.

A continuum shell finite element model for impact simulation of woven fabrics. *International Journal of Impact Engineering*, vol. 34, n° 1, 2007, p. 104–119, Elsevier.

[SHE 07] SHERBURN M.

Geometric and mechanical modelling of textiles. PhD thesis, University of Nottingham, 2007.

- [SIM 92] SIMO J. C., LAURSEN T.
An augmented Lagrangian treatment of contact problems involving friction. *Computers & Structures*, vol. 42, n° 1, 1992, p. 97–116, Elsevier.
- [SPE 07] SPENCER A., SOLDATOS K.
Finite deformations of fibre-reinforced elastic solids with fibre bending stiffness. *International Journal of Non-Linear Mechanics*, vol. 42, n° 2, 2007, p. 355–368, Elsevier.
- [STA 06] STANKOVICH S., DIKIN D. A., DOMMETT G. H., KOHLHAAS K. M., ZIMNEY E. J., STACH E. A., PINER R. D., NGUYEN S. T., RUOFF R. S.
Graphene-based composite materials. *nature*, vol. 442, n° 7100, 2006, p. 282–286, Nature Publishing Group.
- [SUR 83] SURANA K. S.
Geometrically nonlinear formulation for the curved shell elements. *International Journal for Numerical Methods in Engineering*, vol. 19, n° 4, 1983, p. 581–615, Wiley Online Library.
- [TEN 07] TEN THIJE R., AKKERMAN R., HUÉTINK J.
Large deformation simulation of anisotropic material using an updated Lagrangian finite element method. *Computer methods in applied mechanics and engineering*, vol. 196, n° 33, 2007, p. 3141–3150, Elsevier.
- [TES 87] FOR TESTING A. S., MATERIALS
ASTM Standards and Literature References for Composite Materials. ASTM, 1987.
- [VAS 10] VASSILIADIS S., KALLIVRETAKI A., PROVATIDIS C.
Mechanical modelling of multifilament twisted yarns. *Fibers and Polymers*, vol. 11, n° 1, 2010, p. 89–96, Springer.
- [VEI 12] DA VEIGA L. B., LOVADINA C., REALI A.
Avoiding shear locking for the Timoshenko beam problem via isogeometric collocation methods. *Computer Methods in Applied Mechanics and Engineering*, vol. 241, 2012, p. 38–51, Elsevier.
- [VIO 09] VIOLEAU D., LADEVÈZE P., LUBINEAU G.
Micromodel-based simulations for laminated composites. *Composites Science and Technology*, vol. 69, n° 9, 2009, p. 1364–1371, Elsevier.
- [WAN 01] WANG Y., SUN X.
Digital-element simulation of textile processes. *Composites science and technology*, vol. 61, n° 2, 2001, p. 311–319, Elsevier.
- [WEM 69] WEMPNER G.
Finite elements, finite rotations and small strains of flexible shells. *International Journal of Solids and Structures*, vol. 5, n° 2, 1969, p. 117–153, Elsevier.

Bibliography

- [WEN 83] WEN R. K., RAHIMZADEH J.
Nonlinear elastic frame analysis by finite element. *Journal of Structural Engineering*, vol. 109, n° 8, 1983, p. 1952–1971, American Society of Civil Engineers.
- [WHI 95] WHITCOMB J., SRIRENGAN K., CHAPMAN C.
Evaluation of homogenization for global/local stress analysis of textile composites. *Composite structures*, vol. 31, n° 2, 1995, p. 137–149, Elsevier.
- [WRI 90] WRIGGERS P., VAN T. V., STEIN E.
Finite element formulation of large deformation impact-contact problems with friction. *Computers & Structures*, vol. 37, n° 3, 1990, p. 319–331, Elsevier.
- [WRI 92] WRIGGERS P., MIEHE C.
On the treatment of contact constraints within coupled thermomechanical analysis. *Finite Inelastic Deformations Theory and Applications*, p. 333–347 Springer, 1992.
- [WRI 94] WRIGGERS P., MIEHE C.
Contact constraints within coupled thermomechanical analysis a finite element model. *Computer Methods in Applied Mechanics and Engineering*, vol. 113, n° 3-4, 1994, p. 301–319, Elsevier.
- [WRI 97] WRIGGERS P., ZAVARISE G.
On contact between three-dimensional beams undergoing large deflections. *Communications in numerical methods in engineering*, vol. 13, 1997, p. 429–438.
- [WRI 06] WRIGGERS P.
Computational contact mechanics. Springer Science & Business Media, 2006.
- [XUE 05] XUE P., CAO J., CHEN J.
Integrated micro/macro-mechanical model of woven fabric composites under large deformation. *Composite Structures*, vol. 70, n° 1, 2005, p. 69–80, Elsevier.
- [YU 02] YU W. R., POURBOGHRAT F., CHUNG K., ZAMPALONI M., KANG T. J.
Non-orthogonal constitutive equation for woven fabric reinforced thermoplastic composites. *Composites Part A: Applied Science and Manufacturing*, vol. 33, n° 8, 2002, p. 1095–1105, Elsevier.
- [YU 05] YU W.-R., HARRISON P., LONG A.
Finite element forming simulation for non-crimp fabrics using a non-orthogonal constitutive equation. *Composites Part A: Applied Science and Manufacturing*, vol. 36, n° 8, 2005, p. 1079–1093, Elsevier.
- [ZAV 00] ZAVARISE G., WRIGGERS P.
Contact with friction between beams in 3-D space. *International Journal for Numerical Methods in Engineering*, vol. 49, n° 8, 2000, p. 977–1006, Chichester, New York, Wiley [etc.] 1969-.

[ZHO 04] ZHOU G., SUN X., WANG Y.

Multi-chain digital element analysis in textile mechanics. *Composites science and Technology*, vol. 64, n° 2, 2004, p. 239–244, Elsevier.

[ZIE 71] ZIEKIEWICZ O.

The finite element method in engineering science. *McGraw Hill, London*, , 1971.

FOLIO ADMINISTRATIF

THESE DE L'UNIVERSITE DE LYON OPEREE AU SEIN DE L'INSA LYON

NOM : GAO
(avec précision du nom de jeune fille, le cas échéant)

DATE de SOUTENANCE : 05 Avril, 2017

Prénoms : Sasa

TITRE : Development of a new 3D beam finite element with deformable section
(Développement d'un nouveau 3D poutre élément finis avec section déformable))

NATURE : Doctorat

Numéro d'ordre : 2017LYSEI026

Ecole doctorale : MEGA

Spécialité : Mécanique - Génie Mécanique - Génie Civil

RESUME :

Le nouvel élément de poutre est une évolution d'un élément de Timoshenko poutre avec un nœud supplémentaire situé à mi-longueur. Ce nœud supplémentaire permet l'introduction de trois composantes supplémentaires de contrainte afin que la loi constitutionnelle 3D complète puisse être utilisée directement. L'élément proposé a été introduit dans un code d'éléments finis dans Matlab et une série d'exemples de linéaires/petites contraintes ont été réalisées et les résultats sont systématiquement comparés avec les valeurs correspondantes des simulations ABAQUS/Standard 3D. Ensuite, la deuxième étape consiste à introduire le comportement orthotrope et à effectuer la validation de déplacements larges / petites contraintes basés sur la formulation Lagrangienne mise à jour. Une série d'analyses numériques est réalisée qui montre que l'élément 3D amélioré fournit une excellente performance numérique. En effet, l'objectif final est d'utiliser les nouveaux éléments de poutre 3D pour modéliser des fils dans une préforme composite textile. A cet effet, la troisième étape consiste à introduire un comportement de contact et à effectuer la validation pour un nouveau contact entre 3D poutres à section rectangulaire. La formulation de contact est dérivée sur la base de formulation de pénalité et de formulation Lagrangian mise à jour utilisant des fonctions de forme physique avec l'effet de cisaillement inclus. Un algorithme de recherche de contact efficace, qui est nécessaire pour déterminer un ensemble actif pour le traitement de contribution de contact, est élaboré. Et une linéarisation constante de la contribution de contact est dérivée et exprimée sous forme de matrice appropriée, qui est facile à utiliser dans l'approximation FEM. Enfin, on présente quelques exemples numériques qui ne sont que des analyses qualitatives du contact et de la vérification de l'exactitude et de l'efficacité de l'élément de 3D poutre proposé.

MOTS-CLÉS : Élément de 3D poutre amélioré; Section rectangulaire; Déformation de la section; Loi constitutionnelle 3D complète; Déplacements larges / petites contraintes; Mise à jour de la formulation Lagrangienne; Contact sans frottement; Lissage Hermite

Laboratoire (s) de recherche : Laboratoire de Mécanique des Contacts et des Solides
UMR CNRS 5514 - INSA de Lyon
20, avenue Albert Einstein 69621 Villeurbanne Cedex France

Directeur de thèse: Professeur Emmanuelle VIDAL-SALLE

Président de jury :

Composition du jury : Christophe BINETRUY Damien SOULAT

Emmanuelle VIDAL-SALLE Nahiène HAMILA

Philippe LE GROGNEC

